

# Berkeley Seismological Laboratory



Annual Report  
July 2008 - June 2009



**Berkeley Seismological Laboratory**  
**Annual Report**  
**July 2008 - June 2009**

### Cover Picture

Remotely operated vehicle (ROV) being deployed to BSL station MOBB. Since February 27, 2009, the BSL's and MBARI's ocean bottom seismometer station, MOBB, is sending data to our datacenter in real time. This is the culmination of a long effort on the part of both institutions. In the week before it was connected to the ocean bottom MARS science node, a 3 km long power and data cable was laid out to the MOBB site.

# Contents

<b>1</b>	<b>Director's Report</b>	<b>1</b>
1	Introduction . . . . .	1
2	History and Facilities . . . . .	1
3	BSL staff news . . . . .	3
4	Acknowledgements . . . . .	3
<b>2</b>	<b>Research Studies</b>	<b>5</b>
1	Tremor-tide Correlations and Near Lithostatic Pore Pressures on the Deep San Andreas Fault . . . . .	6
2	Detection of Missing Repeating Earthquakes Using Recurrence Elements Analysis . . . . .	8
3	TerraSAR InSAR Investigation of Active Crustal Deformation . . . . .	10
4	Creep Measurements on the Concord Fault from PS-InSAR . . . . .	12
5	Seismicity Changes and Aseismic Slip on the Sunda Megathrust Preceding the $M_w$ 8.4 2007 Earthquake	14
6	Moment Moment Tensors for Very Long Period Signals at Etna Volcano, Italy . . . . .	16
7	Temporal Variations in Crustal Scattering Structure near Parkfield, California, from Receiver Functions	18
8	Remote Triggering of Fault-Strength Changes on the San Andreas Fault at Parkfield . . . . .	20
9	Source Analysis of the Memorial Day Explosion, Kimchaek, North Korea . . . . .	22
10	Towards a continuous seismic wavefield scanning . . . . .	24
11	The rupture process of the Parkfield SAFOD target earthquakes obtained from the empirical Greens function waveform inversion method . . . . .	26
12	Nonvolcanic Tremor Evolution in the Parkfield, CA Region . . . . .	28
13	Stability of Local and Regional Coda: Application to the Wells, Nevada Sequence . . . . .	30
14	Anomalous Moment Tensor Solutions for The Geysers, CA . . . . .	32
15	Statistical Testing of Theoretical Rupture Models Against Kinematic Inversions . . . . .	34
16	Testing ElarmS in Japan . . . . .	36
17	Real-time Earthquake Detection and Hazard Assessment by ElarmS Across California . . . . .	38
18	Joint Inversion of Group Velocity Dispersion and Long Period Waveforms for Upper Mantle Structure	40
19	Reactivation of an Archean Craton: Constraints from P- and S-wave Tomography in North China . .	42
20	Plume vs. Plate: Convection Beneath the Pacific Northwest . . . . .	44
21	Imaging Shallow Cascadia Structure with Ambient Noise Tomography . . . . .	46
22	Seismic Anisotropy Beneath Cascadia and the Mendocino Triple Junction: Interaction of the Subducting Slab with Mantle Flow . . . . .	48
23	Recovering the Attenuation of Surface Waves from One-Bit Noise Correlations: A Theoretical Approach	50
24	The Origin of Seismic Anisotropy in the D" . . . . .	52
25	Toward a 3D Global Attenuation Model in the Lower Mantle from the Earth's Free Oscillations . . . .	54
26	Anisotropic North American Lithosphere and its Boundary with Asthenosphere . . . . .	56
27	Crustal Stress and Mechanical Anisotropy of the Lithosphere in Western North America . . . . .	58
28	Berkeley 3-D Isotropic and Anisotropic S-velocity Model of North American Upper Mantle, Updated to June 2008 . . . . .	61
29	Weak Mantle in NW India Probed by Postseismic GPS Measurements Following the 2001 Bhuj Earthquake . . . . .	63
30	Comprehensive Test Ban Monitoring: Contributions from Regional Moment Tensors to Determine Source Type and Depth . . . . .	66

<b>3</b>	<b>BSL Operations</b>	<b>67</b>
1	Berkeley Digital Seismic Network . . . . .	69
2	California Integrated Seismic Network . . . . .	78
3	Northern Hayward Fault Network . . . . .	83
4	Parkfield Borehole Network (HRSN) . . . . .	93
5	Bay Area Regional Deformation Network . . . . .	103
6	Northern California Earthquake Data Center . . . . .	109
7	Data Acquisition and Quality Control . . . . .	119
8	Northern California Earthquake Monitoring . . . . .	124
9	Outreach and Educational Activities . . . . .	130
	<b>Glossary</b>	<b>132</b>
	<b>Appendix I Publications, Presentations, and Panels 2008-2009</b>	<b>134</b>
	<b>Appendix II Seminar Speakers 2008-2009</b>	<b>148</b>
	<b>Appendix III Organization Chart 2008-2009</b>	<b>150</b>

# Chapter 1

## Director's Report

### 1 Introduction

As in previous years, I am pleased to introduce the 2008-09 Berkeley Seismological Laboratory Annual Report. This report covers two interrelated activities at BSL: basic research and real time earthquake monitoring operations. Chapter 2 describes the research accomplishments; Chapter 3 details progress in our development of infrastructure and facilities.

The basic research spans many topics in seismology and tectonics. They range from studies of the earth's deep structure and dynamics to various aspects of earthquake physics; from microearthquakes and tremor studies to studies of earthquake mechanisms and rupture spanning different times scales; and from slow tectonic deformation, to real time seismology and earthquake early warning. These are described in 30 short contributions in Chapter 2 of this report.

This year, I wish to particularly highlight two major accomplishments on the operational side of the BSL. First, after almost ten years of sustained efforts involving our CISN partners at the US Geological Survey and Caltech, and after many intermediate steps, we finally have a completely integrated earthquake notification system across the State of California. Notably, as of June 2009, completely mirrored systems operate continuously and in real time across the San Francisco Bay (at Berkeley and USGS Menlo Park), backing each other up in case of downtime due to failure or maintenance. This system relies on complementary seismic data from the Berkeley and USGS Northern California networks. The next step, which we are starting to plan, is to integrate real time GPS data into the system. This involves coordination with USGS Menlo Park in Northern California, and with various partners in southern California (i.e. USGS, UCSD). Towards this goal, we have continued to convert GPS data acquisition from our continuous GPS BARD (BARD network) to high rate sampling (1Hz), and have recently reorganized and consolidated the BARD data acquisition and processing system. Second, in March 2009, the autonomous ocean floor broadband station MOBB (Monterey Bay Ocean

Bottom Broad Band Observatory), which we have operated in collaboration with the Monterey Bay Aquarium Research Institute (MBARI) since 2002, was connected to the MARS cable (<http://www.mbari.org/mars>). It is now sending data continuously and in real time to the BSL, where we are integrating the data with those of the land-based stations, as a demonstration project for earthquake real-time notification.

Finally, I note that the development of replacement electronics for the STS-1 very broadband seismometers, under the technical leadership of our collaborator, Metrozet, Inc. has been completed. We are now actively assisting Metrozet in the ambitious goal of building a modernized version of the mechanical sensor. This unique seismometer, which revolutionized global seismology in the last 20 years, has not been produced by Streckeisen & Co. for several years. This raised considerable concerns in the international community. The BSL spearheaded the new development effort and helped secure funding for it from the NSF EAR-Instruments and Facilities program. We are designing a new baseplate for these seismometers, as well as participating in the testing of the new sensors.

The following sections give a brief historical overview of the BSL, and finally some BSL staff news.

### 2 History and Facilities

The Berkeley Seismological Laboratory (BSL), formerly the Berkeley Seismographic Station (BSS), is the oldest Organized Research Unit (ORU) on the UC Berkeley campus. Its mission is unique in that, in addition to research and education in seismology and earthquake-related science, it is responsible for providing timely information on earthquakes (particularly those that occur in northern and central California) to the UC Berkeley constituency, to the general public, and to various local and state government and private organizations. The BSL is therefore both a research center and a facility/data resource, which sets it apart from most other ORUs. A major component of our activities is focused on developing and maintaining several regional obser-

vational networks, and participating, along with other agencies, in various aspects of the collection, analysis, archival, and distribution of data pertaining to earthquakes, while maintaining a vigorous research program on earthquake processes and Earth structure. In addition, the BSL staff spends considerable time on public relations activities, including tours, talks to public groups, responding to public inquiries about earthquakes, and, more recently, World-Wide-Web presence (<http://seismo.berkeley.edu/>).

UC Berkeley installed the first seismograph in the Western Hemisphere at Mount Hamilton (MHC) in 1887. Since then, it has played a leading role in the operation of state-of-the-art seismic instruments and in the development of advanced methods for seismic data analysis and interpretation. Notably, the installation, starting in 1927, of Wood-Anderson seismographs at 4 locations in northern California (BKS, ARC, MIN and MHC) allowed the accurate determination of local earthquake magnitude ( $M_L$ ) from which a unique historical catalog of regional earthquakes has been maintained to this day, providing crucial input to earthquake probabilities studies.

Over the years, the BSS continued to keep apace of technological improvements. The first centrally telemetered network using phone lines in an active seismic region was installed by BSS in 1960. The BSS was the first institution in California to operate a 3-component "broadband" system (1963). It played a major role in the early characterization of earthquake sources using "moment tensors" and source-time functions. The BSS also made important contributions to the early definitions of detection/discrimination of underground nuclear tests and, jointly with UCB Engineering, to earthquake hazards work. Starting in 1986, the BSS acquired 4 state-of-the-art broadband instruments (STS-1), while simultaneously developing PC-based digital telemetry, albeit with limited resources. As the telecommunication and computer technology made rapid progress, in parallel with broadband instrument development, paper record reading was completely abandoned in favor of largely automated digital data analysis.

The current facilities of BSL have been built progressively over the last two decades, efforts initiated by significant "upgrade" funding from UC Berkeley in 1991-1995. The BSL currently operates and acquires data, continuously and in real-time, from over 60 regional observatories. These house a combination of broadband and strong motion seismic instrumentation installed in vaults, borehole seismic instrumentation, the permanent GPS stations of the Bay Area Regional Deformation (BARD) network, and electromagnetic sensors. The seismic data are fed into the BSL real-time processing and analysis system. Since 1996, they are used in conjunction with data from the USGS NCSN network in the joint earthquake notification program for northern California. This

program capitalizes on the complementary capabilities of the networks operated by each institution to provide rapid and reliable information on the location, size and other relevant source parameters of regional earthquakes. In recent years, a major emphasis in BSL instrumentation has been in densifying the state-of-the-art seismic and geodetic networks. At the same time, research efforts have been directed toward the development of robust methods for quasi-real time, automatic determination of earthquake source parameters and predicted strong ground motion, using a sparse network combining broadband and strong motion seismic sensors, as well as permanent geodetic GPS receivers. Recently research emphasis has been directed toward the development of "earthquake early warning" capabilities

The Berkeley Digital Seismic Network (BDSN), a regional network of 32 digital broadband and strong motion seismic stations with continuous telemetry to UC Berkeley, is the backbone of the BSL operations. This network provides the basic regional data for the real-time estimation of location, size and rupture parameters for earthquakes of M 3 and larger in central and northern California, within our Rapid Earthquake Data Integration (REDI) program. It is the Berkeley contribution to the California Integrated Seismic Network (CISN). The REDI program was replaced this June by the CISN software (see 8). The data from the BDSN also provide a fundamental database for the investigation of three-dimensional crustal structure and its effects on regional seismic wave propagation. This is ultimately crucial for estimating ground shaking for future earthquakes. Most stations also record auxiliary temperature/pressure channels, valuable in particular for background noise quality control. Complementing this network is a  $\sim 25$  station "high-resolution" network of borehole seismic sensors located along the Hayward Fault (HFN) and under the Bay Area bridges, operated jointly with the USGS/Menlo Park and linked to the Bridge Safety Project of the California Department of Transportation (Caltrans). The latter has facilitated the installation of sensor packages at 15 bedrock boreholes along 5 east bay bridges in collaboration with Lawrence Livermore National Laboratory (LLNL). A major science goal of this network is to collect high signal-to-noise data for micro-earthquakes along the Hayward Fault to gain insight into the physics that govern fault rupture and its nucleation. The BSL also operates and maintains the 13 element Parkfield borehole seismic array (HRSN). This array provides high quality data on micro-earthquakes, clusters and most recently tremors, and is an important reference for the San Andreas Fault Observatory at Depth (SAFOD). Since April 2002, the BSL collaborates with MBARI on the operation of a permanent broadband ocean bottom station, MOBB.

In addition to the seismic networks, the BSL oper-

ates, maintains and processes data from the 30 permanent geodetic stations of the BARD Network. It archives and distributes this data as well. Where possible, BARD sites are collocated with BDSN sites to minimize telemetry costs. In particular, sites are progressively being upgraded to 1 Hz sampling. This will support one focus of BSL research, the development of analysis methods which will combine seismic and geodetic data to rapidly estimate source parameters of significant earthquakes.

Finally, two of the BDSN stations (PKD, SAO) also share data acquisition and telemetry with 5-component electromagnetic sensors installed with the goal of investigating the possibility of detection of tectonic signals. In 2002-2003, automated quality control software was implemented to monitor the electromagnetic data.

Archival and distribution of data from these and other regional networks is performed at the Northern California Earthquake Data Center (NCEDC), operated at the BSL in collaboration with USGS/Menlo Park. The data reside on a mass-storage device (current holdings  $\sim 40$  terabytes), and are accessible “on-line” over the Internet (<http://www.ncedc.org>). Among others, data from the USGS Northern California Seismic Network (NCSN), are archived and distributed through the NCEDC. The NCEDC also maintains, archives and distributes the ANSS earthquake catalog.

Core University funding to our ORU has until now provided salary support for one staff scientist and several technical and administrative staff members, representing about 30% of the total infrastructure support. The remaining support comes from extra-mural grants and contracts, primarily from the USGS, NSF, and the State of California, through its Emergency Management Agency (CalEMA, formerly OES). We acknowledge valuable recent contributions from other sources such as Caltrans and PEER, as well as our Earthquake Research Affiliates. The effects of drastic budget cuts in FY09-10 are temporarily being offset by ARRA funding from the USGS. Over the next two years, these funds will allow us to upgrade the aging equipment at most of our remote observatories. This will put us in a better position to design the next generation earthquake notification system, the move towards earthquake early warning, using a combination of seismic and geodetic data.

### 3 BSL staff news

Changes in BSL staff in 2008-09 are as follows.

In the past year, the following graduate students associated with BSL completed their PhD’s: Ahyi Kim joined Schlumberger in Cambridge (UK) in summer 2009; Sean Ford is now a post-doc at Lawrence Livermore National Laboratory.

In the global seismology group, post-doc Laurent Stehly left for a research position at the University of

Nice (France). Post-doc Nicolas Houlié left in July 2009 and now holds a research position at the University of Leeds (UK). There have been several new arrivals: Scott French, Patrick Stutz-Boyer, Ana Luz Acevedo-Cabrera and Hong-Han Huang joined the BSL as graduate students in the Fall of 2009. Mathias Obrebski joined Richard Allen’s group as a post-doc in the Fall of 2008. Ingrid Johanson returned to Roland Burgmann’s group as a post-doc in October 2009. Since Nicolas Houlié’s departure in the Summer of 2009, she is helping out with the BARD program. After a brief stay in Hawaii, where she is finishing up a research project, she will take on an assistant researcher’s position at BSL and provide guidance to the field and data acquisition staff on matters related to BARD, and participate in the development of high rate GPS data assimilation in our earthquake notification system.

BSL hosted the following visiting scientists in 08-09: Liang Zhao (Institute of Geophysics, Chinese Academy of Sciences, Beijing) and Michael Slawinski (Department of Earth Sciences at Memorial University in Newfoundland, Canada). Shweta Sangewar (India Institute of Technology) and Fabian Walter (ETH Zürich, Switzerland) were summer interns in 2008.

As a result of a campus wide reorganization of the research administration of Organized Research Units, our four administrative staff have been laid off, effective November 30, 2009. Kristen, Tina and Yolanda have been rehired at RES (Research Enterprise Services), the new agency which will provide business administration to ORUs at Berkeley. Meanwhile, Kate is enjoying her new baby daughter Audrey and prospecting for job opportunities. They have been outstanding members of the BSL team, and we are sorry to see them go in spite of all our efforts. I wish them all the best for the future.

The greater BSL family has also grown, almost explosively, in the past year. We have welcomed four children of BSL staff and students in the past year. A baby boy, Kaito Taira, was born to Taka’aki Taira and his wife Akiko in August. Kate Lewis and her husband Justin had a girl, Audrey, in October. November brought two, somewhat early arrivals: Freeman McCarty was born to Jennifer Taggart and her husband Kevin McCarty, and Arieh Wurman-Fenton was born to Gilead Wurman and his wife Lori Fenton. We wish them all happiness and health.

### 4 Acknowledgements

I wish to thank our technical and administrative staff, scientists and students for their efforts throughout the year and their contributions to this Annual Report. Individual contributions to activities and report preparation are mentioned in the corresponding sections, except for the Appendix section, which was prepared by Kate

Lewis, Kristen Jensen and Jennifer Taggart.

I also wish to specially thank the individuals who have regularly contributed to the smooth operation of the BSL facilities: Mario Aranha, Rich Clymer, Doug Dreger, John Friday, Jarrett Gardner, Peggy Hellweg, Nicolas Houlié, Bill Karavas, Oleg Khainovski, Rick Lellinger, Pete Lombard, Rick McKenzie, Bob Nadeau, Doug Neuhauser, Charley Paffenbarger, Jennifer Taggart, Bob Uhrhammer, and Stephane Zuzlewski, and in the administrative office, Kristen Jensen, Kate Lewis, Tina Barber-Riggins and Yolanda Andrade. I also wish to thank our undergraduate assistants, Chris Rawles, Danny Feucht, Josef Matlak, Eric Winchell, Alicia Adams and Amanda Truyol for their contributions to our research and operations activities.

I am particularly grateful to Jennifer Taggart and Peggy Hellweg, for their help in putting together this Annual Report, and bringing it to closure under the present difficult circumstances.

The Annual Report of the Berkeley Seismological Laboratory is available on the WWW at [http://seismo.berkeley.edu/annual\\_report](http://seismo.berkeley.edu/annual_report).

# Chapter 2

# Research Studies

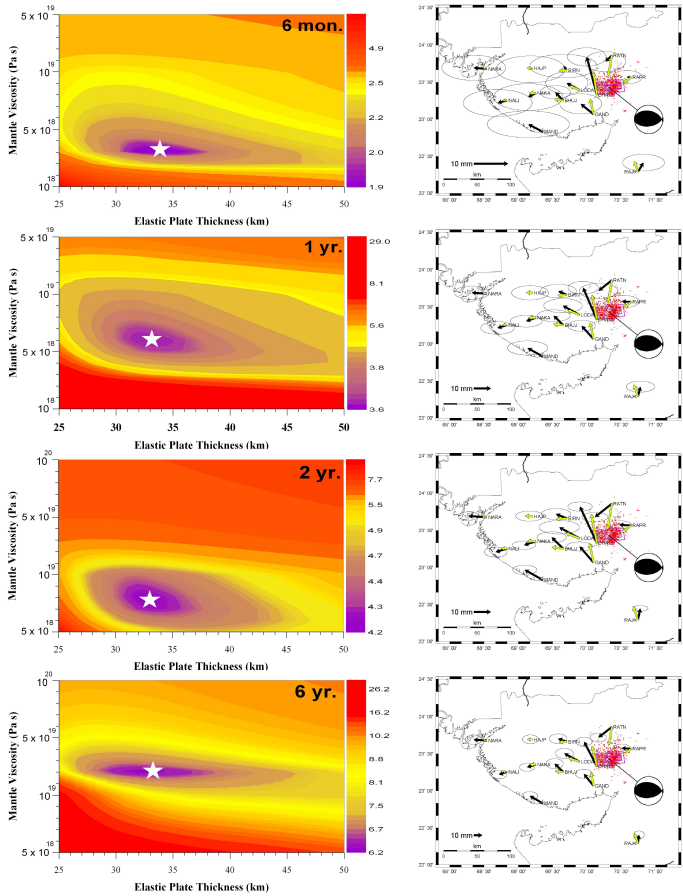


Figure 2.1: Model results. The RMS misfit between the calculated and observed horizontal displacements as a function of elastic plate thickness ( $H_p$ ) and asthenosphere viscosity ( $\eta_a$ ) for the two layer Earth model as a function of time since the earthquake. The star marks the best-fit displacement model with the lowest RMS error value. The best-fit horizontal displacements for each of the best-fit models is plotted adjacent to its misfit plot. Vectors in black denote the observed displacement tipped with 95% confidence ellipses and yellow arrows are the calculated model displacements. (Figure from Section 29)

# 1 Tremor-tide Correlations and Near Lithostatic Pore Pressures on the Deep San Andreas Fault

Amanda Thomas, Robert Nadeau, and Roland Bürgmann

## 1.1 Introduction

Early studies of non-volcanic tremor (NVT) attempted to relate the tremor signal and flow processes of fluids introduced from metamorphic dehydration in the subducting crust, but more recent evidence from subduction zone tremor in Japan and Cascadia indicates that tremor is directly associated with shear failure (*Shelly et al., 2006*). The presence of fluids and the significant impact small stress perturbations, such as tidal forcing, have on tremor activity implies low effective normal stresses are present in the tremor source region (*Gomberg et al., 2008; Miyazawa and Brodsky, 2008; Peng et al., 2008a; Rubinstein et al., 2007*).

Following the initial discovery in Japan and Cascadia, two additional tremor varieties were discovered in different tectonic environments: widespread triggered tremor, activated by dynamic stress changes associated with the passage of teleseismic surface waves (*Gomberg et al., 2008; Rubinstein et al., 2007*), and continuous tremor located deep on the San Andreas fault, near the 2004 Parkfield mainshock (*Nadeau and Dolenc, 2005*). The Parkfield tremor demonstrates several notable dissimilarities when compared to tremor in Cascadia and Japan, including continuous occurrence, changes in activity levels due to nearby intermediate-size earthquakes, and absence of an accompanying geodetic signature (*Nadeau and Dolenc, 2005; Smith, 2009*). In this study, we investigate the influence of tidal loading conditions on non-volcanic tremor on the San Andreas fault in order to determine if the Parkfield tremor is modulated by tides, resolve which tidal stresses affect tremor, and explore implications about the source region conditions.

## 1.2 Methods and Preliminary Results

We develop our analysis in parallel for the tremor catalog and two earthquake catalogs. We consider a regional catalog of events within  $.5^\circ$  of Cholame, and a repeating micro-earthquake catalog located along the creeping segment of the San Andreas fault (*Nadeau and McEvilly, 2004*). We compute the extensional and shear strains induced in the lithosphere by the solid earth and ocean tides (*Agnew, 1997*). Assuming 2-D plane strain and linear elasticity, with an elastic modulus of 30 GPa and Poisson ratio of  $.25$ , we then convert the strains to stresses and resolve those stresses onto the fault normal and parallel (shear) directions on the San Andreas fault ( $N45^\circ W$ ). For each catalog, the normal, shear, and Coulomb stresses and stress rates are computed for the

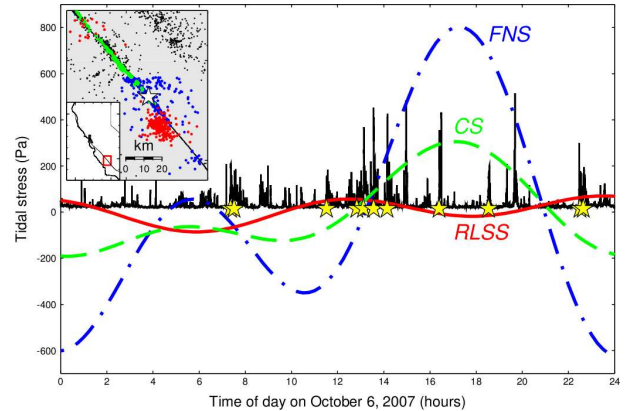


Figure 2.2: Example one-day tremor time series with superimposed tidal signals. Black is RMS envelope of tremor activity in Cholame. Red, blue, and green curves are the tidally induced fault-normal stress (FNS), right-lateral shear stress (RLSS), and Coulomb stress (CS) for  $\mu=0.4$ . Yellow stars mark tremor start times. Some short spikes in the RMS envelope are micro-earthquakes. Inset map shows tremor locations in red, regular earthquakes in blue, and the repeating earthquake catalog in green. Background earthquake activity is shown in black. White star indicates epicenter of the 2004 Parkfield earthquake.

start time of each event (Figure 2.2).

To investigate the influence of both the stress magnitude and rate on tremor occurrence, we divide the tremor into “quadrants” depending on the sign of the loading condition under which they occur. The tidal signal consists of a superposition of multiple harmonic functions, thus the amount of time that the tides induce a given load is not equal for all loading conditions. If tremor and tides are uncorrelated, the number of tremors that occur under a particular tidal loading condition will be directly proportional to the amount of time that condition exists. We use a chi-square test to establish the existence of a correlation using the null hypothesis that tremor start times are randomly distributed with respect to tidal influence. For the tremor catalog, the level of correlation of the normal, shear, and Coulomb stresses exceed the 99% significance level, while the correlation levels for the other catalogs are statistically insignificant. The lack of correlation in the earthquake catalogs is not surprising given the size of the catalogs and results from previous efforts to establish a significant tidal triggering of earth-

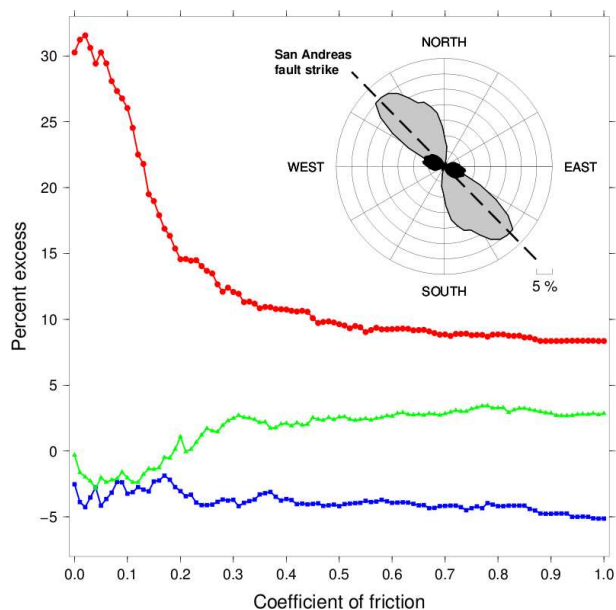


Figure 2.3: Percentage of excess events (i.e. above long term average) during times of positive  $\Delta CS$  parallel to the San Andreas fault vs. effective coefficient of friction. Values for the tremor, regular, and repeating event catalogs are shown as red circles, blue squares, and green triangles respectively. Standard deviations ( $2\sigma$ ) were computed using a bootstrap procedure on each friction value of each catalog. Maximum  $2\sigma$  errors over all possible friction values are 5.66%, 5.80%, and 4.66% for the tremor, regular, and repeating catalogs respectively. The inset diagram displays the positive percent excess tremor for FNS (black) and RLSS (grey) relative to the fault orientation.

quakes in California (Beeler and Lockner, 2003; Lockner and Beeler, 1999).

We further explore this apparent correlation by comparing tremor start times with the loading conditions they occur under. Correlation between tremor occurrence and tidal stressing rate is insignificant for all components. Induced shear stresses ( $\Delta RLSS$ ) demonstrate the most compelling correlation of the three magnitude comparisons, with distinct increases in tremor activity that correspond to positive (right-lateral) shear stresses parallel to the San Andreas fault and equally apparent decreases when values are negative. Additionally, the tremor surpluses and deficits become more pronounced as  $\Delta RLSS$  increases to peak values of  $\pm 150$  Pa. Though normal stresses changes ( $\Delta FNS$ ) are much larger, they only exhibit a weak correlation at large, positive (tensile) values of greater than 1000 Pa. Coulomb stresses ( $\Delta CS = \Delta RLSS + \mu \Delta FNS$ ,  $\mu = 0.4$ ) exhibit less correlation than the shear stress alone.

Assuming tremor is caused by a frictional Coulomb

failure process, the optimal friction coefficient is the value that maximizes the number of events that occur during times of encouraged failure stress (Figure 2.3). Tremors show a marked increase for friction values near zero with a peak above 30% excess for  $\mu = 0$ . Percent excess for both the regular and repeating earthquake catalogs does not exceed 5%. This demonstrates that tidally induced shear stresses parallel to the San Andreas fault, while of much smaller magnitude than normal stress changes, have the most robust correlation with non-volcanic tremor near Parkfield. Since the stress perturbations are so small relative to the overburden stresses at these depths, this finding is indicative of very low effective normal stresses or near-lithostatic pore pressures at depth. Finally, going back to the initial assumption of the strike of the San Andreas fault in our stress calculations, we perform the same analysis to determine the percent excess tremor with respect to any vertical fault orientation (Figure 2.3, inset). The peak percent excess occurs at  $N44^\circ W$ , nearly parallel to the strike of the San Andreas fault.

### 1.3 Acknowledgements

Supported by the USGS through awards 06HQGR0167, 07HQAG0014, and 08HQGR0100, by the NSF through awards EAR-0537641, EAR-0544730, and the GRFP.

### 1.4 References

- Agnew, D. C., NLOADF: A program for computing ocean-tide loading, *JGR-Solid Earth*, 102, B3, 5109-5110, 1997.
- Beeler N. M., D. A. Lockner, Why earthquakes correlate weakly with the solid Earth tides: Effects of periodic stress on the rate and probability of earthquake occurrence, *J. Geophys. Res.*, 108(B8), 2391, doi:10.1029/2001JB001518, 2003.
- Gomberg, J., et al., Widespread triggering of nonvolcanic tremor in California, *Science*, 319, 5860, 173-173, 2008.
- Lockner, D. A., and N. M. Beeler, Premonitory slip and tidal triggering of earthquakes, *JGR-Solid Earth*, 104, B9, 20133-20151, 1999.
- Miyazawa M., E. E. Brodsky (2008), Deep low-frequency tremor that correlates with passing surface waves, *J. Geophys. Res.*, 113, B01307, doi:10.1029/2006JB004890.
- Nadeau, R. M., and T. V. McEvilly, Periodic pulsing of characteristic microearthquakes on the San Andreas Fault, *Science*, 303, 5655, 220-222, 2004.
- Nadeau, R. M., and D. Dolenc, Nonvolcanic tremors deep beneath the San Andreas Fault, *Science*, 307, (5708), 389-389, 2005.
- Peng, Z. G., et al., Strong tremor near Parkfield, CA, excited by the 2002 Denali Fault earthquake, *Geophys. Res. Lett.*, 35, 23, 2008a.
- Rubinstein, J. L., et al., Non-volcanic tremor driven by large transient shear stresses, *Nature*, 448, 7153, 579-582, 2007.
- Shelly, D. R., et al., Low-frequency earthquakes in Shikoku, Japan, and their relationship to episodic tremor and slip, *Nature*, 442, 7099, 188-191, 2006.
- Smith, E. F., A Search in Strainmeter Data for Slow Slip Associated with Triggered and Ambient Tremor near Parkfield, California, *Jour. Geophys. Res.*, In preparation, 2009.

## 2 Detection of Missing Repeating Earthquakes Using Recurrence Elements Analysis

Kate Huihsuan Chen, Roland Bürgmann, and Robert M. Nadeau

### 2.1 Introduction

Stress perturbations influence earthquake recurrence and are of fundamental importance to understanding the earthquake cycle and determining earthquake hazard. The large population of repeating earthquakes on the San Andreas fault at Parkfield provides a unique opportunity to examine the response of the repeating events to the occurrence of moderate earthquakes. We analyze 187  $M$ -0.4 to 1.7 repeating earthquake sequences (RES) from the High Resolution Seismic Network catalog to estimate the impact of  $M$  4-5 events on RES's timing. Here we adopt a recurrence element analysis based on five recurrence elements (Fig. 1a): (1)  $dt+$ : the time difference between a major earthquake and the first subsequent recurrence of a repeating event; (2)  $dt-$ : the time difference between a major earthquake and the most recent repeating event; (3)  $Tr_{cos}$ : the recurrence interval spanning the major event; that is, the sum of  $dt-$  and  $dt+$ ; (4)  $Tr_{post}$ : the duration of the first full recurrence interval following the major event, and (5)  $Tr_{pre}$ : last recurrence interval just preceding the potential trigger. These elements are divided by the average 1987-1998 recurrence interval of a given RES to obtain the normalized values of  $dt+^*$ ,  $dt-^*$ ,  $Tr_{cos}^*$ ,  $Tr_{post}^*$ , and  $Tr_{pre}^*$ . Very short recurrence elements of  $dt+^*$  (i.e., smaller than 10% of the typical cycle) can indicate the immediate triggering due to the major event, whereas longer than 1  $Tr_{cos}^*$ ,  $Tr_{post}^*$ , and  $Tr_{pre}^*$  reflect a population of missing events.

### 2.2 Recurrence elements associated with $M$ 4-5 events

For each RES, the five recurrence elements associated with every  $M$  4-5 event are calculated (Fig. 1a). In Fig. 1b, the RES within 5 km distance from the major events tend to have a high fraction of short  $dt+^*$  ( $< 0.1$ ). Fig. 1b-d also show the percentage of events within a given distance range that have a  $dt+^*$  less than the threshold specified. For example, more than 30% of the events within 2 km distance have  $dt+^* < 0.1$ , whereas within distances of greater than 5 km  $\sim 10\%$  of the RES exhibit such rapid recurrence. The percentage of short  $dt+^*$  remain unchanged for events beyond 5 km. To confirm that the observed short  $dt+$  population indicates the triggering effect of  $M$  4-5 events, we compare the observed distribution of  $dt+^* < 0.1$ ,  $0.1-0.2$ , and  $> 0.5$  with  $dt+^*$  values generated from randomly generated times of the five  $M$  4-5 events. The 30 sets of 5 randomly generated  $M$

4-5 times (150 runs in total) produce roughly equal percentages of  $dt+^*$  at most distances, as shown by the blue lines in Figure 1. The random behavior of the small  $dt+^*$  population ( $dt+^* < 0.1$ ) is strikingly different from the real population in the near field of the  $M$  4-5 events ( $< 5$  km). Beyond 5 km, however, the observed  $dt+^* < 0.1$  distribution matches the synthetic  $dt+^*$ . Compared to  $dt+^*$  curves, the fraction of short  $dt-^*$  measured over the same range of distances do not reveal systematic change with distance. The percentages of the observed  $dt-^*$  at all distances match the value of  $dt-^*$ , as one can expect from random behavior.

### 2.3 Undetected repeating events?

In Figure 2, the histogram of  $Tr_{pre}^*$  reveals a somewhat broader distribution with median value of 1.62. The median  $Tr_{pre}^*$  is about a half cycle shorter than the median value of 1.14 and 1.29 for  $Tr_{cos}^*$  and  $Tr_{post}^*$ , respectively. This suggests a general pattern of shortened interval at and following the time of  $M$  4-5 events. Note that the small secondary peak in Fig. 2b is about twice the normalizing interval, indicating some missed recurrences that may have occurred during the trigger event. Given that a single skipped event in a sequence leads to a  $Tr_{cos}^*$  value of slightly greater than 1, the second peak at  $Tr_{cos}^* \sim 2$  is suggestive a number of unrecognized repeating event. And since the secondary peak near 2 is minor, the undetected repeating events are unlikely to have significant influence on the  $M$  4-5 triggering effect. We also note that  $Tr_{post}^*$  is also somewhat reduced compared to pre-event recurrences, indicating the possible role of afterslip or general acceleration of slip in the early 1990s.

### 2.4 Summary

We illustrate the effect of major events on earthquake cycles of nearby characteristically repeating micro-earthquakes and determine the distance over which triggering can be documented. We find evidence that the five  $M$  4-5 events that occurred at Parkfield triggered small, nearby repeating earthquakes. The triggering effect can only be seen in the near-field ( $< 5$  km) by the measures of rapid recurrence subsequent to the major event. A small population of missing repeating events at the time of a major event is also detected by the longer-than-average intervals spanning and following a major event. In future

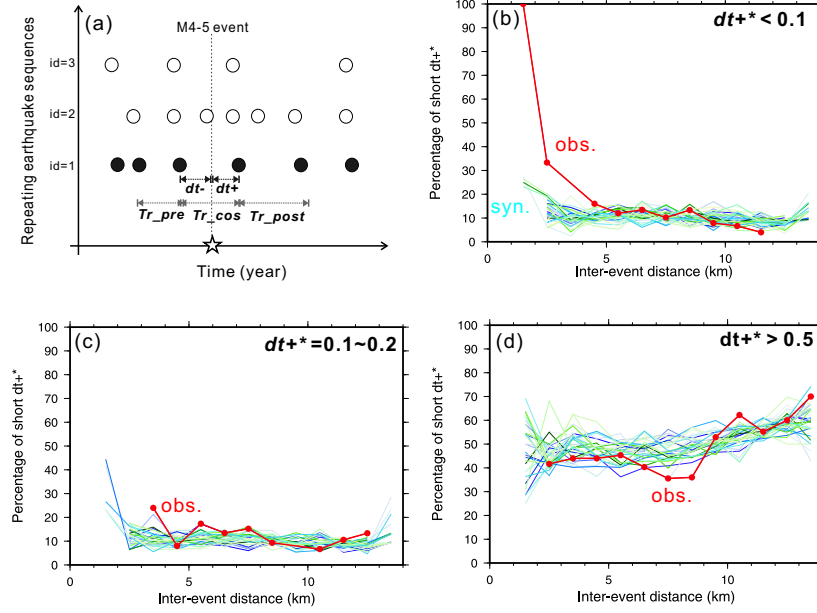


Figure 2.4: (a) Schematic illustration of the five recurrence elements,  $dt+$ ,  $dt-$ ,  $Tr_{pre}$ ,  $Tr_{cos}$ , and  $Tr_{pos}$ . Percentage of (b)  $dt+^* < 0.1$  (c)  $0.1 < dt+^* < 0.2$  (d)  $dt+^* > 0.5$  as a function of distance from  $M$  4-5 events for real data (red line) and synthetic data (blue lines generated by 30 sets of 5 randomly drawn of  $M$  4-5 event times). Note that the percentage in each distance bin (1 km) is calculated when the  $dt+^*$  number is greater than 3.

work, we will consider whether interaction with nearby  $M < 4$  events plays an additional important role in the RES recurrence patterns. We will also explore in detail the response of the RES to the  $M$  6 2004 Parkfield earthquake.

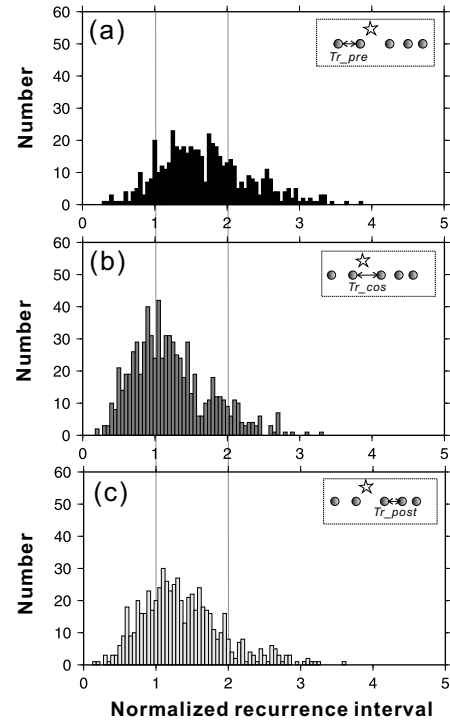


Figure 2.5: Histograms of  $Tr_{pre}^*$ ,  $Tr_{cos}^*$ , and  $Tr_{post}^*$  determined by the average recurrence intervals of full period. Grey lines denote the normalized recurrence intervals of 1 and 2.

## 3 TerraSAR InSAR Investigation of Active Crustal Deformation

Ling Lei and Roland Bürgmann

### 3.1 Introduction

This project aims to utilize advanced analysis of TerraSAR data to investigate the dynamics and interactions of solid Earth deformation processes, such as earthquakes and fault creep, and Earth surface processes, such as land subsidence and groundwater movements, in a densely populated, urban region, the San Francisco Bay Area. Results from TerraSAR data will be carefully compared and integrated with InSAR data from other spacecraft, including the ERS-1/2, Envisat, RADARSAT-1, and ALOS satellites, and will be integrated in a rigorous analysis and monitoring effort of active surface deformation in the region. Ongoing deformation imaging reveals a number of natural hazards, including elastic strain accumulation about seismologic faults, active landsliding, land subsidence and rebound, and settling of unconsolidated sediments that are highly susceptible to liquefaction. Up to now, we have ordered and received 20 TerraSAR-X Spotlight Single Look Complex (SLC) images and 4 Stripmap SLC images delivered by the German Aerospace Centre (DLR) and obtained a few primary preliminary results.

### 3.2 Data analysis and processing

The TerraSAR-X images were acquired over the San Francisco Bay Area, particularly around an area of active landsliding, coastal subsidence, and shallow Hayward fault creep near the city of Berkeley. Berkeley is situated between  $37.45^\circ$  and  $38.00^\circ$  latitude, and  $237.30^\circ$  and  $238.00^\circ$  longitude. The data acquisition interval is from November, 2008 to July, 2009. Four types of Spotlight images and one type of Stripmap image in time sequence were ordered and acquired: spot\_012, spot\_038, spot\_049, spot\_075, and strip\_003, having different look angles and pass directions. The data acquired with the standard Spotlight mode are with 1m pixel resolution, 10 km wide swath, and HH polarization. A TerraSAR-X Spotlight scene covers approximately  $10*5\text{km}^2$ . Actually, there are 122 spotlight beams called spot\_001 to spot\_122 and 8 different beams of Spotlight data over the Berkeley area. But the recommended performance beams of Spotlight images are spot\_010 to spot\_079. So we chose four recommended beams of all the available beams for the Bay Area. Details of the data set used are mentioned in Table 2.1. Access to the SAR data is via FTP about 10 days after acquisition date.

The data is supplied in TerraSAR-X standard SLC COSAR (COMplex SAR) format with orbital information in an Extensible Markup Language (XML) header.

The file contains integer real-complex components with double sampling and calibration constants for values. The COSAR file contains all focused complex SAR data of one beam in a burst-by-burst order, together with sample validity and position annotation. Stripmap and Spotlight images consist of one burst in that sense. The huge variety of level 1b product types for TerraSAR-X (complex, detected, geocoded) requires product annotation in an extensible and dynamic format.

I am using ROLPAC to do the interferograms. But ROLPAC was designed to process raw data rather than SLC images. So there are two main problems. One is that ROLPAC does the azimuth spectrum filtering (cutting out the part of the azimuth spectrum that does not overlap) in the "roi" program. So "resamp\_roi" has to be changed to do the azimuth spectrum filtering in the interferogram formations. The other is that there is a significant difference between the way that ROLPAC and other SAR processors use the Doppler centroid in the SLC formation. ROLPAC is set up to process the SLC in the original geometry, but the TerraSAR processor produces the SLC images in a deskewed geometry. The deskewing moves the data to adjust for the squint or angle between the radar line of sight (LOS) and projects it perpendicular to the orbit track.

Another problem is the processing with the Spotlight data. In order to form coherent Spotlight interferograms from two SAR observations, the following two conditions must be met: the ground projected-range spectra of both observations must overlap, and the received Doppler frequency spectra must overlap as well. The nonstationary squint angle during spotlight imaging also causes a negative drift of the Doppler centroid frequency in the SAR data. So the linear Doppler drift in azimuth has to be removed and Doppler centroid set to zero before making interferograms. We are now still working on those problems and will hopefully get better results in the near future. Here are some preliminary results: a Stripmap interferogram (Figure 2.6) and a Spotlight interferogram (Figure 2.7). I also plotted the landslides areas around Berkeley Hills. There are four large, slow moving, deep-seated landslides. All the landslides extend through residential areas and move on the order of cm/year, each covering an area of roughly  $0.25\text{-}1.00\text{ km}^2$

### 3.3 Acknowledgements

We thank the German Aerospace Centre (DLR) for providing TerraSAR-X data for this project. We thank Paul Lundgren, Eric J. Fielding, and Paul Rosen for

Date	Time	Polarization Mode	Polarization Channels	Incidence Angles	Pass Direction	Beam
2008-11-26	14:23:42UTC	Single	HH	21.78	D	spot_012
2008-12-18	14:23:40UTC	Single	HH	21.78	D	spot_012
2009-01-09	14:23:38UTC	Single	HH	21.78	D	spot_012
2009-02-22	14:23:38UTC	Single	HH	21.78	D	spot_012
2009-04-07	14:23:38UTC	Single	HH	21.78	D	spot_012
2008-11-18	2:00:28UTC	Single	HH	34.14	A	spot_038
2009-01-12	2:00:24UTC	Single	HH	34.14	A	spot_038
2000-02-25	2:00:24UTC	Single	HH	34.14	A	spot_038
2009-04-10	2:00:20UTC	Single	HH	34.14	A	spot_038
2009-07-18	2:00:29UTC	Single	HH	34.14	A	spot_038
2008-11-21	14:15:09UTC	Single	HH	38.94	D	spot_049
2008-12-24	14:15:08UTC	Single	HH	38.94	D	spot_049
2009-02-28	14:15:07UTC	Single	HH	38.94	D	spot_049
2009-04-13	14:15:02UTC	Single	HH	38.94	D	spot_049
2009-07-21	14:15:11UTC	Single	HH	38.94	D	spot_049
2008-11-23	2:09:01UTC	Single	HH	47.82	A	spot_075
2008-12-26	2:08:59UTC	Single	HH	47.82	A	spot_075
2009-03-02	2:08:56UTC	Single	HH	47.82	A	spot_075
2009-04-15	2:08:53UTC	Single	HH	47.82	A	spot_075
2009-07-23	2:09:02UTC	Single	HH	47.82	A	spot_075
2009-05-10	14:23:39UTC	Single	HH	21.45	D	strip_003
2009-05-21	14:23:43UTC	Single	HH	21.45	D	strip_003
2009-07-26	14:23:39UTC	Single	HH	21.45	D	strip_003
2009-08-06	14:23:43UTC	Single	HH	21.45	D	strip_003

Table 2.1: Information on the data acquired

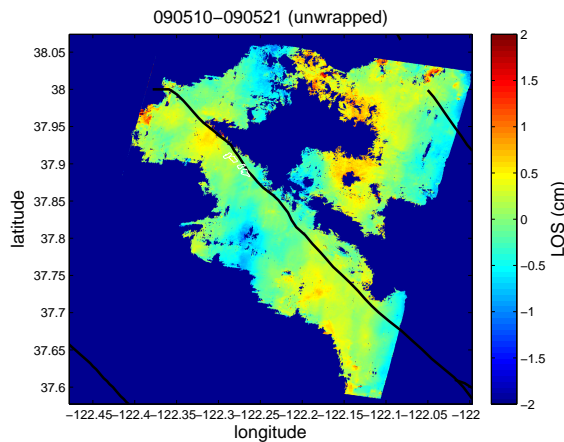


Figure 2.6: Interferogram for Stripmap pair of 10<sup>th</sup> May and 21<sup>st</sup> May, 2009

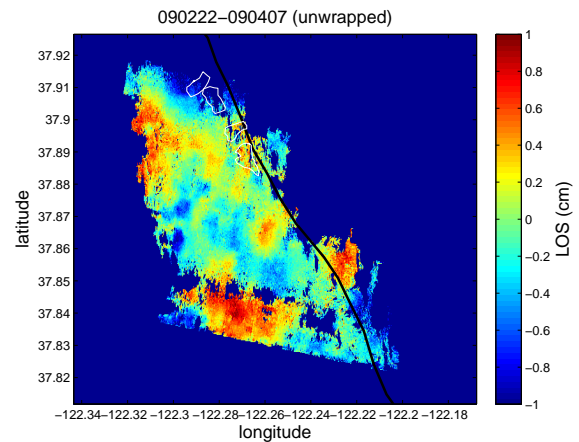


Figure 2.7: Interferogram for Spotlight pair of 22<sup>nd</sup> Feb. and 7<sup>th</sup> April, 2009

providing TerraSAR reading codes and beneficial discussions.

### 3.4 References

- TerraSAR-X Ground Segment Basic Product Specification Document, TX-GS-DD-3302.
- TerraSAR-X Ground Segment Level 1b Product Format Specification, TX-GS-DD-3307.

Bürgmann, R., E. Fielding, and J. Sukhatme, Slip along the Hayward fault, California, estimated from space-based synthetic aperture radar interferometry, *Geology*, 26, 559-562, 1998.

Eineder, M., N. Adam, and R. Bamler, Spaceborne Spotlight SAR Interferometry With TerraSAR-X, *IEEE Trans. Geosci. Remote Sens.*, 5, 1524-1535, 2009.

## 4 Creep Measurements on the Concord Fault from PS-InSAR

Ingrid Johanson, Roland Bürgmann, Alessandro Ferretti (TRE, Milan) and Fabrizio Novali (TRE, Milan)

### 4.1 Introduction

We use PS-InSAR (permanent scatterer interferometric synthetic aperture radar) measurements to study surface creep on the Concord fault in the Eastern Bay Area. Creep on the Concord fault has previously been measured in two locations using alignment arrays (*McFarland et al.*, 2009). The alignment arrays found that creep occurs at rates of 2.5-3.5 mm/yr and mostly in episodes every 3-5 years. InSAR provides dense measurements of ground motion that allow us to measure fault creep along several cross-fault profiles and gain a sense of the distribution of creep along-strike. The PS-InSAR method identifies and integrates individual points with stable phase measurements (outcrops, buildings, utility poles, etc.) in all SAR acquisitions of an area of interest. PS-InSAR provides time-series of range-change measurements that we can use to resolve deformation rates at high precision ( $<1$  mm/yr). This may allow us to also resolve some of the variability in the Concord fault's creep rate.

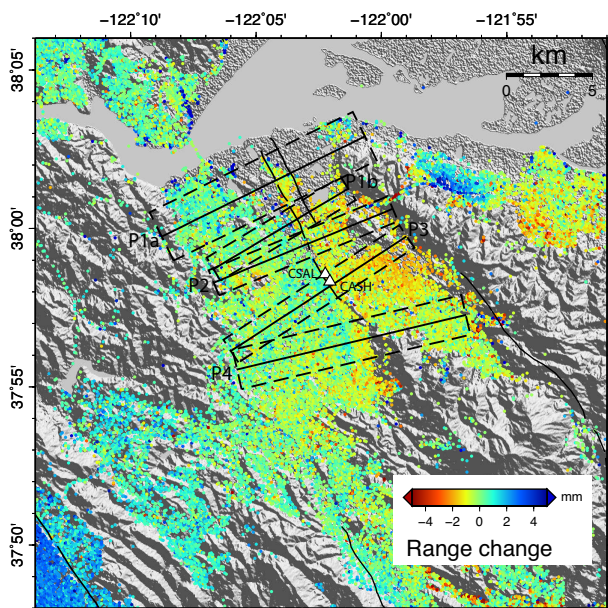


Figure 2.8: Overview map showing mean velocity of each PS-InSAR points from 46 InSAR scenes spanning 1992-2001. Dashed boxes are the areas included in the swath averages, which are then projected onto the solid black centerlines. The two alignment arrays, CSAL and CASH, are shown as white triangles and fall mostly within Profile 3 (P3).

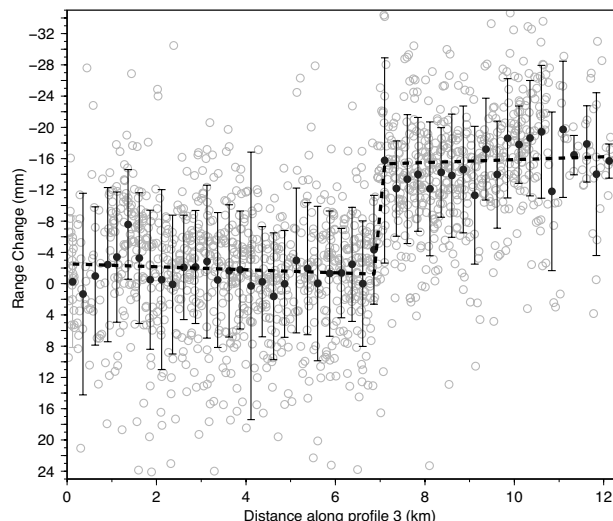


Figure 2.9: An example of a swath average profile; this is for profile 3 on 12/9/2001, referenced to 5/6/1992. Grey circles are the actual PS-InSAR points within the dashed box in Figure 2.8 and projected onto the centerline. Black circles are the derived swath averages; averages of all points inside a 0.25 km bin. Error bars are one standard deviation of the PS-InSAR points comprising each swath average. The dashed black line is fit to the data using a linear inversion and the fault creep is measured from the offset of the profile at the fault trace.

### 4.2 Measuring creep from PS-InSAR

We use 46 acquisitions from the European Space Agency's ERS1 & 2 satellites, on descending track 70, frame 2853, and spanning from 1992 through 2001. The data were processed using the PS-InSAR method of *Ferretti et al.* (2001) to produce time series of range change (change in distance between the ground and satellite) for each point shown in Figure 2.8. To measure creep on the Concord fault, we look at motion along several profiles through the Permanent Scatterers (PSs), crossing the Concord fault. We use swath averaging to construct each profile. Within each swath, shown as dashed lines in Figure 2.8, points within 0.25 km bins perpendicular to the fault are averaged together and projected onto the centerline. For example, all points between 0.5 and 0.75 km west of the fault are averaged together to provide one point on the profile and their standard deviation provides an estimate of the profile point's uncertainty.

A swath average profile is constructed for all 46 acqui-

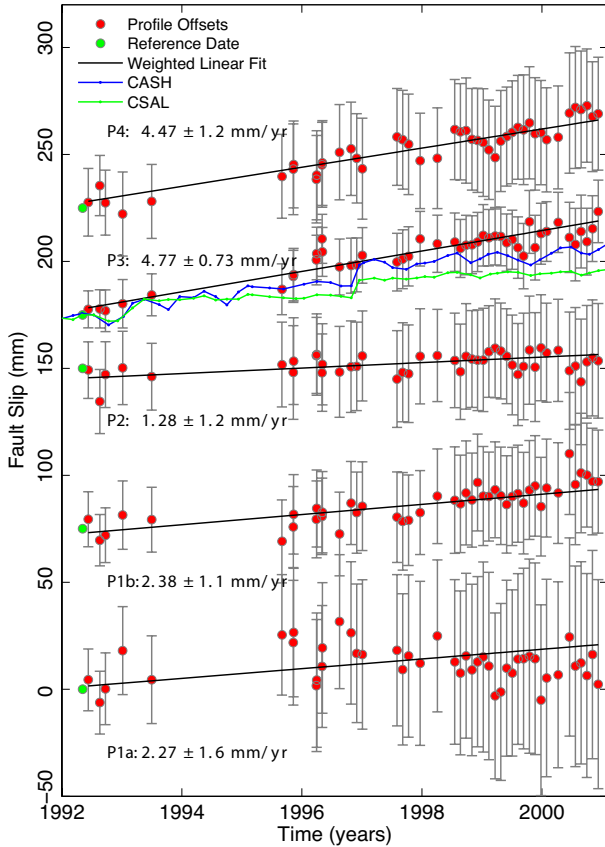


Figure 2.10: Surface creep through time for the five profiles shown in Figure 2.8. Individual time series are offset from each other for clarity. The creep rate as determined from a weighted linear inversion is printed next to each series. Alinement array measurements from sites CSAL and CASH are plotted with Profile 3 (P3) for comparison.

sition dates on each of the five profiles, for a total of 230 profiles (an example is shown in Figure 2.9). A linear inversion is performed on each profile to obtain the offset at the fault trace, produced by the shallowly creeping fault. Each offset value represents the amount of creep on the Concord fault since the beginning of the time series in 1992.

### 4.3 Long-term creep rates

Time series of profile offsets for all five profiles are shown in Figure 2.10. By fitting a line to the offsets, we can obtain a measurement of the creep rate at each profile. The two northern-most profiles (P1a & P1b) have creep rate of 2.3-2.4 mm/yr; this is very low, but measurable within the calculated uncertainty of 1.1-1.6 mm/yr. The creep rate continues to be low southward through profile 2 (P2), where the measured rate could be zero within uncertainty. Creep picks up fairly suddenly at pro-

file 3 (P3), which is near the portion of the fault known to creep from alinement arrays. Time series of creep measurements from the alinement arrays are plotted with the time series from P3 in Figure 2.10. Both arrays measure slightly lower creep rates than is indicated by P3, but support the idea that the creep rate is increasing toward the south. CSAL is the more northern alinement array and is on the north edge of P3 (see Figure 2.8); it has a lower creep rate (2.8 mm/yr) than CASH (3.7 mm/yr), which is located toward the center of P3. P3 incorporates more data to the south of CASH, which may explain its higher creep rate. Higher rates of creep continue in profile 4 (P4), our southern-most profile.

### 4.4 Time-variable creep

Creep on the Concord fault has also been shown by alinement array measurements to be episodic, with a 3-5 year period. This variability is within the uncertainty in the profile offsets and could not be independently detected using the PS-InSAR data. However, offsets for P3 match some of the variability in alinement array CASH, particularly post-1998, suggesting that there is information available in the PS-InSAR data on the time variability of Concord fault creep.

### 4.5 Acknowledgements

This work was supported by USGS-NEHRP external grant #08-HQGR-0095. SAR data are copyrighted by the European Space Agency and were obtained via the WInSAR consortium.

### 4.6 References

Ferretti, A., C. Prati, and F. Rocca, Permanent scatterers in SAR interferometry, *IEEE Trans. Geosci. Remote Sens.*, 39, 8-20, 2001.  
 McFarland, F., J. Lienkaemper, and S. J. Caskey, Data from theodolite measurements of creep rates on San Francisco Bay region faults, California; 1979-2009, *USGS Open file report 09-1119*, 2009.

## 5 Seismicity Changes and Aseismic Slip on the Sunda Megathrust Preceding the $M_w$ 8.4 2007 Earthquake

Kelly Grijalva, Roland Bürgmann, and Paramesh Banerjee (Earth Observatory of Singapore)

### 5.1 Introduction

The September 12, 2007 Sumatra  $M_w$  8.4 earthquake initiated  $\sim 750$  km south of the 2005 epicenter. Twelve hours later, a deeper  $M_w$  7.9 aftershock ruptured further to the north. Their occurrence, close in time and space to the 2004  $M_w$  9.2 Sumatra-Andaman earthquake, 2005  $M_w$  8.7 Nias earthquake, and 2000  $M_w$  8.0 Enggano earthquake, suggests the possibility of these being triggered events. Coulomb failure stress models have shown that the 2000 earthquake had a larger impact at the 2007 hypocenter than the 2004 and 2005 earthquakes, and could have contributed to its southern location. We investigate seismicity changes and GPS-measured velocities, in the 2007 rupture region, for alternative triggering evidence.

### 5.2 Seismicity Rate Changes

We investigate seismicity rate changes in Southern Sumatra using the standard Beta-statistic approach (e.g. *Reasenburg & Simpson, 1992*). Beta will be positive when the postseismic rate is higher than the background seismicity rate, and negative when it is lower. Our earthquake catalog consists of the preferred events from IRIS SeismiQuery (<http://www.iris.washington.edu/SeismiQuery>). The magnitude of completeness for this catalog, which starts in 1980, is 4.7. In order to reduce the effect of aftershocks, we use ZMAP (*Wiemer, 2001*) to decluster our catalog.

The number of annual earthquakes increased greatly for the time period following the 2000 earthquake and before the 2004 earthquake. When calculating an average value of  $\beta$  for the 2007 high-slip region, approximated by longitude  $99^\circ$ -  $102.5^\circ$  and latitude  $1^\circ$ -  $5^\circ$ S, the largest two spikes in  $\beta$  occur after the 2000 and 2005 earthquakes (Figure 2.11).

Figure 2.12 shows  $\beta$  calculated for 1 year time intervals and spatially binned into  $1^\circ$ squares. In general, the seismicity level has been extremely elevated in Western Sumatra and the offshore region north of the equator. In 2005, there was a cluster of aftershocks near Siberut Island, as evident by  $\beta > 10$ . From 2005-2007, there was a more moderate increase in seismicity near the Mentawai Islands of Sipora, North Pagai, and South Pagai, regions that slipped during the 2007 earthquake sequence. In 2005, there were moderate seismicity increases of up to  $\beta = 4$ , in the  $1^\circ$ squares surrounding the 2007 hypocenter. There was a slight decrease in seismicity in the squares containing the 2007 and 2000 epicenters. In 2006, the

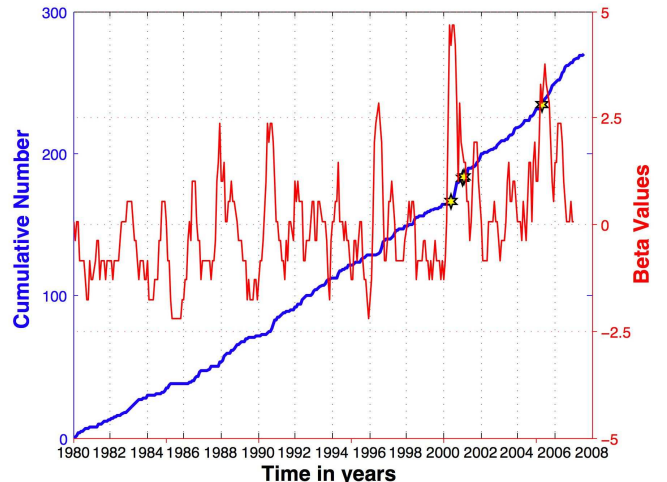


Figure 2.11: Beta values in the 2007 high-slip region are plotted in red (see Figure 2.13 for high-slip contours). The blue line indicates the cumulative number of  $M \geq 4.7$  earthquakes since 1980. The yellow stars indicate earthquakes with  $M > 6.5$ .

seismicity increased in the 2007 and 2000 squares, but decreased significantly in the surrounding region. The  $\beta$  values continued to decrease down to average levels during the first 9 months of 2007, before the September earthquake. If one compares the post-2004 seismicity levels with just the 1980-1999 catalog, thereby removing the effect of the 2000 earthquake, the seismicity levels are significantly higher in the epicentral region.

### 5.3 Aseismic Slip on the Megathrust

GPS-measured velocities in Southern Sumatra have been centimeters above their interseismic rates during the years following the 2004 earthquake (*Sumatran GPS Array* data). Figure 2.13 shows the 2006 and 2007 (up to the September earthquake) GPS velocities in the 2007 high-slip region, with horizontal and vertical interseismic velocities removed (*Apel et al., 2006; Natawidjaja et al., 2007*). We invert these GPS velocities for dipslip motion on the Sunda megathrust. The 2006 and 2007 inversions reveal an increased level of coupling on the deeper portion of the seismogenic zone, from  $\sim 15$ - $75$  km depth, northwest of the  $M_w$  8.4 high-slip patch. In addition, there was centimeters of aseismic reverse-slip over the region that slipped during the 2007 main event.

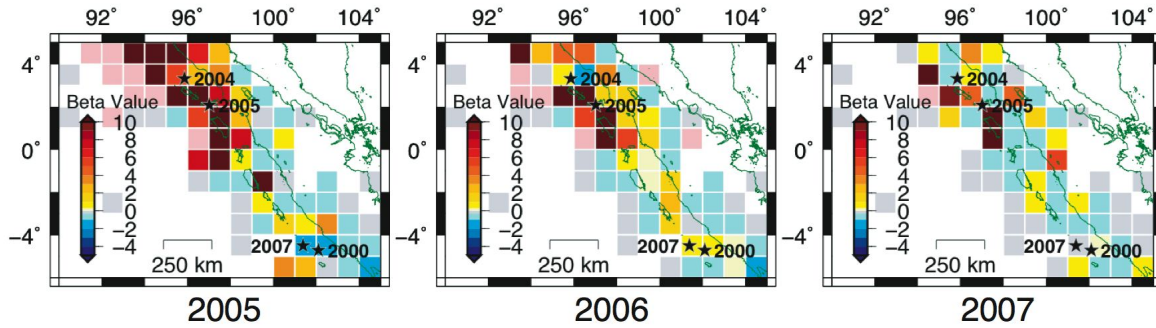


Figure 2.12: Beta values showing the relative change in seismicity following the 2004 earthquake compared to the time period 1980-2004. The pink squares signify regions where there were no earthquakes during the preseismic period.

## 5.4 Discussion and Future Work

The 2007 earthquake location may be the result of delayed dynamic triggering from the large number of earthquakes following the 2000 and 2005 earthquakes. The increased level of seismicity may be associated with the observed aseismic slip transients, as in the case of the afterslip following the 2005 earthquake. More stress modeling is needed to determine whether this observed aseismic slip contributed significantly to the timing and location of the 2007 earthquake.

## 5.5 Acknowledgments

This work is supported by the National Science Foundation grant EAR 0738299. The GPS data is provided by the Tectonics Observatory, LIPI and SOPAC.

## 5.6 References

Apel, E., R. Bürgmann, P. Banerjee, and B. Nagarajan, Geodetically constrained Indian Plate motion and implications for plate boundary deformation, *Eos Trans. AGU*, 85(52), Fall Meeting Supplement, T51B-1524, 2006.

Konca, A. O., J. Avouac, A. Sladen, A. J. Meltzner, K. Sieh, P. Fang, Z. Li., J. Galetzka, J. Genrich, M. Chlieh, D. H. Natawidjaja, Y. Bock, E. J. Fielding, C. Ji, and D. V. Helmberger, Partial rupture of a locked patch of the Sumatra megathrust during the 2007 earthquake sequence, *Nature*, 465, 631-635, 2008.

Natawidjaja, D. H., K. Sieh, M. Chlieh, J. Galetzka, B. W. Suwargadi, H. Cheng, R. L. Edwards, J. Avouac, and S. N. Ward, Source parameters of the great Sumatran megathrust earthquakes of 1797 and 1833 inferred from coral microatolls, *J. Geophys. Res.*, 111, 10.1029/2005JB004025, 2006.

Reasenber, P. A. and R. W. Simpson, Response of Regional Seismicity to the Static Stress Change Produced by the Loma Prieta Earthquake, *Science*, 255, 1687-1690, 1992.

Wiemer, S., A software package to analyse seismicity: ZMAP, *Seismol. Res. Lett.*, 72, 373-382, 2001.

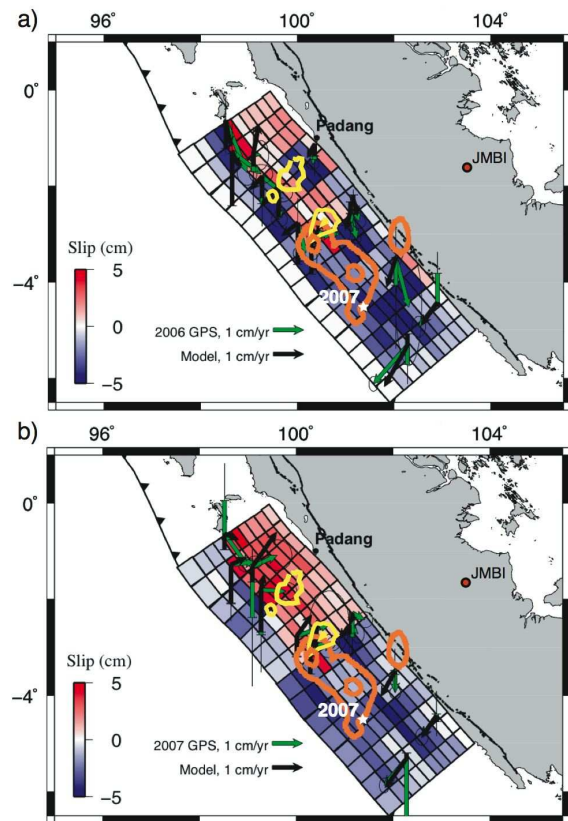


Figure 2.13: Inverted slip on the Sunda megathrust, for a) 2006, and b) 2007 up to September 12th earthquake. Positive slip values indicate stronger coupling and negative slip values indicate aseismic slip on the megathrust. The 1-m and 5-m slip contour lines for the 2007  $M_w$  8.4 earthquake are shown in orange and for the  $M_w$  7.9 aftershock in yellow (Konca et al., 2008).

# 6 Moment Moment Tensors for Very Long Period Signals at Etna Volcano, Italy

Margaret Hellweg, Andrea Cannata (INGV, Catania), Stefano Gresta (Universita Catania), Sean Ford, Guiseppe Di Grazia (INGV, Catania)

## 6.1 Introduction

Very long period signals (VLP, 10 s - 30 s) associated with long period events (0.5 Hz - 5 Hz) were observed at Etna Volcano, Italy, during June-November 2005. They are only recorded at the broadband stations nearest to Etna's craters, ECPN, EBEL, EPDN and EPLC. These stations are part of the permanent seismic network run by the Catania Section of the Istituto Nazionale di Geofisica e Vulcanologia (INGV). Although the signal-to-noise (S/N) ratio for these VLPs is in general only poor to fair, they seem to recur, and can be classified into two families. We improved the S/N by stacking (see 2008 Annual Report), and determined moment tensors for the VLP events using the complete waveform, full moment tensor inversion program (*Minson and Dreger, 2008*).

## 6.2 Moment Tensor Results

We calculated both deviatoric and full moment tensors for the VLP stacks of Family I and Family II using the complete waveform inversion code described by *Minson and Dreger (2008)* and synthetic Green's functions for very shallow source depths. The velocity model used to calculate the Green's functions described a simple half-space with a P-wave velocity of 2.0 km/s and a S-wave velocity of 1.2 km/s. A suite of moment tensor inversions was performed at grid points (horizontal spacing 0.25 km; depths in km: 0.25, 0.50, 0.75, 1.0, 1.5) within the volcanic edifice (locations shown in Figure 2.14). The origin of the rectangular grid was the centroid of the four summit stations. Etna's topography was not included in the calculation of the Green's functions.

For both families, the moment tensor solutions with the best variance reduction (VR) were in the same region of the edifice as the locations determined for the VLP events using radial semblance (*Cannata, et al., 2009*). For Family I, the best solutions had VR > 70% and were best explained by sources that are 60-70% isotropic (ISO) (Figure 2.14). For Family II, they had VR > 60% and 60-70% ISO. Deviatoric solutions for both families had much poorer VR and waveform fits were clearly less satisfactory.

In moment tensor inversions, the signal to noise ratio (SNR) of the data is clearly important. Fifteen years of experience of moment tensor analysis in California include small events down to M 3.5 and below (*Hellweg et al., 2006*). Although events along the central San Andreas Fault are known to be purely double couple (DC),

deviatoric moment tensor solutions for small events with low SNR in the band of analysis (10 s - 50 s) may have up to 30% of their energy modeled by a compensated linear vector dipole (CLVD) mechanism. For the VLP

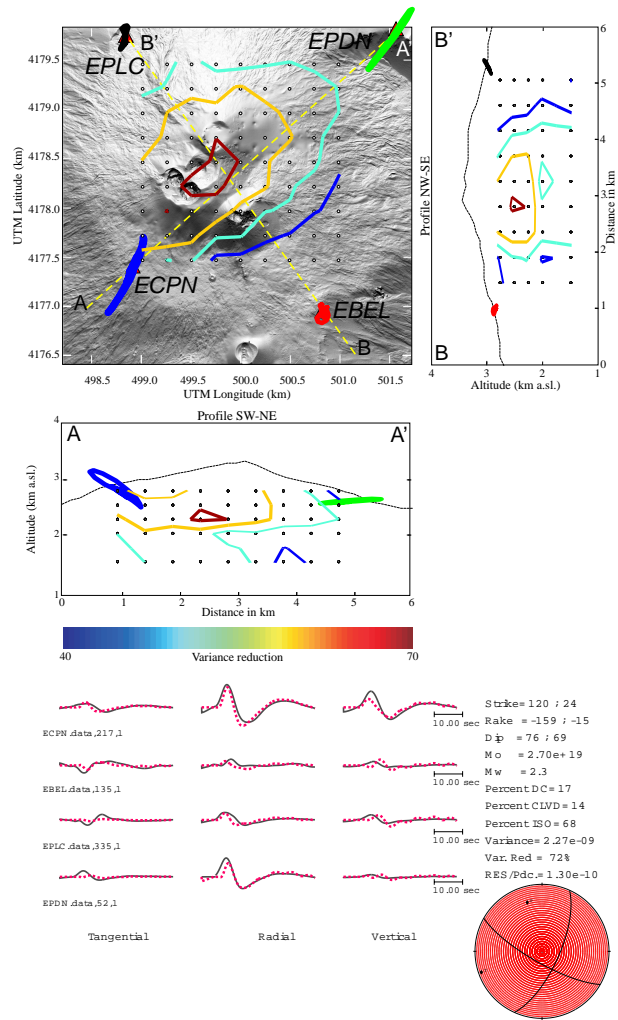


Figure 2.14: Full moment tensor results for Family I events. The map and cross sections show the particle motion at the four summit stations, as well as the search grid and the spatial variation of VR. The source type is plotted on the diamond shaped graph. The bottom panel shows the waveform fits and the mechanism. Note that the amplitudes of the waveforms are scaled so that they can be compared. Results for Family II are very similar.

events of Mt. Etna, even the stacks analysed here, the SNR is low. The DC and CLVD elements of the best solutions vary from grid point to grid point. The eigenvalues describing the deviatoric portions of the solutions also primarily vary randomly in space, with a preference of the largest eigenvector toward a subhorizontal orientation and a slight predominance of SW orientations. Thus, we are convinced that the deviatoric parts of the moment tensor solution are most likely to be efforts of the inversion to explain the noise. They cannot be used to interpret the geometry of the source without better data. There is no reason to suppose that a fit including single-force elements (e.g. *Chouet et al., 2003, Chouet et al., 2005*) would provide greater insight into the source of the VLP events. On “source-type” plots (*Hudson et al., 1989*), it is notable that all of the moment tensor solutions plot somewhere between “explosion” and “opening crack” sources. The scatter gives some sense of the uncertainty in the solutions.

### 6.3 Perspectives

Using Green’s functions for full moment tensors calculated using a simple half space velocity model, inversions using the algorithm described in *Minson and Dreger (2008)* indicate that a volume change explains a large portion of the waveforms. We intend to follow up with further analysis to investigate the effects of the simple velocity structure, using Green’s functions calculated for the locally used velocity model. We also hope to investigate single source type solutions (i.e. only DC, only CLVD, only ISO), and hope to have longer wavessnippets to improve our understanding of the signal to noise ratio.

### 6.4 References

Cannata, A., M. Hellweg, G. Di Grazia, S. Ford, S. Alparone, S. Gresta and P. Montalto, Long Period and Very Long Period events at Mt. Etna volcano: characteristics, variability and causality, and implications for their sources, *J. Volcanol. Geotherm. Res.*, in press, 2009.

Chouet, B., P. Dawson, T. Ohminato, M. Martini, G. Saccorotti, F. Giudicepietro, G. De Luca, G. Milana and R. Scarpa, Source mechanism of explosions at Stromboli Volcano, Italy, determined from moment-tensor inversions of very-long-period data, *J. Geophys. Res.* *108*, doi:10.1029/20042JB001919, 2003.

Chouet, B., P. Dawson and A. Arciniega-Ceballos, Source mechanism of Vulcanian dagassing at Popocatepetl Volcano, Mexico, determined from waveform inversions of very long period signals, *J. Geophys. Res.* *110*, doi:10.1029/2004JB003524, 2005.

Green, D., and J. Neuberg, Waveform classification of volcanic low-frequency earthquake swarms and its implication at Soufriere Hills Volcano, Monserrat, *J. Volcanol. Geotherm. Res.*, *153*, 51-63, 2006.

Hellweg, M., D. Dolenc, L. Gee, D. Templeton, M. Xue, D. Dreger and B. Romanowicz, Twelve Years and Counting: Regional Moment Tensors in and around Northern California *Seismol. Res. Lett.*, *77(2)*, 221, 2006.

Hudson, J.A., R.G. Pearce and R.M. Rogers, Source type plot for inversion of the moment tensor, *J. Geophys. Res.*, *9(B1)*, 765-774, 1989.

Minson, S. and D. Dreger, Stable Inversions for Complete Moment Tensors, in press *Geophys. Journ. Int.*, 2008.

# 7 Temporal Variations in Crustal Scattering Structure near Parkfield, California, from Receiver Functions

Pascal Audet

## 7.1 Introduction

The accurate determination of crustal velocity structure in the region surrounding a fault is an essential component in the investigation of fault processes since it yields important information on the composition and state of the crust (e.g. anisotropy, pore-fluid pressure, etc). In addition, temporal variations in crustal architecture (i.e. 4-D imaging) can provide key constraints on the dynamics of faulting. One method that provides accurate point measurements of crustal velocity structure is based on the characterization of the scattering structure beneath a recording station using teleseismic events, i.e. the so-called receiver function method. The technique is based on the deconvolution of the source time function, approximated by the P-wave train, from the S-components of motion. The resulting seismograms represent an approximation to the Earth's Green function, and are used to determine the depth and velocity of discrete crustal layers. A novel use of the receiver function method is proposed here which makes use of decade-long high-quality records from permanent broadband stations to estimate temporal variations in crustal scattering structure.

## 7.2 4-D imaging using receiver functions

The conventional receiver function method has been applied to data from the Parkfield broadband seismic station PKD, and results demonstrate the existence of a lower crustal, low-velocity layer with strong (~15%) anisotropy (Ozacar and Zandt, 2009). Using 12 years of data at station PKD (~1000 events, Figure 2.15), we calculate the power spectral density (PSD) for each individual, unfiltered receiver function and bin into 12 month-long, 90% overlapping segments within which we calculate the median PSD and total power by integrating the PSD. Results show a clear change in PSD and spectral power after the 2003  $M_w$  6.5 San Simeon earthquake with a subsequent decrease (~2 dB) in the post-seismic background PSD level (Figure 2.16). Careful investigation of both event distribution and instrument response functions estimated from noise records reveal that the change is not due to uneven source distribution or instrumental bias. Moreover, this change is observed only for events coming from the back-azimuth range 0°-200°(dominated by events originating from South-Central America), which sample the crust along strike and southwest of the San Andreas Fault near Parkfield (Figure 2.15).

Variations in PSD levels do not constrain the depth of

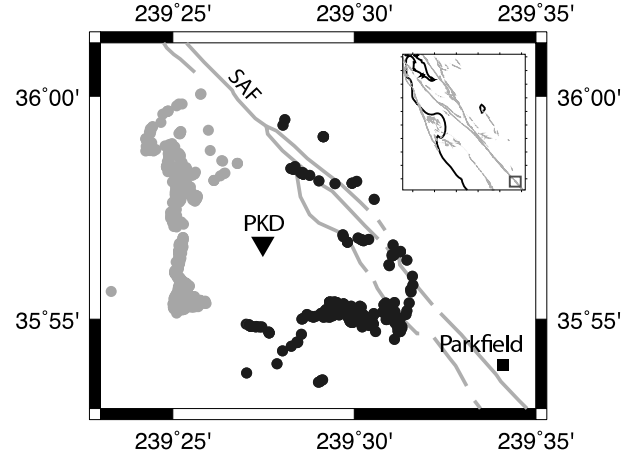


Figure 2.15: Moho piercing points (grey and black dots) of receiver functions around station PKD near Parkfield, California, with respect to study region (inset). Events from eastern azimuths (0°-200°- black dots) sample the crustal structure along the strike of the San Andreas Fault.

this change; however, given its azimuthal dependence, it is unlikely that it originates at shallow levels. Its manifestation at periods of 0.5-3 s where PSD is highest suggests a depth-integrated effect that may be related to crack opening, non-linear damage, or permeability-enhanced pore-fluid flow. Reduced PSD levels imply a decrease in scattering energy from structure, i.e. smaller impedance contrasts across interfaces, which is consistent with redistribution of crustal pore-fluids and the breaking of impermeable barriers due to shaking (i.e. damage). The fact that the Parkfield earthquake did not have a similarly strong effect on the PSD levels may reflect the total re-equilibration of pore-fluid pressures in the crustal column after the San Simeon earthquake.

Such questions may be addressed by complementary methods that provide depth resolution (e.g. time-domain receiver functions, ambient-noise tomography, etc.) and using different data sets. These results are consistent with time-varying crustal S-velocities from ambient noise correlation studies and the coincident modulation of tremor activity near Parkfield following the 2003 San Simeon and 2004 Parkfield earthquakes (Brenquier et al., 2008). This preliminary study indicates that the receiver function method bears the potential for investigating 4-D faulting processes, albeit only as a diagnostic tool.

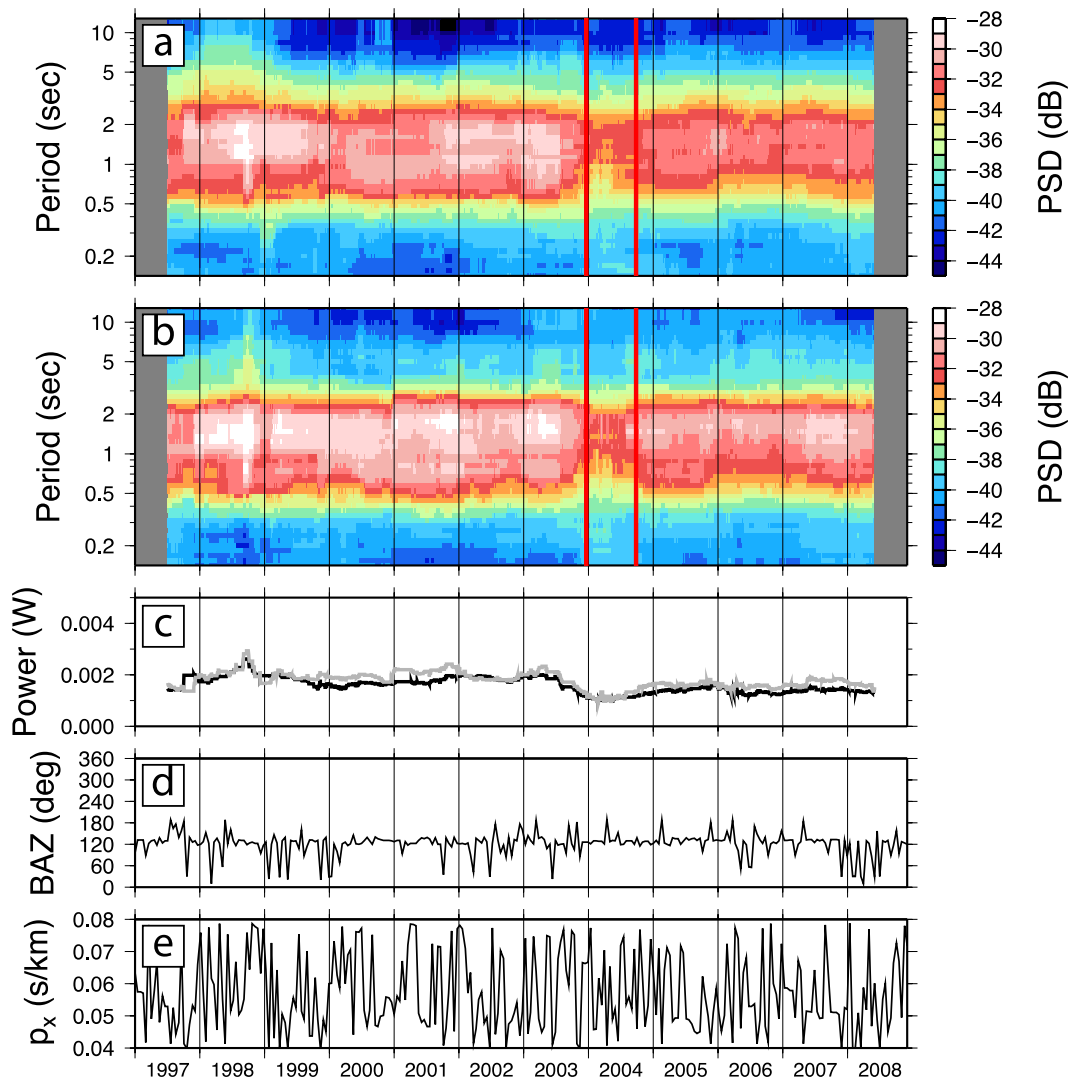


Figure 2.16: Temporal variations in receiver functions at station PKD for back-azimuths  $0^{\circ}$ - $200^{\circ}$ . Top panels show power-spectral density (PSD) of receiver functions binned within 90% overlapping, 12-month windows for radial (a) and transverse (b) components. Panel (c) shows the corresponding variations in total power (black line - radial; grey line - transverse). Distribution of events with respect to back-azimuth and slowness of incoming wave-fields is presented in (d,e). Vertical lines indicate times of the San Simeon (2003) and Parkfield (2004) earthquakes.

### 7.3 Acknowledgements

This work was funded by the Miller Institute for Basic Research in Science (UC Berkeley).

### 7.4 References

- Brenguier, F., M. Campillo, C. Hadziioannou, N.M. Shapiro, R.M. Nadeau, and E. Larose, Postseismic relaxation along the San Andreas fault at Parkfield from continuous seismological observations, *Science*, 321, 1478-1481, 2008.
- Ozacar A. A., and G. Zandt, Crustal structure and seismic anisotropy near the San Andreas fault at Parkfield, California, *Geophys. J. Int.*, in press, 2009.

# 8 Remote Triggering of Fault-Strength Changes on the San Andreas Fault at Parkfield

Taka'aki Taira, Paul G. Silver (Carnegie Institution of Washington), Fenglin Niu (Rice University), and Robert M. Nadeau

## 8.1 Introduction

Fault strength is a fundamental property of seismogenic zones, and its temporal changes can increase or decrease the likelihood of failure and the ultimate triggering of seismic events. While changes in fault strength have been suggested to explain various phenomena, such as the remote triggering of seismicity, there has been, to our knowledge, no means of actually monitoring this important property in situ. Here we argue that  $\sim 20$  years of observation (1987-2008) of the Parkfield area at the San Andreas Fault have revealed a means of monitoring fault strength. We have identified a long-term change in fault strength most likely induced by the 2004  $M_w$  9.1 Sumatra-Andaman earthquake (SM04) (Taira *et al.*, 2009). The change possessed two manifestations: temporal variations in the properties of seismic scatterers - likely reflecting the stress-induced migration of fluids - and systematic temporal variations in the characteristics of repeating-earthquake sequences that are most consistent with changes in fault strength.

## 8.2 Fault-Strength Change

The time-varying properties of seismic scatterers have recently been used to probe stress-induced changes in the San Andreas Fault zone near Parkfield in central California (Niu *et al.*, 2003; Taira *et al.*, 2008). As a measure of temporal scatterer behavior from one earthquake to the next, we use the decorrelation index  $D(t)=1-C_{\max}(t)$  derived from the cross correlation of two seismograms, where  $C_{\max}(t)$  is the maximum cross correlation (Niu *et al.*, 2003). Using tightly-clustered repeating microearthquakes (Nadeau and McEvilly, 1999) recorded by the High-Resolution Seismic Network (Figure 2.17a), we have been able to track the behavior of a group of time-dependent scatterers (the target scatterer) that was first identified by Niu *et al.* (2003), for a 22-year period (1987-2008) (Figure 2.17b). The target scatterer has been interpreted as fluid-filled fractures, and their temporal variations as due to the stress-induced migration of fluids near the target scatterer.

There are three excursions in  $D(t)$ . The 1<sup>st</sup> excursion is coincident with the 1993 Parkfield Aseismic Transient (PAT93). It initiated around 1993 (Figure 2.17b), peaked in the mid 1990s and slowly decayed over about a subsequent  $\sim 7$ -year period. The 2<sup>nd</sup> excursion (September 2004) is associated with the 2004 Parkfield earthquake (PK04) (Figure 2.17c) and decayed back to the pre-earthquake level after about 2-3 months. The 3<sup>rd</sup> ex-

cursion in  $D(t)$  occurred about three months after the 2004 Parkfield earthquake (Figure 2.17c). The magnitude of change in  $D(t)$  is comparable to that observed for the other two transients. The increase in  $D(t)$  takes place over three months, after which time  $D(t)$  decays slowly over a subsequent  $\sim 1$  year period (Figure 2.17c).

There are also changes in repeating-earthquake properties that accompany this 3<sup>rd</sup> excursion in  $D(t)$ . Following the 2004 Parkfield earthquake, there is a characteristic increase in recurrence interval  $T_r$  as is typically observed postseismically. This trend, however, is interrupted roughly three months after the 2004 Parkfield earthquake. In 6 of the available 13 sequences, there is a systematic reduction in  $T_r$  that reaches a minimum about 6 months after the 2004 Parkfield earthquake. To explore this apparent disruption further, we removed the post-seismic effect by the 2004 Parkfield earthquake, assuming Omori's law,  $T_r(t)=at^p$  where  $t$  is time after the earthquake and  $a$  and  $p$  are constants to be estimated, and computed the residual recurrence interval  $\hat{T}_r(t)=T_r(t)/(at^p)$ .

Using all available sequences, we find that the log of the residuals increases by roughly a factor of 2 beginning three months after the 2004 Parkfield earthquake. This increased variability suggests an additional perturbation to  $T_r$  and a temporal change in the mechanical properties of the fault. An interesting feature of this variability is that there is a positive correlation between  $\hat{T}_r$  and seismic moment  $M_0$  (Figure 2.17d). Such a correlation is consistent with a slip-predictable model for earthquake occurrence (Shimazaki and Nakata, 1980), where the stress drop and  $T_r$  are both determined by the failure strength of the fault for constant loading rate and constant minimum stress. Assuming rupture area is constant among members of a repeating-earthquake sequence (Nadeau and Johnson, 1998), then fault slip will be proportional to  $M_0$  which should in turn be proportional to stress drop. The most dramatic correlation that we found is for sequence K3 (5 km depth) (Figure 2.17d). This sequence also has the least variability in event location, so that the assumption of constant fault area should be the most valid. A reduction in  $\hat{T}_r$  (and  $M_0$ ) around 6 months after the 2004 Parkfield earthquake indicates a temporary weakening of the fault.

We have localized the onset time of the 3<sup>rd</sup> excursion in  $D(t)$ , utilizing all of the repeating-earthquake sequences that displayed a change in  $D(t)$ . We find that the excursion must have initiated between December 21 (se-

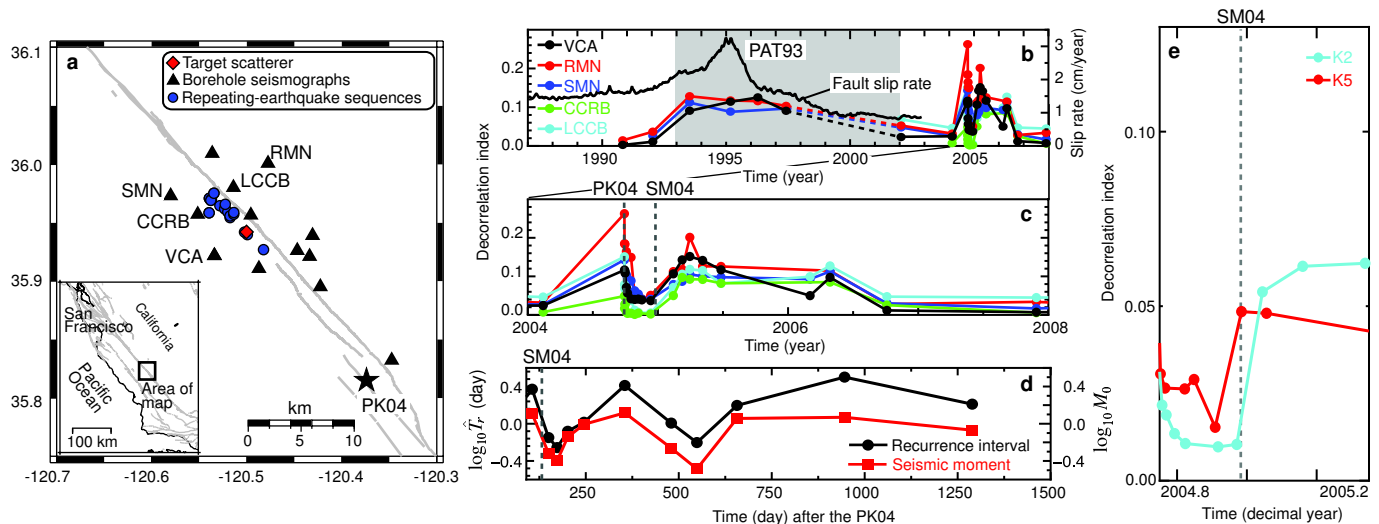


Figure 2.17: (a) Map view of the study area.  $D(t)$  for sequence K3 during (b) 1987-2008 and (c) 2004-2008. (d)  $\hat{T}_r$  and  $M_0$  normalized by its average for sequence K3. (e) Average  $D(t)$  using the lowest-noise stations VCA, LCCB, and CCRB, for sequences K2 and K5.

quence K2) and December 26, 2004 (sequence K5) (Figure 2.17e). The most dramatic tectonic event to occur within the 5-day time window is the 26 December 2004  $M_w$  9.1 Sumatra-Andaman earthquake, whose origin time is 7 hours before the end of the interval. The timing strongly suggests that the dynamic stresses from this earthquake, estimated to be about 10 kPa [based on the amplitude of long period surface waves ( $>30$  s) which are likely to have the strongest impact on fluid flow], induced fluid flow that caused both a structural change in the fault zone region [i.e. changes in  $D(t)$ ] and, through variations in pore pressure, consequent changes in the strength of the fault. It is now well documented that such dynamic stresses are capable of remotely triggering seismicity. The present study suggests that these same dynamic stresses can actually produce long-term ( $\sim 1$  year for our study) changes in fault strength.

### 8.3 Conclusions

We showed that temporal changes in seismic scatterer properties and characteristics (frequency and magnitude) of repeating microearthquakes constitute a proxy for changes in fault strength, proposing that they provide a means of continually monitoring fault zone strength which is an important parameter in assessing earthquake potential of a fault.

### 8.4 Acknowledgements

The present study was supported by the National Science Foundation EAR-0337308, EAR-0408947, EAR-0409024, EAR-0453638, EAR-0537641, EAR-0544730,

and DTM-2025-01 and by the Department of Terrestrial Magnetism, Carnegie Institution of Washington. The Parkfield High-Resolution Seismic Network is operated by University of California, Berkeley Seismological Laboratory with financial support from the U.S. Geological Survey through National Earthquake Hazards Reduction Program award 07HQAG0014.

### 8.5 References

- Nadeau, R.M. and L.R. Johnson, Seismological studies at Parkfield VI: Moment release rates and estimates of source parameters for small repeating earthquakes, *Bull. Seismol. Soc. Am.*, *88*, 790-814, 1998.
- Nadeau, R.M. and T.V. McEvilly, Fault slip rates at depth from recurrence intervals of repeating microearthquakes, *Science*, *285*, 718-721, 1999.
- Niu, F., P.G. Silver, R.M. Nadeau, and T.V. McEvilly, Migration of seismic scatterers associated with the 1993 Parkfield aseismic transient event, *Nature*, *426*, 544-548, 2003.
- Shimazaki, K. and T. Nakata, Time-predictable recurrence model for large earthquakes, *Geophys. Res. Lett.*, *7*, 279-282, 1980.
- Taira, T., P.G. Silver, F. Niu, and R.M. Nadeau, Detecting seismogenic stress evolution and constraining fault zone rheology in the San Andreas Fault following the 2004 Parkfield earthquake, *J. Geophys. Res.*, *113*, B03303, doi:10.1029/2007JB005151, 2008.
- Taira, T., P.G. Silver, F. Niu, and R.M. Nadeau, Remote triggering of fault-strength changes on the San Andreas Fault at Parkfield, *Nature*, doi:10.1038/nature08395, 2009 (accepted for publication).

# 9 Source Analysis of the Memorial Day Explosion, Kimchaek, North Korea

Douglas Dreger, Sean Ford (LLNL), William Walter (LLNL)

## 9.1 Introduction

The Democratic People’s Republic of Korea (DPRK) announced it conducted a second nuclear test on 25 May 2009. Within hours of the test, and before the official DPRK announcement, several organizations, including the U.S. Geological Survey National Earthquake Information Center and the Comprehensive Test Ban Treaty Organization (CTBTO), reported a seismic signal in the magnitude range 4.5 to 4.7 near the vicinity of the 2006 DPRK nuclear test (CTBTO Press Centre, 2009a). However, the International Monitoring System of the CTBTO did not detect radioactive noble gases that would confirm the test of a nuclear-device (Clery, 2009).

In our previous work (Ford *et al.*, 2009a) we showed it was possible to identify explosions at the Nevada Test Site with a full moment tensor inversion of seismic waveforms from nearby stations in the Western US. In this contribution, we show that the best-fit source for the

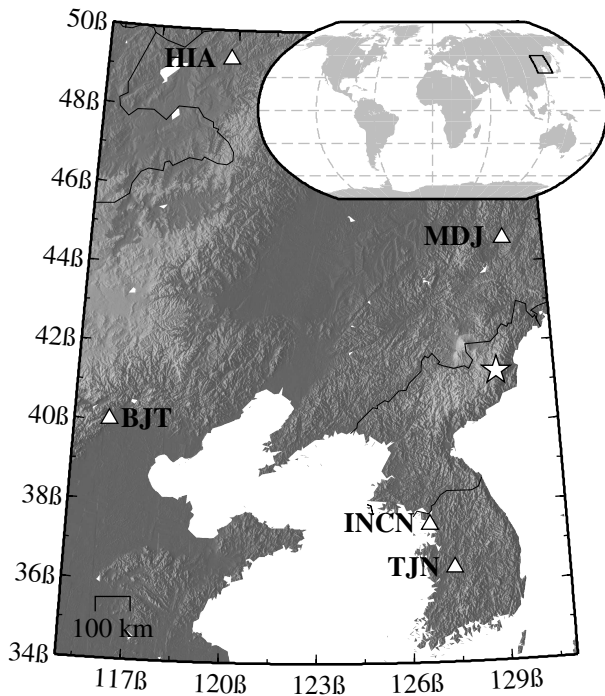


Figure 2.18: Map of the Yellow Sea / Korean Peninsula region. The North Korea explosion is identified with a star and the stations with triangles. The region is outlined in the global inset map.

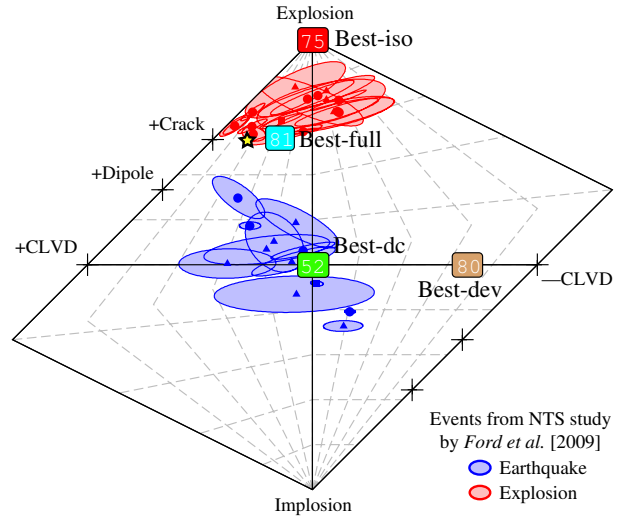


Figure 2.19: Source-type plot with various solutions and their associated fit percent. Note that the Best-DC solution is at the center ( $[\epsilon, k] = [0, 0]$ ) and the Best-dev solution is along the abscissa ( $k = 0$ ). Also plotted are results for explosions at the Nevada Test Site (NTS) from Ford *et al.* [2009a] with their associated 95% error ellipses. Error ellipses for the North Korea test are smaller than the plotted symbol.

2009 Memorial Day event near Kimchaek, North Korea is dominantly isotropic, which is consistent with an explosion. A more detailed description of this work is found in Ford *et al.* (2009b)

## 9.2 Results

Three component waveform data from Global Seismograph Network (GSN) and China Digital Seismograph Network (CDSN) stations MDJ, INCN, BJT and HIA along with station TJN from the Ocean Hemisphere Project Seismological Network (Figure 2.18) are instrument corrected, integrated to displacement, and band-pass filtered using an 6<sup>th</sup> order acausal Butterworth filter with corners at 0.02 and 0.10 Hz. Green’s functions were computed using a model appropriate for the region. The Green’s functions were aligned with the data based on a location and origin time of 00:54:43.38, 25 May 09, 41.2986°/129.0694° (D. Dodge, unpublished data, 2009), and timing shifts of less than 5 seconds (maximum half-cycle recommended by Ford *et al.* (2009a))

were employed to maximize the fit to the data. A source depth of 600m was initially assumed. Explosion, earthquake (double-couple or DC), deviatoric, and full moment tensor solutions were evaluated. The explosion and DC solutions were obtained with a grid-search to find the best-fitting parameters, whereas the deviatoric and full moment tensor solutions were calculated with a least-squares linear inversion.

As Figure 2.19 shows, the pure explosion model fits the data with a variance reduction of 75% and yields an isotropic moment of  $1.8 \times 10^{22}$  dyne-cm ( $M_w 4.1$ ; all seismic moment values are calculated with the method of *Bowers and Hudson (1999)*). In contrast, the pure DC earthquake solution fits the data much worse at 52% with  $M_0 = 3.8 \times 10^{22}$  dyne-cm ( $M_w 4.4$ ). The fact that the single degree of freedom explosion model fits so much better than the four degree of freedom DC model is highly significant and indicates that such a comparison can be a useful discriminant. The strike, rake, and dip of the best-fit DC is  $50^\circ$ ,  $-85^\circ$ , and  $10^\circ$ , respectively. Such a steep dip-slip mechanism is unusual for an earthquake. Of all sources calculated by the Global CMT Project (<http://www.globalcmt.org/>) less than 1.6% have dips of less than  $10^\circ$ . This type of information may be used as an additional indication of anomalous sources. The DC overpredicts the Love wave amplitude on the transverse components at almost all stations and underpredicts the Rayleigh wave amplitudes, especially at station INCN. The pure explosion does not produce Love waves, and therefore the actual source is a composite.

The full moment tensor inversion fits the data at 81% and yields an isotropic moment of  $3.6 \times 10^{22}$  dyne-cm, and a total moment of  $6.3 \times 10^{22}$  dyne-cm ( $M_w 4.5$ ). The deviatoric moment tensor inversion fits the data at 80% and a total moment of  $3.2 \times 10^{22}$  dyne-cm ( $M_w 4.3$ ). If the deviatoric source is decomposed to a compensated linear vector dipole (CLVD) and DC sharing the same principal axes, then the source is 70% CLVD. The similarity in fits between the dominantly CLVD deviatoric source and dominantly isotropic full moment tensor shows that at shallow depths, a vertical CLVD mechanism can effectively mimic an explosion at the distances and periods analyzed here. The full moment tensor isotropic moment is two times larger than the pure explosion, indicating that the compound source of the full moment tensor solution (DC+CLVD+Isotropic) required to fit the Love waves also modifies the Rayleigh waves, causing the isotropic component to increase in order to compensate.

The best-fitting sources are far from the center, indicating that the source is anomalously non-DC (Figure 2.19). Along with the best-fitting sources the solutions and their 95% error ellipses for explosions at the Nevada Test Site (NTS) and earthquakes in the Western US from *Ford et al. (2009a)* are also plotted. The best-fit full moment tensor plots in the same region as the explosions,

close to the solution for the 2006 North Korean test, and away from the earthquake population. The error ellipses for the best-fit sources from this study are all smaller than the symbol used to plot the solutions due to the very high signal-to-noise of the event records.

Unlike earthquake inversions, the isotropic radiation of a predominantly explosive source does not allow constraint of the source depth by comparing fits at different depths at the frequencies examined here (e.g. *Ford et al., 2009a*). Event locations put the source at less than 1 km, so the results discussed above assume a source depth of 600 m. *Ford et al., (2009b)* examines the sensitivity of isotropic moment with source depth

### 9.3 Conclusions

Modeling of low-frequency, regional distance waveforms identifies the Memorial Day event in Kimchaek, North Korea as decidedly non-tectonic with the best-fit model dominated by an explosion source. While the source type is well determined to be non-DC, the isotropic moment of the full moment tensor inversion has some uncertainty and the  $M_w$  is between 4.4 and 4.6. Comparison of pure explosion and pure double-couple models indicate that the simpler explosion model fits the waveform data substantially better than the higher degree of freedom DC model, where the isotropic moment of the explosion model is  $1.8 \times 10^{22}$  dyne-cm ( $M_w 4.1$ ). However, there are Love waves observed at several stations indicating that the source must have some non-isotropic component. Possible causes of the tangential displacement are additional tectonic sources, tensile failure at depth, and anisotropic propagation.

### 9.4 Acknowledgements

This research was supported by the National Nuclear Security Administration, contract DE-FC52-06NA27324.

### 9.5 References

- Bowers, D., and J. A. Hudson, Defining the scalar moment of a seismic source with a general moment tensor, *Bull. Seism. Soc. Am.*, 89(5), 1390-1394, 1999.
- Clery, D., Test ban monitoring: No place to hide, *Science*, 325, 382-385, 2009.
- CTBTO Press Centre, Next phase in the analysis of the announced DPRK nuclear test, Press Release 27 May 09, 2009a.
- Ford, S. R., D. S. Dreger and W. R. Walter, Identifying isotropic events using a regional moment tensor inversion, *J. Geophys. Res.*, 114, B01306, doi:10.1029/2008JB005743, 2009a.
- Ford, S. R., D. S. Dreger and W. R. Walter, Source Analysis of the Memorial Day Explosion, Kimchaek, North Korea, *in press Geophys. Res. Lett.*, 2009b.
- Hudson, J. A., R. G. Pearce, and R. M. Rogers, Source type plot for inversion of the moment tensor, *J. Geophys. Res.*, 94, 765-774, doi:10.1029/JB094iB01p00765, 1989.

# 10 Towards a continuous seismic wavefield scanning

Aur lie Guilhem, Doug S. Dreger and Bob Uhrhammer

## 10.1 Introduction

The Mendocino Triple Junction (MTJ) region is tectonically very complex, and as a result it is the seismically most active region of Northern California, with earthquakes (including potential large earthquakes  $M > 7$ ) occurring on the Mendocino Transform Fault, along the Cascadia subduction zone, and in the offshore Gorda/Juan de Fuca plate. In addition to typical intra- and inter- plate seismic events, a variety of anomalous seismic events, including repeating earthquakes, slow/low-stress-drop earthquakes, and nonvolcanic tremors, are observed. In order to more effectively monitor the offshore region, we implement an automatic scanning of the continuous long-period ( $> 10$  sec) broadband seismic records to continuously detect, locate and determine moment tensors of events within minutes following their occurrence. Because the analysis will be done every two seconds, this scanning offers the possibility of rapidly identifying any large damaging and potentially tsunamigenic events.

## 10.2 Method

We follow the algorithm proposed by Kawakatsu (1998) and used in Japan by Tsuruoka *et al.*, 2009. A seismogram  $d$  recorded at a station  $k$  can be represented as the convolution of the response of the medium to an impulsive source  $G$  with the moment tensor elements  $m$  for a source  $s$ :  $\sum_i G_i^{sk}(t)m_i^s = d^k(t)$  (1). The normal equation based on (1) is given by:  $\sum_i A_{ji}^s m_i^s = b_j^s$  (2).  $A$  is a square matrix and the least-squares solution of the moment tensor  $\hat{m}$  is then given by:  $\hat{m} = A^{-1}b$  (3). The moment tensor  $m$  can be obtained by a simple matrix multiplication once  $b$  is calculated. The variance reduction (VR) obtained from the residual between data and synthetic seismograms is used to evaluate the fit for each calculation.

This analysis is performed over a grid search between  $40.0^\circ$  and  $43.0^\circ$  latitude ( $0.2^\circ$  interval),  $-128^\circ$  and  $-123^\circ$  longitude ( $0.2^\circ$  interval), and 5 to 38 km depth (3km interval) (Figure 2.20). For each point of the grid, a moment tensor is generated every two seconds, using 380 sec of broadband velocity seismograms filtered between 20 and 50 sec from four stations of the Berkeley Digital Seismic Network (BDSN) - HUMO, ORV, WDC, and YBH - and a previously generated catalog of Green's functions. The best calculated VR gives the preferred solution for an event.

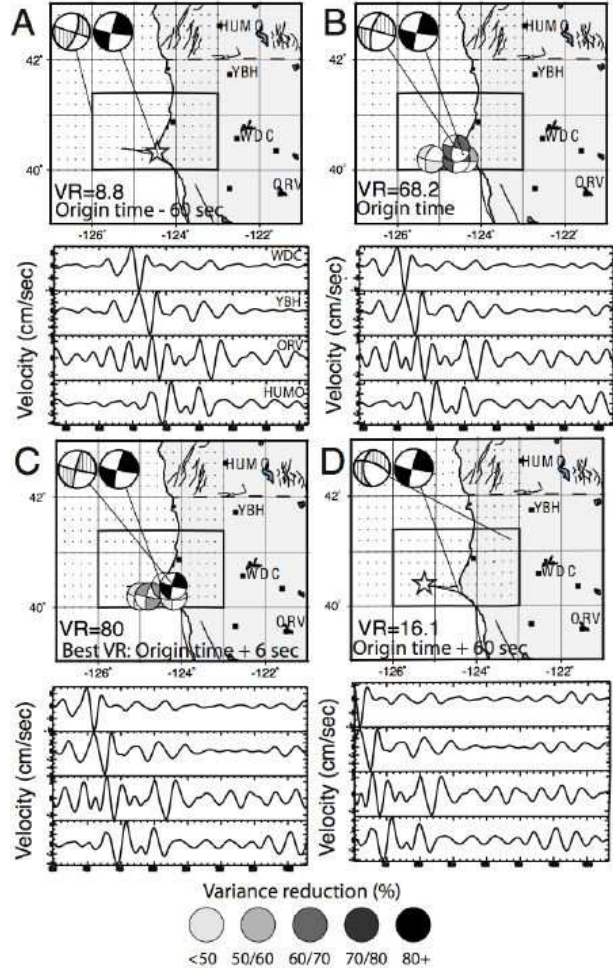


Figure 2.20: Preliminary test for a  $M_w 5.0$  earthquake in the MTJ. The large dashed beach ball diagram represents the best mechanism (largest VR indicated on the map) determined for each window, and the large black one shows the reference solution from the Berkeley Moment Tensor catalog. The smaller beach ball diagrams represent the solutions obtained for each time period. The waveforms (vertical velocity seismograms) show the data used in the computation for each time window. A) Analysis performed for 380 sec starting 60 sec before the original time. B) Data starts at the origin time (ANSS catalog) of the earthquake. C) Best time given by the best VR computed for the grid search (here 6 sec after the ANSS catalog time). D) Window starts 60 sec after the origin time.

### 10.3 Preliminary results

We performed preliminary tests of the continuous seismic scanning using different magnitude earthquakes (from  $M_w$ 4.2 to  $M_w$ 7.2) located in the study region (Figure 2.20). We centered the grid search around the origin time of the events (about 90 sec before and 60 after), and we reduced the grid search to increase the computational timing of the calculations. For the five studied earthquakes we are able to retrieve their characteristics (origin time, location, magnitude, and mechanism) by searching for the maximum VR (between 69 and 80% agreement between data and synthetics). Additional tests have been performed for periods of seismic noise and teleseismic wave arrivals to evaluate the response of the designed technique when no event was generated in the study region.

Also, because the Mendocino region lies in the southernmost part of the Cascadia subduction zone, which is capable of great and potentially tsunamigenic earthquakes, we performed a synthetic test for a  $M_w$ 8.2 reverse earthquake along the trench. We simulated synthetic waveform data for the four stations, filtered between 100 and 200 sec period. 480 sec were inverted, beginning 50 sec before the origin time and ending 50 sec afterward, and the best VR was determined for each point of the grid. Such a multi point-source inversion gives promising results for large earthquakes and can be employed in parallel to the single point-source analysis.

### 10.4 Implementation of the continuous scanning

The preliminary tests utilized archived seismic data rather than the realtime data that will be processed when the system is in service. We plan to use HH and HL channels (80 sps to 100 sps) from the four stations, decimated to 1 sps and filtered between 20-50 sec and 100-200 sec. Tests of the recursive filters, computed in only a fraction of a second for the 12 channels simultaneously, have been done, and they show very good agreement with similar filters computed in SAC. Also, because a realtime system might mean a lack of incoming data, we performed a jack-knife test to measure the effects of missing channels on the stability of the moment tensor solution for a  $M_w$ 5.0 earthquake (Figure 2.21). The mechanism and magnitude of an earthquake are stable. However the VR may change by tens of percentage points, which may result in the non detection of an event if the threshold is set at 65%. Also, missing two or three channels from different stations can worsen the result compared to missing one or two stations, especially if those missing channels contained most of the energy of the earthquake. As a result, we intend to remove all stations with missing channels from the computation and account for missing stations when computing the VR.

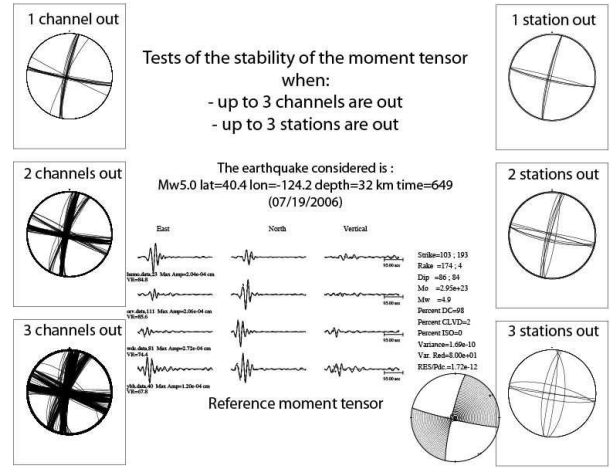


Figure 2.21: Test of the stability of the moment tensor with missing channel(s) and station(s). To symbolize the missing traces, we multiplied the data by zero. The beach ball diagrams on the right and left sides of the figure show the variation in the strikes. The central part of the figure shows the optimal solution obtained with the 12 working channels.

### 10.5 Conclusions

We are designing a continuous seismic waveform scanning system that will allow the detection, location, and determination of the magnitude and mechanism of any earthquakes of  $M_w$ 3.5+ located in the vicinity of the MTJ. The combination of single point-source and multiple point-source inversions by the implementation of two parallel calculations (20-50 sec and 100-200 sec periods) will be useful for the detection of small to great earthquakes in the region. Such realtime monitoring will provide faster results than the currently used procedures. However, HUMO is currently in a triggered mode for the HH and HL channels. We will need to either obtain continuous datastreams or consider replacing it with another seismic station. Finally, the MTJ region is also known for the occurrence of unusual seismicity, in particular for slow/low-stress-drop earthquakes, and such a technique considering long period data may then help in the search for these unusual earthquakes.

### 10.6 References

- Kawakatsu, H., On the realtime monitoring of the long-period seismic wavefield, *Bull. Earthquake Res. Inst.*, 73, 267-274, 1998.
- Tsuruoka, H., H. Kawakatsu, and T. Urabe, GRiD MT (grid-based real-time determination of moment tensors) monitoring the long-period seismic wavefield, *Phys. Earth Plan. Int.*, 175, 8-16, 2009.

# 11 The rupture process of the Parkfield SAFOD target earthquakes obtained from the empirical Greens function waveform inversion method

Ahyi Kim, Douglas Dreger, and Taka'aki Taira

## 11.1 Introduction

*Nadeau et al.* (1995) found that the seismicity on the San Andreas fault at Parkfield is highly clustered and individual clusters consist of sequences of near periodically repeating small earthquakes of similar seismic moment. *Nadeau and Johnston* (1998) studied the moments, slip rate, and recurrence intervals of these repeating earthquakes, and found that the stress drop of small earthquakes is quite high and, remarkably, increases with decreasing seismic moment. For example, for one of the SAFOD target M2.1 (*Hickman et al.*, 2004) earthquakes, the relationship developed by *Nadeau and Johnston* (1998) yields a stress drop of 100 MPa (correcting for a rigidity of 12 GPa for hypocentral depth of 2.1 km; e.g. *Dreger et al.*, 2007). On the other hand, a spectral corner frequency method yields an average stress drop for the same earthquake of 8.9-22.1 MPa (*Imanishi et al.* 2004; *Imanishi and Ellsworth*, 2006). Recently, *Dreger et al.* (2007) investigated the rupture processes of a sequence of repeating M2.1 SAFOD target earthquakes using the eGf deconvolution method. In that study, they found that peak stress drops between 66.7-93.9 MPa. We applied an eGf waveform inversion method to the  $M_w$ 2.1 repeating earthquakes and compared rupture process models, static stress drop distributions, and waveform fits with those from the eGf deconvolution method.

## 11.2 Method

Inspired by *Hartzell et al.* (1978), we directly inverted observed seismograms using the linear least-squares method of *Hartzell and Heaton* (1983) in which the finite-source is discretized with a finite distribution of point sources in both space and time instead of inverting deconvolved moment rate functions. In this method, the point sources are triggered by the passage of a circular rupture front. The Greens function from each subfault to station is defined by the waveform of a small earthquake, or eGf, located near the hypocenter of each subfault. One advantage of this method is that propagation differences over the fault are better represented for each station. The observed seismogram at location  $x$  for the main event,  $U$ , is expressed by the discrete form of the general representation theorem:

$$U(x, t) = \sum_{k=1}^K \mu_k A_k u_k \cdot eGf(x, x_k, t + \delta t_k)$$

where  $x_k$  is the location of subfault.  $A_k, \mu_k$ , and  $u_k$  are subfault area, rigidity, and slip for the  $k$ th subfault of a total of  $K$  subfaults. The phase delay term includes

both the delay due to rupture propagation and the travel time difference between the eGf hypocenter and the subfault. We assume that each eGf has the same mechanism as the main event, an acceptable approximation for small earthquakes. The variation of mechanism in the main shock can also potentially be accounted for if eGfs are well distributed over the fault plane. For our San Andreas fault applications, the focal mechanisms of events vary little over a wide range of magnitudes (*Thurber et al.*, 2006). To stabilize the inversion, we employed a slip positivity constraint using the non-negative, least-squares routine of *Lawson and Hanson* (1974), as well as spatial smoothing. The weight of the smoothing constraint was determined by trial and error by finding the smallest value that produced a smoothed model with close to the maximum fit to the data measured by the variance reduction,

$$VR = \left[ 1 - \frac{\sum_i (d_i - s_i)^2}{\sum_i d_i^2} \right] \times 100$$

where  $d_i$  and  $s_i$  represent the data and synthetic time series, respectively. The subscript  $i$  is an index over station, component, and time. The size of the subfault was chosen to produce a temporally smooth kinematic process with respect to the sample rate of the data.

## 11.3 Computational setup

We used three-component velocity waveforms recorded at five of the Berkeley Seismological Laboratory's High Resolution borehole Seismic Network (HRSN) stations to examine the rupture processes of the same 5 repeating earthquakes studied by *Dreger et al.* (2007). We also performed eGf deconvolution inversions using the 5 stations, to allow comparison with our waveform inversion results. Locations of repeating earthquakes and stations are shown in Figure 2.22. For the inversion, we used the same fault parametrization as *Dreger et al.* (2007), a  $150 \times 150 m^2$  fault decomposed into 31 by 31 square subfaults of  $4.8 \times 4.8 m^2$ . The strike, dip, and rake are 137, 90, and 180, respectively. The records from HRSN are sampled at 250 sps, which gives an effective bandwidth of 100 Hz. The subfault size is consistent with approximately a quarter of the wavelength of S waves assuming a velocity of 2.3 km/s at 2.1 km depth. We used the same  $M_w$ 0.68 event (eGf 1) as *Dreger et al.* (2007)

for the Greens function. eGf 1 is located about 10 m away from the centroid of the target events (Dreger *et al.*, 2007). Since the eGf is a real earthquake, the waveforms contain a rise time which can bias the slip model to be more compact than it actually is. To cancel this effect, we convolved an assumed eGf rise time of 0.008 seconds with the data before performing the inversion. (Dreger *et al.* (2007)).

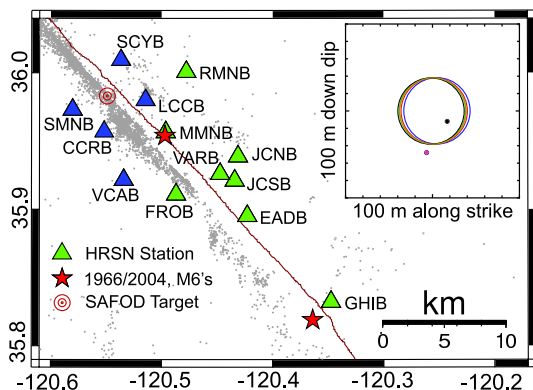


Figure 2.22: Map showing the HRSN station locations (blue triangles are the stations used in this study) and SAFOD repeating target events (star). The inset shows the cross-sectional view of the relative locations of the five studied M2.1 repeating events (larger colored circles), and  $M_w$  0.68 eGf 1 (red dot) and  $M_w$  0.64 eGf 6 (blue dot). The size of the circles shows the respective areas of a 100 MPa event. For comparison, the large gray circle shows the inferred area for a 10 MPa event.

## 11.4 Inversion results and interpretations

As an example of the results, slip model and stress drop distribution are shown for EVT4 in Figure 2.23. Typically, the slip distribution is circular with a diameter of about 50 m, and the average slip of the main asperity is 3.3 -4.0 cm. The peak slip amplitudes were found to be 10-13 cm. Using our spatially variable slip distribution model, we computed the coseismic stress change on the fault plane using the method of Ripperger and Mai (2007) (Figure 2.23). The computed static stress drop distribution shows that the small patch has a peak stress drop of 63.9-89.4 MPa, which is consistent with the values reported by Dreger *et al.* (2007). However, the average stress drop of 5 MPa is consistent with the typical range of between 1-10 MPa. The rupture process of small earthquakes is complicated, just as in large earthquakes, in terms of spatially variable slip. Also, the SAFOD target events appear to occur on a localized fault patch of high strength capable of earthquakes with high stress drop. The very high peak stress drop that is obtained implies that small-dimension, high-strength asperities exist on the San Andreas Fault.

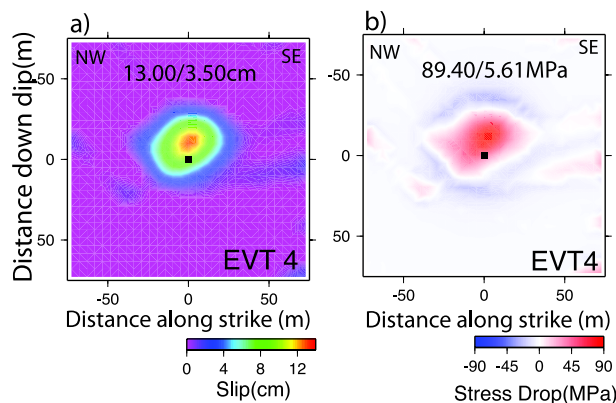


Figure 2.23: Left: Slip model obtained for EVT4. Right: Stress drop distribution for EVT4. For both figures, the number indicates the peak/average slip for each event.

## 11.5 Acknowledgements

We thank Bob Nadeau for providing the repeating earthquake catalog.

## 11.6 References

- Dreger, D., R. M. Nadeau, and A. Chung (2007), Repeating earthquake finite source models: Strong asperities revealed on the San Andreas Fault, *Geophys. Res. Lett.*, 34, L23302, doi:10.1029/2007GL031353.
- Hartzell S. H. (1978), Earthquake aftershocks as Green's function, *Geophys. Res. Lett.* 5, 1-4.
- Hickman, S., M. Zoback, and W. Ellsworth (2004), Introduction to special section: Preparing for the San Andreas Fault Observatory at Depth, *Geophys. Res. Lett.*, 31, L12S01, doi:10.1029/2004GL020688.
- Imanishi, K., W. L. Ellsworth, and S. G. Prejean (2004), Earthquake source parameters determined by the SAFOD Pilot Hole seismic array, *Geophys. Res. Lett.*, 31, L12S09, doi:10.1029/2004GL019420.
- Imanishi, K., and W. L. Ellsworth (2006), Source scaling relationships of microearthquakes at Parkfield, CA, determined using the SAFOD pilot hole seismic array, in Earthquakes: Radiated Energy and the Physics of Earthquake Faulting, R. E. Abercrombie, A. McGarr, H. Kanamori and G. Di Toro (Editors), *American Geophysical Monograph* 170, 81-90.
- Lawson, C. L., and R. J. Hanson (1974), Solving Least Squares Problems, Prentice Hall, Englewood Clives, New Jersey, 340 pp.
- Nadeau, R. M., W. Foxall, and T. V. McEvilly (1995), Clustering and periodic recurrence of microearthquakes on the San Andreas Fault at Parkfield, California, *Science*, 267, 503-507.
- Nadeau, R. M., and L. R. Johnson (1998), Seismological studies at Parkfield VI: Moment release rates and estimates of source parameters for small repeating earthquakes, *Bull. Seismol. Soc. Am.*, 88, 790-814.
- Ripperger, J., and P.M. Mai (2004), Fast computation of static stress changes on 2D faults from final slip distributions, *Geophys. Res. Lett.*, 31, L18610.
- Thurber, C., H. Zhang, F. Waldhauser, J. Hardebeck, A. Michaels, and D. Eberhart-Phillips (2006), Three-dimensional compressional wavespeed model, earthquake relocations, and focal mechanisms for the Parkfield, California, region, *Bull. Seism. Soc. Am.*, 96, S38-S49.

## 12 Nonvolcanic Tremor Evolution in the Parkfield, CA Region

Robert M. Nadeau and Aurélie Guilhem

### 12.1 Introduction

Nonvolcanic tremors have generally been observed in transition zones between freely slipping and locked faults, and in many locations, tremor activity is also seen to increase with detectable transient fault zone deformation (slow-slip events) (*Liu and Rice, 2007*). These associations suggest that tremor activity is closely related to the processes responsible for generating earthquakes. We analyzed tremor activity in the Parkfield region of California between 27 July 2001 and 21 February 2009, during a period when two strong earthquakes occurred in the region: the  $6.5M_w$  San Simeon earthquake in 2003 and the  $6.0M_w$  Parkfield earthquake in 2004 (Figure 2.24).

### 12.2 Detection, Size, Location

Using borehole seismic data from the High Resolution Seismic Network (HRSN) at Parkfield, CA, 2198 tremor events (12,547 minutes of activity) were detected during the period (Figure 2.25), with event activity lasting from 3 to nearly 21 minutes. Significant activity also occurred below the detection threshold. The average seismic energy released during the tremors was typically equivalent to a  $0.5M_w$  earthquake, and energies ranged over  $1.5 M_w$  units. Data from five seismographic networks (BP, BK, NC, CI, and TA) were combined to locate the tremors (Figure 2.25). Approximately 90% of the tremors occurred adjacent to the locked Cholame segment of the San Andreas fault (SAF). An additional 5-10% occurred  $\sim 65$  km to the northwest in the vicinity of Monarch Peak, CA. Tremors in both zones occurred at between  $\sim 15$  and 30 km depths.

### 12.3 Evolution

A sudden increase and subsequent decay of tremor activity (aftertremors) began immediately after the 2003 San Simeon and 2004 Parkfield earthquakes (Figure 2.25A). In addition, approximately 3 weeks before the Parkfield earthquake, an unusually strong episode of activity (foretremor) lasting  $\sim 5$  days also occurred (*Nadeau and Guilhem, 2009*).

The decay of tremor activity after the Parkfield earthquake continued until mid-2006 when annual rates began again to increase, reaching  $\sim 181\%$  of the pre-San Simeon level during the final year of our analysis (Figure 2.25A). Before the Parkfield earthquake, tremor activity in the Monarch Peak tremor zone (Figure 2.24) was low (Figure 2.25B). However, beginning  $\sim 10$  days after the Parkfield event, activity in this zone increased significantly and

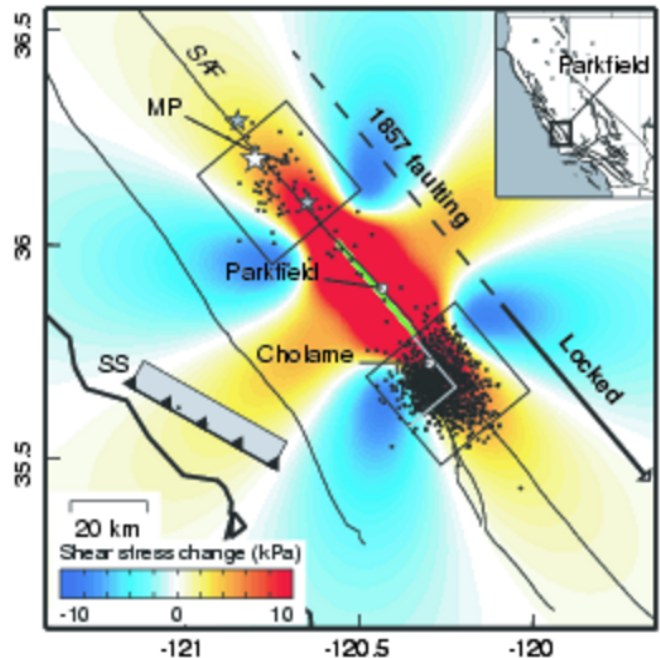


Figure 2.24: Study region with 1250 well-located tremors (black dots). Thirty kilometer square boxes (black) define the Monarch Peak (MP) and Cholame tremor zones. Color contours give regional shear-stress change at 20 km depth from the Parkfield earthquake (green segment) along the San Andreas Fault (SAF). The thrust type San Simeon earthquake rupture is represented by the grey rectangle and hatched line labeled SS. The currently locked Cholame segment is  $\sim 63$  km long (solid portion of arrow) and is believed capable of rupturing on its own in an  $\sim M7$  earthquake. The grey lines within the Cholame box bound the west quadrant where quasi-periodic episodes predominate. White star indicates the epicenter and gray stars the foreshocks of the 1857 Ft. Tejon earthquake.

has continued at an elevated rate. After the Parkfield earthquake, persistent episodes of quasi-periodic tremor also emerged that are reminiscent of episodic tremor observed in some subduction zones (Figure 2.25A) (*Rogers and Dragert, 2003*).

The episodic component of the tremors are most persistent and regular in the western quadrant of the Cholame tremor zone that is bounded by the SAF to the northeast and by the seismic-aseismic transition into the locked Cholame segment to the southeast (Figures 2.24, 2.25C and D). This localization of tremor behavior suggests that there are differences in the process generating tremor

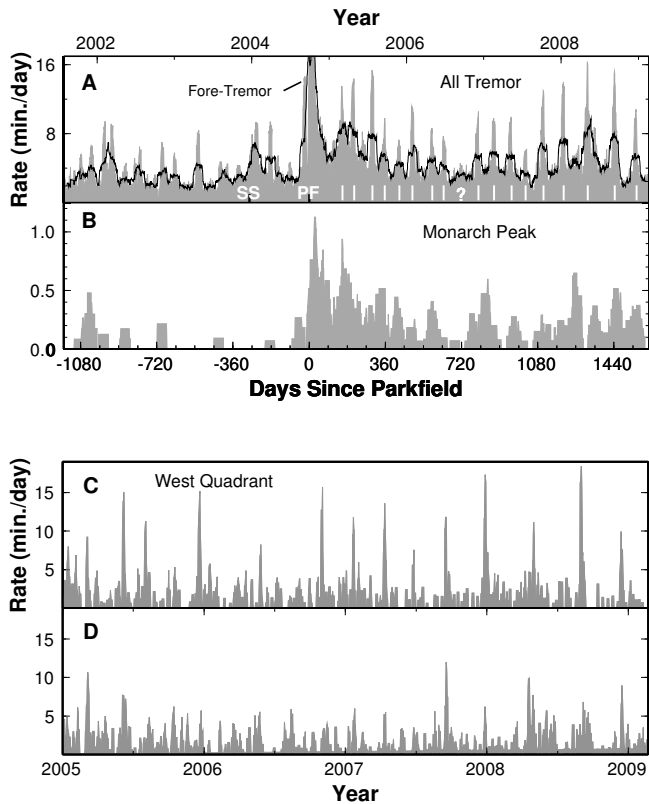


Figure 2.25: Time histories of tremor activity. (A) Fifteen-day (grey) and 45-day (black) smoothed rate histories for all tremors in the study area. Times of the San Simeon and Parkfield earthquakes are SS and PF, respectively. Intense foretremor (Fore-Tremor) activity occurred  $\sim 3$  weeks before PF. Fifteen- and 45-day peak values just after PF are 31.1 and 18.9 minutes/day, respectively. White bars are interpreted times of quasi-periodic episodes. Label ? is time of a weak or missing episode. (B) History of tremor in the Monarch Peak zone (45-day smoothed). (C) History since 2005 of activity (5-day smoothed) in the western quadrant of the Cholame zone (Figure 2.24) (423 tremors; 2835 cumulative minutes of activity) showing strong episodic behavior. (D) Same as (C) for Cholame tremors outside the west quadrant (416 tremors; 2423 cumulative minutes) showing significantly less episodic behavior.

in different subregions of the SAF and that tremor in the Cholame zone is distributed both normal-to and along-strike of the SAF at depth.

## 12.4 Stress Change

Static Coulomb- and shear-stress changes in the tremor zones from the 2003 San Simeon and 2004 Parkfield earthquakes on SAF aligned planes were small (6 to 14 kPa), but increases in tremor rates correspond with the increases in Coulomb- and shear- stresses. Static normal-

stress changes from the earthquakes do not clearly correspond to the tremor rate changes, suggesting that normal-stress change may not play a significant role in stimulating the SAF tremor. The Coulomb stress changes that stimulated the SAF tremors are roughly an order of magnitude smaller than those typically reported for the triggering of earthquakes (*King et al.*, 1994). This suggests that tremors are a more sensitive indicator of stress change than earthquakes.

## 12.5 Implications

The periodic tremor and persistent elevated activity after the Parkfield quake are not consistent with expectations of exponentially decaying post-seismic stress after an earthquake (*Savage and Langbein*, 2008). Because the SAF tremor changes have persisted for over 4 years since Parkfield, they could be signaling a shift in the process of deformation and stress accumulation beneath this hazardous portion of the SAF. Faulting from the great  $M_w$  7.8 1857 Ft. Tejon earthquake appears to have propagated from the Monarch Peak area southeastward along the SAF for  $\sim 350$  km, through Parkfield and the Cholame tremor zone (*Topozada et al.*, 2002) (Figure 2.24). The Cholame segment is now fully locked and last ruptured 152 years ago as part of the great 1857 event.

## 12.6 Acknowledgements

The HRSN is funded by USGS grant 07HQAG0014. Research was supported by USGS grants 06HQGR0167 and 08HQGR0100, and by NSF grants EAR0537641 and EAR0544730.

## 12.7 References

- King, G.C.P., R.S. Stein and J. Lin, Static Stress Changes and the Triggering of Earthquakes, *Bull. Seism. Soc. Am.*, 84, 935-953, 1994.
- Liu, Y. and J.R. Rice, Spontaneous and triggered aseismic deformation transients in a subduction fault model, *J. Geophys. Res.*, 112, B09404, 2007.
- Nadeau, R.M. and A. Guilhem, Nonvolcanic Tremor Evolution and the San Simeon and Parkfield, California, Earthquakes, *Science*, 325, 191-193, 2009.
- Rogers, G. and H. Dragert, Episodic Tremor and Slip on the Cascadia Subduction Zone: The Chatter of Silent Slip, *Science*, 300, 1942-1943, 2003.
- Savage, J.C. and J. Langbein, Postearthquake relaxation after the 2004 M6 Parkfield, California, earthquake and rate-and-state friction, *J. Geophys. Res.*, 113, B10407, 2008.
- Topozada, T.R., D.M. Branum, M.S. Reichle and C.L. Hallstrom, San Andreas Fault Zone, California:  $M \geq 5.5$  Earthquake History, *Bull. Seism. Soc. Am.*, 92, 2555-2601, 2002.

# 13 Stability of Local and Regional Coda: Application to the Wells, Nevada Sequence

Kevin Mayeda

## 13.1 Abstract

For this year, we have studied the near-regional Lg-coda from the  $M_w$  6.0 Wells, Nevada earthquake of February 21, 2008 as well as a local  $M_w$  4.2 event from the San Francisco Bay area that exhibited a clear case of source directivity. The Wells event sequence was unique because the U.S. Array broadband seismic deployment had recorded this event along with its aftershocks, thus providing excellent station coverage and redundancy. Figure 2.26 below shows that the local to near-regional coda is very stable in comparison to the direct Lg. We have formed amplitude ratios, in this case 3.5 Hz, between the mainshock and a selected aftershock. The coda velocity and envelope shape functions were found to be virtually identical from station to station, in spite of significant geologic variation for paths traveling east versus those to the north and north-west. Though this event did not exhibit strong directivity (*D. Dreger, pers. comm., 2009*), we still see a radiation pattern in the direct Lg ratios, or perhaps random variation between the two sources. However, for the coda, we see significantly less variation, confirming that the coda is not sensitive to the source mechanism.

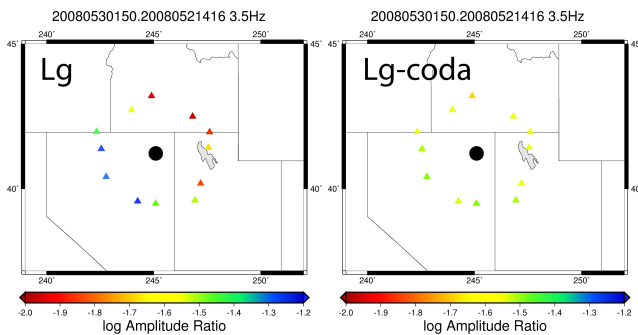


Figure 2.26: Left figure above shows source ratios for Lg at 3.5 Hz for 12 stations surrounding the Wells mainshock region, roughly 200 km in epicentral distance. We observe large variations even though path and site response are removed by forming the source amplitude ratio. In sharp contrast, the right figure shows the coda-derived source ratios for the same event pair and frequency. As found in other studies, the coda is significantly less variable.

For our second example, we studied an  $M_w$  4.2 event that occurred along the Hayward fault in the San Francisco Bay area on July 20, 2007. This event was very

interesting because there were seismic stations equidistant from the mainshock along the strike of the Hayward fault. The mainshock exhibited over a factor of 10 larger amplitude in the north-westerly direction (along strike) relative to the south-east direction. Figure 2.28 shows that station CVS to the north-west has much larger direct wave amplitudes than station MHC to the south-east; however, the coda envelopes are exactly the same after a few tens of seconds. In addition, an aftershock for the same stations and frequency bands does not show any directivity.

## 13.2 Conclusions

We have documented the coda's property of insensitivity to both the source radiation pattern and directivity. The examples shown in Figures 2.26, 2.27, and 2.28 are strong evidence that the coda's averaging properties also applies to the source heterogeneity, not just path heterogeneity. The recent 2008  $M_w$  5.8 Wells, Nevada earthquake was well recorded by the U.S. Array, and we show that the local-to-near-regional coda is virtually insensitive to the source radiation pattern and directivity effects. In addition, we demonstrate that the coda wavefield becomes homogenized a few tens of seconds past the expanding direct-wave front.

## 13.3 References

Mayeda, K., L. Malagnini, W.R. Walter, A new spectral ratio method using narrow band coda envelopes: Evidence for non-self-similarity in the Hector Mine sequence, *Geophys. Res. Lett.*, doi:10.1029/2007GL030041, 2007.

## Comparison for 20080521416.20080921316

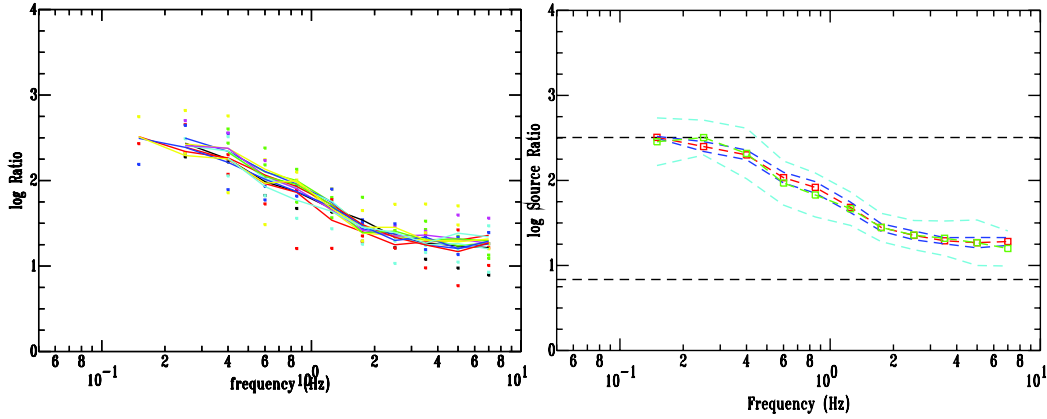


Figure 2.27: Left figure above shows spectral ratios taken between the Wells mainshock and a co-located aftershock. Solid lines represent coda ratios at the 12 stations and colored dots are the direct Lg source ratios. All stations are roughly 200 km in distance. The figure on the right shows the average and standard deviation for both coda and Lg. For the coda, red is the mean and blue is the  $\pm 1$  standard deviation and for Lg, green is the mean and light blue is the  $\pm 1$  standard deviation. See *Mayeda et al. (2007)* for methodology details.

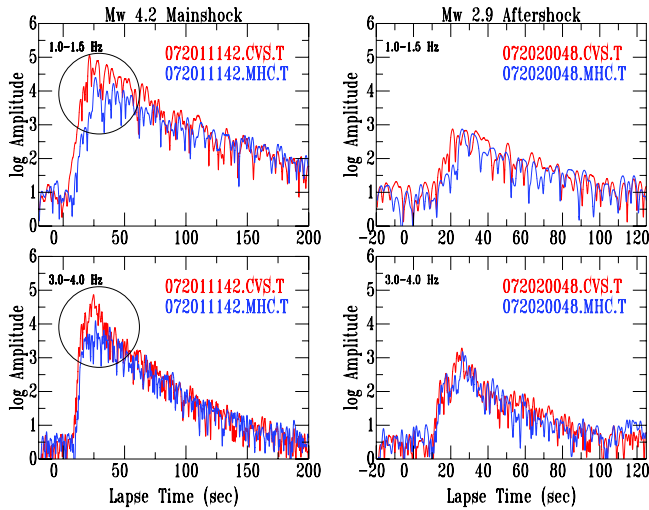


Figure 2.28: We show a clear case of source directivity (left column) that results in roughly a factor or 10 larger amplitude for the direct waves at station CVS, located to the north of the event and along strike relative to station MHC located to the south. However, the coda levels at both stations are identical. An aftershock shows no evidence of directivity (right column).

## 14 Anomalous Moment Tensor Solutions for The Geysers, CA

Jennifer Taggart, Summer Ohlendorf (UW - Madison), Sean Ford (LLNL), Peggy Hellweg, and Doug Dreger

### 14.1 Introduction

The Geysers, CA, hosts a Calpine geothermal plant that is an important source of geothermal energy in California. Seismicity in the region is high and has greatly increased in recent years, correlating with geothermal energy production by Calpine. Seismicity is generally shallow, and earthquakes in the region tend to be small ( $M_w < 4.5$ ). The bulk of the seismicity is thought to be induced by geothermal operations. Part of the Clear Lake Volcanic Field, The Geysers appear to have formed in a gap created as the Mendocino Triple Junction migrated north. An underlying pluton forms the geothermal heat source close to the surface.

### 14.2 Research Objectives

Moment tensor solutions are calculated in real time for most events with  $M_w \geq 3.5$  in Northern California (Pasyanos *et al*, 1996, Romanowicz *et al*, 1993) using the waveform moment tensor inversion code developed by Dreger (Minson and Dreger, 2008). Routine moment tensor solutions for The Geysers, computed with pure double couple (DC) and compensated linear vector dipole (CLVD) components (deviatoric solutions), often have a high non DC component. Non DC elements in the solutions to these Geysers events may be real (Dreger *et al*, 2000, Dreger *et al*, 2008, Ford *et al*, 2008), especially for the larger events ( $M_w 4+$ ). A program for full moment tensor inversions, including the isotropic (ISO) component, is available, and large events with a significant non DC component warrant a closer look with this code.

Mechanisms appear to cluster and vary. Some events, mostly in the southeast corner of the region, have solutions with high DC components that appear to reflect strike slip faulting. Others, scattered through the northern part of the region, may have normal faulting. In addition, the moment magnitudes routinely computed with the moment tensor program frequently have a higher  $M_w$  than  $M_L$ , indicating some difference in the radiated energy from these events that may correspond to a real difference in the events (see map, Figure 2.29).

### 14.3 Full Moment Tensors at The Geysers

We are reviewing moment tensors for some of the Geysers events. Our first efforts have used two different procedures, discussed here. For six events, Group I, chosen for their occurrence during the USARRAY installation in Northern California (see table), we first gathered all

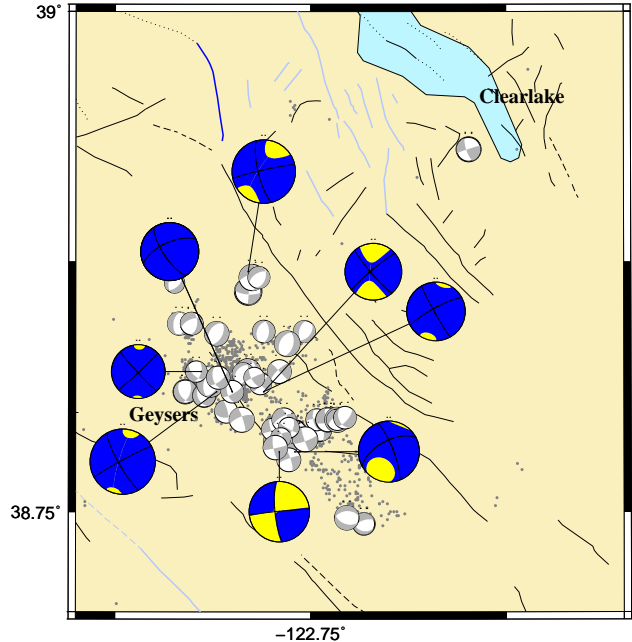


Figure 2.29: The first approach yielded six full moment tensor solutions with significant ISO components, while the second approach yielded one high DC solution and one solution with a significant ISO component. Green's function source depth for Group I is 2 km; for Group II, 5 km. Dark gray dots indicate 2008 background seismicity for The Geysers, while light gray beach balls represent best fit DC solutions from the BSL moment tensor catalog in that region (1990 through January 2009). Black beach balls represent full moment tensors from the two groups.

available low-noise data within 5 degrees of each event and then removed all stations with a best-fit variance reduction of 40% or below. Our best moment tensor solutions used data from between 20 and 60 stations. The large number of stations used provided robust solutions (Ohlendorf, 2008). As Geysers seismicity tends to be shallow, a source depth of 2 km was used. Group II comprised two events with only 46% and 18% respective DC components in the Berkeley Moment Tensor Catalog. Review of Group II events followed the procedure normally used during routine event review at UCB. Final solutions had 11 and 14 stations, respectively.

All six Group I events had best fitting moment tensor solutions with significant non DC components

Date	Location	Type	Stations	DC/CLVD/ISO (percent)	VR (percent)
5/12/2006	38.814 -122.814	Full	65	53/1/46	71.1
10/20/2006	38.867 -122.787	Full	62	44/21/35	69.5
04/30/2007	38.820 -122.823	Full	27	37/15/50	65.6
07/20/2007	38.810 -122.800	Full	24	13/21/66	59.1
12/1/2007	38.733 -122.933	Full	20	18/31/50	65.1
11/17/2005	38.814 -122.782	Full	21	51/25/24	54.7
1/4/2009	38.782 -122.773	Deviatoric	13	61/39/0	80.7
1/4/2009	38.782 -122.773	Full (ISO off)	11	82/18/0	81.6
1/4/2009	38.782 -122.773	Full	11	83/11/5	81.7
5/30/2008	38.776 -122.764	Deviatoric	14	39/61/0	77.9
5/30/2008	38.776 -122.764	Full (ISO off)	14	64/36/0	74.3
5/30/2008	38.776 -122.764	Full	14	20/44/36	75.6

Table 2.2: Top: Full moment tensors at source depth 2 for the Group I events. Bottom: Best solutions at source depth 5 for the Group II events using the deviatoric code, the full moment tensor code with the ISO option turned off, and the full moment tensor from the full moment tensor code.

(total%*ISO*+%*CLVD* 47-87%). Interestingly, the deviatoric solution from the full moment tensor code immediately yielded a significantly higher %DC for both Group II events, which was not expected. The full moment tensor solution further resolved the first event as having 83% DC (using a source depth of 5 km). The full moment tensor solution for the latter event looked primarily explosive, with only 20% DC.

## 14.4 Perspectives

The deviatoric solutions found with the full moment tensor code for both Group II events yielded significantly higher DC components than the best deviatoric solutions for those events determined using the deviatoric code. We intend to investigate this further.

In Figure 2.29, Group I and II events are located in the same area, the southern region of The Geysers, where Berkeley’s best DC solutions appear to reflect strike slip mechanisms.

The Berkeley Moment Tensor catalog (<http://seismo.berkeley.edu/~mike/solutions.new/>) contains numerous Geysers events, which will be reviewed with the full moment tensor code to determine whether they have significant ISO components. Computing full moment tensors for these events, especially for the larger events, may yield more information about the causes of seismicity at The Geysers.

## 14.5 Acknowledgements

Earthquake monitoring and reporting activities at the BSL are supported by the CISN funding of the California Governor’s Office of Emergency Services under contract 6023-5 and the US Geological Survey project 07HQAG0013.

## 14.6 References

- Ohlendorf, S., and D. Dreger, Evidence for Dilational Processes Accompanying Earthquakes at The Geysers Geothermal Field, California, The Third Annual Geoscience Graduate Symposium, Department of Geology and Geophysics, UW-Madison, Madison, WI, May 7-8, 2009 (poster).
- Dreger, D. S., H. Tkalic, and M. Johnston, Dilational processes accompanying earthquakes in the Long Valley Caldera, *Science*, 288, 122-25, 2000.
- Dreger, D., S.R. Ford, and W.R. Walter, Source analysis of the Crandall Canyon, Utah mine collapse, *Science*, 321, 217, 2008.
- Ford, S. R., D. S. Dreger and W. R. Walter, Source Characterization of the August 6, 2007 Crandall Canyon Mine Seismic Event in Central Utah, *Seism. Res. Lett.*, 114, B01306, doi:10.1029/2008JB005743.
- Minson, S. and D. Dreger, Stable Inversions for Complete Moment Tensors, *Geophys. Journ. Int.*, 174(2), 585-592, doi:10.1111/j.1365-246X.2008.03797.x.
- Pasyanos, M.E., D.S. Dreger, and B. Romanowicz, Toward Real-Time Estimation of Regional Moment Tensors, *Bull. Seism. Soc. Am.*, 86, 1255-1269, 1996.
- Romanowicz, B. D. Dreger, M. Pasyanos, and R. Uhrhammer, Monitoring of Strain Release in Central and Northern California Using Broadband Data, *Geophys. Res. Lett.*, 20, 1643-1646, 1993.

# 15 Statistical Testing of Theoretical Rupture Models Against Kinematic Inversions

Gilead Wurman, Richard M. Allen, Douglas S. Dreger, and David D. Oglesby (UC Riverside)

## 15.1 Introduction

The process by which earthquake ruptures initiate and propagate is usually expressed as one of two broadly-defined mechanisms: the cascade model and the preslip model. There is a diversity of modeling results that alternately support either cascade- or preslip-type rupture. At least some of the disagreement between the studies may be due to the high degree of variability among kinematic slip inversions, even for the same event. The recent development of the SRCMOD database makes it possible to examine many fault models in a statistical fashion to suppress the effects of this variability. Although the slip at the beginning of rupture is poorly resolved in kinematic inversions, using such a large number of events allows us to make first-order observations of any relationships.

## 15.2 Method

We examine 152 inversions of 80 different earthquakes in the SRCMOD database (<http://www.seismo.ethz.ch/srcmod>) as well as 7 teleseismic and 8 joint geodetic/teleseismic inversions provided by M. E. Pritchard (Pritchard *et al.*, 2006, 2007; Pritchard and Fielding, 2008; Loveless *et al.*, in review), for a total of 167 inversions and 95 events. We take the final slip distribution for each inversion and reconstruct the time-evolution of slip on the fault from rupture time and rise time information. We calculate the moment release within a given time window by summing the moment based on inferred slip at each grid point. For models with point-wise rupture time or rise time data, we initiate slip on each grid point at the associated rupture time, and increase slip to the final amount in a linear ramp over the associated rise time. In models where one or both of these parameters is not recorded point-wise, we take the reported average rupture velocity or rise time and assume a rupture front expanding isotropically from the hypocenter.

## 15.3 Relationship between early and final moment

The cascading hypothesis implies that at any given time after rupture initiation all earthquakes have the same magnitude. We can approximate this magnitude via the relation  $M_0 = \mu SD = \mu \cdot \pi(V_R t)^2 \cdot \alpha V_R t = \pi \mu \alpha (V_R t)^3$  where  $\mu = 3 \times 10^{11}$  dyne-cm,  $S = \pi(V_R t)$  is the fault area after  $t$  seconds assuming a rupture velocity  $V_R = 3 \times 10^5$  cm/s, and  $D = \alpha V_R t$  is the mean

slip with  $\alpha = 10^{-5}$ . We find that a source duration of 1 second corresponds to a moment of approximately  $2.5 \times 10^{23}$  dyne-cm, or  $M_w$  4.9. Thus in the cascading end-member case, any earthquake larger than magnitude 5 should look like a magnitude 5 at one second after nucleation. We can visualize this null hypothesis in Figure 2.30a. The solid diagonal line represents the limit in which the initial magnitude after 1 second is equal to the final magnitude, meaning the rupture has propagated to completion. Since there is no way for the initial magnitude to exceed the final magnitude, no points may lie above this solid line. This can potentially introduce a spurious positive slope to the data, and we minimize this by culling all data points for which the final magnitude is less than the reference magnitude. The hypothesis for a deterministic model is that there will be some positive scaling of the magnitude at 1 second with the final magnitude of the earthquake, yielding a positive slope to the data.

Figure 2.30b-e shows the initial magnitude plotted against the final magnitude for each event for four time windows ranging from 1 second to 8 seconds. We manually pick outliers, and exclude any events for which the initial magnitude is 99% or more of final magnitude, as those events have effectively terminated by the end of the time window. We also exclude all events with a final magnitude less than the reference magnitude for the null hypothesis as described above. The null hypothesis of cascading rupture can be rejected with greater than 95% confidence. The slope of the best-fit lines for all time windows between 1 and 10 seconds are strongly positive, suggesting some degree of non-self-similar behavior for these models. For time windows between 8 and 10 seconds the confidence is not as high as for time windows between 1 and 7 seconds. As rupture evolves, it experiences progressively more of the fault plane's heterogeneities and therefore has progressively more information about the likely final size of the earthquake. We therefore expect the initial magnitude to scale more strongly with final magnitude for longer time windows. One explanation for the degradation in scaling for longer time windows is that more and more events are being excluded due to having completed rupture, thus reducing the number of data points available for analysis. In Figure 2.30b-d, the number of points used for the fit varies between 112 and 128, and by 8 seconds (Figure 2.30e) that number has fallen to 80. Another possibility is that longer time windows afford greater resolution of the slip within the time

window, implying that the strong correlation observed for shorter time windows is a spurious result of poorly resolved slip in such short time spans. The influence of poorly resolved slip can be approximated visually by noting the open symbols, which represent models for which the time window was either shorter than the average rise time for the model or for which only one grid element had begun slipping in that time window.

We attempt to reduce the influence of poorly resolved slip by disregarding all of the “open” data points from Figure 2.30 which represent cases where the slip is likely to be particularly poorly resolved owing to the time window being too short. In addition, we recalculate both the initial and final magnitude for each point, disregarding any slip which is less than 10% of the peak slip for the model. This is to account for the fact that slip below 10% of peak slip is generally regarded as being poorly resolved in kinematic inversions and thus an unstable component of the slip models. Remarkably, the correlation between early and final magnitude is now even stronger, with the null hypothesis being rejected at greater than 99% confidence for all time windows. This suggests that poor resolution of slip in short time windows is not generating a spurious correlation between early and final magnitude. Rather, the analysis suggests that the decreasing number of data points in longer time windows (owing to more ruptures having run to completion) is primarily responsible for the weaker correlation for 8-10 second time windows seen in Figure 2.30.

## 15.4 Conclusions

We observe a strong scaling of early slip and magnitude with the final magnitude of these events. This result is inconsistent with the hypothesis that earthquakes are cascading rupture phenomena. After filtering the data the scaling remains robust, and in fact is more prominent, indicating that poor resolution of early slip is not the cause of the observed scaling. Given these findings, we must allow for the possibility that earthquakes are not purely cascading phenomena, and that magnitude is at least in part influenced by processes in the early part of the rupture process.

## 15.5 Acknowledgements

We thank Matt Pritchard for providing 15 of the slip models used in this study.

## 15.6 References

Loveless, J.P., M.E. Pritchard and N. Kukowski, Testing mechanisms of seismic segmentation with slip distributions from recent earthquakes along the Andean margin, *Tectonophysics*, in review.

Pritchard, M.E. and E.J. Fielding, A study of the 2006 and 2007 earthquake sequence of Pisco, Peru, with InSAR

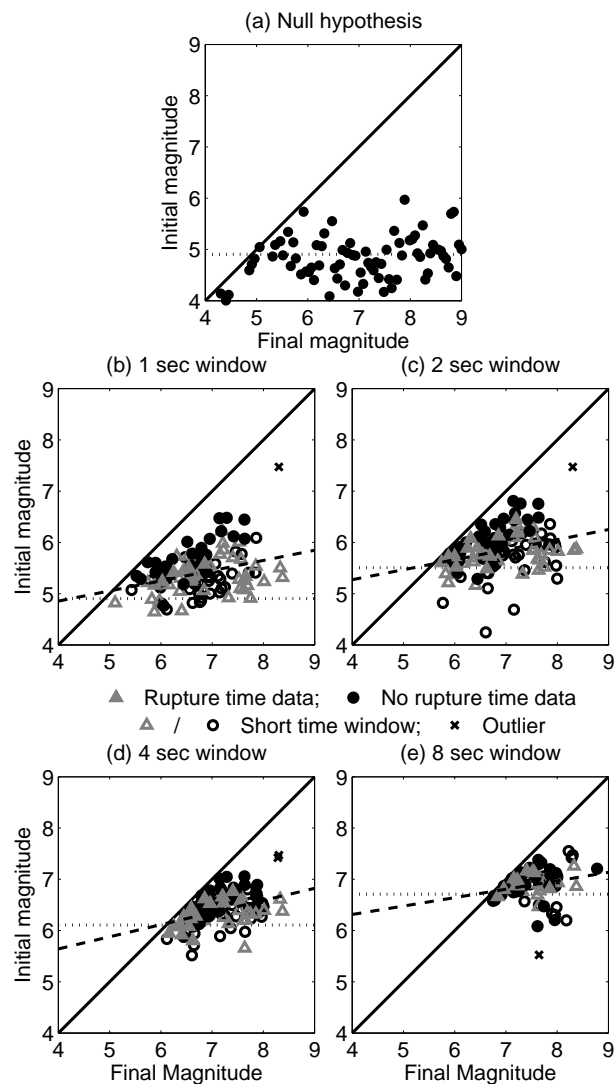


Figure 2.30: (a) Graphical expectation for the null hypothesis, that earthquakes are cascading ruptures. Dotted line represents the theoretical magnitude after 1 second. (b-e) Initial vs. final magnitude for time windows of 1, 2, 4 and 8 seconds. Dashed line represents the least-squares best fit to the data.

and teleseismic data, *Geophys. Res. Lett.*, *35*, L09308, doi:10.1029/2008GL033374, 2008.

Pritchard, M.E., C. Ji and M. Simons, Distribution of slip from 11  $M_w > 6$  earthquakes in the northern Chile subduction zone, *J. Geophys. Res.*, *111*, B10302, doi:10.1029/2005JB004013, 2006.

Pritchard, M.E., E.O. Norabuena, C. Ji, R. Boroschek, D. Comte, M. Simons, T. Dixon and P.A. Rosen, Geodetic, teleseismic, and strong motion constraints on slip from recent southern Peru subduction zone earthquakes, *J. Geophys. Res.*, *112*, B03307, doi:10.1029/2006JB04294, 2007.

## 16 Testing ElarmS in Japan

Holly Brown and Richard Allen

### 16.1 Introduction

Earthquake early warning systems detect the initial P-waves from an earthquake, rapidly estimate the magnitude of the event, and predict subsequent ground shaking in the region. Earthquake Alarm Systems, or ElarmS, is a network-based earthquake early warning algorithm that uses the amplitude and frequency content of P-waves from multiple stations to estimate the size and damage potential of an earthquake in realtime.

ElarmS has been tested on multiple California datasets (*Allen and Kanamori, 2003; Olson and Allen, 2005; Tsang, et al., 2007; Wurman, et al., 2007*). However there are limited numbers of recent, well-recorded, large earthquakes in California. We test ElarmS with a dataset of large earthquakes from Japan to improve the robustness of the system and to examine the adaptability of the algorithm to other seismic environments.

We then analyze the accuracy of the ElarmS magnitude estimates, location estimates, and ground shaking predictions, and produce error distributions for each of these three ElarmS outputs. The distributions depend on the quantity of available data, and can be accessed in realtime for uncertainty estimation during an event. We use the error distributions to create a model of the errors in the system. The model identifies the greatest source of error in the final ElarmS output.

### 16.2 Dataset

The dataset consists of 84 earthquakes, which occurred in Japan between September 1996 and June 2008 (Figure 2.31). The magnitudes range from 4.0 to 8.0, with 43 events of magnitude 6.0 or greater. The largest event is the 26 September 2003 Tokachi-Oki event, with magnitude 8.0.

The events were recorded by Japan's Kyoshin Net (K-NET) strong motion network. K-NET consists of 1,000 digital strong-motion seismometers spaced approximately 25km apart throughout Japan. Each station records ground motions as large as 2000  $cm/s^2$ .

### 16.3 Method

ElarmS estimates magnitude from the frequency content and peak displacement of the first few seconds of P-wave at each reporting station. Allen and Kanamori (2003) and Olson and Allen (2005) demonstrated an empirical relationship between magnitude and the observed maximum predominant period,  $t_{pmax}$ , of the P-wave. Wurman, et al., (2007) documented a relationship be-

tween magnitude and peak displacement,  $P_d$ , of the first few seconds of P-wave. ElarmS uses both relationships independently to calculate two magnitude estimates for a given event, and then averages the estimates together. As additional stations record P-wave arrivals, ElarmS incorporates their period and displacement measurements into the average to create a single magnitude estimate for the event.

ElarmS calculates event location by a three-dimensional grid search. Observed P-wave arrival times are compared to those predicted for a hypocenter at each node of the grid. For the Japanese events, grid layers occur in 10km depth increments, down to 80km.

When ElarmS has an estimated hypocenter and magnitude, it applies these to National Earthquake Information Center (NEIC) ShakeMap attenuation relations to predict ground shaking in the surrounding region. Initially, the prediction is based entirely on the estimated location and magnitude. As stations report peak ground shaking, the observations are incorporated into the predictions.

### 16.4 Error Distributions

We isolate the location, magnitude and ground shaking processing steps to determine independent error distributions for each of these steps. The error in each step depends on the number of stations triggering, the number of seconds of P-wave arrival, and the number of stations reporting peak ground shaking observations. Thus we have separate error distributions for each quantity of inputs. Figure 2.31 shows the mean error for each distribution curve.

### 16.5 Error Model

We use these error distributions to create an error model for ElarmS processing. The model calculates the total error in the system, after magnitude, location, and attenuation relation errors have propagated through to the final prediction of shaking. In total, we consider 1081 different combinations of data input quantities, and create a separate error distribution for each combination. These are collectively shown in Figure 2.32a. These 1081 distributions are contained in an ElarmS library, which can be accessed in realtime. Given any combination of number of stations reporting, number of seconds of P-wave arrival, and number of peak ground shaking observations, the appropriate error distribution can be consulted to produce a realtime estimate of uncertainty in the ElarmS prediction of ground shaking.

Table 1: Mean $\pm$ standard deviation of error distributions used by error model.						
	0 stations	1 station	2 stations	3 stations	4 stations	5 stations
Magnitude error, 1 sec of P-wave	-	-0.38 $\pm$ 0.63	-0.33 $\pm$ 0.56	-0.37 $\pm$ 0.57	-0.39 $\pm$ 0.56	-0.41 $\pm$ 0.56
Magnitude error, 2 sec of P-wave	-	-0.2 $\pm$ 0.57	-0.15 $\pm$ 0.5	-0.18 $\pm$ 0.54	-0.21 $\pm$ 0.52	-0.22 $\pm$ 0.50
Magnitude error, 3 sec of P-wave	-	-0.09 $\pm$ 0.53	-0.05 $\pm$ 0.48	-0.08 $\pm$ 0.52	-0.10 $\pm$ 0.49	-0.10 $\pm$ 0.47
Magnitude error, 4 sec of P-wave	-	0.01 $\pm$ 0.52	0.04 $\pm$ 0.46	0.03 $\pm$ 0.48	0.03 $\pm$ 0.44	0.02 $\pm$ 0.43
Magnitude error, 5 sec of P-wave	-	0.04 $\pm$ 0.50	0.07 $\pm$ 0.45	0.07 $\pm$ 0.48	0.07 $\pm$ 0.43	0.06 $\pm$ 0.42
Location error	-	33.6 $\pm$ 17.9	32.1 $\pm$ 21.4	32.5 $\pm$ 18.7	18.8 $\pm$ 13.6	21.1 $\pm$ 16.8
PGA prediction error	0.11 $\pm$ 0.30	0.09 $\pm$ 0.35	0.08 $\pm$ 0.37	0.06 $\pm$ 0.29	0.10 $\pm$ 0.28	0.03 $\pm$ 0.30

Figure 2.31: Mean errors in magnitude estimates, location estimates, and peak ground shaking predictions. Location error is in km. PGA error is the ratio of the predicted PGA to the observed PGA; a factor-of-two error in the predicted PGA relative to the observed PGA corresponds to an error of 0.7.

From the model we isolate the error contribution of each processing step, by “turning off” each contribution in turn. For example, Figure 2.32c shows the error model when the location estimate exactly equals the catalog location (zero location error); all error in the system comes from magnitude estimation and the attenuation relations used to predict ground shaking. Figure 2.32d is the error model when the magnitude estimate exactly equals the catalog magnitude, and error is contributed only by location and attenuation relations. Figure 2.32b is the error model when the attenuation relations are perfect, and all error comes from the location and magnitude estimates. Note the sharper, higher peak in Figure 2.32b. This indicates less error in the system for this scenario. That is, if the attenuation relations were perfect, the error in ElarmS’ output would be significantly reduced. We conclude from this that the prediction of ground motions, produced from NEIC ShakeMap attenuation relations, contributes far more error to the final ElarmS prediction of localized shaking than do the magnitude estimate or location estimate. This suggests that more work should be devoted to improving attenuation relations, and that regional relations should be used whenever possible.

## 16.6 Conclusion

ElarmS’ successful tests on Japanese events confirm that the ElarmS algorithm is relevant in a subduction zone environment and for large-magnitude events. The error distribution curves and error model show that the attenuation relations contribute the largest source of error to the final ElarmS prediction of ground shaking.

## 16.7 Acknowledgements

We thank K-NET for the use of their data. This work was funded by USGS/NEHRP award 06HQAG0147.

## 16.8 References

Allen, R.M., and H. Kanamori, The potential for earthquake early warning in southern California, *Science* 300, 786-

789, 2003.

Olson, E.L., and R.M. Allen, The deterministic nature of earthquake rupture, *Nature* 438, 212-215, 2005.

Tsang, L., R.M. Allen, and G. Wurman, Magnitude scaling relations from P-waves in southern California, *Geophys. Res. Lett.* 34, L19304, 2007.

Wurman, G., R.M. Allen and P. Lombard, Toward Earthquake Early Warning in Northern California, *J. Geophys. Res.* 112, B08311, 2007.

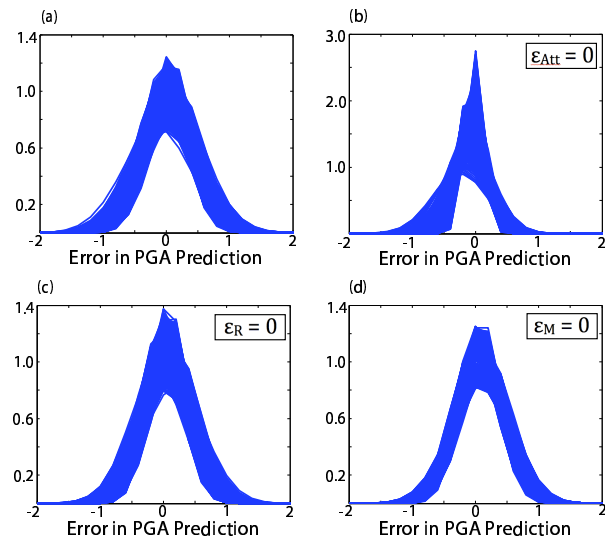


Figure 2.32: Error Model, with 1081 individual error distributions, based on differing quantities of input data (number of stations, number of seconds, number of PGA observations). (a) Complete error model. Error is contributed by magnitude estimate, location estimate, and attenuation relations (used to predict ground shaking). (b) Error model when attenuation relations error is removed. (c) Error model when location error is removed. (d) Error model when magnitude error is removed.

# 17 Real-time Earthquake Detection and Hazard Assessment by ElarmS Across California

Holly Brown, Richard Allen, Margaret Hellweg, Oleg Khainovski, Peter Lombard, Douglas Neuhauser, and Adeline Souf

## 17.1 Introduction

ElarmS is a network-based methodology for rapid earthquake detection, location, and hazard assessment in the form of magnitude estimation and peak ground motion prediction. The methodology is currently being tested as part of the real-time seismic system in California, leveraging the resources of the California Integrated Seismic Network (CISN) and the Advanced National Seismic System. ElarmS processing modules at three network processing centers reduce waveforms to a few parameters. These are then collected and processed at UC Berkeley to provide a single statewide prediction of future ground shaking that is updated every second.

The development of a statewide realtime warning system has presented several methodological and programming challenges. Here we focus on the system delays as data is passed between processing centers.

## 17.2 Method

ElarmS uses the P-wave recorded on velocity and acceleration sensors to detect, locate, and estimate the magnitude of an earthquake. The initial estimate of location is beneath the first station to trigger, then between the first two stations based on the arrival times. Once three triggers are available the event is located using a grid search to minimize arrival time residuals. The depth for all events in California is set at 8 km.

The ElarmS magnitude estimate is based on the amplitude and frequency content of the P-wave arrival. For a given trigger, the maximum observed displacement,  $P_d$ , and predominant period,  $t_{pmax}$ , are converted to a magnitude estimate using empirical scaling relations [Allen and Kanamori, 2003; Tsang et al., 2007; Wurman et al., 2007]. Magnitude estimates for all triggered stations are averaged at each time step to provide a single estimate for the event.

The methodology naturally divides into a waveform processing module (WP) and an event monitoring module (EVM). WP operates on each data channel individually to reduce the seismic waveform to parameters including trigger times,  $P_d$ ,  $P_v$ ,  $t_{pmax}$ , peak ground velocity (PGV), peak ground acceleration (PGA) and signal-to-noise levels. The WP module can therefore be distributed. It currently runs at UC Berkeley processing waveforms from the Berkeley Digital Seismic Network (network code BK) at the USGS Menlo Park, processing the Northern California Seismic Network (NC) and some USGS Strong Motion Network (NP) data, and at

Caltech/USGS Pasadena processing Southern California Seismic Network (CI), the Anza Network (AZ), and additional NP data. WP output parameters are telemetered to UC Berkeley where a single implementation of the EVM module integrates data from across the state to detect and analyze earthquake occurrence in real-time.

The EVM module currently processes waveform data from 383 stations (222 velocity instruments and 381 accelerometers) of the BK, NC, NP, CI, and AZ networks (Figure 2.33). The real-time implementation of ElarmS is now processing all stations in California that can be used by the system.

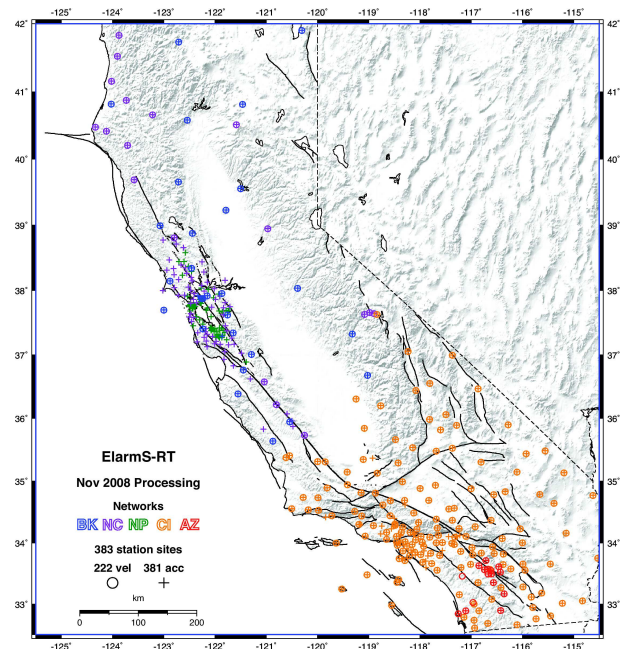


Figure 2.33: Map of stations currently used by realtime system.

## 17.3 Results

Every second required to telemeter data is a second reduction in warning time. Minimizing the time needed for data telemetry and processing is therefore an important aspect of a network-based early warning system. Figure 2.33 shows the current data latencies for ElarmS in California. The first cause of latency is the delay in getting data to the first shared memory region at its network processing site at UC Berkeley, Caltech/USGS Pasadena, or

USGS Menlo Park (Figure 2.33a). Most of this delay is due to packetization of data. Data loggers at each station wait until a data packet is full before sending it across the telemetry system. Modifications to the configuration of many data loggers could reduce the size of these packets, reducing the overall latency. The actual telemetry (communication) delay at most sites most of the time is a fraction of a second, although packets can be delayed, resulting in the long tail to the distribution. The median waveform data latencies are 2.0, 6.5, 6.6, 6.6, and 11.5 second for NC, CI, BK, NP, and AZ, respectively. AZ has long latencies because AZ data is forwarded from Scripps to Caltech before it is processed by ElarmS. The median latency over all station channels is 6.5 sec.

Once the waveform data has arrived at the first shared memory region at a network center, WP processes the data to determine parameters. Parameters from Caltech/USGS Pasadena and USGS Menlo Park are then forwarded to UC Berkeley where they are incorporated into EVM as they arrive. Figure 2.33b shows the total latency in incorporating P-wave trigger times into the EVM output representing the current latency of the entire system. The median delay is 11.8 seconds and the distribution has a positive-skew, meaning that most frequent latency is in the 9-10 second window but there is a long tail at higher latencies. The actual processing of data by WP or EVM takes a fraction of a second. Most of the additional latency is therefore due to the process of moving data between the shared memory regions at the various stages of processing (including between network centers).

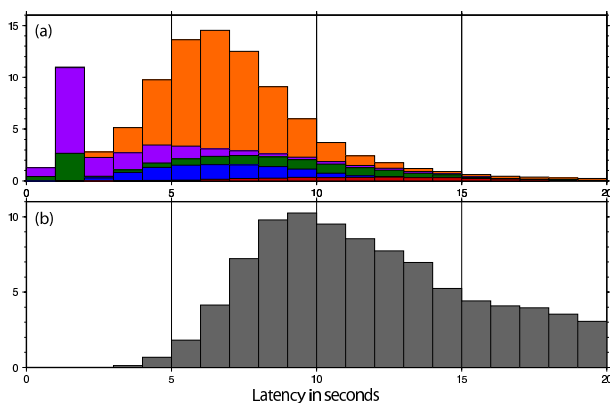


Figure 2.34: Histogram of latencies in the statewide system. (a) Waveform telemetry latency: delay between the absolute time of a P-wave trigger and when it arrives at the network processing center. Blue is BK, purple is NC, green is NC, orange is CI, red is AZ. (b) Total ElarmS latency: delay between the absolute time of a P-wave trigger and the timestamp of the EVM output file that incorporates that trigger.

## 17.4 Conclusions

The state-wide, real-time test of ElarmS has only just begun (November 2008) so there will be additional methodology development necessary to handle the myriad technical issues that arise as a result of processing the approximately 15 billion observations per day that arrive with varying data latencies and various seismological and electronic sources of noise. In addition, further development is necessary to minimize the warning latency by improving the codes (currently 5 second delay) and upgrading station hardware (currently 6.5 second delay).

## 17.5 Acknowledgements

The real-time implementation and testing of ElarmS in California is part of a project by the California Integrated Seismic Network (<http://www.CISM.org/>) to test several early warning methodologies in the state. We have worked in collaboration with M. Böse, E. Hauksson, T. Heaton and K. Solanki at Caltech; T. Jordan and P. Maechling at USC and SCEC; D. Given and D. Oppenheimer at the USGS; M. Zeleznik of Saya Systems; and G. Cua at the Swiss Seismological Service. The project is funded by the USGS through cooperative agreement 06HQAG0147.

## 17.6 References

- Allen, R. M., and H. Kanamori, The potential for earthquake early warning in southern California, *Science* 300, 786-789, 2003.
- Allen, R. M., H. Brown, M. Hellweg, O. Khainovski, P. Lombard, and D. Neuhauser, Real-time earthquake detection and hazard assessment by ElarmS across California, *Geophys. Res. Lett.* 36, L00B08, 2009.
- Böse, M., E. Hauksson, K. Solanki, H. Kanamori, and T. H. Heaton, Real-time testing of the on-site warning algorithm in southern California and its performance during the July 29 2008  $M_w$ 5.4 Chino Hills earthquake, *Geophys. Res. Lett.* 36, L00B03, 2009.
- Tsang, L., R.M. Allen, and G. Wurman, Magnitude scaling relations from P-waves in southern California, *Geophys. Res. Lett.* 34, L19304, 2007.
- Wurman, G., R.M. Allen and P. Lombard, Toward Earthquake Early Warning in Northern California, *J. Geophys. Res.* 112, B08311, 2007.

# 18 Joint Inversion of Group Velocity Dispersion and Long Period Waveforms for Upper Mantle Structure

Vedran Lekic and Barbara Romanowicz

## 18.1 Introduction

Surface waves and overtones provide excellent constraints on crustal, upper mantle, and transition zone structure. They offer far better radial resolution of shallow structure than is possible with teleseismic body waves, while simultaneously having excellent global coverage and signal-to-noise ratios. Indeed, since its development a quarter century ago (Woodhouse and Dziewonski, 1984), the modeling of long period waveforms of surface waves and overtones using approximate techniques has made possible the development of high resolution models of upper mantle shear wave velocity and radial anisotropy (Panning and Romanowicz, 2006; Kustowski et al., 2008).

However, the ray- and perturbation theory that underlies these efforts can result in modeling errors that exceed the noise level of the observed waveforms (Panning et al., 2009). In the case of realistic crustal structure, the modeling inaccuracies can significantly contaminate the retrieved images of mantle velocity and radial anisotropy (Lekic et al., 2009). Fortunately, the development of computational techniques capable of fully modeling wave propagation through a complex, heterogeneous medium such as the Earth (Spectral Element Method: e.g. Capdeville et al., 2003) has enabled tomographers to move away from approximate techniques.

The superior accuracy of the spectral element method comes at a far greater computational cost than that associated with approximate techniques. In particular, crustal structure comprising thin layers substantially increases computational costs. At the same time, inaccuracies in existing global crustal models like CRUST2 (Bassin et al., 2000) can contaminate the retrieved mantle images. Because of this, there is a need for a new crustal model that avoids the meshing of thin layers while increasing the accuracy of crustal corrections. Long period waveforms lack the resolution necessary for crustal inversion, so we supplement our waveform dataset using  $1 \times 1^\circ$  Rayleigh and Love group velocity dispersion maps provided by *M. Ritzwoller (personal communication)* spanning the 25-150 sec period range.

Here, we present preliminary results of a joint inversion of group velocity dispersion and long period waveforms for crustal and upper mantle elastic structure.

## 18.2 Method

Tomographic imaging of the Earth's interior using waveforms is a non-linear process requiring an iterative procedure. Each iteration involves a forward modeling

step in which three-component waveforms with periods longer than 60 s are calculated using the spectral element method through a 3D model of isotropic shear wavespeed ( $V_S$ ) and radial anisotropy ( $\xi$ ). The partial derivatives relating model perturbations to time-domain misfits between data and synthetics are calculated using non-linear asymptotic coupling theory (NACT: *Li and Romanowicz, 1995*). Model updates are obtained by following the procedures described in *Mégnin and Romanowicz (2000)* and references therein.

In order to account for non-linear effects of model perturbations on group velocities and develop an unbiased starting crustal model, we begin by creating 21,000 candidate models which span a variety of crustal  $V_S$  (2-4 km/s).  $V_S$  is scaled to compressional wavespeed and density using relations of *Brocher (2003)*. In order to avoid meshing thin crustal layers, we fix crustal thickness to 60 km and mimic the response of a layered isotropic medium by introducing anisotropy (i.e.  $\xi$  is allowed to vary between 0.6 and 1.4). The models are represented as degree 3 polynomials, and their group velocities are calculated using a modified MINEOS code (*Woodhouse, 1988*).

Once we obtain a starting crustal model, we regionalize it by grouping similar velocity profiles into 4 clusters, and then summarizing each cluster by a single model of mean density and slownesses. For each reference profile, we then calculate group velocity dispersion curves and partial derivatives relating logarithmic group velocity perturbations from the reference values to perturbations in  $V_S$  and  $\xi$ . The most appropriate regional kernels are then used to obtain a model update which minimizes the logarithmic misfits between predictions and the group velocity dispersion at each point on the Earth. This ensures that the perturbations are always within the linear regime.

## 18.3 Results

Figure 2.35 compares the  $V_S$  structure of the uppermost mantle obtained using CRUST2 and long period waveforms alone (A: left) and our new Earth model obtained by jointly inverting long period waveforms and group velocity dispersion constraints (B: right). The differences between the models are prominent at shallow depths, where model B exhibits substantially stronger correlation between  $V_S$  anomaly and age of oceanic plates. At 100 km, the models are similar, though further differences emerge at 250 km, at which depth model B shows fewer fast anomalies beneath Asia, save for those

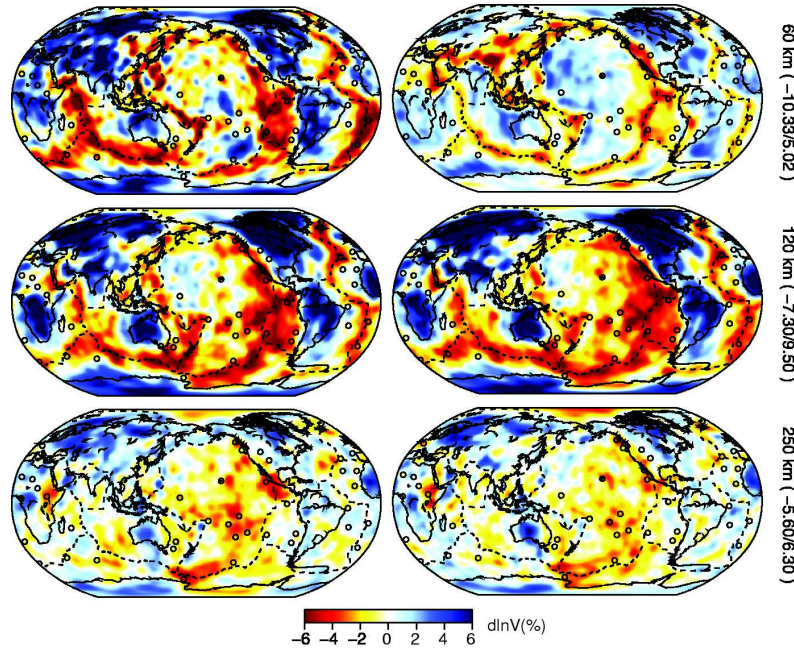


Figure 2.35: Models developed using long period waveforms with (right) and without (left) higher frequency group velocity dispersion maps.

corresponding to the Siberian and Finnoscandian cratons.

The model developed using CRUST2 fits Love waves two times worse than Rayleigh waves, even when inverting for radial anisotropy variations. However, by including higher frequency group velocity measurements and inverting for crustal structure, we improve the fits to both Love and Rayleigh waves and bring them closer to parity.

We plan to carry out further iterations and resolution tests to quantify the benefits of joint inversion of long period waveforms and shorter period group velocity dispersion curves.

## 18.4 Acknowledgements

This research was supported by National Science Foundation grant NSF/EAR-0308750.

## 18.5 References

Bassin, C., Laske, G. and G. Masters, 2000. The Current Limits of Resolution for Surface Wave Tomography in North America. *EOS Trans AGU* 81, F897.

Brocher, T.M., 2003. Empirical Relations between Elastic Wavespeeds and Density in the Earth's Crust. *BSSA*, 95, 2081-2092.

Capdeville, Y., E. Chaljub, J.P. Vilotte and J.P. Montagner, 2003. Coupling the spectral element method with a modal solution for elastic wave propagation in global Earth models. *Geophys. J. Int.*, 152, 34-66.

Lekic, V., M. Panning and B. Romanowicz, 2009. A simple method for improving crustal corrections in waveform tomography. *Submitted to Geophys. J. Int.*

Li, X.D. and B. Romanowicz, 1995. Comparison of global waveform inversions with and without considering cross-branch modal coupling, *Geophys. J. Int.*, 121, 695-709.

Megnin, C. and B. Romanowicz, 2000. The three-dimensional shear velocity structure of the mantle from the inversion of body, surface and higher-mode waveforms. *Geophys. J. Int.*, 143, 709-728.

Panning, M. and B. Romanowicz, 2006. A three-dimensional radially anisotropic model of shear velocity in the whole mantle. *Geophys. J. Int.*, 167, 361-379.

Panning, M.P., Y. Capdeville, and B.A. Romanowicz, 2009. Seismic waveform modelling in a 3-D Earth using the Born approximation: potential shortcomings and a remedy. *Geophys. J. Int.*, 177, 161-178.

Woodhouse, J.H. and A.M. Dziewonski, 1984. Mapping the upper mantle: three dimensional modeling of Earth structure by inversion of seismic waveforms. *J. Geophys. Res.* 89, 5953-5986.

Woodhouse, J.H., 1988. The calculation of eigenfrequencies and eigenfunctions of the free oscillations of the Earth and the Sun. *Seismological Algorithms*, ed. Doornbos, D.J., 321-370.

# 19 Reactivation of an Archean Craton: Constraints from P- and S-wave Tomography in North China

Liang Zhao, Richard M. Allen, Tianyu Zheng, and Shu-Huei Hung

## 19.1 Introduction

Cratonic nuclei often induce stress concentration and strain localization at their boundaries (Tommasi and Vauchez, 2001), but internally remain stable over very long geological periods. However, the unusual reactivation of the NCC challenges the classical views concerning the strength and stability of cratonic lithosphere. It is proposed that the North China Craton (NCC) (Figure 2.36) formed in the Paleoproterozoic by the amalgamation of two Archean blocks, the Eastern and Western Blocks (EB and WB), along the Central Block (CB) (e.g., Zhao *et al.*, 2001). While there is a growing consensus that lithospheric rifting has occurred in the EB and extended to the CB (Xu *et al.*, 2004; Zhao *et al.*, 2008), evidence for the vertical and horizontal distribution of lithospheric reactivation still remains unclear. This study is the first to provide high-resolution imaging of both P- and S- wave velocities in an effort to understand the process of reactivation of an Archean craton.

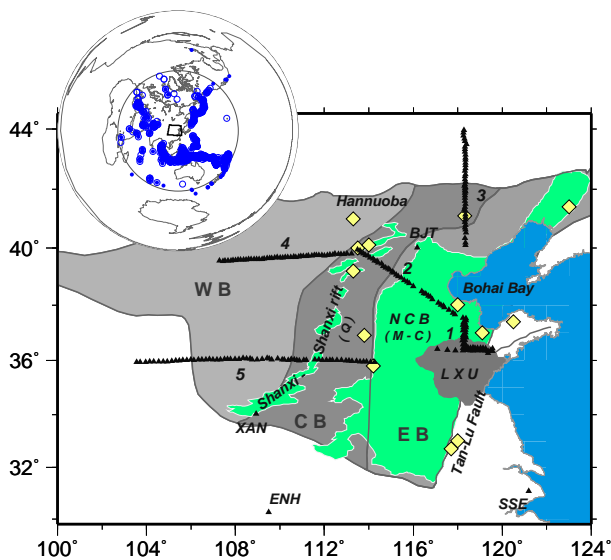


Figure 2.36: Simplified tectonic map showing major tectonic units of the NCC and seismic station locations. The triangles mark stations; yellow diamonds represent locations of Cenozoic basalts; green shadow zones indicate pull-apart basins; numbers indicate the indices of NCISP sub-arrays.

## 19.2 P- and S-wave Velocity Models and Resolution Tests

Our results show that structures imaged by finite-frequency kernel methods (Figure 2.37) and ray-based methods are very similar, except that the kernel-based models yield higher root-mean-square amplitude of P and S wave velocity perturbation, as expected (Hung *et al.*, 2004). The first-order features of our models, for both P- and S-waves, include: (1) A north-south trending narrow low-velocity region with dimension of 800 km north-south and 200-300 km east-west is located at the base of the CB lithosphere, and extends to more than 300 km depth. The northernmost and southernmost parts extend to more than 500 km depth. (2) A region of high-velocity extends to more than 250-300 km depth beneath the WB, in contrast to the much shallower high-velocity zones beneath the CB and EB.

Resolution tests show that the resolution is good down to 600km depth for anomalies  $\geq 200$  km even for data with 30% noise in the regions with good sampling coverage, and the downward smearing length is less than 50 km.

## 19.3 Conclusions

Finite-frequency kernel based P- and S-wave velocity images show that a N-S trending low velocity anomaly extends from beneath the CB to at least 500 km. High-velocity anomalies extend to more than 250-300 km depth beneath the WB, and to shallower depths beneath the CB and the EB. The imaged structure suggests that the presence of warm material with a source at least as deep as the transition zone is responsible for reactivation of the NCC. The pre-existing weak zone within the CB of the craton likely acted as a sublithospheric corridor for the warm mantle material.

## 19.4 Acknowledgements

This work was completed during L. Zhao's visit to Berkeley Seismology Lab sponsored by K.C. Wong Education Foundation, Hongkong. We thank M. Xue, M. Obrebski, H.Y. Yuan, R. Porritt, W.W. Xu, L. Chen and C. Paffenbarger for constructive help.

## 19.5 References

Hung, S., et al., Imaging seismic velocity structure beneath the Iceland hot spot: A finite frequency approach, in *J. Geophys. Res.*, 109, B08305, doi:10.1029/2003JB002889, 2004.

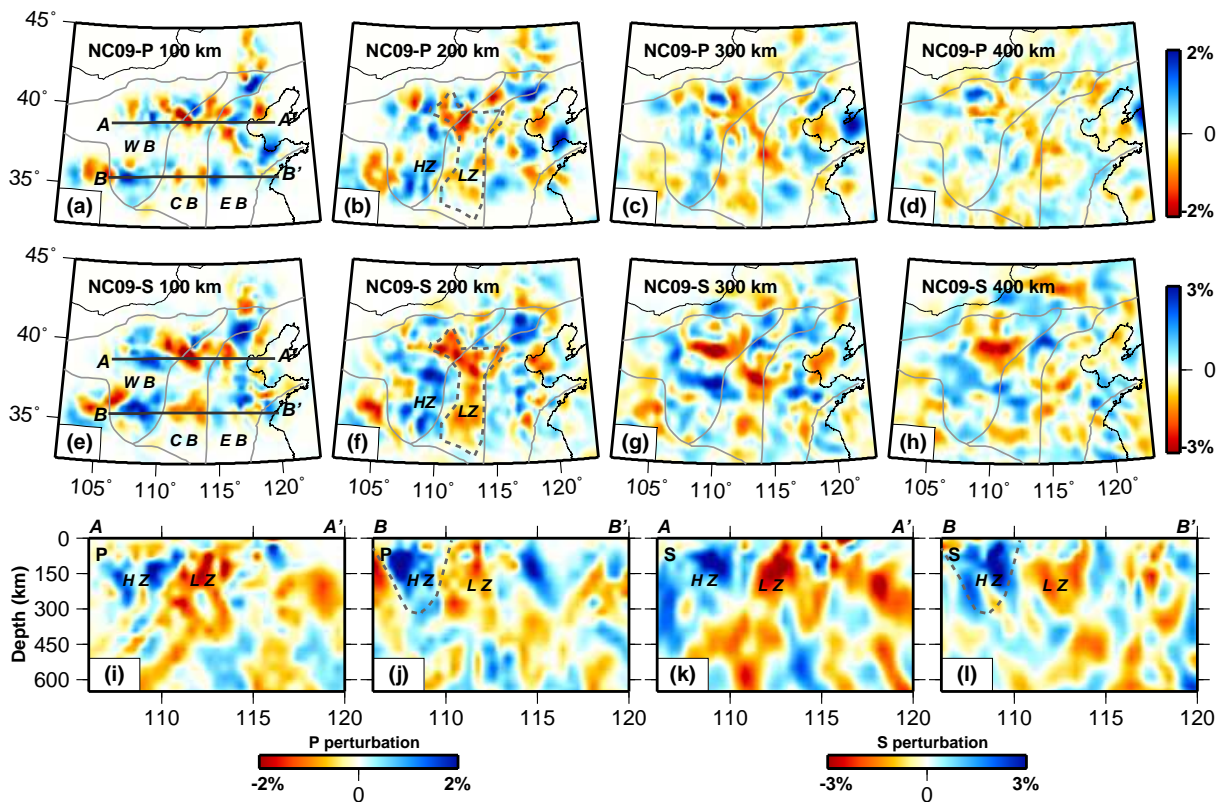


Figure 2.37: P- and S-wave velocity perturbations resolved from finite-frequency tomography. (a)-(d) P-wave velocity perturbations at indicated depths. (e)-(h) S-wave velocity perturbation. Cross sections are presented along A-A' and B-B' in (i) and (j) for the P-wave and (k) and (l) for S-wave model. Closed dashed lines on (b) and (f) give the outline of recognized N-S low velocity zone beneath the CB; dashed line on (j) represents high-velocity zone beneath the WB. LZ: low-velocity zone; HZ: high-velocity zone.

Tommasi, A., and A. Vauchez, Continental rifting parallel to ancient collisional belts: an effect of the mechanical anisotropy of the lithospheric mantle, in *Earth Planet. Sci. Lett.*, 185, 199-210, 2001.

Xu, Y., et al., Contrasting Cenozoic lithospheric evolution and architecture in the eastern and western Sino-Korean craton: constraints from geochemistry of basalts and mantle xenoliths, in *J. Geology*, 112, 593-605, 2004.

Zhao, G., et al., Archean blocks and their boundaries in the North China Craton: lithological, geochemical, structural and P-T path constraints and tectonic evolution, in *Precambrian Res.* 107, 45-73, 2001.

Zhao, L., et al., Insight into craton evolution: Constraints from shear wave splitting in the North China Craton, in *Phys. Earth Planet. Inter.*, 168, 153-162, 2008.

## 20 Plume vs. Plate: Convection Beneath the Pacific Northwest

Mathias Obrebski, Richard M Allen, Mei Xue (Tongji University, Shanghai, China) Shu-Huei Hung (National Taiwan University, Taipei, Taiwan)

### 20.1 Introduction

The Pacific Northwest of western North America is unusual in that both a subducting slab and a hotspot occur within 1000 km of one another. The Juan de Fuca plate (JdF) that continues to subduct today (Figure 2.38) is a remnant corner of the Farallon plate. Subduction beneath the Pacific Northwest has been continuous for more than  $\sim 150$  Ma (Atwater, 1989) and we would expect, and previous work has imaged, several thousand kilometers of slab extending deep into the mantle (Sigloch *et al.*, 2008). The westernmost US hosts major Neogene to Quaternary volcanic provinces. The Columbia River Basalts (CRB) are the product of a phase of massive volcanic outpouring that occurred 17 Ma. The Yellowstone Snake River Plain is a bimodal volcanic trend that exhibits a time progressive sequence of calderas. Two groups of hypotheses have been proposed to explain this surface geology: a stationary deep-seated whole mantle plume (Pierce *et al.*, 2000; Camp and Ross, 2004; Smith *et al.*, in review), or various lithospheric-driven processes of fracture and volcanism (Dickinson, 1997; Humphreys *et al.*, 2000; Christiansen *et al.*, 2002). Nevertheless, seismic imaging efforts to constrain the geometry of any Yellowstone plume anomaly through the mantle have been inconclusive.

### 20.2 Data and Method

Here we compile a seismic waveform dataset consisting of teleseismic body-waves, both direct and core phases, recorded at seismic stations across the western United States. We use data from the US from Earthscope's US-Array, the regional seismic networks and temporary seismic deployments that together provide an array of more than 1000 seismometers with an unprecedented density and spatial extent. Relative body-wave traveltime delays are measured by cross-correlation in the 1.25 to 0.5 sec frequency band for compressional arrivals and 50 to 10 sec for shear arrivals. We use events at greater than  $30^\circ$  epicentral distance with magnitude greater or equal to 5.5 from January 2006 to July 2009. The compressional-arrival dataset is derived from 30,670 traveltime observations of direct P from 127 earthquakes. The shear-arrival dataset includes 38,750 travel-time measurements, 34,850 S-wave observations from 142 events and 3,900 SKS observations from 24 events. In this study, we combine this regional dataset with a tomographic technique utilizing finite frequency sensitivity kernels. The banana-doughnut-shaped kernels account for the frequency- and depth-dependent width of the region to which teleseismic body-waves are sensitive and account for wave-front

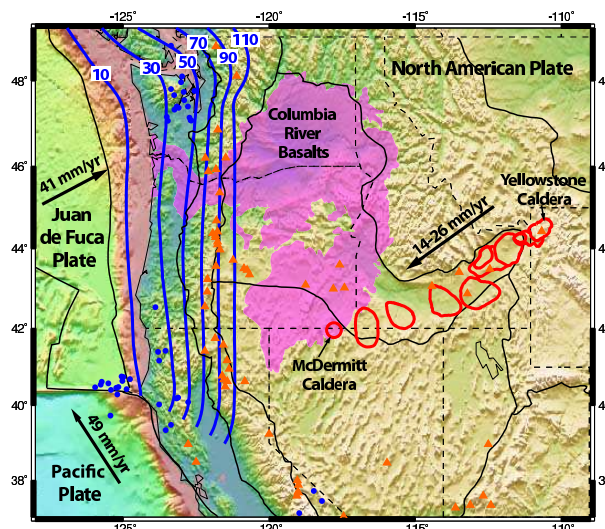


Figure 2.38: Geologic-tectonic features of the Pacific Northwest of the United States overlaid on topography and bathymetry. The Juan de Fuca plate is subducting beneath the North American plate with an oblique convergence rate of 41 mm/yr. The estimated depth of the top of the subducting slab is shown with blue contours labeled in km. The location of all  $M > 4$  earthquakes with depth  $> 35$  km since 1970 are shown as blue dots. Volcanoes are shown as orange triangles. The Yellowstone Hotspot Track exhibits a series of time-progressive calderas (red outline) from McDermitt ( $\sim 16.1$  Ma) to the currently active Yellowstone Caldera. The track is approximately parallel to the absolute plate motion of North America. The Columbia River Flood Basalt Province was a massive outpouring of basalt from  $\sim 16.6$  to  $\sim 15.0$  Ma and is shown in pink.

healing effects. Our tomographic method uses paraxial kernel theory to calculate the forward scattering sensitivity kernels for teleseismic arrival times (Hung *et al.* 2004).

### 20.3 Results and Discussion

The main features imaged in both our P and S models (Figure 2.39) include a whole mantle plume beneath Yellowstone emplaced between slab fragments, the surprisingly short and uneven Juan de Fuca plate, and the presence of a fossil slab fragment adjacent to the currently subducting slab. Interpreted together, all these features are strong indications that the Yellowstone plume broke

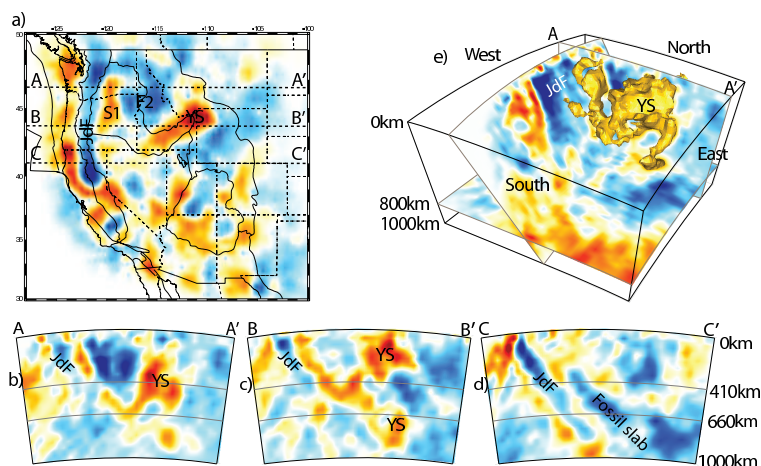


Figure 2.39: Cross sections through our P model. (a) Constant depth slice at 200 km showing the continuous high-velocity Juan de Fuca slab and the strong low-velocities below the Yellowstone Caldera. (b) through (d) are E-W cross-sections at locations shown in (a). The currently subducting slab is visible in all sections though the amplitude of the slab anomaly reduces from south to north. The Yellowstone plume has a strong signature as deep as 900km in (b) and (c). The parallel fossil-slab anomaly is strong in (d). (e) is composed of an oblique section through the Juan de Fuca slab, a constant depth slice at 800km, the E-W vertical slice (b) and a 3D isosurface that illustrates the 3D geometry of the Yellowstone plume.

through the Farallon slab to reach the surface, and that it thermally consumed part of the slab. We propose that as the plume head rose towards the surface the Farallon slab first stopped it. Due to continuous thermal erosion and flexure imposed by the increasing volume of hot and buoyant plume material, the portion of the slab located above the head of the plume weakened and was assimilated by it. Free from structural barrier, the resulting blend continued its ascent to the surface and fed the CRB. The geochemistry of the of the Grande Ronde basalts, representing the climax stage of the CRB and more than 80% of the volume of the CRB, has been interpreted as a heterogeneous source of plume material containing fragments of oceanic crust (Takahahshi *et al.*, 1998), consistent with this interpretation. Farther from the plume conduit, the slab that was not thermally consumed eventually broke. Assuming a subduction rate of around 5cm/y to account for the higher Pacific-North America convergence velocity during the Neogene (Riddihough, 1984), the slab rupture evidenced by our model would have been achieved at the time of or slightly before the CBR outpouring.

## 20.4 References

- Atwater, T., Plate tectonic history of the northeast Pacific and western North America, in Winterer, E. L., Hussong, D. M., and Decker, R. W., eds., *The Eastern Pacific Ocean and Hawaii: Geological Society of America, Boulder, Colorado, The Geology of North America*, v. N, 21-72, (1989).
- K. Sigloch, N. McQuarrie, G. Nolet, Two-stage subduction history under North America inferred from multiple-

- frequency tomography, *Nature Geoscience*, 1, 458 (2008).
- K. L. Pierce, L. A. Morgan, R. W. Saltus, Yellowstone plume head: Postulated tectonic relations to the Vancouver slab, continental boundaries and climate, Open-File Report 00-498, U.S. Geological Survey, (2000).
- V. E. Camp, M. E. Ross, Mantle dynamics and genesis of mafic magmatism in the intermontane Pacific Northwest, *J. Geophys. Res.* 109, B08204, (2004).
- R. B. Smith *et al.*, Geodynamics of the Yellowstone Hotspot and Mantle Plume: Seismic and GPS Imaging, Kinematics, and Mantle Flow, *J. Vol. Geotherm. Res.*, (in review).
- W. R. Dickinson, OVERVIEW: Tectonic implications of Cenozoic volcanism in coastal California, *Geol. Soc. Am. Bull.*, 109, 936 (1997).
- E. D. Humphreys, K. G. Dueker, D. L. Schutt, R. B. Smith, Beneath Yellowstone: Evaluating Plume and Nonplume Models Using Teleseismic Images of the Upper Mantle, *GSA Today*, 10, 1 (2000).
- R. L. Christiansen, G. R. Foulger, J. R. Evans, Upper-mantle origin of the Yellowstone hotspot, *Geol. Soc. Am. Bull.*, 114, 1245 (2002).
- E. Takahahshi, K. Nakajima, T. L. Wright, Origin of the Columbia River basalts: melting model of a heterogeneous plume head, *Earth Planet. Sci. Lett.*, 162, 63 (1998).
- R. Riddihough, Recent Movements of the Juan de Fuca Plate System, *J. Geophys. Res.*, 89, B8, (1984)

# 21 Imaging Shallow Cascadia Structure with Ambient Noise Tomography

Robert W. Porritt and Richard M. Allen

## 21.1 Introduction

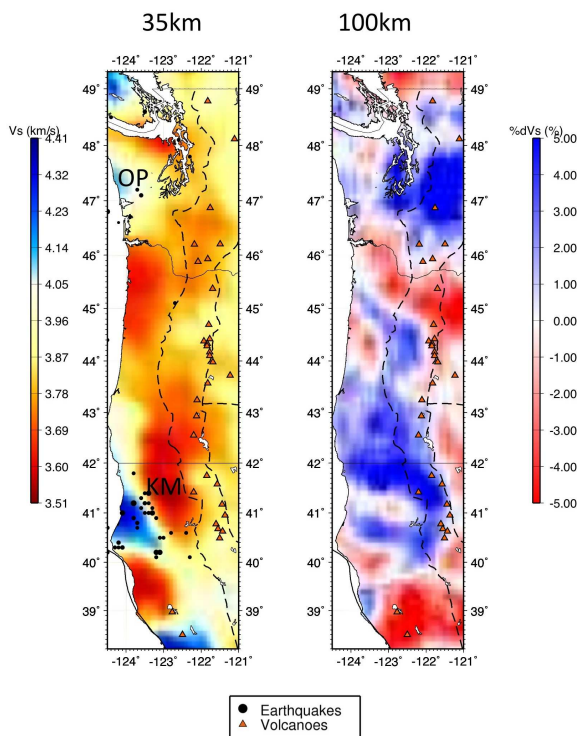


Figure 2.40: A - depth slice at 35km below mean sea level. This is plotted in best fit velocity to show crustal to uppermost mantle structure. B - slice at 100km depth plotted in relative velocity to highlight lateral variation.

Along strike variation has been observed along the Cascadia Subduction Zone in studies with a variety of data sets. Body-wave tomography shows a broad zone in the center of the slab with a weak high velocity signal in an atypically quiescent seismic zone (*Obrebski and Allen, 2009*). Primitive basalts in the arc volcanoes change characteristics along strike, defining four distinct magma sources or plumbing systems (*Schmidt et al, 2007*). Most striking, however, is the change in recurrence rate of episodic tremor and slip throughout the region (*Brudzinski and Allen, 2007*). These disparate observations may reflect regional variations in the lithosphere. This study seeks to connect these previous observations by developing a short period surface wave model of structure in the region using ambient seismic noise as the source.

## 21.2 Data Processing

Data for this study comes from the Berkeley Digital Seismic Network (BDSN), Southern California Earthquake Center, the Canadian National Seismic Network, and USArray with a focus on two Flexible Array Experiments. The Flexible Array deployments, FlexArray Along Cascadia For Segmentation (FACES) and Mendocino Broadband, were deployed in 2007 and are nearing the completion of their two year deployments. This is one of the first studies utilizing the approximately one hundred stations in these broadband experiments.

Detailed processing flow for computing group and phase velocity maps can be found in *Benson et al, 2007*. Group and phase velocity mean values and errors are computed using a jack knife approach from cross correlations of 11 months of continuous data. Dispersion curves over the model space and their corresponding errors are utilized in a Monte Carlo inversion scheme (*Shapiro and Ritzwoller, 2002*) using PREM as a starting model to compute smooth one dimensional velocity profiles on each tenth of a degree by tenth of a degree node from the surface to 150km depth. The profiles are concatenated together and corrected for topography to build a three dimensional model. To better visualize lateral variations

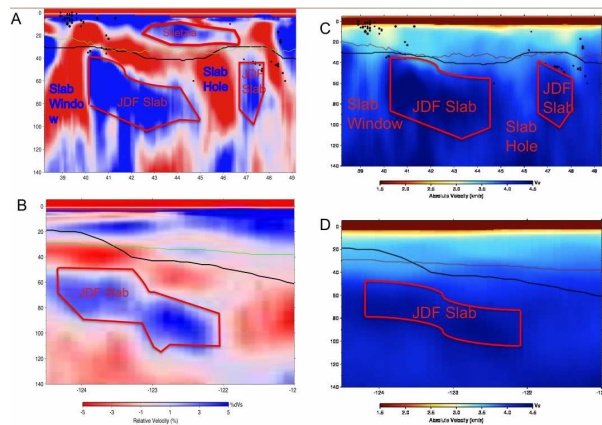


Figure 2.41: A - Longitudinal cross section along 123.2°W. B - Latitudinal cross section along 44.5°N. C - same as A, but in best fit velocity. D - same as B, but in best fit velocity. Key aspects of the model are highlighted. Thin red and thin green lines show the estimate of Moho based on greatest vertical gradient within  $\pm 10$ km of Crust2.0

in the mantle, a one-dimensional mean model is extracted and used to compute a three dimensional model of velocity relative to that one-dimensional model.

### 21.3 Results

Figure 2.40 shows two representative slices at constant depth in the Pacific Northwest. In the 35km depth slice, the semi-circular pattern of the Olympic Peninsula (OP), with faster rocks in the center and lower velocities around the outer part, is clearly seen, and the crustal root of the Klamath Mountains (KM) is also clear as a slow mass in the mantle. In the 100km depth section, the overlay of the main arc volcanoes closely matches the edge of the slab. Figure 2.41 shows two cross sections along 123.2°W and 44.5°N respectively. Figures 2.41 A and B are shown in velocity relative to a one-dimensional model, while C and D are in best fit velocity from the inversion. Overlain are the slab contours from *Audet et al*, 2009 in black and black circles showing earthquakes.

The structure is largely consistent with what would be expected; however, unexpected structural variations are apparent. Examples of expected structures include: deep crustal roots of the Klamath mountains, the border between the slab window and the slab following the trend of the Mendocino Fracture Zone, and the high velocity slab dipping the same way as the receiver functions suggest. The offset between the receiver function top of the slab and this image may reflect a layer of oceanic sediments of varying thickness overlying the main basaltic oceanic lithosphere in the subducting slab.

There is a reduction in the velocity of the subducting Juan de Fuca slab between 45°N and 47°N in a similar location as the weakening of the high velocity slab shown in *Obrebski and Allen*, 2009. There is also a high velocity lower crustal layer between 43°N and 47°N which correlates with the Siletzia terrain (*Brudzinski and Allen*, 2007). The Siletzia terrain has the longest recurrence interval of episodic tremor and slip (ETS) events throughout the subduction zone. Because this is a high shear wave velocity zone and ETS is less active in this zone, it is likely this is a region of lower fluid content than the rest of the subduction zone. Further analysis incorporating receiver functions and estimates of  $V_p/V_s$  ratio could confirm this finding.

### 21.4 Acknowledgements

We would like to acknowledge our co-PI's and collaborators on the flexible array experiments. The Mendocino Broadband experiment was made possible through NSF grants EAR0643392 and EAR0745934, with help from Gene Humphreys, Leland O'Driscoll, Alan Levander, and Yongbo Zhao for fieldwork and discussions. The FlexArray Along Cascadia was funded through NSF grant EAR0643007 with co-PI Mike Brudzinski and his students Devin Boyarko and Stefany Sit.

We thank Morgan Moschetti, Michael Ritzwoller, Yingji-Yang, Nikolai Shapiro, and Fan-Chi Lin for help with the ambient noise tomography processing flow to create the model. Data from this study came from the Earthscope USArray/Transportable Array, the Canadian National Seismic Network through the AutoDRM system, the Berkeley Digital Seismic Network, and the Southern California Earthquake Center.

Field assistance has been provided by the following: Derry Webb, Marcos Alvarez, Lloyd Carothers, Eliana Arias Dotson, Pat Ryan, Lisa Linville, Pallavi Chethan, Kevin Jensen, Chris McMillan, Stefany Sit, Andrew Tran, Summer Ohlendorf, Dan'L Martinez, Valerie Zimmer, Will Levandowski, Amanda Thomas, Heidi Reeg, Nickles Badger, Tom Owens, Eileen Evans, Holly Brown, Joanne Emerson, Ajay Limaye, Rick Lellinger, Mathias Obrebski, Samanta Cubias, Caroline Eakin, Liang Zhao, and David Belt.

This work has been made possible with the resources available through the PASSCAL instrument center at New Mexico Tech.

### 21.5 References

- Audet, P., Bostock, M. G., Christensen, N. I., and Peacock, S. M., Seismic evidence for overpressured subducted oceanic crust and megathrust fault sealing, *Nature*, 457, 76-78, 2009.
- Benson, G.D., Ritzwoller, M.H., Barmin, M.P., Levshin, A.L., Lin, F., Moschetti, M. P., Shapiro, N.M., Yang, Y., Processing seismic ambient noise data to obtain reliable broadband surface wave dispersion measurements, *Geophysical Journal International*, 169, 1239-1260, 2007.
- Bostock, M.G., Hyndman, R.S., Rondenay, S., and Peacock, S. M., An inverted continental Moho and serpentinization of the forearc mantle, *Nature*, 417, 53-539, 2002.
- Brudzinski, M. and Allen, R. M., Segmentation in Episodic Tremor and Slip All Along Cascadia, *Geology*. 35 (10) 907-910, 2007.
- Obrebski, M. J., and Allen, R. M., Plume Vs. Plate: Convection beneath the Pacific Northwest, *Berkeley Seismological Laboratory Annual Report*, 2009.
- Schmidt, M. E., Grunder, A.L., and Rowe, M., Segmentation of the Cascades Arc as indicated by Sr and Nd isotopic variation among primitive basalts, *Earth and Planetary Science Letters*, 266, 166-181, 2007.
- Shapiro, N. M., and Ritzwoller, M. H., Monte-Carlo inversion for a global shear velocity model of the crust and upper mantle, *Geophysical Journal International*, 151, 88-105, 2002.
- Xue, M., and Allen, R. M., The Fate of the Juan de Fuca Plate: Implications for a Yellowstone Plume Head, *Earth and Planetary Science Letters*, 264, 266-276, 2007.

# 22 Seismic Anisotropy Beneath Cascadia and the Mendocino Triple Junction: Interaction of the Subducting Slab with Mantle Flow

Caroline M. Eakin, Mathias Obrebski, Richard M. Allen, Devin C. Boyarko (Miami Univeristy, Ohio), Michael R. Brudzinski (Miami Univeristy, Ohio) and Robert Porritt

## 22.1 Introduction

The tectonic history of Cascadia is well characterized from plate reconstructions and tomography, but how subduction has affected mantle flow is relatively unknown. Such knowledge about the mantle flow field is primarily obtained from studies of mantle anisotropy using observations such as shear wave splitting. Cascadia and the Mendocino Triple Junction (MTJ) are generally lacking in such observations compared to other subduction zones worldwide, despite showing patterns that are unique to the global data set, i.e. trench normal fast directions beneath the slab (Long and Silver, 2008).

## 22.2 Data and Methods

Here we present shear wave splitting observations made using the datasets from FAME (Flexible Array Mendocino Experiment) and FACES (Flexible array Along Cascadia Experiment for Segmentation) networks (Figure 2.42). Data was available over the time period of Oct 2007-Sept 2008 for FAME and Nov 2007-July 2009 for FACES. Events of magnitude greater than 6.3, occurring within the given time period and in the epicentral distance range 85° to 130° were selected. Fifty suitable events were identified from which SKS and SKKS phases were analyzed. Calculations of shear wave splitting were performed using SplitLab (Wüstfeld et al., 2007). Splitting measurements at each station were then stacked following a quality assessment.

## 22.3 Results

A stacked result was obtained at 63 stations (Figure 2.42). The splitting pattern is highly uniform throughout Cascadia with a mean fast direction of N67°E. This direction is normal to the trench and is comparable to the absolute motion of North American plate, the absolute motion of the Gorda-Juan de Fuca (G-JdF) plate (as shown by motion vectors on Figure 2.42), and also the subduction direction. The average delay time is 1.25 seconds.

On the west coast at the latitude of the MTJ, the observed fast direction dramatically rotates by almost 90 degrees. The mean splitting direction for stations south of the MTJ is N71°W with an average splitting time of 1.48 seconds. There is also a gradual rotation from the NW-SE orientation immediately south of the triple junction back to a NE-SW orientation at stations to the east

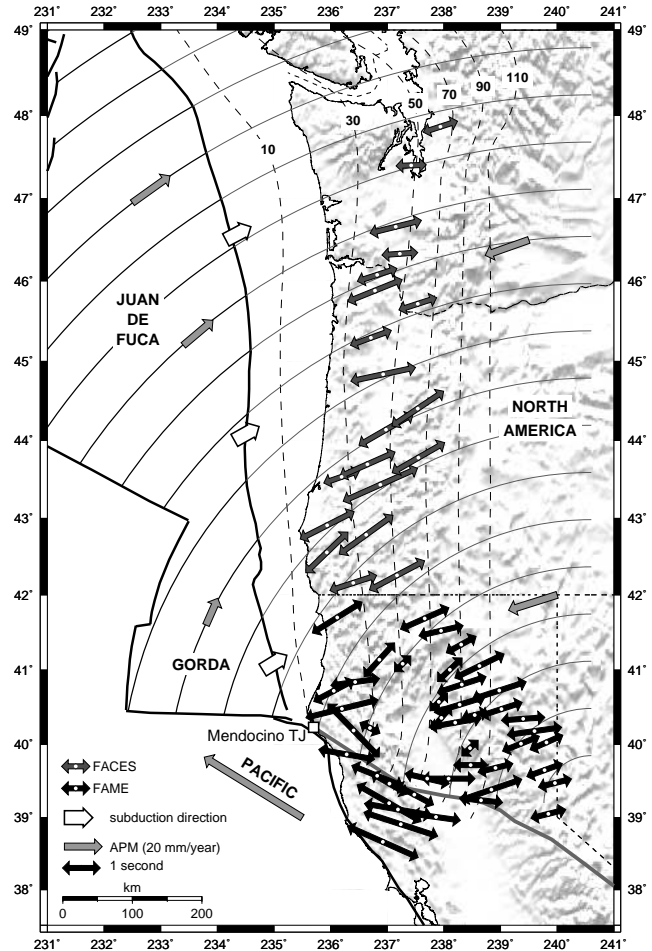


Figure 2.42: Tectonic map for the study region including stacked shear wave splitting results. Orientation of arrows represents the fast direction, and their length is proportional to the delay time. Thin black lines (motion vectors) have been drawn to emphasize the rotational movement of the G-JdF plate as determined from its absolute plate motion. Thick black lines are plate boundaries, interpolated edge of the G-JdF slab is in grey. Estimated depths of the top of the subducting slab are drawn as dashed lines.

across the southern half of the FAME network (Figure 2.42).

Figure 2.43 shows our results, previous splitting observations in the region (Wang et al., 2008; West et al., 2009;

Zandt and Humphreys, 2008 and references therein), and a vertical average (100-400 km) of tomographically imaged upper mantle velocities from the DNA09 P-wave model. The rotation of the splits south of the triple junction corresponds to the low velocity region that wraps around the southern end of the slab.

## 22.4 Sources of Anisotropy and Mantle Flow

After considering the multiple possible source regions of anisotropy in a subduction zone, the sub-slab mantle is considered to be the most likely candidate. It is the only region that is large enough (>200km) to produce the size of the observed delay times and is capable of generating the consistent splitting orientation throughout the subduction zone. As the fast direction is parallel to subduction of the G-JdF plate, this is consistent with entrained mantle flow beneath the slab as the source of the anisotropy.

The rotation of splitting south of the MTJ (Figure 2.43) suggests that the anisotropy is due to flow around the southern edge of the slab. During rollback, as the trench migrates in the direction of the oceanic plate, mantle material from below is forced around the edge of the slab into the mantle wedge which is under lower pressure. Such a mechanism has been inferred to account for trench-parallel splitting underneath subducting slabs, as the mantle tries to move around the slab which is undergoing rollback (Long and Silver, 2008). This study has produced evidence for flow around the slab edge from rollback but without trench parallel flow beneath the subducting plate. This is unique to Cascadia where the effect of rollback on the mantle flow field only appears to be at the slab edge.

Fig.2.43 also shows the regional pattern of splitting for the entire western US. The large scale circular pattern centered upon Nevada has been previously modeled as toroidal flow around the G-JdF slab (Zandt and Humphreys, 2008). More recently West et al. (2009) have interpreted a high velocity anomaly beneath central Nevada (Fig.2.43) as a lithospheric drip that could also explain the same circular pattern of splits. In our study we interpret the anisotropy as flow around the southern edge of the Gorda slab but on a smaller scale than previously proposed by Zandt and Humphreys (2008). The improved level of detail provided by our results allows us to distinguish that flow around the slab edge is a separate feature from anisotropy associated with the Nevada anomaly.

## 22.5 Acknowledgements

This work was funded by NSF awards EAR-0643392, EAR-0745934 and EAR-0643077. We extend our thanks to Andreas Wüstfeld for providing guidance concerning

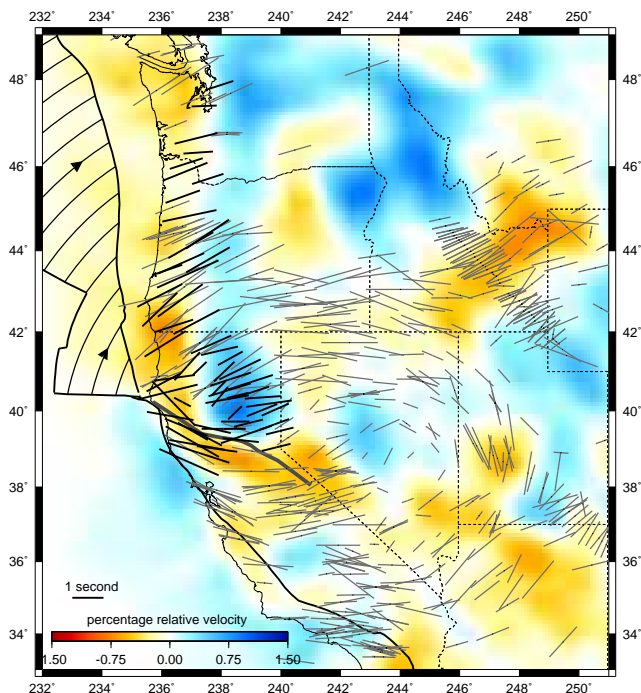


Figure 2.43: Regional splitting pattern overlain on the vertically averaged (100-400km depth) upper mantle velocity anomaly from DNA09 P-wave model. Our splitting results are shown in black and those of previous studies are in grey (see text). Curved black lines on the G-JdF plate represent the direction of its absolute plate motion.

SplitLab, and to Gene Humphreys, Maureen Long, John West and George Zandt for sharing their shear wave splitting data sets.

## 22.6 References

- Long, M.D., and P.G. Silver, The Subduction Zone Flow Field from Seismic Anisotropy: A Global View, *Science*, 319, 315-318, 2008.
- Wang, X., J.F. Ni, R. Aster, E. Sandvol, D. Wilson, C. Sine, S.P. Grand, and W.S. Baldrige, Shear-wave splitting and mantle flow beneath the Colorado Plateau and its boundary with the Great Basin, *Bull. Seis. Soc. Am.*, 98, 2526-2532, 2008.
- West, J.D., M.J. Fouch, J.B. Roth and L.T. Elkins-Tanton, Vertical mantle flow associated with a lithospheric drip beneath the Great Basin, *Nature Geoscience*, 2, 439-444, 2009.
- Wüstfeld, A., G. Bokelmann, C. Zaroli, and G. Barroul, SplitLab: A shear-wave splitting environment in Matlab, *Computers and Geosciences*, 34, 515-528, 2007.
- Zandt, G. and E. Humphreys, Toroidal mantle flow through the western US slab window, *Geology*, 36, 295-298, 2008.

# 23 Recovering the Attenuation of Surface Waves from One-Bit Noise Correlations: A Theoretical Approach

Paul Cupillard, Laurent Stehly and Barbara Romanowicz

## 23.1 Introduction

Cross-correlation of ambient seismic noise recorded by a pair of stations is now commonly recognized to contain the Green's function between the stations. Travel times extracted from such data have been extensively used to get images of the Earth interior. Some studies have also attempted to explore the information contained in the amplitude (Larose *et al.*, 2007; Gouedard *et al.*, 2008; Matzel, 2008; Prieto *et al.*, 2009). In a recent work, Cupillard and Capdeville (2009) carried out numerical experiments showing that the attenuation of surface waves can be recovered from one-bit noise correlations in the case of a uniform distribution of noise sources on the surface of the Earth (Figure 2.44). We here provide a theoretical explanation for such a surprising result.

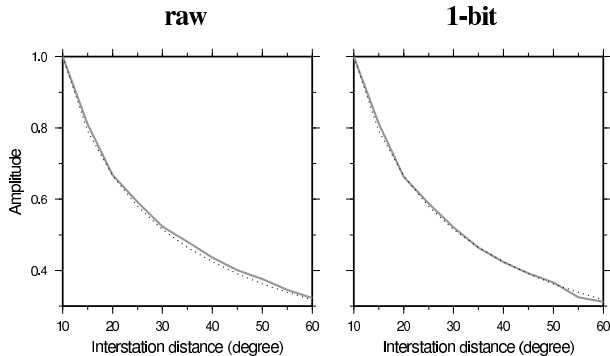


Figure 2.44: Results from Cupillard and Capdeville (2009). These authors generate synthetic noise on the surface of a 1D Earth model and compute correlations using a stream of twelve stations. Then, they compare the amplitude decay of the correlations (gray line) with the amplitude decay of the Rayleigh wave Green's functions (dotted line). The two curves match well, even when applying one-bit normalization to the noise records.

## 23.2 Amplitude of the raw noise correlation

Consider two receivers A and B that are separated by a distance  $\Delta$  in a homogeneous medium in which the wave speed is  $v$ . Noise sources are distributed in this medium, and each receiver therefore records a time-signal. We denote by  $A(t)$  (respectively  $B(t)$ ) the recording from A (respectively B).

We assume that these signals can be decomposed in the following manner:

$$A(t) = A^c(t) + A^i(t) \quad (2.1)$$

$$B(t) = B^c(t) + B^i(t) \quad (2.2)$$

such that the cross-correlation  $C_{AB}(t)$  between the signals can be written

$$C_{AB}(t) = \frac{1}{T} \int_0^T A^c(\tau) B^c(t + \tau) d\tau, \quad (2.3)$$

where  $T$  is the length of the signals. We designate  $A^c(t)$  and  $B^c(t)$  as coherent, whereas  $A^i(t)$  and  $B^i(t)$  are called incoherent.

We also assume that

$$B^c(t_0 + \tau) \propto A^c(\tau), \quad (2.4)$$

where  $t_0 = \Delta/v$ , so we have

$$C_{AB}(t_0) = \sigma_{A^c} \sigma_{B^c}, \quad (2.5)$$

where  $\sigma_{A^c}$  (respectively  $\sigma_{B^c}$ ) is the standard deviation of  $|A^c(t)|$  (respectively  $|B^c(t)|$ ).

## 23.3 Amplitude of the one-bit noise correlation

Using notations and assumptions made in the previous section, we can now find out what the amplitude of the one-bit noise correlation contains.

One-bit normalization consists of retaining only the sign of the raw signal by replacing all positive amplitudes with a 1 and all negative amplitudes with a -1. Thus, we can write

$$C_{AB}(t) = \int \text{sgn}[A(\tau)] \text{sgn}[B(t + \tau)] d\tau \quad (2.6)$$

$$= n_1(t) - n_{-1}(t), \quad (2.7)$$

where  $n_1(t)$  (resp.  $n_{-1}(t)$ ) is the number of samples for which  $\text{sgn}[A(\tau)] = \text{sgn}[B(t + \tau)]$  (resp.  $\text{sgn}[A(\tau)] \neq \text{sgn}[B(t + \tau)]$ ).

For some samples  $\tau$ ,  $|A^i(\tau)| > |A^c(\tau)|$  or  $|B^i(t + \tau)| > |B^c(t + \tau)|$ : at one of the two stations, the incoherent noise has a larger amplitude than the coherent noise and so controls the sign of the sample for this station. As the incoherent noise is random, the two events  $\text{sgn}[A(\tau)] = \text{sgn}[B(t + \tau)]$  and  $\text{sgn}[A(\tau)] \neq \text{sgn}[B(t + \tau)]$  have the same probability, so for this population of samples we have  $n_1(t) = n_{-1}(t)$ .

For the other samples,  $|A^i(\tau)| < |A^c(\tau)|$  and  $|B^i(t + \tau)| < |B^c(t + \tau)|$ : the coherent noise controls the sign of both  $A(\tau)$  and  $B(t + \tau)$ , so  $\text{sgn}[A(\tau)] = \text{sgn}[A^c(\tau)]$  and  $\text{sgn}[B(t + \tau)] = \text{sgn}[B^c(t + \tau)]$ . Equation 2.4 yields  $\text{sgn}[B(t_0 + \tau)] = \text{sgn}[A^c(\tau)]$ , so for this population of samples we have  $n_{-1}(t_0) = 0$ .

Now we can write

$$C_{AB}(t_0) = nP_1P_2, \quad (2.8)$$

where  $n$  is the total number of samples in the correlation,  $P_1$  is the probability that  $|A^c(t)| > |A^i(t)|$  and  $P_2$  is the probability that  $|B^c(t)| > |B^i(t)|$ . Assuming that coherent and incoherent noise are both gaussian, we are able to express  $P_1$  and  $P_2$ . Denoting by  $\sigma_{A^i}$  (respectively  $\sigma_{B^i}$ ) the standard deviation of  $|A^i(t)|$  (respectively  $|B^i(t)|$ ), we find

$$C_{AB}(t_0) = n \left[ 1 - \frac{2}{\pi} \tan^{-1} \left( \frac{\sigma_{A^i}}{\sigma_{A^c}} \right) \right] \left[ 1 - \frac{2}{\pi} \tan^{-1} \left( \frac{\sigma_{B^i}}{\sigma_{B^c}} \right) \right] \quad (2.9)$$

### 23.4 The case of a uniform distribution of noise sources

Equation 2.9 has been established with no hypothesis on the distribution of noise sources. We have found that the amplitude of the one-bit noise correlation is related to physical quantities. In this section, we evaluate these quantities in the case of a uniform distribution of noise sources.

We assume that  $A^c(t)$  is due to the contribution of all the noise sources in the coherent zone (denoted by  $\Omega^c$  in the following) as defined by Snieder (2004). This coherent zone is an hyperboloid whose parameters depend on inter-station distance and frequency. Using the central-limit theorem, we write

$$\sigma_{A^c}^2 = \int_{\Omega^c} \sigma_A^2(x) dx. \quad (2.10)$$

In this equation,  $\sigma_A(x)$  is the standard deviation of the signal recorded in A due to a source in  $x$ . Considering surface waves at the angular frequency  $\omega$ , we have

$$\sigma_A(x) \propto \frac{1}{\sqrt{x}} \exp\left(-\frac{\omega x}{2vQ}\right), \quad (2.11)$$

where  $Q$  is the quality factor of the medium.

Using equation 2.11 in equation 2.10, we obtain

$$\sigma_{A^c}^2 \propto \Delta \cos^{-1} \left( \frac{\Delta - \frac{\lambda}{6}}{\Delta} \right) [K_1(\beta) + K_2(\beta)] e^\beta, \quad (2.12)$$

where  $\lambda$  is the wavelength,  $K_1$  and  $K_2$  are Bessel functions of the second kind and  $\beta = \frac{\omega \Delta}{2vQ}$ .

The same procedure enables us to compute  $\sigma_{B^c}$ ,  $\sigma_{A^i}$  and  $\sigma_{B^i}$ . We finally get two analytical expressions for

$C_{AB}(t_0)$ : one for the raw noise correlation and one for the one-bit noise correlation. We do not provide these expressions because they are too long, but we plot them in Figure 2.45. It is clear that the two amplitude decays correspond to the decay of the Rayleigh wave Green's function.

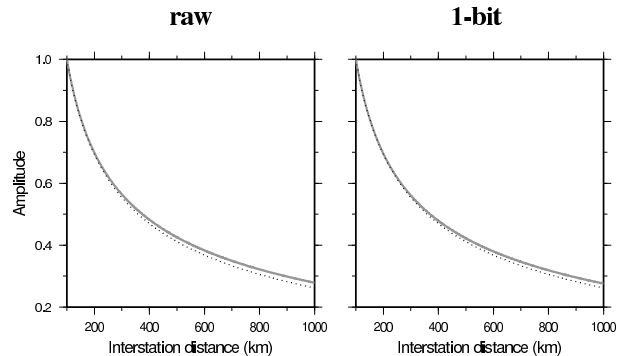


Figure 2.45: The amplitude decay of the correlations predicted by our theory (gray line) is compared with the decay of the Rayleigh wave Green's function (dotted line). The curves have been obtained using  $\lambda = 50 \text{ km}$  and  $Q = 300$ .

### 23.5 References

- Capillard, P. and Y. Capdeville, On the amplitude of surface waves obtained by noise correlation and the capability to recover the attenuation: a numerical approach, *Geophys. J. Int.*, submitted.
- Gouépard, P., P. Roux, M. Campillo and A. Verdel, Convergence of the two-points correlation function toward the Green's function in the context of a prospecting dataset, *Geophysics*, 73(6), V47-V53, 2008.
- Larose, E., P. Roux and M. Campillo, Reconstruction of Rayleigh-Lamb dispersion spectrum based on noise obtained from an air-jet forcing, *J. Acoust. Soc. Am.*, 122(6), 3437, 2007.
- Matzel, E., Attenuation tomography using ambient noise correlation, *Seism. Res. Lett.*, 79(2), 358, 2008.
- Prieto, G. A., J. F. Lawrence and G. C. Beroza, Anelastic Earth structure from the coherency of the ambient seismic field, *J. Geophys. Res.*, 144, B07303, doi:10.1029/2008JB006067, 2009.
- Snieder, R., Extracting the Green's function from the correlation of coda waves: a derivation based on stationary phase, *Phys. Rev. E*, 69, 046610, 2004.

## 24 The Origin of Seismic Anisotropy in the D''

Sanne Cottaar, Paul Cupillard, Allen McNamara, Barbara Romanowicz, and Rudy Wenk

### 24.1 Introduction

The D'' zone at the base of the mantle is a boundary layer, both chemically and thermally. Complex dynamic processes are the cause of lateral heterogeneities, with sharp boundaries at the edge of superplumes (e.g. *Toh et al.*, 2005). Another characteristic of D'' is the presence of strong and laterally varying anisotropy. A global long-wavelength model for S-wave velocity and radial anisotropy shows that, in general, SH phases are faster than SV phases (*Panning and Romanowicz*, 2006). This observation leads to the idea that flow causes anisotropy by alignment of anisotropic minerals.

The goal of this research is to investigate seismic anisotropy and sharp velocity boundaries in the D'' region by combining geodynamics, mineral physics, and seismic modeling. Different seismic velocity models will be created to test hypotheses of possible microscopic and macroscopic processes. Comparing data computed for the models with real data will confirm or rule out these processes as a possibility for the lowermost mantle.

This contribution is an overview of ongoing research.

### 24.2 Geodynamics

The two-dimensional geodynamical model (provided by Allen McNamara) is refined to emphasize deformation in D'' (*McNamara and Zhong* 2004). Lagrangian tracers travel through the lowermost part of the model, providing strain information. Horizontal shear deformation increases near the CMB, while vertical deformation is strong in the upwelling region. An example of development along a tracer is shown in Figure 2.46. A great number of data points of several tracers are combined to create a static (snapshot) model.

### 24.3 Mineral Physics

Calculating the seismic velocities from the strain requires knowing elastic constants and deformation mechanisms at the temperature and pressure conditions of D''. These are measured for the most abundant minerals: perovskite ( $MgSiO_3$ ) and periclase ( $MgO$ ).

We predict the seismic response of a suite of different mineral phases and assemblages. Post-perovskite is proposed as one of the possible anisotropic minerals. In fast regions, the top of the D'' is characterized by a velocity discontinuity, possibly caused by the pPv transition of  $MgSiO_3$  (e.g. *Wookey et al.*, 2005). For pPv we will try different elastic constants and deformation systems. Disparate results for elastic constants are found compu-

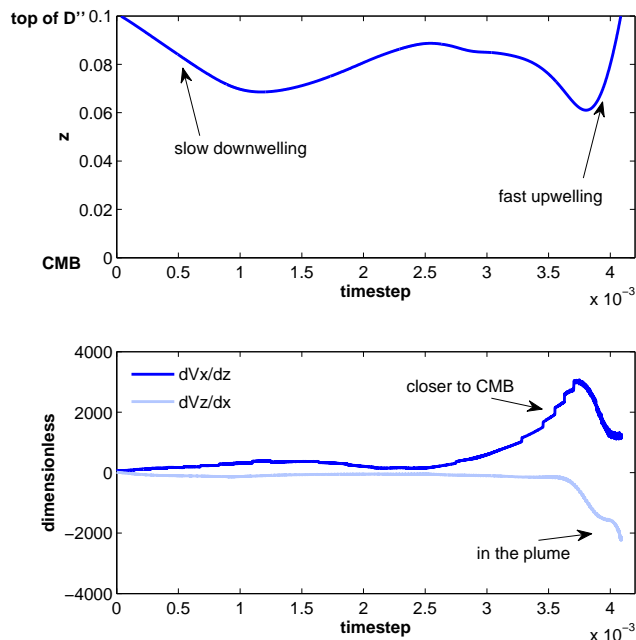


Figure 2.46: Top figure shows the depth of the Lagrangian tracer in the geodynamical model with time. The bottom figure shows the development of strain. Horizontal strain is higher deeper in the mantle and vertical strain increases in the plume.

tationally by *Stackhouse et al.* (2005) and *Wentzocovitch et al.* (2006). Various slip-systems are found by theoretical work and in deformation experiments (e.g. *Merkel et al.*, 2007). It has also been suggested that ferropericlase, ( $Mg, Fe$ )O, might be the dominant cause of seismic shear anisotropy (e.g. *Marquardt et al.*, 2009).

Although other origins of anisotropy, like SPO and melt inclusions, have been proposed, they are not considered in this project.

### 24.4 Synthetic Data

Slices of two-dimensional velocity models extend the model in the third dimension and will be implemented in sandwiched C-SEM (Coupled Spectral Element Method, *Capdeville et al.*, 2003). Sandwiched-CSEM couples the SEM part in the lower mantle to a computationally faster 1D normal mode solution in the rest of the Earth. Eventually, the data will be calculated down to periods of  $\sim 10$  seconds. The predicted waveforms will be compared to observations.

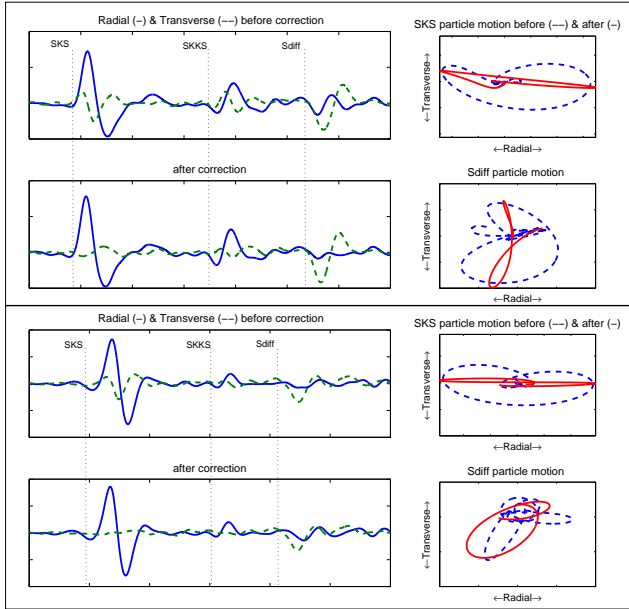


Figure 2.47: Observations for 7.1  $M_w$  event at 530 km depth in Mindanao, Philippines. Top four figures show data before and after correction for station HLID at a distance of  $108^\circ$ . The lower four are for station A04A at  $101^\circ$ .

## 24.5 Real Data

Several phases are used to study the D<sup>''</sup>. The S-wave, the core-reflected S (ScS) and the diffracted phase (Sdiff) have shown that D<sup>''</sup> is anisotropic.

Data from deep earthquakes are needed to avoid source-side anisotropy in the upper mantle. Unfortunately, the azimuthal coverage of this data is not very good. Vertical transverse isotropy (VTI) can, however, be measured along one path by the splitting of S-waves into SH and SV phases. Coverage has been greatly improved by the USArray, providing a large number of stations at the correct distance from deep earthquakes in the region of Indonesia and Fiji-Tonga. These paths cover the boundaries of the Pacific superplume.

Before measuring anisotropy in D<sup>''</sup>, the phases need to be corrected for the receiver side anisotropy. The SKS has a shorter path in D<sup>''</sup>, but an almost similar path through the upper mantle. Therefore, we correct the Sdiff phase with values measured for SKS at similar azimuth using (a modified version of) SplitLab (Wüsterfeld *et al.*, 2007). Figure 2.47 shows examples of how this decreases and increases anisotropy in D<sup>''</sup>.

## 24.6 Future Work

Besides varying a number of assumptions with the models, several major improvements are needed to make

the models more realistic. One of the improvements will be to use a three-dimensional model providing more realistic strains.

Possible mineral phase transitions will be implemented. This could test the occurrence of sharp horizontal and vertical velocity boundaries or transitional zones.

## 24.7 Acknowledgements

This project is funded by NSF's CSEDI program under grant number NSF EAR-0757608.

## 24.8 References

- Capdeville, Y., B. Romanowicz, and A. To, Coupling spectral elements and modes in a spherical earth: an extension to the "sandwich" case, *Geophys. J. Int.*, 154, 44-57, 2003.
- McNamara, A.K. and S. Zhong, The influence of thermochemical convection on the fixity of mantle plumes, *EPSL* 222, 485, 2004.
- Merkel S., A.K. McNamara, A. Kubo, S. Speziale, L. Miyagi, Y. Meng, T. S. Duffy, H.-R. Wenk, Deformation of (Mg,Fe)SiO<sub>3</sub> post-perovskite and D<sup>''</sup> anisotropy, *Science*, 316, 1729-1732, 2007.
- Marquadt, H., S. Speziale, H. J. Reichmann, D. J. Frost, F. R. Schilling and E. J. Garnero, Elastic Shear Anisotropy of Ferropicrcline in Earth's Lower Mantle, *Science*, 324, 224, 2009.
- Panning, M. and B. Romanowicz, A three dimensional radially anisotropic model of shear velocity in the whole mantle, *Geophys. J. Int.*, 167, 361-379, 2006.
- Stackhouse, S., J.P. Brodholt, J. Wookey, J.-M. Kendall and G.D. Price, The effect of temperature on the seismic anisotropy of the perovskite and post-perovskite polymorphs of MgSiO<sub>3</sub>, *EPSL* 230, (1-2), 1-10, 2005.
- Toh, A., B. Romanowicz, Y. Capdeville and N. Takeuchi, 3D effects of sharp boundaries at the borders of the African and Pacific Superplumes: observation and modeling, *Earth and Planet. Sci. Lett.*, 233, 137-153, 2005.
- Wentzcovitch, R.M., B.B. Karki, M. Cococcioni, and S. de Gironcoli, Thermoelastic properties of MgSiO<sub>3</sub>-perovskite: insights on the nature of the Earth's lower mantle, *PRL* 92, doi:10.1103/PhysRevLett92.018501, 2004.
- Wookey, J., S. Stackhouse, J. Kendall, J. Brodholt, and G. D. Price, Efficacy of the post-perovskite phase as an explanation for lowermost-mantle seismic properties, *Nature*, 438, 1004, 2005.
- Wüsterfeld, A., G. Bokelmann, C. Zaroli and G. Barrool, SplitLab: A shear-wave splitting environment in Matlab, *Computers and Geosciences* 34(5), 515-528, 2007.

# 25 Toward a 3D Global Attenuation Model in the Lower Mantle from the Earth’s Free Oscillations

Shan Dou and Barbara Romanowicz

## 25.1 Introduction

In the past two decades, seismic velocity tomography has benefited from rapidly growing data quality, coverage, and computational capability, and has provided snapshots of the present velocity variations in the Earth’s mantle. On the other hand, the study of attenuation has lagged behind that of the elastic velocities because of more complexity in its measurements and interpretation. However, attenuation is important for at least two reasons:

1) Attenuation is considerably more sensitive to temperature variations than elastic velocities. While elastic velocities have a quasi-linear dependence upon temperature variations, seismic attenuation depends exponentially on temperature (e.g., *Jackson, 1993; Karato, 1993*). Therefore, attenuation tomography is important for studying temperature variations within the Earth, and combining elastic and anelastic studies has the potential to separate different effects of chemical composition, water content, partial melting, etc.

2) Attenuation causes physical dispersion of seismic velocities, and this effect needs to be corrected for velocity models.

## 25.2 Methods and Work Plan

Lower mantle imaging is especially difficult compared with that of the upper mantle because surface waves lose their sensitivity to such deep structures. Therefore, lower mantle tomography mostly relies on deep-turning teleseismic body waves and normal mode data. In addition to the contamination from the upper-mantle structure, body-wave datasets suffer from an uneven distribution of events and stations, which can bias the images by over-interpreting the unsampled regions in the lower mantle. Since the Earth’s free oscillations involve the vibration of the whole planet, mode observations have the capacity to resolve deeper structures in the mantle at long wavelengths, and are much less likely to be biased by the uneven distribution of earthquake sources and seismic receivers.

Contamination caused by elastic effects and source complexity can lead to large uncertainties in attenuation measurements. Even if we minimize the uncertainties caused by the source term, elastic processes, especially the effects of scattering and multipathing (i.e. the focusing/defocusing phenomena due to the transverse gradients of elastic structure), are not well constrained, and yield generally very noisy attenuation datasets. There-

fore, we will first start by establishing a new and higher-quality three-dimensional lower mantle elastic structure from modal constraints. This new lower mantle tomographic model can not only serve as a prerequisite for resolving attenuation structure, but can also be used to test the quality of the data set and the accuracy of our measurement and inversion methods.

The constraints on the Earth’s three-dimensional structure extracted from normal modes data mainly rely on detailed analysis of the free oscillation spectrum. In a spherically symmetric, non-rotating, purely elastic, and isotropic idealized 1-D earth model (the SNREI model), the spectrum of each mode is expected to be a sharp and narrow peak. However, the spectra peaks of the real earth demonstrate splitting, broadening, and overlapping in the observed modes, which indicates that the fine structure of the spectra of these records carries important information on the interior three dimensional elastic and anelastic structure of the Earth. Owing to the high quality digital data set assembled in the last 20 years on the global broadband seismic network, and owing to the occurrence of several very large earthquakes, especially the 2004 great Sumatra-Andaman earthquakes mentioned above, putting new constraints on the large-scale attenuation in the lower mantle from normal modes is promising.

Three main stages are involved in retrieving structural information from modal data: 1) Gather many spectra from time series of a large earthquake ( $M_w \geq 7.5$ ); 2) Retrieve spectra of a mode or modes combination from the spectra, and repeat the process for many other large events; 3) Repeat for other modes, build up a greatly expanded catalogue of normal modes sensitive to the lower mantle, and invert for the 3D model of the lower mantle.

## 25.3 Preliminary Results and Prospective Work

Two main approaches frequently used in deriving tomographic models from normal mode spectra will both be applied, and results will be compared with each other: (1) The “one-step” method: directly derive tomographic models from fitting modal spectra by solving a non-linear inverse problem in a least-square iterative way (e.g. *Li et al. 1991, Hara and Geller 2000; Kuo and Romanowicz 2002*); (2) The “two-step” method: the splitting matrix

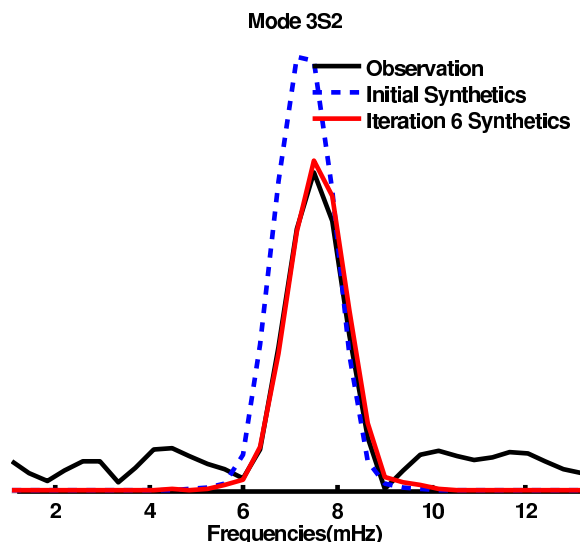


Figure 2.48: Modeling of the spectrum of multiplet  $3S_2$  with the ISF procedure, for a recording of the 9 October 1994 Kuril Island earthquake at station SBC (Santa Barbara, US). Black line: Observed amplitude spectrum; dashed blue line: spectrum generated from the initial splitting coefficients used in the ISF procedure; red line: spectrum after six iterative fittings.

is simplified into its equivalent function on the sphere, known as the “splitting function” (Woodhouse and Giardini 1985). It is a similar procedure to that commonly used in surface wave tomography, in which one first determines 2D maps of phase velocity over a range of frequencies and then uses these to infer the 3D structure perturbations needed to explain the inferred phase velocity maps. Because the nonlinear stage of this approach only needs a relatively smaller number of parameters represented by the splitting function, the computation cost is smaller than the “one-step” method.

We start with the “two-step” method for the elastic structure inversion, where the Iterative Spectral Fitting (ISF) method (Ritzwoller et al. 1986, 1988) is applied in the process of splitting function inversion. Figure 2.48 shows an example of the ISF method. For mode  $3S_2$ , we can clearly see the improvement of spectra fitting within six iterations. The associated splitting function images are shown in Figure 2.49.

We hope to obtain constraints on the long wavelength attenuation structure at the base of the mantle by combining the mode data with the Berkeley waveform dataset, which provides constraints on upper mantle attenuation (following the Ph.D. work of Vedran Lekic). Even if we can only resolve the longest wavelengths (degrees 2 or possibly up to 4), this will be important for the understanding of the nature of the two low velocity regions at the base of the mantle, commonly referred

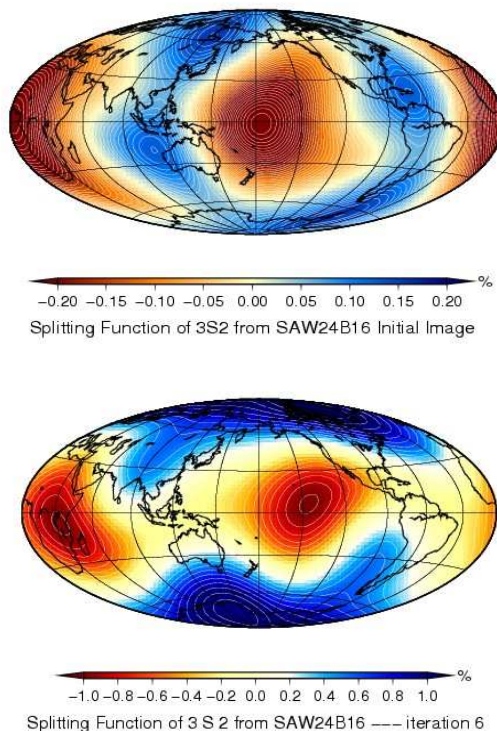


Figure 2.49: Splitting function for mode  $3S_2$ . Upper panel: splitting function obtained from the initial splitting coefficients (the model is the Berkeley mantle model SAW24B16); Lower panel: splitting function after six iterations of ISF procedure.

to as “superplumes,” whose thermo-chemical nature is still under debate (e.g. Masters et al. 1982, Romanowicz 1998, Bijwaard and Spakman 1999, Ishii and Tromp 1999, Romanowicz 2001, Trampert et al. 2004, Gung and Romanowicz 2004, Anderson 2005).

## 25.4 References

- Ritzwoller M, Masters G, and Gilbert F, Observations of anomalous splitting and their interpretation in terms of aspherical structure with low frequency interaction coefficients: Application to uncoupled multiplets, *Journal of Geophysical Research*, 91, 10203-10228, 1986.
- Ritzwoller M, Masters G, and Gilbert F, Constraining aspherical structure with low frequency interaction coefficients: Application to uncoupled multiplets, *Journal of Geophysical Research*, 93, 6369-6396, 1988.
- Romanowicz B and Mitchell B, Deep Earth Structure — Q of the Earth from Crust to Core, *Treatise on Geophysics, Volume 1*, 775-803, 2007.
- Widmer-Schmidrig R and Laske G, Theory and Observations — Normal Modes and Surface Wave Measurements, *Treatise on Geophysics, Volume 1*, 67-125, 2007.

# 26 Anisotropic North American Lithosphere and its Boundary with Asthenosphere

Huaiyu Yuan and Barbara Romanowicz

## 26.1 Introduction

Since the pioneering work by *Vinnik* (1984) and *Sliver* (1988), seismic anisotropy has been extensively used to infer upper mantle strain induced fabrics caused by the past and present time mantle deformation processes (e.g. *Park and Levin*, 2002). Successful correlation of the mapped seismic anisotropy field with many tectonic phenomenon in North America (e.g., edge flow of the continent keels (*Fouch et al.*, 2000); lithospheric drip (*West et al.*, 2009); toroidal flow (*Zandt and Humphreys*, 2008); fossil slab stacking (*Bostock* 1998; *Snyder* 2003, 2008; *Gorman et al.*, 2002; *Mercier et al.*, 2009); rifting (*Gok et al.*, 2003); hotspot tracks (*Walker* 2004; *Schutt et al.*, 1998; *Eaton and Federiksen* 2007); lithosphere thickening (*Deschamps et al.* 2008); and lithosphere-asthenosphere-boundary topography (*Plomerova et al.*, 2002)) has greatly improved our understanding of the dynamics and revolution of the continent.

Using long-period surface waveform tomographic inversion, here we show that the seismic anisotropy beneath North American cratons is strongly stratified, characterized by abrupt changes of fast velocity symmetry axis with depth. At the lithosphere and asthenosphere boundary (LAB), the observed craton-wide change of the anisotropy fast axis towards the absolute plate motion direction defines an anisotropic LAB of the North American upper mantle.

## 26.2 Tomographic Approach

We perform a two-stage inversion to acquire the 3-D azimuthal anisotropy structure in the North American Continent upper mantle. First we simultaneously invert over 150000 3-component long period surface wave fundamental and overtone waveforms to obtain the isotropic  $V_s$  and radial anisotropy  $X_i$  structure. Then we further perturb the optimal  $V_s$  and  $X_i$  model (shown in the next research contribution) from the first step for two azimuthal 2-psi coefficients  $G_c$  and  $G_s$ . Station averaged shear wave splitting measurements are added, which greatly improves the inversion resolution to the deeper mantle (*Marone and Romanowicz*, 2007).

## 26.3 North American Azimuthal Anisotropy: Lithospheric Stratification

Figure 2.50 shows the inverted azimuthal anisotropy structure at selected depths. Those depths are chosen to present upper and lower lithosphere and asthenosphere depths based on estimates from other studies, including

seismic velocity, petrology and lithosphere electrical resistivity (e.g., *van der Lee*, 2002; *Griffin et al.*, 2004; *Darbyshire et al.*, 2000, 2007; *Snyder* 2008; *Chen et al.*, 2008; *McKenzie and Priestley* 2008). At shallow depth (70 km, Figure 2.50a), the craton fast axis is generally plate motion direction parallel, except beneath the east central US and the Labrador Sea/Baffin Island, where the fast axis is pointing north. In the lower lithosphere (150km), the craton region has a nearly uniform north-pointing fast axis, with exclusions of east-west striking fast axis beneath North Dakota Trans-Hudson Orogen and north-east Grenville province. At deeper depth (250km), the fast axis aligns everywhere to the plate motion direction. These images thus demonstrate stratified anisotropic layers beneath the continent, with two lithospheric layers clearly presented in some of the cratons.

## 26.4 North American Azimuthal Anisotropy: Anisotropic LAB

To further constrain the change between the lithosphere and asthenosphere anisotropy, we look for the gradient of the fast velocity axis near the cratonic LAB depths estimated from other studies, with combined constraints from our isotropic velocity  $V_s$  and radial anisotropy  $X_i$  (see *Eaton* (2009) for various seismic definitions of the LAB). Results shown in Figure 2.51 are derived from our tomographic inversion results only.

Our anisotropic LAB is consistently uniform in the depth range of 180-240 km beneath the cratons, except the Wyoming craton, whose LAB is substantially shallower (Figure 2.51a). A depth profile across the major cratons of the study area clearly shows a two layer anisotropy domain in the Archean craton lithosphere, and the abrupt transition of the fast axis to the plate motion direction parallel across the LAB. The unique two-layer pattern of the lithospheric anisotropy may suggest multiple-stage continent lithosphere formation processes (e.g., *Arndt* 2009). Alternatively, *Thybo* (2006) suggests a ubiquitous low velocity zone at 100 km depth due to lowered solidus of normal mantle rocks by the presence of limited amounts of fluids. This is consistent with the velocity drop around 100km depth in our isotropic  $V_s$  image (upper right panel in Figure 2.50b); however causes of the anisotropy change associated with the low velocity zone are unknown. The anisotropy stratification changes when going into the late Proterozoic Grenville and even younger Appalachian orogens, reflecting somehow different lithosphere formation processes in this area.

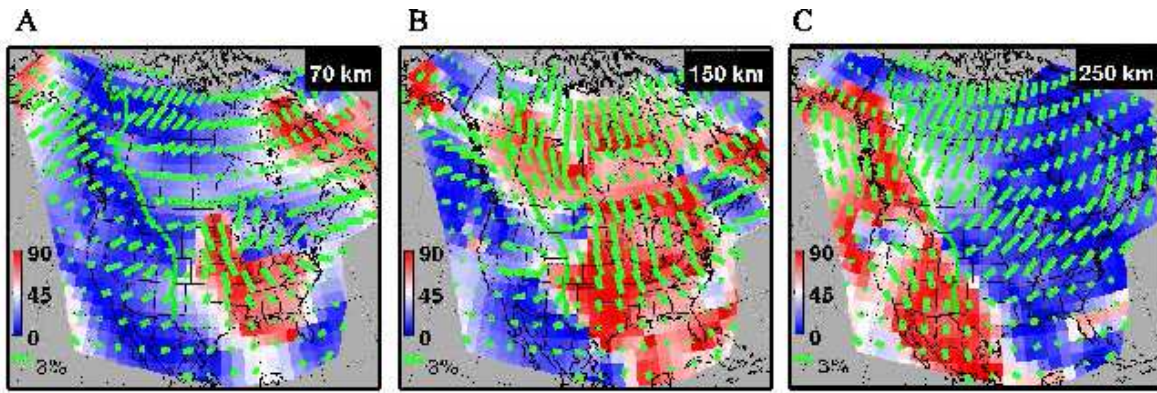


Figure 2.50: Azimuthal anisotropy at selected depths. Sticks on each sub-plot show both the fast velocity symmetry axis direction and the anisotropy strength. The deviation of the inverted fast axis from the absolute plate motion direction (*Gripp and Gordon, 2002*) is drawn in the background such that blue regions show a fast axis parallel to the absolute plate motion direction and red regions perpendicular to it. The Rocky Mountain front (green curve) separates the stable cratons and active west Cordillera.

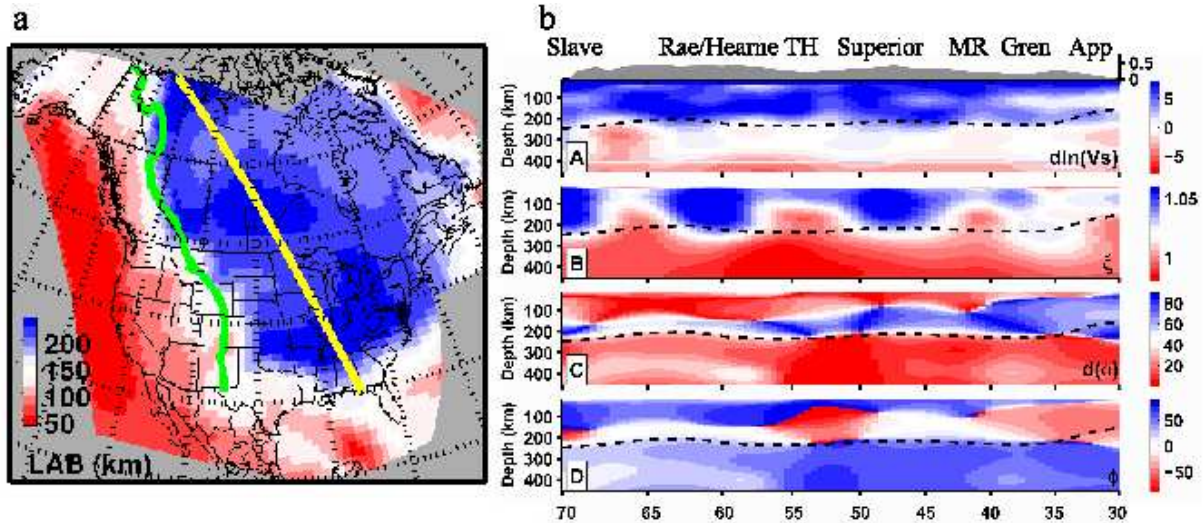


Figure 2.51: LAB estimates. A cratonic cross section through the yellow line is shown in b. From top to bottom, isotropic  $V_s$  variation, radial anisotropy (with respect to isotropy), deviation of the fast axis direction from the plate motion direction, and the absolute value of the inverted fast axis direction. Black dotted line is the LAB measurements shown in a. TH, Trans-Hudson Orogen, MR, Mid-continent Rift, Gren, Grenville Orogen, and App, Appalachian Orogen.

## 26.5 Conclusions

Overall, our tomographic inversion reveals a layered anisotropic cratonic upper mantle. The strong lithospheric layering suggests different stages of the cratonic formation. Detecting anisotropy changes from surface wave tomography makes it possible to obtain large scale and high resolution LAB measurements at once.

## 26.6 Acknowledgements

We thank the IRIS DMC and Canadian National Data Center for providing the waveform data. This project is supported by NSF EAR-0643060.

## 26.7 References

References are listed in the Section 27.5.

## 27 Crustal Stress and Mechanical Anisotropy of the Lithosphere in Western North America

Pascal Audet

### 27.1 Introduction

The flexural rigidity of continental lithosphere can be estimated from isostatic transfer functions (admittance, coherence) relating topography and gravity anomalies using the equation for the flexure of a thin elastic plate. There is growing evidence that such transfer functions are anisotropic, and inferred weak directions correlate with principal directions of crustal stress, indicating either more complicated models of loading, and/or anisotropic rigidities. Here we derive isostatic response functions using the equations for the flexure of a thin elastic plate that incorporate the effects of in-plane loading. We then calculate local 1-D and 2-D wavelet admittance and coherence functions in western North America, and invert for either rigidity anisotropy or in-plane force.

### 27.2 Isostatic response functions

Flexural isostasy describes the condition that loads must be supported at some depth within the lithosphere via elastic plate flexure. The flexural rigidity  $D \propto ET_e^3$ , where  $E$  is Young's modulus and  $T_e$  is the elastic thickness, is a rheological property that governs the resistance of the plate to bending. A popular method of estimating the flexural rigidity is based on calculating transfer functions relating gravity and topography and inverting using isostatic response functions obtained from plate flexure equations (Forsyth, 1985). In the case where an isotropic plate is loaded both horizontally by in-plane force  $n$  and surface load  $q$ , the flexure equation is written

$$D\nabla^4 w(\mathbf{r}) = q(\mathbf{r}) + n(\mathbf{r}), \quad (2.13)$$

where  $w$  is plate deflection at the Moho, and  $\mathbf{r} = (x, y)$ . For an orthotropic plate, equation (2.13) becomes

$$\left[ D_x \frac{\partial^4}{\partial x^4} + 2B \frac{\partial^4}{\partial x^2 \partial y^2} + D_y \frac{\partial^4}{\partial y^4} \right] w(\mathbf{r}) = q(\mathbf{r}) + n(\mathbf{r}),$$

where  $D_x$  and  $D_y$  are rigidities in two perpendicular directions, and  $B$  is the torsional rigidity approximated by  $B \approx \sqrt{D_x D_y}$ . The vertical load at the surface is given by

$$q(\mathbf{r}) = \rho_c g h(\mathbf{r}) - (\rho_m - \rho_c) g w(\mathbf{r}),$$

where  $g$  is gravitational acceleration,  $h$  is the topography,  $\rho_c$  and  $\rho_m$  are crustal and mantle density, respectively, and we will use the shorthand  $\Delta\rho = \rho_m - \rho_c$ . In-plane forces are given by

$$n(\mathbf{r}) = \left[ N_x \frac{\partial^2}{\partial x^2} + N_y \frac{\partial^2}{\partial y^2} + 2N_{xy} \frac{\partial^2}{\partial x \partial y} \right] w(\mathbf{r}),$$

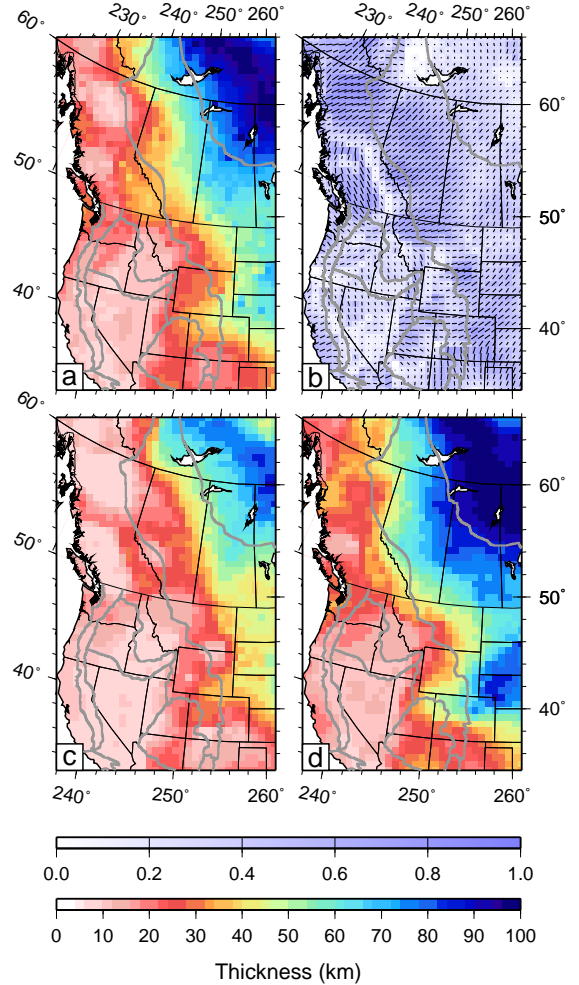


Figure 2.52: Elastic thickness results for western North America. a) Isotropic  $T_e$ ; b) Direction of  $T_{min}$  ( $\beta$ ); c)  $T_{min}$ ; d)  $T_{max}$ . Shading in b) is given by  $(T_{max} - T_{min})/T_{max}$ . Grey lines indicate major tectonic boundaries.

where  $N_x$ ,  $N_y$  represent axial loads (compression is negative) in the  $x$  and  $y$  directions, respectively, and  $N_{xy}$  denotes shear loading. Solving these equations in the Fourier domain yields linear isostatic response functions relating Moho deflection to surface topography that take the form

$$\Theta(\mathbf{k}) = \frac{\rho_c}{\Delta\rho} \left[ 1 + \frac{\psi(D_x, D_y, \mathbf{k})}{\Delta\rho g} + \frac{\zeta(N_x, N_y, N_{xy}, \mathbf{k})}{\Delta\rho g} \right]^{-1},$$

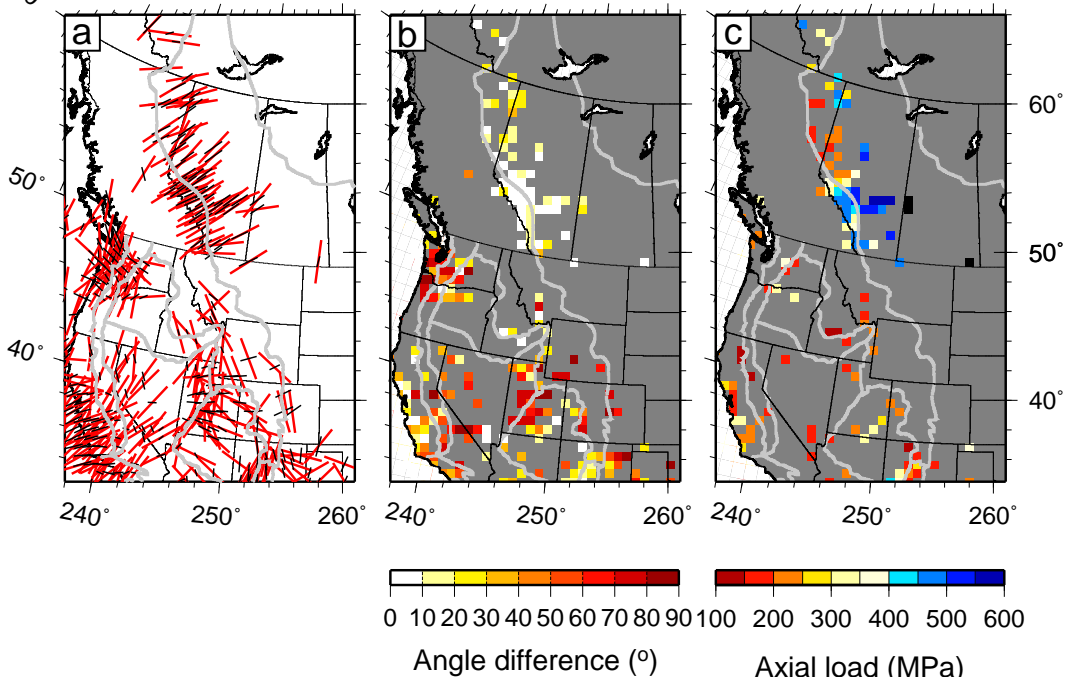


Figure 2.53: Comparison between  $\beta$  and orientation of maximum horizontal compressive stress. a) shows crustal stress indicators (red bars) and co-located weak directions (black bars); b) is the angular difference between both indicators; and c) is the estimated in-plane load necessary to fit the observed 2-D admittance and coherence.

where  $\mathbf{k} = (k_x, k_y)$ , and  $|\mathbf{k}| = k$ . The functions  $\psi$  and  $\zeta$  correspond to

$$\psi = \begin{cases} Dk^4 & \text{isotropic plate} \\ (\sqrt{D_x}k_x^2 + \sqrt{D_y}k_y^2)^2 & \text{orthotropic plate.} \end{cases}$$

$$\zeta = \begin{cases} 0 & \text{no in-plane force,} \\ N_x k_x^2 + N_y k_y^2 + 2N_{xy} k_x k_y & \text{with in-plane force.} \end{cases}$$

For subsurface loading the isostatic function is

$$\Phi(\mathbf{k}) = \frac{\rho_c}{\Delta\rho} \left[ 1 + \frac{\psi(D_x, D_y, \mathbf{k})}{\rho_c g} + \frac{\zeta(N_x, N_y, N_{xy}, \mathbf{k})}{\rho_c g} \right].$$

Isostatic response functions are combined to form theoretical admittance ( $Q$ ) and coherence ( $\gamma^2$ ) functions between Bouguer gravity and topography

$$Q(\mathbf{k}) = 2\pi\Delta\rho G e^{-|\mathbf{k}|z_c} \frac{(\Theta + \Phi f^2 \Theta^2)}{(1 + f^2 \Theta^2)}, \quad (2.14)$$

$$\gamma^2(\mathbf{k}) = \frac{(1 + \Phi \Theta f^2)^2}{(1 + f^2 \Theta^2)(1 + f^2 \Phi^2)}, \quad (2.15)$$

where  $f$  is the ratio between surface and subsurface loads,  $G$  is the gravitational constant, and  $z_c$  is the depth of compensation, taken at the Moho.

### 27.3 Results for western North America

We calculated the wavelet admittance and coherence in western North America following the method of *Audet and Mareschal* (2007) and inverted the corresponding isostatic quantities to yield estimates of  $D$  for the

isotropic case, and  $D_{min}, D_{max}$  and  $\beta$  (i.e. the direction of  $D_{min}$ ) for the orthotropic case. We give results in terms of elastic thickness using the relation  $D = \frac{ET^3}{12(1-\nu^2)}$ , where  $T$  can be either  $T_e$ , or  $T_{min}, T_{max}$  (Figure 2.52). Low values ( $T_e < 30$  km) are found across most of western North America, increasing toward the continental interior. In the northeastern craton,  $T_e$  values can reach 100 km. Maps of  $T_{min}$  and  $T_{max}$  follow the same general patterns as the isotropic  $T_e$ , whereas  $\beta$  is oriented dominantly SW-NE, except in the highly deforming regions of western United States, where it is highly variable in both magnitude and direction.

We further compared the weak direction with orientations of maximum horizontal compressive stress from the World Stress Map project <http://dc-app3-14.gfz-potsdam.de/>. We re-sampled stress indicators onto the  $T_e$  grid and calculated the angular difference between both directions (Figure 2.53a,b). There is good agreement in the Canadian Cordillera and near the coast of California, both regions where stress regime is compressional. An exception is the arc and forearc in the Pacific Northwest, where compressive stress directions are parallel to the coast whereas weak directions are perpendicular, perhaps reflecting more complex loading near the subduction zone. Angle difference is large ( $> 45^\circ$ ) in extensional regimes, such as Basin and Range and western Colorado Plateau.

These correlations allow us to use isostatic functions for the isotropic plate with axial loading to fit the 2-

D coherence and admittance in order to estimate load magnitudes where angular difference is within  $30^\circ$ . We use isotropic  $T_e$  and  $\beta$  obtained previously, and estimate total axial load (Figure 2.53c). Preliminary results indicate loads on the order of 100-600 MPa, which are up to three times larger than estimates from dynamical models of deformation using a uniformly thick (100 km) elastic plate (Humphreys and Coblenz, 2007). Such large discrepancy also suggests that, in addition to lithospheric stress, significant rigidity anisotropy must be involved in producing anisotropy in the observed transfer functions. Lastly we note that shear loads were not modeled at this point, which will be the focus of future efforts.

## 27.4 Acknowledgements

This work was funded by the Miller Institute for Basic Research in Science (UC Berkeley).

## 27.5 References

Audet, P., and J.C. Mareschal, Wavelet analysis of the coherence between Bouguer gravity and topography: Applications to the elastic thickness anisotropy in the Canadian Shield, *Geophys. J. Int.*, 168, 287-298, 2007.

Forsyth, D.W., Subsurface loading and estimates of the flexural rigidity of continental lithosphere, *J. Geophys. Res.*, 90, 12, 623-12, 632, 1985.

Humphreys, E.D., and D. Coblenz, North American dynamics and western U.S. tectonics, *Rev. Geophys.*, 45, RG3001, 2007.

# 28 Berkeley 3-D Isotropic and Anisotropic S-velocity Model of North American Upper Mantle, Updated to June 2008

Huaiyu Yuan and Barbara Romanowicz

## 28.1 Introduction

We present here the isotropic and radial anisotropy part of our 3-D North American upper mantle shear wave velocity model. This new model is constructed starting from a new global 1D reference Earth model, based on a combination of seismic and mineral physics data (Cammarano and Romanowicz, 2007), which is smooth at 220 km, and a crustal correction approach that takes into account the non-linearities involved (Lekic and Romanowicz, submitted).

## 28.2 North American Isotropic Vs and Radial Anisotropy model

The pronounced findings of the Vs model include: 1) high velocity cratonic roots extend to 200-250 km depth range (A-E); 2) at shallow depth (< 200km; A-D) low velocities flank the cratonic region from the west and the south, with a sharp transition along the Rocky Mountain Front; 3) a high velocity feature exists from 450 to 600 km (H) in transition zone beneath the western US; and 4) small scale (100km) velocities correlate with surface geological features, e.g., the Rio Grande rift, Colorado Plateau, and the Eastern Snake River Plain in the western US.

The radial anisotropy model (I-L) is plotted with respect to an isotropic reference. The dominant feature above 200 km is the faster  $V_{sh}$  than  $V_{sv}$  or  $X_i > 1$  everywhere. Abnormal  $X_i$  is spotted beneath the northeastern Pacific rise, the Rio Grande Rift, the Nevada Basin and Range, and the central Trans-Hudson Orogen, suggesting  $V_{sv}$  is faster in those regions. At >300km, most of the radial anisotropy has disappeared, except beneath the western US where  $X_i < 1$ , indicating a probable deep origin of the anomaly. A negative  $X_i$  anomaly is observed in the vicinity of the East Pacific Rise at all depths (I to L), suggesting a probable deep (> 300km) origin of this anomaly.

## 28.3 References

Arndt, N. T., et al. (2009), Origin of Archean subcontinental lithospheric mantle: Some petrological constraints, *Lithos*, 109(1-2), 61-71.

Bostock, M. G. (1998), Mantle stratigraphy and evolution of the Slave Province, *J. Geophys. Res.*, 103(B9), 21,183-121,200.

Cammarano, F. and B. Romanowicz (2007), High-Pressure Geoscience Special Feature: Insights into the nature of the transition zone from physically constrained in-

version of long-period seismic data, *PNAS*, 104, 9139-9144, doi:10.1073/pnas.0608075104

Chen, C.-W., et al. (2007), New constraints on the upper mantle structure of the Slave craton from Rayleigh wave inversion, *Geophys. Res. Lett.*, 34(L10301), doi:10.1029/2007GL029535.

Darbyshire, F. A., et al. (2000), Central structure of central and northern Iceland from analysis of teleseismic receiver functions, *Geophys. J. Int.*, 143(1), 163-184.

Darbyshire, F. A., et al. (2007), New insights into the lithosphere beneath the Superior Province from Rayleigh wave dispersion and receiver function analysis, *Geophys. J. Int.*, 169(3), 1043-1068.

Deschamps, F., et al. (2008), Stratified seismic anisotropy reveals past and present deformation beneath the East-central United States, *Earth Planet. Sci. Lett.*, 274(3-4), 489-498.

Eaton, D. W., and A. Frederiksen (2007), Seismic evidence for convection-driven motion of the North American plate, *Nature*, 446(7134), 428-431.

Eaton, D. W., et al. (2009), The elusive lithosphere-aesthenosphere boundary (LAB) beneath cratons, *Lithos*, 109(1-2), 1-22.

Fouch, M. J., et al. (2000), Shear wave splitting, continental keels, and patterns of mantle flow, *J. Geophys. Res.*, 105(3), 6255-6275.

Griffin, W. L., et al. (2004), Lithosphere mapping beneath the North American plate, *Lithos*, 77(1-4), 923-944.

Gok, R., et al. (2003), Shear wave splitting and mantle flow beneath LA RISTRA, *Geophys. Res. Lett.*, 30, 1614, doi:10.1029/2002GL016616.

Gorman, A. R., et al. (2002), Deep Probe: Imaging the roots of western North America, *Can. J. Earth Sci.*, 39(3), 375-398.

Gripp, A. E., and R. G. Gordon (2002), Young tracks of hotspots and current plate velocities, *Geophys. J. Int.*, 150(2), 321.

Marone, F., et al. (2007), 3D radial anisotropic structure of the North American upper mantle from inversion of surface waveform data, *Geophys. J. Int.*, doi: 10.1111/j.1365-246X.2007.03456.

Marone, F., and B. Romanowicz (2007), The depth distribution of azimuthal anisotropy in the continental upper mantle, *Nature*, 447(7141), 198-201.

Mckenzie, D., and K. Priestley (2008), The influence of lithospheric thickness variations on continental evolution, *Lithos*, 102(1-2), 1-11.

Mercier, J. P., et al. (2008), The teleseismic signature of fossil subduction: Northwestern Canada, *J. Geophys. Res.*, 113.

Park, J., and V. Levin (2002), Seismic anisotropy: Tracing plate dynamics in the mantle, *Science*, v296, 485-489.

Plomerova, J., et al (2002), Mapping the lithosphere-aesthenosphere boundary through changes in surface-wave anisotropy, *Tectonophysics*, 358(1-4), 175-185.

Savage, M. K., and A. F. Sheehan (2000), Seismic anisotropy and mantle flow from the Great Basin to the Great Plains, western United States, *J. Geophys. Res.*, 105(6), 13,715-713,734.

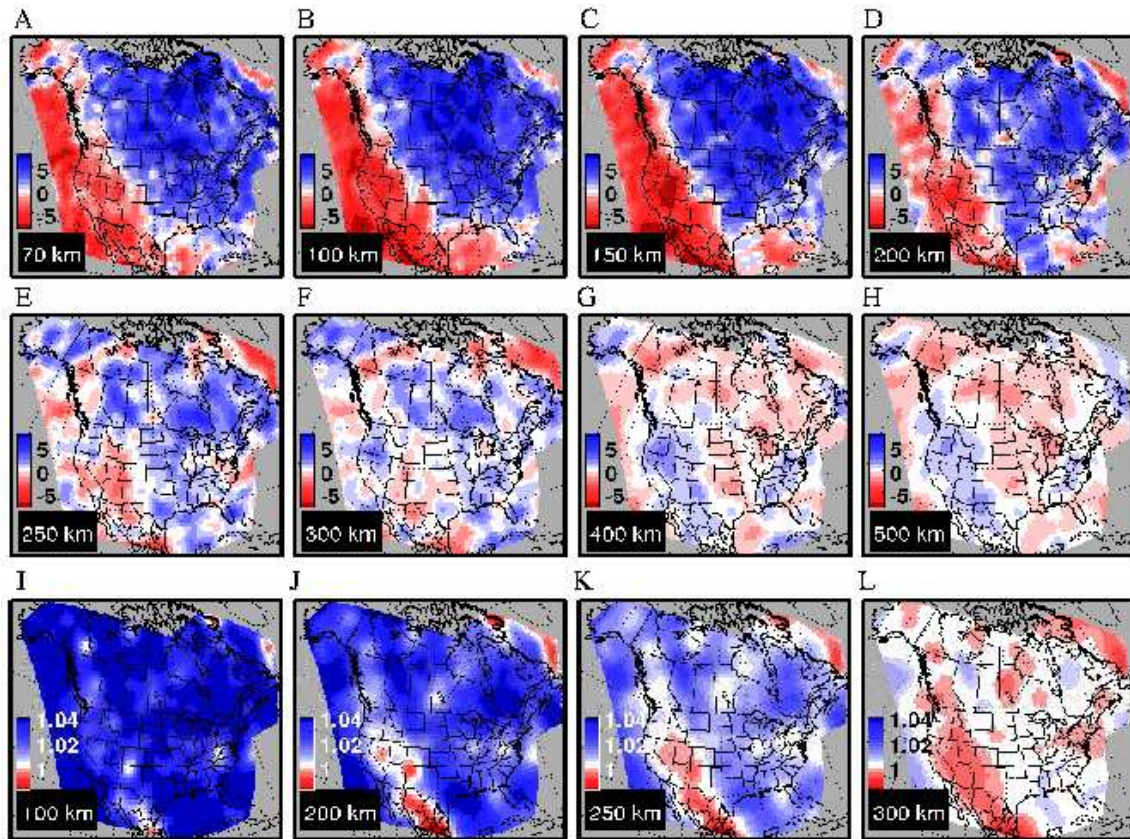


Figure 2.54: Figure 3-D isotropic  $V_s$  (A-H) and radial anisotropy  $\xi$  (I-L) model of North America upper mantle.

Schutt, D., et al. (1998), Anisotropy of the Yellowstone Hot Spot wake, eastern Snake River plain, Idaho, in *Geodynamics of lithosphere and Earth's mantle; seismic anisotropy as a record of the past and present dynamic processes.*, edited by J. Plomerova, et al., pp. 443-462, Birkhaeuser Verlag, Basel, Switzerland.

Silver, P. G., and W. W. Chan (1988), Implications for continental structure and evolution from seismic anisotropy, *Nature*, 335, 34-39.

Snyder, D. B. (2008), Stacked uppermost mantle layers within the Slave craton of NW Canada as defined by anisotropic seismic discontinuities, *Tectonics*, 27.

Thybo, H. (2006), The heterogeneous upper mantle low velocity zone, *Tectonophysics*, 416(1-4), 53-79.

van der Lee, S. (2002), High-resolution estimates of lithospheric thickness from Missouri to Massachusetts, USA, *Earth Planet. Sci. Lett.*, 203(1), 15-23.

Vinnik, L., et al. (1984), Anisotropy of the lithosphere according to the observations of SKS and SKKS waves, *Dokl. Akad. Nauk SSSR*, 278, 1335.

Waite, G., et al. (2005), Models of lithosphere and asthenosphere anisotropic structure of the Yellowstone hotspot from shear wave splitting, *J. Geophys. Res.*, 110(B11304), doi:10.1029/2004JB003501.

Walker, K. T., et al. (2004), Shear-wave splitting beneath the Snake River Plain suggests a mantle upwelling beneath eastern Nevada, USA, *Earth Planet. Sci. Lett.*, 222(2), 529-542.

West, J. D., et al. (2009), Vertical mantle flow associ-

ated with a lithospheric drip beneath the Great Basin, *Nature Geosci.*, 2(6), 439-444.

Zandt, G., and E. Humphreys (2008), Toroidal mantle flow through the western US slab window, *Geology*, 36(4), 295-298.

# 29 Weak Mantle in NW India Probed by Postseismic GPS Measurements Following the 2001 Bhuj Earthquake

D. V. Chandrasekhar and Roland Bürgmann

## 29.1 Introduction

Transient crustal deformations induced by large earthquakes are used to infer the rheology of the continental crust and the upper mantle. Generally, these studies find that the elastically strong part of the continental crust is 15-30 km thick, that the lower crust has a higher viscosity than the uppermost mantle, and that the mantle asthenosphere has a low viscosity ( $< 5 \times 10^{19}$  Pa s) (Bürgmann and Dresden, 2008). However, all of the postseismic deformation transients considered to date are from active plate boundary zones with strongly thinned lithosphere ( $< 60$  km), and relatively hot and hydrated mantle asthenosphere. In contrast, studies of postglacial rebound in stable shield areas (Fennoscandia, North America) indicate an elastic plate thickness of  $\sim 100$  km overlying a high viscosity substratum ( $> 10^{20}$  Pa s) (Milne et al., 2001). The Bhuj earthquake of January 26, 2001 in Kachchh, India is the largest event ( $M_w$  7.6) in the last 50 years to strike the Indian shield in its recorded history, lies  $> 300$  km from the nearest active Plate boundary and provides a unique opportunity to probe the rheology of the deep lithosphere in an intraplate region. We use GPS displacements to models of postseismic deformation caused by the earthquake to assess the viscous strength of the lower crust and upper mantle.

## 29.2 Postseismic GPS Observations

Time series of GPS-measured surface displacements document transient deformation during 6 years following the Bhuj earthquake. We update and expand on initial results from this network published by Reddy and Sunil, 2007 who provide further detail on the GPS observations and analysis. Sites are labeled in the maps of Figure 2.55. Time series of positions of each site in the well-determined ITRF 2000 are obtained from the combined quasi-observations and provide relative position time series from February 2001 to January 2007 of each site with respect to a station at Ahmedabad (AHMD). The time series show the decaying nature of the postseismic motions and are well represented by a log function  $a' + b' \log(t)$ , where  $t$  is the time (yr) and  $a'$  and  $b'$  are constants to fit the displacement time series. We used the logarithmic curve-fit values to estimate total displacements at each site with respect to AHMD for 6 months, 1 year, 2 years and 6 years after the Bhuj earthquake.

## Viscoelastic models and results

The broadly distributed nature of the postseismic deformation field suggests a deeply buried source of transient deformation and thus we primarily consider models of viscous relaxation in our investigation. To calculate the viscoelastic postseismic deformation we adopt the earthquake source parameterization of Antolik and Dreger (2003), which is also consistent with geodetic constraints on the rupture (Chandrasekhar et al., 2004; Schmidt and Bürgmann, 2006). The location of the rupture is shown in the maps in Figure 2.55. Strike, dip, rake, and seismic moment are  $82^\circ$ ,  $51^\circ$ ,  $77^\circ$ , and  $1.6 \cdot 10^{20}$  Nm, respectively. The model rupture is 40 km long and 10–32 km deep. The slip distribution of Antolik and Dreger (2003) is simplified with a larger amount of slip (8.2 m) confined to the center ( $25 \times 15 \text{ km}^2$ ) and less slip (1.7 m) on the surrounding part. We calculate postseismic deformation using VISCO1D (Pollitz, 1997), for a simple layered Earth model consisting of an elastic plate overlying a viscoelastic substrate. The free model parameters are the thickness  $H_p$  of the elastic plate and the viscosity  $\eta_a$  of the viscoelastic material below. The minimum root mean-square error (RMS) between the observed and predicted motions is found at  $H_p = \sim 34$  km for all time periods considered (Figure 2.55), which is close to the local crustal thickness inferred from seismic data (Sarkar et al., 2001). Optimal effective mantle viscosities increase with time from  $\eta_a = 3 \times 10^{18}$  Pa s for the first 6 month period to  $2 \times 10^{19}$  Pa s for the full 6 years displacements, which is consistent with a stress dependent rheology of the upper mantle (Freed and Bürgmann, 2004). An increase of the coseismic moment of the rupture by  $1 \frac{1}{2}$  times raises the effective viscosity estimates by 30-50% for the different time intervals considered, given that some teleseismic moment estimates are as high as  $3.6 \times 10^{20}$  Nm (Wesnousky et al., 2001). We also estimate the viscosity of a 15-km-thick lower crustal layer separate from the upper mantle. The misfit suggests that the observed data do not require relaxation of the lower crust and indicate a lower bound of  $10^{20}$  Pa s on its effective viscosity. We find very small contribution of mainshock induced pore-pressure changes to the near-field horizontal deformation and subsidence of as much as 65 mm localized over the buried coseismic rupture. None of the afterslip models demonstrate the observed pattern or magnitude of motions of the GPS network, suggesting that viscous relaxation and afterslip are distinctly different.

## Discussion and Conclusions

The estimated first-order viscoelastic structure deduced consists of an elastic plate whose thickness is  $\sim 34$  km and an underlying viscoelastic asthenosphere whose effective viscosity is  $2 \times 10^{19}$  Pa s, during the 6-year observation period. Estimated effective viscosities increase with time suggesting power-law rheology due to dislocation creep. Modest, shallow afterslip may have contributed to the near-field GPS. The inferred viscosity of the upper mantle below the Bhuj region is closer to that found for thermally weakened and hydrated mantle below western North America and other back-arc or former back-arc regions (viscosity estimates generally range from  $0.1 - 1 \times 10^{19}$  Pa s below 40-60 km depth) than that found from ice-unloading studies over the North American and Fennoscandian cratons (ranging from  $0.5 - 1 \times 10^{21}$  Pa s below a  $>100$  km thick elastic lithosphere). The low mantle viscosity deduced may be the result of thermal weakening due to the late Cretaceous Reunion (Deccan) plume, which is indicated by a 200-km-wide seismic wave speed anomaly in the uppermost mantle beneath the region (Kennett and Widiyantoro, 1999). In contrast, the apparent strength of the lower crust is consistent with a mafic and dry composition indicated by unusually high seismic velocities at lower crustal depths (Mandal and Pujol, 2006), which may have developed in association with intrusive activity during an early Jurassic period of rifting (Chandrasekhar and Mishra, 2002). The mantle lithosphere in the Gujarat region in NW India appears to be weaker than fully intact continental shields. Relaxation of remote stresses in such a weak zone can concentrate stress in the overlying crust and lead to the observed intraplate seismicity in this region.

## 29.3 Acknowledgements

This study was accomplished while DC was visiting researcher at the University of California, Berkeley, USA, funded by the DST, New Delhi through a BOYSCAST fellowship. RB acknowledges support by NSF grant EAR-0738298.

## 29.4 References

Antolik, M., Dreger, D., Rupture process of the 26 January 2001  $M_w$  7.6 Bhuj, India, earthquake from teleseismic broadband data, *Bull. Seismol. Soc. Am.*, *93*, 1235-1248, 2003.

Bürgmann, R., Dresen, G., Rheology of the lower crust and upper mantle: Evidence from rock mechanics, geodesy and field observations, *Ann. Rev. Earth Plan. Sci.*, *36*, 531-567, 2008.

Chandrasekhar, D.V., Mishra, D. C., Some geodynamic aspects of Kutch basin and seismicity: An insight from gravity studies, *Current Science*, *83*, 492-498, 2002.

Chandrasekhar, D.V., Mishra, D. C., Singh, B., Vijayakumar, V., Bürgmann, R., Source parameters of the Bhuj earthquake, India of January 26, 2001 from height and gravity changes, *Geophys. Res. Lett.*, *31*, doi:10.1029/2004GL020768, 2004.

Freed, A. M., Bürgmann, R., Evidence of power-law flow in the Mojave desert mantle, *Nature*, *430*, 548-551, 2004.

Kennett, B. L. N., Widiyantoro, S., A low seismic wavespeed anomaly beneath northwestern India: A seismic signature of the Deccan Plume?, *Earth and Planetary Science Letters*, *165*, 145-155, 1999.

Mandal, P., Pujol, J., Seismic imaging of the Aftershock zone of the 2001  $M_w$  7.7 Bhuj earthquake, India, *Geophys. Res. Lett.*, *33*, 1-4, 2006.

Milne, G. A., Davis, J. L., Mitrovica, J. X., Scherneck, H. -G., Johansson, J. M., Vermeer, M., Koivula, H., Space-geodetic constraints on glacial isostatic adjustment in Fennoscandia, *Science*, *291*, 2381-2385, 2001.

Pollitz, F. F., Gravitational viscoelastic postseismic relaxation on a layered spherical Earth, *J. Geophys. Res.*, *102*, 17921-17941, 1997.

Reddy, C. D., Sunil, P. S., Post-seismic crustal deformation and strain rate in Bhuj region, western India, after the 2001 January 26 earthquake, *Geophysical Journal International*, *172*, 593-606, doi: 10.1111/j.1365-1246X.2007.03641.x., 2008.

Sarkar, D., Reddy, P. R., Sain, K., Mooney, W. D., Catchings, R. D., 2001. Kutch seismicity and crustal structure, *Geol. Soc. Am. Programs*, *262*, 2001.

Schmidt, D. A., Bürgmann, R., InSAR constraints on the source parameters of the 2001 Bhuj earthquake, *Geophys. Res. Lett.*, *33*, doi:10.1029/2005GL025109, 2006.

Wesnousky, S. G., Seeber, L., Rockwell, K. T., Thakur, V., Briggs, R., Kumar, S., Ragona, D., Eight days in Bhuj: Field report bearing on surface rupture and genesis of the January 26, 2001 Republic Day earthquake of India, *Seismol. Res. Lett.*, *72*, 514-524, 2001.

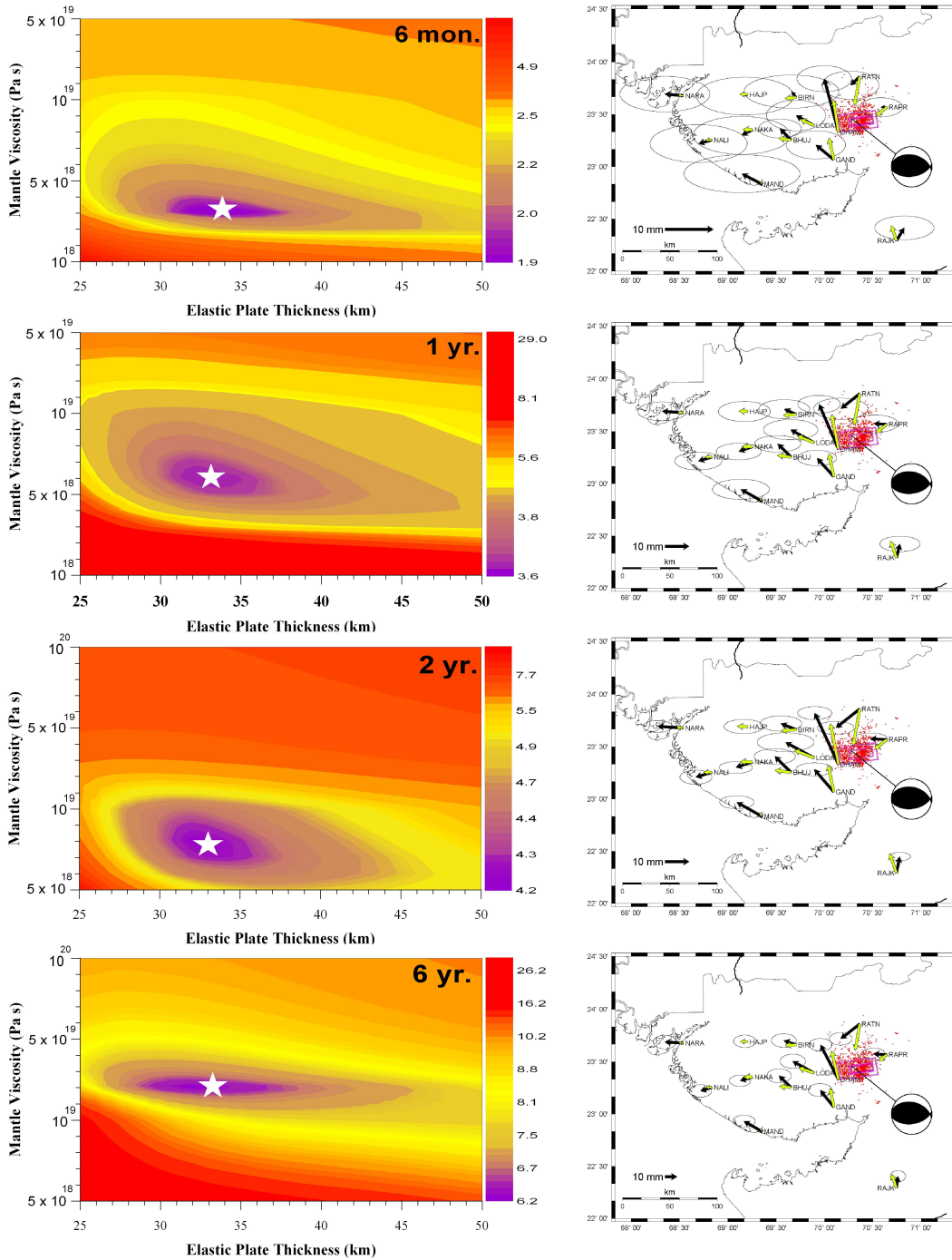


Figure 2.55: Model results. The RMS misfit between the calculated and observed horizontal displacements as a function of elastic plate thickness ( $H_p$ ) and asthenosphere viscosity ( $\eta_a$ ) for the two layer Earth model as a function of time since the earthquake. The star marks the best-fit displacement model with the least RMS error value, whose best-fit horizontal displacements are plotted adjacent to the misfit plot. Vectors in black denote the observed displacement tipped with 95% confidence ellipses and yellow arrows are the calculated model displacements. (See color version of this figure at the front of the research chapter)

## 30 Comprehensive Test Ban Monitoring: Contributions from Regional Moment Tensors to Determine Source Type and Depth

Margaret Hellweg, Douglas Dreger and Barbara Romanowicz

### 30.1 Introduction

Regional distance moment tensor (MT) analysis can be used, even for relatively small magnitude events ( $M > 3.4$ ), to discriminate explosions from naturally occurring earthquakes. For earthquakes, MT analysis can also provide insight into an event's size, depth and type of faulting. Mechanism information is also important for applications like assessing earthquake effects and tsunami warning. In this project, we apply the UC Berkeley full moment tensor code (*Minson and Dreger, 2008*) to a suite of events recorded regionally at broadband seismic stations operated by the International Monitoring System (IMS).

### 30.2 Events and Green's Function

For regional moment tensor analysis using the full moment tensor code, it is important to have data from three or more stations with good signals in the period band between 10 s and 100 s or more, depending on the size of the event. Typically, for events with  $M < 4$ , we use the period band 10 s – 50 s, for  $4 < M < 5$  the band 20 s – 50 s, and for  $5 < M < 7$  the band 20 s – 100 s.

Reviewing the distribution of primary IMS stations certified by April 2009, we chose the region from 30°E – 70°E and from 20°N – 45°N, for its seismicity and IMS

station availability. From the many events in the Reviewed Event Bulletin (REB), we selected two sequences from Western Iran (Figure 2.56) for two reasons: (a) Their epicenters were only about 20 km apart, so propagation paths to regional stations would be similar, and (b) the mechanisms of the largest events, as given in the GCMT catalog (Figure 2.56), were different. Magnitudes as given in the REB and in the PDE catalog (NEIC) are shown in Figure 2.56 for the mainshocks and other selected events. Of the approximately 20 events in each sequence, five were chosen from the REB, spanning a range of depths and magnitudes (Figure 2.56).

Green's functions were calculated for two 1D velocity models. The first is a generic 1D global model, *iasp91*. The second 1D velocity model is adapted from the *Pasyanos, et al. (2004)* 3D model for the region. For the chosen events, seismic moment magnitude ( $M_w$ ), depth and source mechanism will be estimated using both types of Green's functions.

### 30.3 Ongoing Work and Perspectives

We received waveform data for the events from the IMS shortly before the ISS09 meeting. Unfortunately, no waveforms were available for stations at distances smaller than 2000 km for any events in 2002. Many of the waveforms for the 2006 events have gaps, and poor signal-to-noise ratios are particularly a problem for the small events. Based on the review of the data, we hope to be able to determine moment tensors for several 2006 events using data from the IMS. We will review recent seismicity in the region to determine whether other events have occurred which could contribute to this study.

### 30.4 Acknowledgements

The work performed for this project was supported by LLNL CTBT Contract B583480. Travel of MH to the ISS09 in Vienna, Austria, to present the interim results was funded by NSF Grant EAR-0926120.

### 30.5 References

Minson, S. and D. Dreger, Stable Inversions for Complete Moment Tensors, *Geophys. Journ. Int.*, 174, 585-592, doi:10.1111/j.1365-246X.2008.03797, 2008.

Pasyanos, M.E., W.R. Walter, M.P. Flanagan, P. Goldstein and J. Bhattacharyya, Building and Testing an a priori Geophysical Model for Western Eurasia and North Africa, *Pure appl. geophys.*, 161, 235281, 2004.

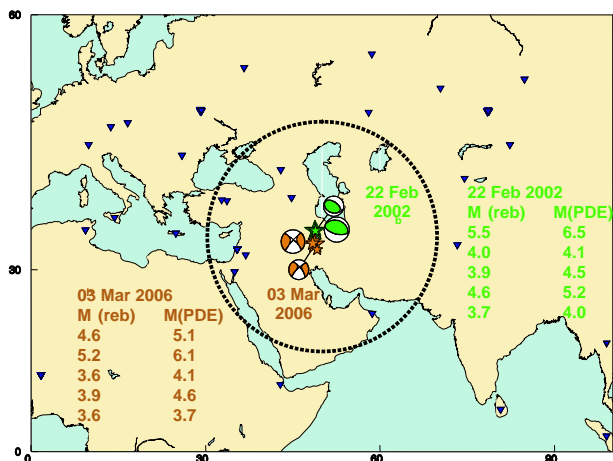


Figure 2.56: Map showing the events chosen for analysis (stars). Certified IMS stations (as of April 2009) are shown as inverted triangles. The mechanisms shown for the largest events are from the GCMT catalog. The tables give the magnitudes of the selected events.

## Chapter 3

# BSL Operations

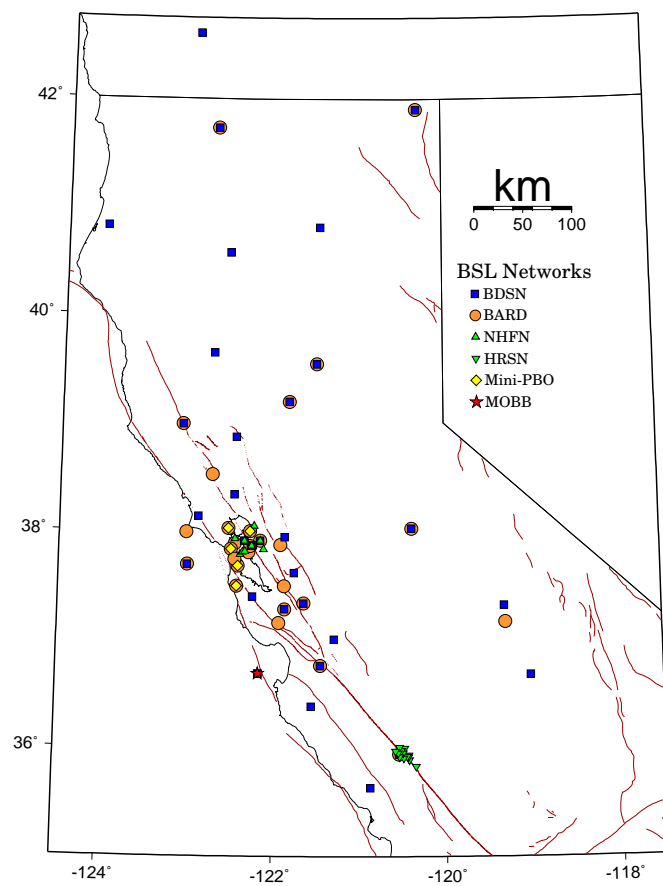


Figure 3.1: Map illustrating the distribution of BSL networks in Northern and Central California.

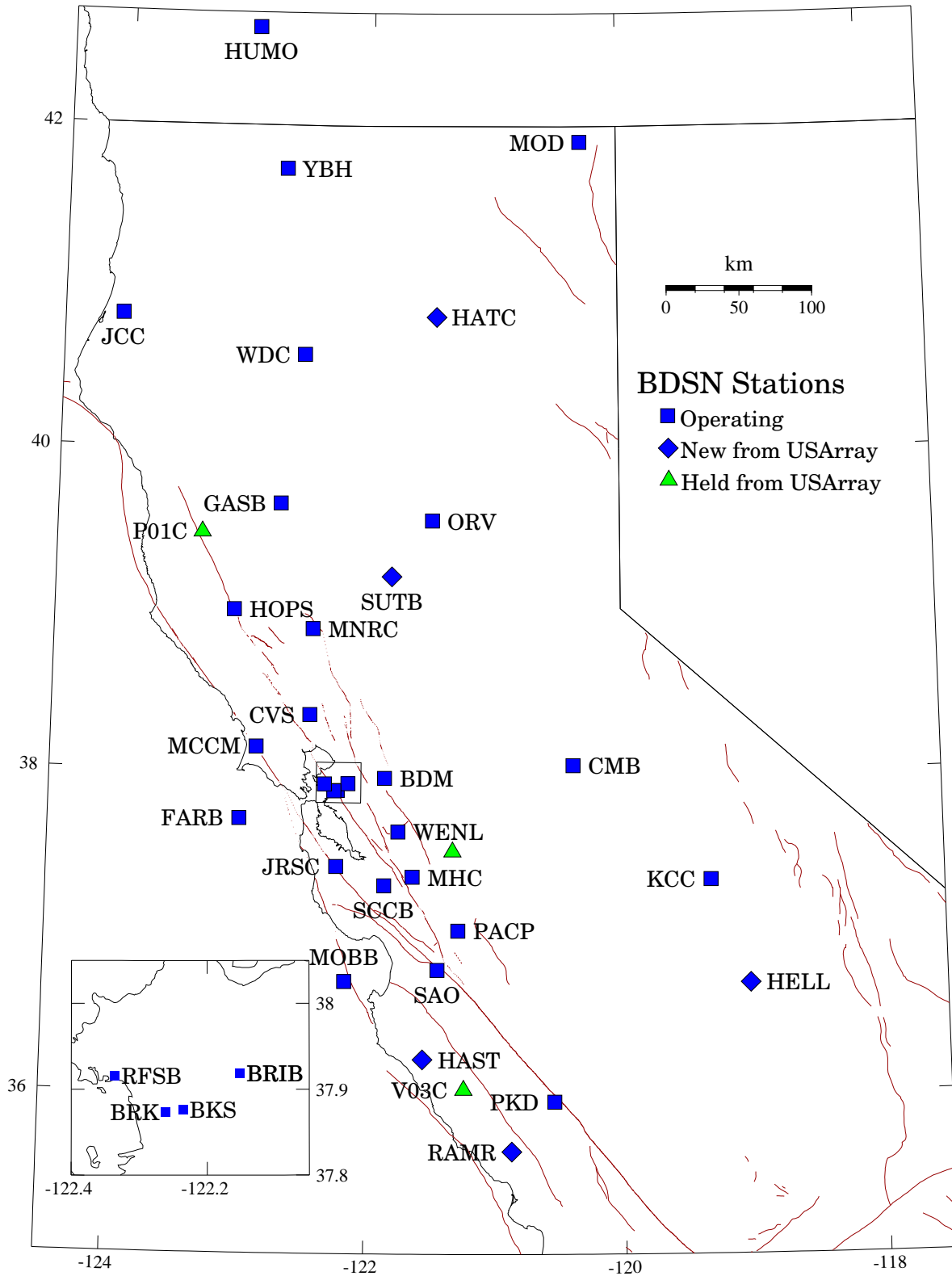


Figure 3.2: Map illustrating the distribution of BDSN stations in Northern and Central California.

# 1 Berkeley Digital Seismic Network

## 1.1 Introduction

The Berkeley Digital Seismic Network (BDSN) is a regional network of very broadband and strong motion seismic stations spanning Northern California and linked to UC Berkeley through continuous telemetry (Figure 3.2 and Table 3.1). The network is designed to monitor regional seismic activity at the magnitude 3+ level as well as to provide high quality data for research in regional and global broadband seismology.

Since 1991, the BDSN has grown from the original 3 broadband stations installed in 1986-87 (BKS, SAO, MHC) to 32 stations, including an autonomous ocean-bottom seismometer in Monterey Bay (MOBB). We take particular pride in high quality installations, which often involve lengthy searches for appropriate sites away from sources of low-frequency noise as well as continuous improvements in installation procedures and careful monitoring of noise conditions and problems. Maintenance and repair were an important focus of this year's efforts. Engineering and research efforts were also devoted to several projects to develop and test new instrumentation (see Chapter 3, Section 7). The project involving new electronics for the STS-1 seismometers, the E300, was completed. One is currently at KCC. We also made progress in testing a new, low-cost sensor for pressure and temperature to be installed at seismic and GPS sites. Finally, the BSL is part of a team to develop and test a new version of the STS-1 seismometer.

The expansion of our network to increase the density of state-of-the-art strong motion/broadband seismic stations and improve the joint earthquake notification system in this seismically hazardous region, one of BSL's long term goals, must be coordinated with other institutions and is contingent on the availability of funding.

Equally important to network growth, data quality and the integrity of the established network must be preserved. The first generation of broadband seismometers installed by the BSL have been operating for almost 25 years. At the same time, the first generation of broadband data loggers are entering their 17th year of service. This requires continued vigilance and the commitment of time and resources to repairs and upgrades.

## 1.2 BDSN Overview

Twenty-eight of the BDSN sites are equipped with three component broadband seismometers and strong-motion accelerometers, and a 24-bit digital data acquisition system or data logger. Two additional sites (RFSB and SCCB) consist of a strong-motion accelerometer and a 24-bit digital data logger. The ocean-bottom station MOBB is equipped with a three component broadband

seismometer. Data from all BDSN stations are transmitted to UC Berkeley using continuous telemetry. Continuous telemetry from MOBB was implemented during the past year. In order to avoid data loss during utility disruptions, each site has a three-day supply of battery power; many are accessible via a dialup phone line. The combination of high-dynamic range sensors and digital data loggers ensures that the BDSN has the capability to record the full range of earthquake motion required for source and structure studies. Table 3.2 lists the instrumentation at each site.

Most BDSN stations have Streckeisen STS-1 or STS-2 three-component broadband sensors (*Wielandt and Streckeisen, 1982; Wielandt and Steim, 1986*). A Guralp CMG-3T broadband sensor contributed by LLNL is deployed in a post-hole installation at BRIB. A Guralp CMG-1T is deployed at MOBB. The strong-motion instruments are Kinematics FBA-23, FBA-ES-T or Metrozet accelerometers with  $\pm 2$  g dynamic range. The recording systems at all sites are either Q330, Q680, Q730, or Q4120 Quanterra data loggers, with 3, 6, 8, or 9 channel systems. The Quanterra data loggers employ FIR filters to extract data streams at a variety of sampling rates. In general, the BDSN stations record continuous data at .01, 0.1, 1.0, 20.0 or 40.0, and 80 or 100 samples per second. However, at some sites, data at the highest sampling rate are sent in triggered mode using the Murdock, Hutt, and Halbert event detection algorithm (*Murdock and Hutt, 1983*) (Table 3.3). In addition to the 6 channels of seismic data, signals from thermometers and barometers are recorded at many locations (Figure 3.3).

As the broadband network was upgraded during the 1990s, a grant from the CalREN Foundation (California Research and Education Network) in 1994 enabled the BSL to convert data telemetry from analog leased lines to digital frame-relay. The frame-relay network uses digital phone circuits which support 56 Kbit/s to 1.5 Mbit/s throughput. Since frame-relay is a packet-switched network, a site may use a single physical circuit to communicate with multiple remote sites through the use of "permanent virtual circuits." Frame Relay Access Devices (FRADs), which replace modems in a frame-relay network, can simultaneously support a variety of interfaces such as RS-232 async ports, synchronous V.35 ports, and ethernet connections. In practical terms, frame relay communication provides faster data telemetry between the remote sites and the BSL, remote console control of the data loggers, services such as FTP and telnet to the data loggers, data transmission to multiple sites, and the capability of transmitting data from several instruments

Code	Net	Latitude	Longitude	Elev (m)	Over (m)	Date	Location
BDM	BK	37.9540	-121.8655	219.8	34.7	1998/11 -	Black Diamond Mines, Antioch
BKS	BK	37.8762	-122.2356	243.9	25.6	1988/01 -	Byerly Vault, Berkeley
BRIB	BK	37.9189	-122.1518	219.7	2.5	1995/06 -	Briones Reservation, Orinda
BRK	BK	37.8735	-122.2610	49.4	2.7	1994/03 -	Haviland Hall, Berkeley
CMB	BK	38.0346	-120.3865	697.0	2	1986/10 -	Columbia College, Columbia
CVS	BK	38.3453	-122.4584	295.1	23.2	1997/10 -	Carmenet Vineyard, Sonoma
FARB	BK	37.6978	-123.0011	-18.5	0	1997/03 -	Farallon Island
GASB	BK	39.6547	-122.716	1354.8	2	2005/09 -	Alder Springs
HAST	BK	36.3887	-121.5514	542.0	3	2006/02 -	Carmel Valley
HATC	BK	40.8161	-121.4612	1009.3	3	2005/05 -	Hat Creek
HELL	BK	36.6801	-119.0228	1140.0	3	2005/04 -	Miramonte
HOPS	BK	38.9935	-123.0723	299.1	3	1994/10 -	Hopland Field Stat., Hopland
HUMO	BK	42.6071	-122.9567	554.9	50	2002/06 -	Hull Mountain, Oregon
JCC	BK	40.8175	-124.0296	27.2	0	2001/04 -	Jacoby Creek
JRSC	BK	37.4037	-122.2387	70.5	0	1994/07 -	Jasper Ridge, Stanford
KCC	BK	37.3236	-119.3187	888.1	87.3	1995/11 -	Kaiser Creek
MCCM	BK	38.1448	-122.8802	-7.7	2	2006/02 -	Marconi Conference Center, Marshall
MHC	BK	37.3416	-121.6426	1250.4	0	1987/10 -	Lick Obs., Mt. Hamilton
MNRC	BK	38.8787	-122.4428	704.8	3	2003/06 -	McLaughlin Mine, Lower Lake
MOBB	BK	36.6907	-122.1660	-1036.5	1	2002/04 -	Monterey Bay
MOD	BK	41.9025	-120.3029	1554.5	5	1999/10 -	Modoc Plateau
ORV	BK	39.5545	-121.5004	334.7	0	1992/07 -	Oroville
PACP	BK	37.0080	-121.2870	844	0	2003/06 -	Pacheco Peak
PKD	BK	35.9452	-120.5416	583.0	3	1996/08 -	Bear Valley Ranch, Parkfield
RAMR	BK	37.9161	-122.3361	416.8	3	2004/11 -	Ramage Ranch
RFSB	BK	37.9161	-122.3361	-26.7	0	2001/02 -	RFS, Richmond
SAO	BK	36.7640	-121.4472	317.2	3	1988/01 -	San Andreas Obs., Hollister
SCCB	BK	37.2874	-121.8642	98	0	2000/04 -	SCC Comm., Santa Clara
SUTB	BK	39.2291	-121.7861	252.0	3	2005/10 -	Sutter Buttes
WDC	BK	40.5799	-122.5411	268.3	75	1992/07 -	Whiskeytown
WENL	BK	37.6221	-121.7570	138.9	30.3	1997/06 -	Wente Vineyards, Livermore
YBH	BK	41.7320	-122.7104	1059.7	60.4	1993/07 -	Yreka Blue Horn Mine, Yreka

Table 3.1: Stations of the Berkeley Digital Seismic Network currently in operation. Each BDSN station is listed with its station code, network id, location, operational dates, and site description. The latitude and longitude (in degrees) are given in the WGS84 reference frame, and the elevation (in meters) is relative to the WGS84 reference ellipsoid. The elevation is either the elevation of the pier (for stations sited on the surface or in mining drifts) or the elevation of the well head (for stations sited in boreholes). The overburden is given in meters. The date indicates either the upgrade or installation time.

Code	Broadband	Strong-motion	Data logger	T/B	GPS	Other	Telemetry	Dial-up
BDM	STS-2	FBA-23	Q4120	X			FR	
BKS	STS-1	FBA-23	Q980	X		Baseplates	FR	X
BRIB	CMG-3T	FBA-ES-T	Q980		X	Strainmeter, EM	FR	X
BRK	STS-2	FBA-23	Q980				LAN	
CMB	STS-1	FBA-23	Q980	X	X	Baseplates	FR	X
CVS	STS-2	FBA-ES-T	Q330HR	X			FR	
FARB	STS-2	FBA-ES-T	Q4120	X	X		R-FR/R	
GASB	STS-2	FBA-ES-T	Q4120	X			R-FR	
HAST	STS-2	FBA-ES-T	Q330HR				R-Sat	
HATC	STS-2	FBA-ES-T	Q330HR				T-1	
HELL	STS-2	FBA-ES-T	Q330				R-Sat	
HOPS	STS-1	FBA-23	Q980	X	X	Baseplates	FR	X
HUMO	STS-2	FBA-ES-T	Q4120	X			VSAT	X
JCC	STS-2	FBA-ES-T	Q980	X			FR	X
JRSC	STS-2	TSA-100S	Q680				FR	X
KCC	STS-1	FBA-23	Q980	X		Baseplates	R-Mi-FR	X
MCCM	STS-2	FBA-ES-T	Q4120				VSAT	
MHC	STS-1	FBA-ES-T	Q980	X	X		FR	X
MNRC	STS-2	FBA-ES-T	Q4120	X			None	X
MOBB	CMG-1T		DM24			Current meter, DPG	None	
MOD	STS-1*	FBA-ES-T	Q980	X	X	Baseplates	VSAT	X
ORV	STS-1	FBA-23	Q980	X	X	Baseplates	FR	X
PACP	STS-2	FBA-ES-T	Q4120	X			Mi/FR	
PKD	STS-2	FBA-23	Q980	X	X	EM	R-FR	X
RAMR	STS-2	FBA-ES-T	Q330				R-FR	X
RFSB		FBA-ES-T	Q730				FR	
SAO	STS-1	FBA-23	Q980	X	X	Baseplates, EM	FR	X
SCCB		TSA-100S	Q730		X		FR	
SUTB	STS-2	FBA-ES-T	Q330HR				R-FR	
WDC	STS-2	FBA-23	Q980	X			FR	X
WENL	STS-2	FBA-ES-T	Q4120	X			FR	
YBH	STS-1 & STS-2	FBA-ES-T	Q980	X	X	Baseplates	FR	X

Table 3.2: Instrumentation of the BDSN as of 06/30/2009. Except for RFSB, SCCB, and MOBB, each BDSN station consists of collocated broadband and strong-motion sensors, with a 24-bit Quanterra data logger and GPS timing. The stations RFSB and SCCB are strong-motion only, while MOBB has only a broadband sensor. Additional columns indicate the installation of a thermometer/barometer package (T/B), collocated GPS receiver as part of the BARD network (GPS), and additional equipment (Other), such as warplless baseplates or electromagnetic sensors (EM). The OBS station MOBB also has a current meter and differential pressure gauge (DPG). The main and alternate telemetry paths are summarized for each station. FR - frame relay circuit, LAN - ethernet, Mi - microwave, POTS - plain old telephone line, R - radio, Sat - Commercial Satellite, VSAT - USGS ANSS satellite link, None - no telemetry at this time. An entry like R-Mi-FR indicates telemetry over several links, in this case, radio to microwave to frame relay. (\*) During most of 2008-2009 the STS-1 at this station was replaced by an STS-2.

at a single site, such as GPS receivers and/or multiple data loggers. Today, 25 of the BDSN sites use frame-relay telemetry for all or part of their communications system.

As described in Section 7, data from the BDSN are acquired centrally at the BSL. These data are used for rapid earthquake reporting as well as for routine earthquake analysis (Section 2 and 8). As part of routine quality control (Section 7), power spectral density (PSD) analyses

are performed continuously and are available on the internet (<http://www.ncedc.org/ncedc/PDF/html/>). The occurrence of a significant teleseism also provides the opportunity to review station health and calibration. Figure 3.4 displays BDSN waveforms for a  $M_w$  7.6 earthquake in the Tonga region on March 19, 2009.

BDSN data are archived at the Northern California Earthquake Data Center. This is described in detail in Section 6

## Electromagnetic Observatories

In 1995, in collaboration with Dr. Frank Morrison, the BSL installed two well-characterized electric and magnetic field measuring systems at two sites along the San Andreas Fault which are part of the Berkeley Digital Seismic Network. Since then, magnetotelluric (MT) data have been continuously recorded at 40 Hz and 1 Hz and archived at the NCEDC (Table 3.4). At least one set of orthogonal electric dipoles measures the vector horizontal electric field,  $E$ , and three orthogonal magnetic sensors measure the vector magnetic field,  $B$ . These reference sites, now referred to as electromagnetic (EM) observatories, are collocated with seismometer sites so that the field data share the same time base, data acquisition, telemetry, and archiving system as the seismometer outputs.

The MT observatories are located at Parkfield (PKD1, PKD) 300 km south of the San Francisco Bay Area, and Hollister (SAO), halfway between San Francisco and Parkfield (Figure 3.2). In 1995, initial sites were established at PKD1 and SAO, separated by a distance of 150 km, and equipped with three induction coils and two 100 m electric dipoles. PKD1 was established as a temporary seismic site, and when a permanent site (PKD) was found, a third MT observatory was installed in 1999 with three induction coils, two 100 m electric dipoles, and two 200 m electric dipoles. PKD and PKD1 ran in parallel for one month in 1999, and then the MT observatory at PKD1 was closed. Starting in 2004, new electromagnetic instrumentation was installed at various Bay Area sites in cooperation with Simon Klemperer at Stanford University. Sensors are installed at JRSC (2004), MHDL (2006) and BRIB (2006/2007).

Data at the MT sites are fed to Quanterra data loggers, shared with the collocated BDSN stations, synchronized in time by GPS and sent to the BSL via dedicated communication links.

In 2009, the BSL led a joint effort toward improving operation and maintenance of these sites with Jonathan Glen and Darcy McPhee from the USGS, and Simon Klemperer at Stanford University.

Engineers from the BSL met scientists from the USGS and Stanford at the station SAO in October of 2008 to assess the condition of the EM/MT system. At that time, the EM coils were found to be not working. They were removed and returned to the manufacturer (EMI Schlumberger). In June 2009, the EM coils had not be reinstalled at SAO. EM/MT equipment at PKD was evaluated in August of 2008. There, the data logger was removed from the PKD EM/MT system and has not yet been returned.

Since it began in 1995, the EM/MT effort has suffered from minimal funding, in part due to the misconception that the EM/MT data could be recorded on unused channels in the seismic data logger. These data loggers had no channels available, however. Thus for each site, an

Sensor	Channel	Rate (sps)	Mode	FIR
Broadband	UH?	0.01	C	Ac
Broadband	VH?	0.1	C	Ac
Broadband	LH?	1	C	Ac
Broadband	BH?	20/40	C	Ac
Broadband	HH?	80/100	C	Ac/Ca
SM	LL?	1	C	Ac
SM	BL?	20/40	C	Ac
SM	HL?	80/100	C	Ac/Ca
Thermometer	LKS	1	C	Ac
Barometer	LDS	1	C	Ac

Table 3.3: Typical data streams acquired at BDSN stations, with channel name, sampling rate, sampling mode, and the FIR filter type. SM indicates strong-motion; C continuous; T triggered; Ac acausal; Ca causal. The LL and BL strong-motion channels are not transmitted over the continuous telemetry but are available on the Quanterra disk system if needed. The HH channels are recorded at two different rates, depending on the data logger. Q4120s and Q330s provide 100 sps and causal filtering; Q680/980s provide 80 sps and acausal filtering.

Sensor	Channel	Rate (sps)	Mode	FIR
Magnetic	VT?	0.1	C	Ac
Magnetic	LT?	1	C	Ac
Magnetic	BT?	40	C	Ac
Electric	VQ?	0.1	C	Ac
Electric	LQ?	1	C	Ac
Electric	BQ?	40	C	Ac

Table 3.4: Typical MT data streams acquired at SAO, PKD, BRIB, and JRSC with channel name, sampling rate, sampling mode, and FIR filter type. C indicates continuous; T triggered; Ac acausal.

additional data logger was purchased. In 2008, the BSL began in-house development of a low cost digitizing solution. While not as feature rich as commercially available data loggers, the prototype 24 bit digitizer was developed and is ready to be deployed for the EM/MT array. Its deployment awaits scheduling by the BSL, USGS, and Stanford University.

### 1.3 2008-2009 Activities

#### Station Upgrades, Maintenance, and Repairs

Given the remoteness of the off-campus stations, BDSN data acquisition equipment and systems are designed, configured, and installed so that they are both cost effective and reliable. As a result, the need for regular station visits has been reduced. Nonetheless, many of the broadband seismometers installed by BSL are from the first generation and are now approaching 25 years in age. Concurrently, the first generation of broadband data loggers are now 17 years old. Computer systems are retired long before this age, yet the electronics that form these data acquisition systems are expected to perform without interruption.

In 2008-2009 one focus of BSL's technical efforts went toward maintaining and repairing existing instrumentation, stations, and infrastructure. While expanding the data acquisition network continues to be a long term goal of BSL, it is equally important to assure the integrity of the established network and preserve data quality.

*YBH:* The BSL has operated instruments at the YBH observatory in Yreka, California since June of 1993. All instrumentation and telemetry equipment is located within the long-abandoned mine. A steel door bars the entrance; recording instruments and telemetry equipment are located 25 meters beyond that door, with the seismometers approximately 25 meters beyond them. In addition to BSL seismometers (see Table 3.2), the YBH observatory includes an STS-2 seismometer and telemetry equipment as part of the CTBTO, as well as GPS equipment for the BARD array. In 1993 when the site was developed, wooden shoring was added within the adit to add support to the original mine entrance. During the past year, it was discovered that some of those timbers had rotted and collapsed. BSL engineers drew up plans and specifications for replacing the timbers. Working with UC Berkeley physical plant, a general engineering contractor was hired in Yreka to remove the rotted material and reshore the area. The reshoring work at the site was completed in March, 2009. BSL engineers visited the site three times to plan, oversee, and accept the work performed by the contractor. During one trip, the BSL engineer replaced the Ashtech GPS receiver with a Trimble NetRS receiver. The Trimble receiver features Ethernet communication and has onboard memory, making it more robust.

*JRSC:* The equipment at station JRSC is operated and

maintained by the BSL on behalf of Stanford University. In March of 2009, equipment at the JRSC site suffered from what appear to be the effects of a nearby lightning strike. The phone company's digital network interface and BSL's frame relay access device (FRAD) were damaged as a result. Several visits to the site were necessary to restore telemetry to Berkeley. At about the same time it was noted the Metrozet TSA-100 strong motion sensor was not responding to ground motion. Investigation revealed that BSL engineers had powered the sensor with the incorrect voltage. The TSA-100 requires 12 V DC power; as the JRSC site had one of the first generation Quanterra Q680 stations, it only had 24 V circuits available. As installed, the TSA-100 instrument ran off of 24 V with no problem for nearly a year. It is not completely clear whether the instrument ultimately failed due to the incorrect voltage or whether the lightning strike caused the failure. In either case, Metrozet has agreed to repair or replace the instrument under warranty. Reinstallation of the strong motion sensor at station JRSC is awaiting the return of the sensor from Metrozet.

*JCC:* The BSL has operated the station JCC at Bay-side, CA, since April of 2001. During power outages caused primarily by winter storms, the on site batteries no longer support station operation for at least three days, but only approximately 30 hours after the AC power fails. During a site visit, BSL engineers replaced batteries installed in 2001. They noted that access to the vault was somewhat restricted due to brush overgrowing the road. It may be necessary to remove the brush at some point. Also during this visit, the STS-2 seismometer was replaced with an instrument that was pre-calibrated using a step test procedure in Berkeley. The STS-2 that was removed from JCC was returned to Berkeley, where a step test calibration was performed. The 17 year old instrument was found to be within 1% of the factory calibrated sensitivity.

*FARB:* The BSL has operated instrumentation on SE Farallon Island continuously since 1994. Initially a GPS receiver was installed, and it was augmented with broadband and strong motion seismic instruments in 1996. Because of the highly corrosive marine environment, the radio telemetry antennas have been replaced every two years. Continuous seismic and GPS telemetry from the island is achieved using redundant 900 MHz and 2.4 GHz digital radio transceivers. The 900 MHz radio link connects the Farallon Island site through the Golden Gate to the Space Science building on the hills of the Berkeley campus. When this radio link became unstable during the past winter, BSL engineers found that the antennas on the Space Science building had been moved. After several meetings, the BSL antennas were restored, bringing the 900 MHz radio link to the Farallons up again. The 2.4 GHz link operates from the island to the University of California Medical Science building in San Francisco.

From San Francisco, a frame relay circuit completes that data link to Berkeley. Over the years, the BSL has come to provide technical support for all radios on the Farallons. During February of 2009, BSL engineers met with representatives from the US Fish and Wildlife Service and the California Academy of Science regarding installation of additional high bandwidth radio links between the mainland and the island. The California Academy of Science wishes to establish a web camera on the Farallons, and they have offered to provide the BSL with data telemetry from the island to once their link is established. The BSL may pursue this after the new radio link has demonstrated its ability to survive the particularly harsh winter weather on the island.

*GASB:* During the last week of May in 2009, a massive lightning strike damaged equipment at GASB. BSL engineers subsequently replaced the Quanterra data logger, the telemetry radio transceiver, and the power supply. All of these devices were behind industrial lightning and surge protectors. Trees within 50 meters of the seismic vault bear evidence of the nearby lightning strikes.

*SAO:* For several years, we have been upgrading the infrastructure at SAO. In May of 2009, the door to the seismic vault at SAO was smashed by vandals. BSL engineers repaired the door, replaced the lock, and added a steel plate to completely cover the exterior of the existing door. General site clean-up included removal and disposal of an office trailer that had been on the site since the mid 1970's, as well as cabling strung through the trees by graduate students at about the same time.

*MCCM:* Twice during the spring of 2009, the Quanterra data logger at MCCM became unresponsive or died. On one of these occasions, the VSAT equipment provided by USNSN was also in a hung state. The other time, the data logger's state of health circuit board was not working and the external clock antenna was damaged; lightning is suspected to have played a role in both outages. In the course of routine network maintenance, BSL engineers replaced half of the batteries installed when the station was commissioned in 2005.

*KCC:* KCC is arguably the BSL's most remote station, located in a Southern California Edison water tunnel deep in the granites of the Sierra Nevada. BSL engineers installed a new Metrozet E300 seismometer electronics package at station KCC in October of 2008. These electronics replace the original, factory-built STS-1 electronics, and offer remote calibration and control of the sensors. Problems were observed with the seismometer calibration sequence using the E300, although the calibration is believed to be correct. It appears that ground loops among the installed instrumentation interfere with the E300 functionality. The Kinometrics FBA-23 strong motion sensor at KCC has a single-ended output, and this type of sensor has been known to cause ground loops. BSL plans to replace all remaining FBA-23 instruments

installed at BDSN stations with differential, and more sensitive strong motion sensors. A return trip to do this at KCC is planned.

*MNRC:* The BSL has operated the seismic observatory at the UC McLaughlin Mine Reserve (MNRC) since 2003. Data from the site are telemetered via digital radio to the summit of Mount Saint Helena and relayed from there to the California Department of Forestry and Fire command center in Napa. In 2008, a new 100 meter tall radio tower was constructed, and during the summer of 2009 the building at its base was completed. BSL engineers made three trips to the site in the past year to reposition antennas in order to maintain telemetry from the MNRC site as construction of the new tower progressed.

*WENL:* The seismic station at Wente Vineyards (WENL) is located at the rear of an adit that is used to age wine. To get clear view of the sky, the GPS antenna used to drive the data logger clock is located approximately 150 meters from the equipment. The antenna has high gain, and the coaxial cable is low loss to support the long distance. During the past year, the external clock reference developed problems. BSL engineers replaced the high gain antenna when clock signals from the GPS satellites were no longer being received. The level of cultural noise at WENL has increased over the past several years, and we are searching for a suitable replacement site.

*HATC:* The seismic station HATC is located at the UC radio astronomical observatory at Hat Creek, California. The seismic site takes advantage of an existing high speed data link between Hat Creek and the Berkeley Campus. Seismic instruments at HATC are powered by solar panels. During the fall of 2008, BSL engineers increased the size of the solar panel array in anticipation of shorter daylight hours during the winter.

*CVS:* The BSL station at CVS is located in the rear of an adit used for aging wine at the Moon Mountain Vineyard, Sonoma, California. During 2008, the winemaker at Moon Mountain brought to our attention the possibility that mold growing in the tunnel, and specifically growing on the plastic instrument case and insulating foam used over the seismometers, could contaminate the wine during the aging process. Although the wine is aged in oak barrels, the mold can taint its taste. We were asked to remove all plastic, wood, and foam from the adit. The BSL used this opportunity to upgrade the entire installation at CVS. The STS2 and FBA were removed, as were the data logger, telemetry equipment, power supplies, and batteries. A new steel instrument enclosure was installed and now houses a new power supply, batteries, and data logger. The old foam covering for the seismometers was replaced with new material and covered with a metal container.

*MOD:* The STS1 seismometers were removed from MOD, so that their electronics could be refurbished, as

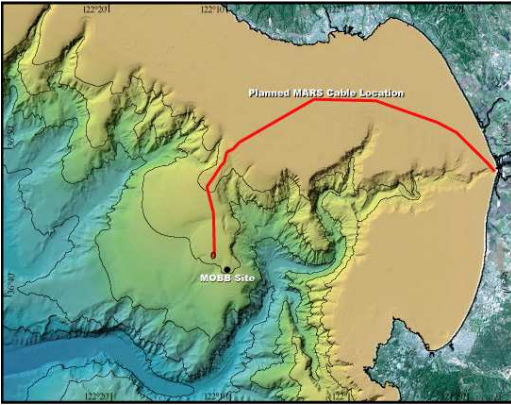


Figure 3.5: Location of the MOBB station in Monterey Bay, California, against seafloor and land topography. The path of the MARS cable is indicated by the solid line.

they were exhibiting reduced sensitivity, increased noise, and non-linear behavior. An STS2 was installed temporarily. The STS1 sensors were returned to Berkeley. Their hinges and connectors are being replaced, and the electronics refurbished. These instruments will be used in testing as part of the NSF funded STS1 development. We expect to return the STS1 seismometers to MOD in 2010.

### The Monterey Bay Ocean Bottom Seismic Observatory (MOBB)

The Monterey Ocean Bottom Broadband observatory (MOBB) is a collaborative project between the Monterey Bay Aquarium Research Institute (MBARI) and the BSL. Supported by funds from the Packard Foundation to MBARI, NSF/OCE funds and UC Berkeley funds to BSL, its goal has been to install and operate a long-term seafloor broadband station as a first step towards extending the on-shore broadband seismic network in Northern California to the seaside of the North America/Pacific plate boundary, providing better azimuthal coverage for regional earthquake and structure studies. It also serves the important goal of evaluating background noise in near-shore buried ocean floor seismic systems, such as may be installed as part of temporary deployments of “leap-frogging” arrays (e.g. Ocean Mantle Dynamics Workshop, September 2002). The project has been described in detail in BSL annual reports since 2002 and in several publications (e.g. *Romanowicz et al.*, 2003, 2006).

The MARS observatory (Figure 3.5, <http://www.mbari.org/mars/>) comprises a 52 km electro-optical cable that extends from a shore facility in Moss Landing out to a seafloor node in Monterey Bay (Figure 3.5). The cable was deployed in the spring of 2007, and node instal-

lation was completed in November 2008. It now can provide power and data to as many as eight science experiments through underwater electrical connectors. MOBB, located 3km from the node, is one of the first instruments to be connected to the cable. The connection was established on February 28, 2009, through an extension cable installed by the ROV *Ventana*, with the help of a cable-laying toolsled. The data interface at the MARS node is 10/100 Mbit/s Ethernet, which can directly support cables of no more than 100 m in length. To send data over the required 3 km distance, the signals pass through a Science Instrument Interface Module (SIIM) at each end of the extension cable (Figure 3.6). The SIIMs convert the MARS Ethernet signals to Digital Subscriber Line (DSL) signals, which are converted back to Ethernet signals close to the MOBB system. Power from the MARS node is sent over the extension cable at 375 VDC, and then converted to 28 VDC in the distal SIIM for use by the MOBB system. The connection to the MARS node eliminates the need for periodic exchange of the battery and data package using ROV and ship. At the same time, it allows us to acquire seismic data from the seafloor in real time (*Romanowicz et al.*, 2009).

The electronics module in the MOBB system has been refurbished to support the connection to the MARS observatory. The low-power autonomous data logger has been replaced with a PC/104 computer stack running embedded Linux. This new computer runs an Object Ring Buffer (ORB), whose function is to collect data from the various MOBB sensors and forward it to another ORB running on a computer at the MARS shore station. There, the data are archived and then forwarded to a third ORB running at the UC Berkeley Seismological Laboratory. The Linux system acquires data (via RS232) from the Guralp digitizer included in the seismometer package, data (via ethernet) from a Q330 Quanterra 24 bit A/D converter which digitizes data from the DPG, and polls and receives data (via RS232) from the current meter. The data are available through the NCEDC. Procedures to include the MOBB data in the Northern California real time earthquake processing are under development.

### 1.4 Acknowledgements

Under Barbara Romanowicz’s general supervision, Peggy Hellweg and Doug Neuhauser oversee the BDSN data acquisition operations, and Bill Karavas heads the engineering team. John Friday, Jarrett Gardner, Rick Lellinger, Taka’aki Taira and Bob Uhrhammer contribute to the operation of the BDSN. Karl Kappler has been responsible for the operation of the EM observatories. Bill Karavas, Bob Uhrhammer, and Peggy Hellweg contributed to the preparation of this section. MOBB is a collaboration between the BSL and MBARI, involving Barbara Romanowicz, Bob Uhrhammer, and Doug

Zürn, W., and R. Widmer, On noise reduction in vertical seismic records below 2 mHz using local barometric pressure, *Geophys. Res. Lett.*, 22, 3537-3540, 1995.

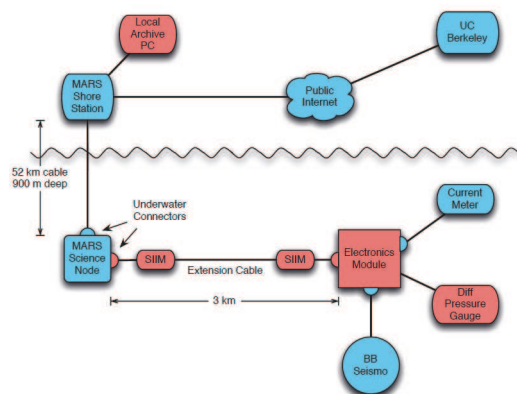


Figure 3.6: Components of the cabled observatory: the MOBB system integrated into the MARS network. MARS-provided components are shown in blue, and components installed or modified by the MOBB team are shown in pink.

Neuhauser from the BSL, and Paul McGill from MBARI. The MBARI team also has included Steve Etchemendy (Director of Marine Operations), Jon Erickson, John Ferreira, Tony Ramirez, and Craig Dawe. The MOBB effort at the BSL is supported by UC Berkeley funds. MBARI supports the dives and data recovery. The MOBB seismometer package was funded by NSF/OCE grant #9911392. The development of the interface for connection to the MARS cable is funded by NSF/OCE grant #0648302.

## 1.5 References

- Cox, C., T. Deaton and S. Webb, A deep-sea differential pressure gauge, *J. Atm. Ocean. Tech.*, 1, 237-245, 1984.
- Crawford W. C., and S. C. Webb, Identifying and removing tilt noise from low-frequency (<0.1 Hz) seafloor vertical seismic data, *Bull. Seis. Soc. Am.*, 90, 952-963, 2000.
- Murdock, J., and C. Hutt, A new event detector designed for the Seismic Research Observatories, *USGS Open-File-Report 83-0785*, 39 pp., 1983.
- Romanowicz, B., D. Stakes, R. Uhrhammer, P. McGill, D. Neuhauser, T. Ramirez, and D. Dolenc, The MOBB experiment: a prototype permanent off-shore ocean bottom broadband station, *EOS Trans. AGU*, Aug 28 issue, 2003.
- Romanowicz, B., D. Stakes, D. Dolenc, D. Neuhauser, P. McGill, R. Uhrhammer, and T. Ramirez (2006), The Monterey Bay Broadband Ocean bottom seismic observatory, *Ann. Geophys.*, 49, 607-623.
- Romanowicz, B., P. McGill, D. Neuhauser and D. Dolenc (2009) Acquiring real time data from the broadband ocean bottom seismic observatory at Monterey Bay (MOBB), *Seismol. Res. Lett.*, 80, 197-202.
- Wielandt, E., and J. Steim, A digital very broadband seismograph, *Ann. Geophys.*, 4, 227-232, 1986.
- Wielandt, E., and G. Streckeisen, The leaf spring seismometer: design and performance, *Bull. Seis. Soc. Am.*, 72, 2349-2367, 1982.

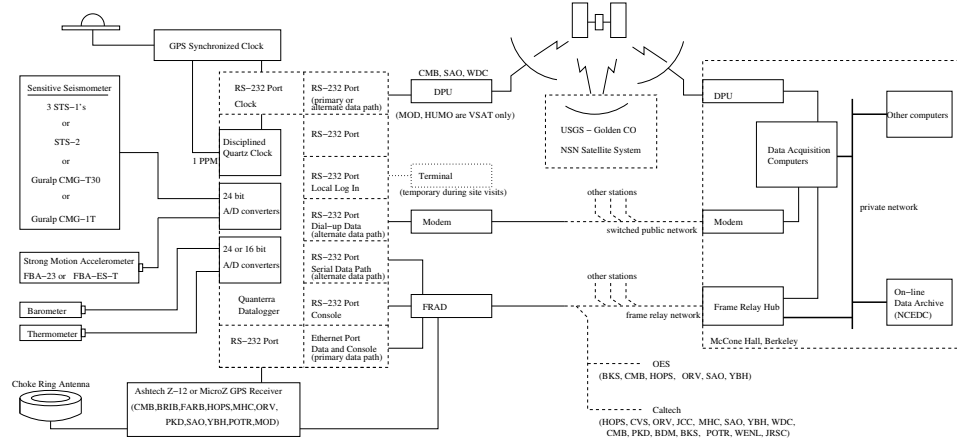


Figure 3.3: Schematic diagram showing the flow of data from the sensors through the data loggers to the central acquisition facilities of the BSL.

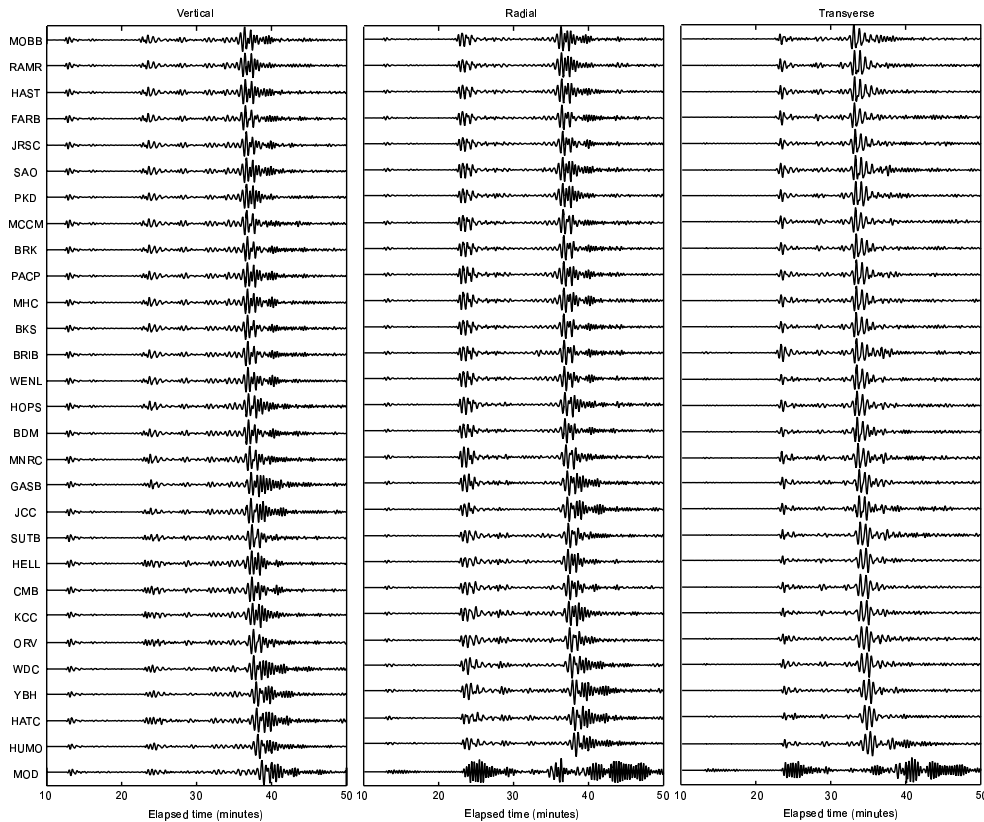


Figure 3.4: Long period waveforms recorded across BDSN from the deep  $M_w$  7.6 teleseism which occurred on March 19, 2009, in Tonga at  $23.050^\circ\text{S}$ ,  $174.668^\circ\text{W}$ . The traces are deconvolved to ground displacement, scaled absolutely, and ordered from top to bottom by distance from the epicenter. The highly similar waveforms recorded across the BDSN provide evidence that the broadband sensors are operating within their nominal specifications, except at MOD.

## 2 California Integrated Seismic Network

### 2.1 Introduction

Advances in technology have made it possible to integrate separate earthquake monitoring networks into a single seismic system as well as to unify earthquake monitoring instrumentation. In California, this effort began in the south with the TriNet Project. There, Caltech, the California Geological Survey (CGS), and the USGS created a unified seismic system for Southern California. With major funding provided by the Federal Emergency Management Agency (FEMA), the California Governor's Emergency Management Agency (CalEMA), and the USGS, monitoring infrastructure was upgraded and expanded, combining resources in a federal, state and university partnership. In 2000, the integration effort expanded to the entire State with the formation of the California Integrated Seismic Network (CISN, see 2000-2001 Annual Report). To this end, UC Berkeley and the USGS Menlo Park and Pasadena offices joined forces with Caltech and the CGS. The CISN is now in the ninth year of collaboration and its eighth year of funding from the Office of Emergency Services (OES).

### 2.2 CISN Background

#### Organization

The organizational goals, products, management, and responsibilities of the CISN member organizations are described in the founding memorandum of understanding and in the strategic and implementation plans. To facilitate activities among institutions, the CISN has three management centers:

- Southern California Earthquake Management Center: Caltech/USGS Pasadena
- Northern California Earthquake Management Center: UC Berkeley/USGS Menlo Park
- Engineering Strong Motion Data Center: California Geological Survey/USGS National Strong Motion Program

The Northern and Southern California Earthquake Management Centers operate as twin statewide earthquake processing centers serving information on current earthquake activities, while the Engineering Strong Motion Data Center is responsible for producing engineering data products and distributing them to the engineering community.

The Steering Committee, made up of two representatives from each core institution and a representative from

OES, oversees CISN projects. The position of chair rotates among the institutions; Barbara Romanowicz took over as chair of the Steering Committee in December 2009 from Rob Clayton.

An external Advisory Committee represents the interests of structural engineers, seismologists, emergency managers, industry, government, and utilities, and provides review and oversight. The Advisory Committee is chaired by Stu Nishenko of Pacific Gas and Electric Company. It last met in January 2009. Agendas from the meetings and the resulting reports may be accessed through the CISN Web site (<http://www.cisn.org/advisory>).

The Steering Committee has commissioned other committees, including a Program Management Group to address planning and coordination and a Standards Committee to resolve technical design and implementation issues.

In addition to the core members, other organizations contribute data that enhances the capabilities of the CISN. Contributing members include: University of California, Santa Barbara; University of California, San Diego; University of Nevada, Reno; University of Washington; California Department of Water Resources; Lawrence Livermore National Lab; and Pacific Gas and Electric.

#### CISN and ANSS

The USGS Advanced National Seismic System (ANSS) is developing along a regionalized model. Eight regions have been organized, with the CISN representing California. David Oppenheimer of the USGS represents the CISN on the ANSS National Implementation Committee (NIC).

Over the past 9 years, ANSS funding in California has been directed primarily to the USGS Menlo Park to expand the strong-motion instrumentation in the San Francisco Bay Area. As a result, more than 100 sites have been installed or upgraded, significantly improving the data available for ShakeMaps.

As the ANSS moves forward, committees and working groups are being established to address issues of interest. BSL faculty and staff have been involved in several working groups of the Technical Integration Committee, including Doug Dreger, Peggy Hellweg, Pete Lombard, Doug Neuhauser, Bob Uhrhammer, and Stephane Zuzlewski.

#### CISN and CalEMA

CalEMA (formerly Office of Emergency Services, OES) has had a long-term interest in coordinated earthquake

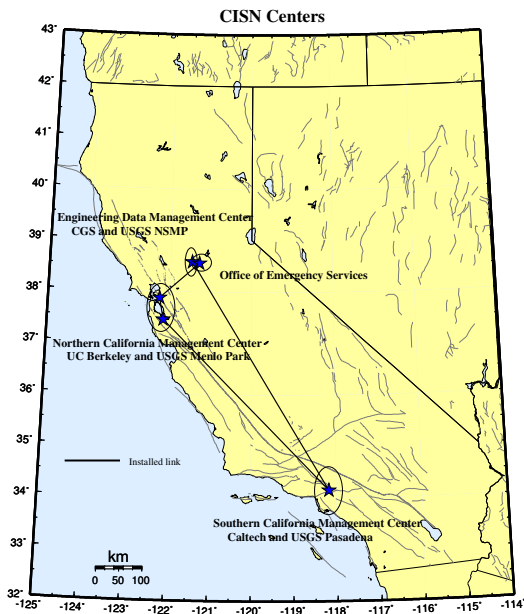


Figure 3.7: Map showing the geographical distribution of the CISP partners and centers. The communications “ring” is shown schematically with installed links (solid lines).

monitoring. The historical separation between Northern and Southern California and between strong-motion and weak-motion networks resulted in a complicated situation for earthquake response. Thus, CalEMA has been an advocate of increased coordination and collaboration in California earthquake monitoring and encouraged the development of the CISP. In FY01-02, Governor Gray Davis requested support for the CISP, to be administered through CalEMA. Funding for California Geological Survey, Caltech and UC Berkeley was made available in spring 2002, officially launching the statewide coordination efforts. Following the first year of funding, CalEMA support led to the establishment of 3-year contracts to the UC Berkeley, Caltech, and the California Geological Survey for CISP activities. We have just completed the first year of the third three-year contract (2008-2011). Past CISP-related activities are described in previous annual reports.

### 2.3 2008-2009 Activities

This year has brought the culmination of our work to implement a new suite of earthquake monitoring software in the NCEMC. The switch to the CISP software package was made in June 2009, and the software is now operating at the BSL and in Menlo Park. CISP funding from CalEMA contributed to this transition, and has supported a number of other activities at the BSL during the past year as well.

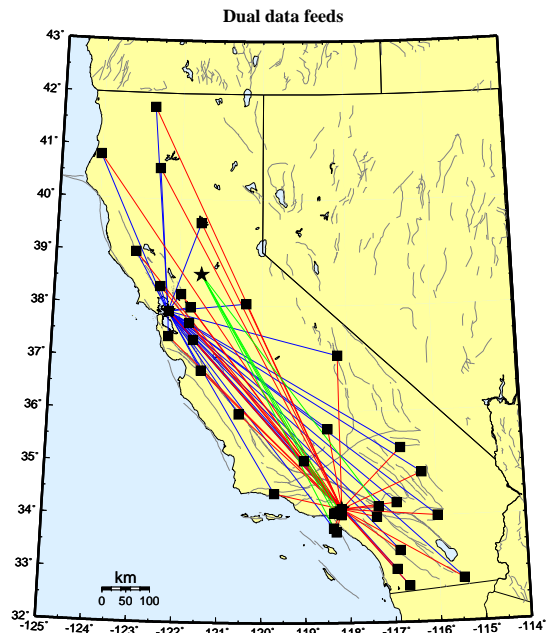


Figure 3.8: Map showing the 30 stations selected to send data directly to the Northern and Southern California processing centers, and the 5 stations that send data directly to the Engineering Data Center and the Southern California processing center.

### Northern California Earthquake Management Center

As part of their effort within the CISP, the BSL and the USGS Menlo Park have completed implementation of the new generation Northern California joint notification system. Section 8 describes the operations of this system and reports on implementation process.

For the restructuring of the Northern California earthquake monitoring system, the USGS Menlo Park and BSL have improved their communications infrastructure. At present, the BSL and the USGS Menlo Park are connected by two dedicated T1 circuits. One circuit is a component of the CISP ring, while the second circuit was installed in 2004-2005 (Figure 3.9) to support dedicated traffic between Berkeley and Menlo Park above and beyond that associated with the CISP.

The installation of the second dedicated T1 between Berkeley and Menlo Park freed up a frame-relay connection deployed by the BSL as part of the CalREN project in mid-1990s. The BSL has reconfigured this frame-relay circuit to serve as a second data acquisition link. BDSN data acquisition is now distributed between two frame-relay T1 circuits, eliminating what had been a single point of failure. An additional Permanent Virtual Circuit (PVC) has also been implemented at each BDSN site so that each station has connections to both T1s. This has improved the robustness of data acquisition at the BSL by providing redundancy in the incoming circuit.

In the long term, the BSL and USGS Menlo Park hope

to be connected by high-bandwidth microwave or satellite service. Unfortunately, we have not yet been able to obtain funding for such an additional communication link.

## 2.4 Statewide Integration

BSL staff are involved in many elements of the statewide integration effort. The Standards Committee, chaired by Doug Neuhauser, continues to define and prioritize projects important to the development and implementation of the statewide earthquake processing system and to establish working groups to address them (see minutes from meetings and conference calls at <http://www.cisn.org/standards/meetings.html>).

*Dual Station Feeds:* Early in the existence of CISN, “dual station feeds” were established for 30 stations (15 in Northern California and 15 in Southern California) (Figure 3.8). The Northern California Earthquake Management Center (NCEMC) is using data from the Southern California stations to estimate magnitudes on a routine basis. A subset of these stations are being used for the moment tensor inversions, a computation that is sensitive to the background noise level.

*Data Exchange:* Pick exchange was initiated between the NCEMC and its Southern California counterpart in 2001-2002. The software CISN has developed to produce and exchange the reduced amplitude timeseries is complete. Currently, these timeseries are being exchanged at the NCEMC, but not yet statewide. Using a common format, the CISN partners continue to exchange observations of peak ground motion with one another following an event or a trigger. This step increases the robustness of generating products such as ShakeMap, since all CISN partners now exchange data directly with one another. This also improves the quality of ShakeMaps for events on the boundary between Northern and Southern California, such as the San Simeon earthquake, by allowing all data to be combined in a single map. Finally, this is a necessary step toward the goal of generating statewide ShakeMaps.

*The Software Calibration & Standardization:* CISN partners have calibrated and standardized much of the software used for automatic earthquake processing and earthquake review. For the past several years, we have worked to prepare a version of the Southern California TriNet software for implementation as CISN software in the NCEMC. The CISN software now serves as the real-time system operating in the NCEMC. The transition was made in June 2009.

- **Magnitude:** Calibrating magnitude estimates was more difficult than originally anticipated. As described in 2003-2004, evidence indicates that there is a bias between the Northern and Southern California estimates of local magnitude  $M_L$ . Efforts to

understand this issue were hampered by the lack of a good statewide dataset. Using a statewide set of earthquakes recorded by the AZ, BK, CI and NC networks, Bob Uhrhammer calculated a new  $\log A_o$  function suitable for statewide use. Station-specific corrections for  $M_L$  have now been defined for most broadband/strong motion stations, and also for strong motion only stations. Now efforts are underway to tie the new system to vertical components, whether short period or broadband. A final component of the magnitude efforts is the determination of a magnitude reporting hierarchy. For the near future, each region will continue to use its own preferences for magnitude reporting.

- **ShakeMap:** At present, ShakeMaps are generated on 5 systems within the CISN. Two systems in Pasadena generate “SoCal” Shakemaps; 2 systems in the Bay area generate “NoCal” Shakemaps; and 1 system in Sacramento generates ShakeMaps for all of California. The Sacramento system uses QDDS to provide the authoritative event information for Northern and Southern California.

The dearth of stations in the near source region of the 2003 San Simeon earthquake raised the issues of how to measure the quality of a ShakeMap and how to quantify the uncertainty. A subset of the Working Group worked on this issue, based on the work of *Hok and Wald (2003)*. *Lin et al (2006)* presented progress toward quantifying ShakeMap uncertainty, and ShakeMaps are now published with a grade.

A second goal of this effort was to improve the robustness of ShakeMap generation and delivery by taking advantage of the fact that ShakeMaps are generated in the Bay Area, Pasadena, and Sacramento. Ongoing efforts in this direction will likely be based on the new USGS ShakeMap webpages at the National Earthquake Information Center.

- **Location Codes:** The CISN adopted a standard for the use of “location” codes (part of the Standard for the Exchange of Earthquake Data (SEED) nomenclature to describe a timeseries based on network-station-channel-location) in the late fall of 2003. USGS and UC Berkeley developers modified the Earthworm software to support their use. After the transition at USGS Menlo Park away from the CUSP analysis system to *Jiggle* in late November, 2006, all networks in the CISN implemented location codes in their systems.
- **Metadata Exchange:** Correct metadata are vital to CISN activities, as they are necessary to ensure valid interpretation of data. CISN is working

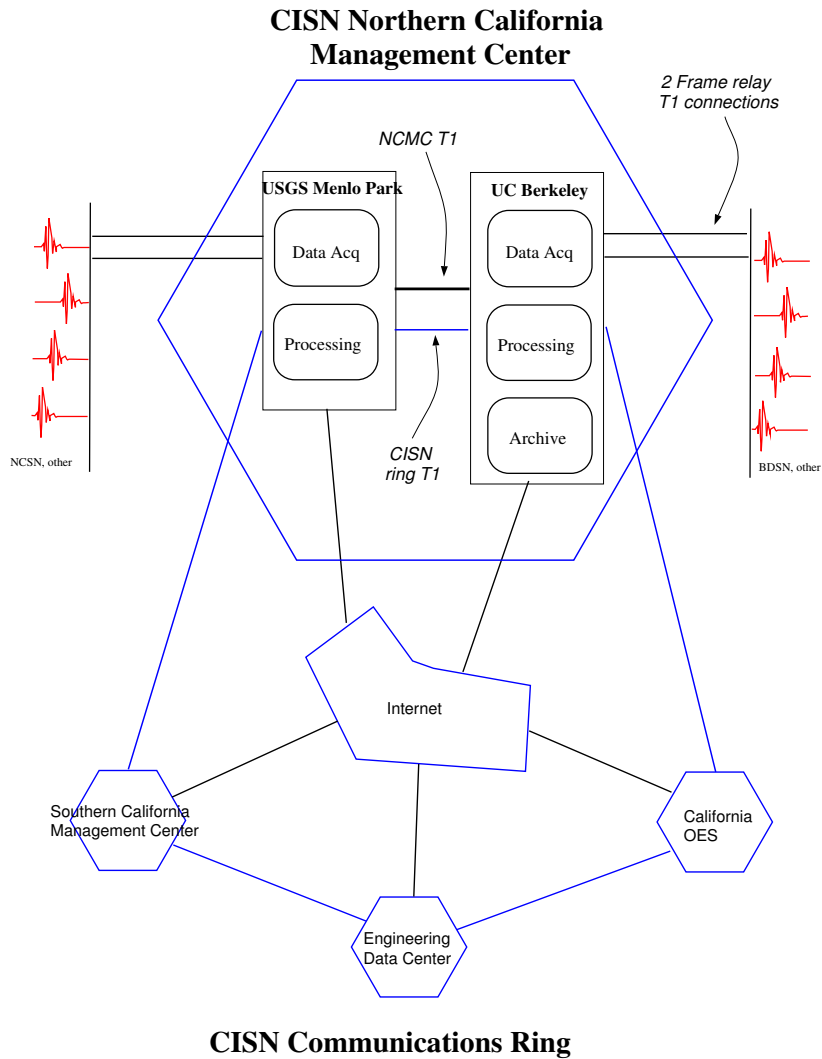


Figure 3.9: Schematic diagram illustrating the connectivity between the real-time processing systems at the USGS Menlo Park and UC Berkeley, forming the Northern California Management Center, and with other elements of the CISN.

on issues related to their reliable and timely exchange. The CISN Metadata Working Group compiled a list of metadata necessary for data processing and developed a model for their exchange. In this model, each CISN member is responsible for the metadata for its stations and for other stations that enter into CISN processing through it. For example, Menlo Park is responsible for the NSMP, Tremor, and PG&E stations, while Caltech is responsible for the Anza data. At the present time, dataless SEED volumes are used to exchange metadata between the NCEMC and the SCEMC. The Metadata Working Group is developing a Station

XML format for metadata exchange. This vehicle is expandable, and will probably allow exchange of a more comprehensive set of metadata than dataless SEED volumes, some of which may be necessary for other systems, for example in V0 formatted data.

- Leap second compatibility: Northern and Southern California databases handled leap seconds differently. A major software programming effort was directed toward resolving this discrepancy. The data processing and analysis software now treats leap seconds consistently. All packages can be config-

ured to pass the time information to the database in nominal or true time, as necessary.

- Standardization: The CISON's focus on standardization of software continues. The complete system is now implemented and providing realtime earthquake information in the NCEMC (see Section 8). The software is currently being implemented at other regional networks of the ANSS.

### CISON Display

CISON Display is an integrated Web-enabled earthquake notification system designed to provide earthquake information for emergency response at 24/7 operations centers. First responders, organizations with critical lifelines and infrastructure, and emergency responders are invited to register for an account at <http://www.cisn.org/software/cisndisplay.htm>.

The application provides users with maps of real-time seismicity and automatically provides access to Web-related earthquake products such as ShakeMaps. CISON Display also offers an open source GIS mapping tool that allows users to plot freely available layers of public highways, roads and bridges, as well as private layers of organizational-specific infrastructure and facilities information. The current version of CISON Display is 1.4. Its primary enhancement over the previous version is the development of a kiosk-mode for public display purposes.

### Earthquake Information Distribution

The USGS hosted a workshop in October 2004 to develop plans for the installation and use of the EIDS software. Doug Neuhauser and Pete Lombard participated in this workshop, which resulted in a document outlining the steps necessary for the installation and migration of the earthquake notification system from the current Quake Data Distribution Services (QDDS) to EIDS. During the past year, the NCEMC participated in a test of the EIDS system.

### Outreach

Since FY05-06, the CISON Web site ([www.cisn.org](http://www.cisn.org)) has been supported by two servers located at Berkeley and Caltech. The Web servers are set up so that the load can be distributed between them, providing improved access during times of high demand. With the increased robustness provided by the new servers, the CISON provides access to certain earthquake products directly from [www.cisn.org](http://www.cisn.org). For example, ShakeMaps are now served directly from the CISON Web site, in addition to being available from several USGS Web servers and the CGS. The design and content of <http://www.cisn.org> continues to evolve. The Web site is an important tool for CISON outreach as well as for communication and documentation among the CISON partners.

The CISON continues to support the dedicated Web site for emergency managers. Following a suggestion from the Advisory Committee, we have designed a Web site to provide personalized access to earthquake information. Known as "myCISON," the Web site is available at [eoc.cisn.org](http://eoc.cisn.org). Access to the Web site is limited to registered users in order to provide highly reliable access. At present, "myCISON" is a single Web server located at UC Berkeley. However, modifications to the database are underway to allow for multiple servers in the future. A second computer, already purchased, will either be installed in Sacramento or in Southern California.

As part of the CISON, the BSL contributed to efforts to raise awareness of earthquakes and preparedness, in this year the 140 anniversary of the 1868 Hayward Fault earthquake on October 21, 2008. In particular, we co-hosted the *Third Conference on Earthquake Hazards in the Eastern Bay Area* as well as organizing and participating in other related activities. Following the Hayward Fault anniversary, and the great Southern California ShakeOut on November 13, 2008, Northern and Southern California outreach efforts were combined in the Earthquake Country Alliance. We are now working toward a statewide California ShakeOut on October 15, 2009 at 10:15 (see <http://www.shakeout.org> for more information and to sign up).

## 2.5 Acknowledgements

CISON activities at the BSL are supported by funding from the Governor's Office of Emergency Services.

Barbara Romanowicz and Peggy Hellweg are members of the CISON Steering Committee. Peggy Hellweg is a member of the CISON Program Management Group, and she leads the CISON project at the BSL with support from Doug Neuhauser. Doug Neuhauser is chair of the CISON Standards Committee, which includes Peggy Hellweg, Pete Lombard, Taka'aki Taira, and Stephane Zuzlewski as members.

Because of the breadth of the CISON project, many BSL staff members have been involved, including: John Friday, Jarrett Gardner, Peggy Hellweg, Bill Karavas, Oleg Khainovski, Rick Lellinger, Pete Lombard, Doug Neuhauser, Charley Paffenbarger, Taka'aki Taira, Bob Uhrhammer, and Stephane Zuzlewski. Peggy Hellweg contributed to this section. Additional information about the CISON is available through reports from the Program Management Group.

## 2.6 References

- Hok, S., and D. J. Wald, Spatial Variability of Peak Strong Ground Motions: Implications for ShakeMap Interpolations, *EOS. Trans. AGU*, 84(46), F1121, 2003.
- Lin, K-W., D. Wald, B. Worden and A.F. Shakal, Progress toward quantifying CISON ShakeMap uncertainty, *Eighth National Conference on Earthquake Engineering, San Francisco, California, April 18-21, 2006*.

## 3 Northern Hayward Fault Network

### 3.1 Introduction

Complementary to the regional surface broadband and short-period networks, the Hayward Fault Network (HFN) (Figure 3.10 and Table 3.5) is a deployment of borehole-installed, wide-dynamic range seismographic stations along the Hayward Fault and throughout the San Francisco Bay toll bridges system. Development of the HFN initiated through a cooperative effort between the BSL (Berkeley Seismological Laboratory) and the USGS, with support from the USGS, Caltrans, EPRI, the University of California Campus/Laboratory Collaboration (CLC) program, LLNL, and LBNL. The project's objectives included an initial characterization period followed by longer-term monitoring effort using a backbone of stations from among the initial characterization set. Subsequent funding from Caltrans, however, has allowed for continued expansion of the backbone station set for additional coverage in critical locations.

The HFN consists of two components. The Northern Hayward Fault Network (NHFN), operated by the BSL, consists of 30 stations in various developmental and operational stages. These include stations located on Bay Area bridges, at free-field locations, and now at sites of the Mini-PBO (MPBO) project (installed with support from NSF and the member institutions of the MPBO project). The NHFN is considered part of the BDSN and uses the network code BK. The Southern Hayward Fault Network (SHFN) is operated by the USGS and currently consists of 5 stations. This network is considered part of the NCSN and uses the network code NC. The purpose of the HFN is fourfold: 1) to contribute operational data to California real-time seismic monitoring for response applications and the collection of basic data for long-term hazards mitigation, 2) to increase substantially the sensitivity of seismic data to low amplitude seismic signals, 3) to increase the recorded bandwidth for seismic events along the Hayward fault, and 4) to obtain bedrock ground motion signals at the bridges from more frequent, smaller earthquakes.

In addition to the NHFN's contribution to real-time seismic monitoring in California, the mix of NHFN sites in near- and far-field sites and the high-sensitivity (high signal-to-noise), high-frequency broadband data recorded by the NHFN also contributes significantly to a variety of scientific objectives including: a) investigating bridge responses to stronger ground motions from real earthquakes; b) obtaining a significantly lower detection threshold for microearthquakes and possible non-volcanic tremor signals; c) increasing the resolution of the fault-zone seismic structure (e.g., in the vicinity of the Rodgers Creek/Hayward Fault step over); d) improv-

ing monitoring of spatial and temporal evolution of seismicity (to magnitudes below  $M \sim 0.0$ ) that may signal behavior indicative of the nucleation of large damaging earthquakes; e) investigating earthquake scaling, physics, and related fault processes; f) improving working models for the Hayward fault; and g) using these models to make source-specific response calculations for estimating strong ground shaking throughout the Bay Area.

Below we focus primarily on activities associated with BSL operations of the NHFN component of the HFN.

### 3.2 NHFN Overview

The initial characterization period of HFN development ended in 1997. During that period, the NHFN sensors provided signals to on-site, stand-alone Quanterra Q730 and RefTek 72A-07 data loggers, and manual retrieval and download of data tapes was required. Also in that year, the long-term monitoring phase of the project began, involving the installation of 24-bit data acquisition and communication platforms and data telemetry to the BSL archives for a backbone of the initial NHFN stations.

Over the years, Caltrans has provided additional support for the upgrade of two non-backbone sites to backbone operational status and for the addition of several new sites to the monitoring backbone. These expansion efforts are ongoing. Also since February 1 of 2007, the 5 stations of the MPBO project have been folded into the NHFN.

Of the 30 stations considered part of the NHFN history, 13 of the stations are currently operational, with telemetered data streams flowing continuously into the BSL's BDSN processing stream with subsequent archival in the Northern California Earthquake Data Center (NCEDC) archive. These include the 5 MPBO sites. Nine of the 30 stations are non-backbone stations that have not been upgraded to continuous telemetry. Though collection of data from these sites has been discontinued, their borehole sensor packages are still in place (having been grouted in), and efforts to find funding for upgrade of these sites with Quanterra Q4120, Q730, or Q330 data loggers and continuous telemetry continue. Two previously active backbone sites (BBEB and SMCB) have been taken out of service permanently. BBEB was taken out of service when its sensor cable was severed by contractors during seismic retrofit work on the east span of the Bay Bridge in August of 2007. The site now operates only as a telemetry repeater site. SMCB (a shallow post-hole site) was taken out of service after it was upgraded to a deep borehole installation in 2007. The upgraded deep borehole site (one of the 30 NHFN stations listed) is now named SM2B.

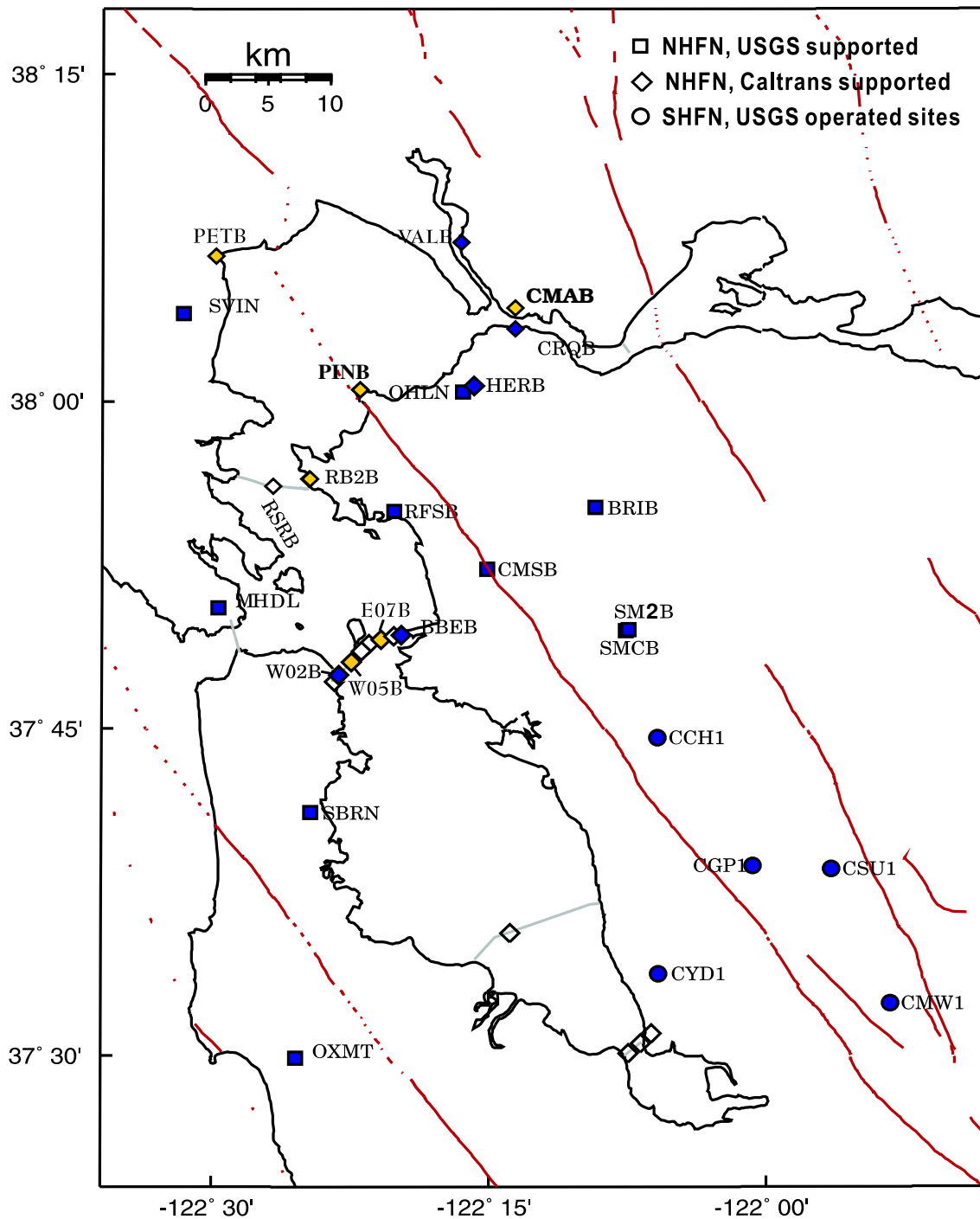


Figure 3.10: Map showing the locations of the HFN stations operated by the BSL (NHFN - squares and diamonds) and the USGS (SHFN - circles). Operational sites are filled blue/black, while sites in progress are yellow/grey. Other instrumented but currently non-operational boreholes are indicated as open symbols. Currently, station BBEB operates only as a telemetry repeater site because access to the borehole was cut off during seismic retrofit work on the eastern span of the Bay Bridge.

Code	Net	Latitude	Longitude	Elev (m)	Over (m)	Date	Location
VALB	BK	38.1215	-122.2753	-24	155.8	2005/11 - current	Napa River Bridge
PETB	BK	38.1189	-122.5011	-30	113	in progress	Petaluma River Bridge
CMAB*	BK	38.06885	-122.22909	19.2	tbd	in progress	Cal Maritime Academy
CRQB	BK	38.05578	-122.22487	-25	38.4	1996/07 - current	CB
HERB	BK	38.01250	-122.26222	-25	217.9	2000/05 - current	Hercules
PINB*	BK	38.0113	-122.3653	tbd	tbd	in progress	Point Pinole
BRIB	BK	37.91886	-122.15179	219.7	108.8	1995/06 - current	BR, Orinda
RFSB	BK	37.91608	-122.33610	-27.3	91.4	1996/01 - current	RFS, Richmond
CMSB	BK	37.87195	-122.25168	94.7	167.6	1994/12 - current	CMS, Berkeley
SMCB	BK	37.83881	-122.11159	180.9	3.4	1997/12 - 2007/06	SMC, Moraga
SM2B	BK	37.8387	-122.1102	200	150.9	2007/06 - current	SMC, Moraga
SVIN	BK	38.03325	-122.52638	-21	158.7	2003/08 - current	MPBO, St. Vincent's school
OHLN	BK	38.00742	-122.27371	-0	196.7	2001/07 - current	MPBO, Ohlone Park
MHDL	BK	37.84227	-122.49374	94	160.6	2006/05 - current	MPBO, Marin Headlands
SBRN	BK	37.68562	-122.41127	4	157.5	2001/08 - current	MPBO, San Bruno Mtn.
OXMT	BK	37.4994	-122.4243	209	194.2	2003/12 - current	MPBO, Ox Mtn.
BBEB	BK	37.82167	-122.32867	-31	150.0	2002/05 - 2007/08 *	BB, Pier E23
E17B	BK	37.82086	-122.33534		160.0	1995/08 - current *	BB, Pier E17
E07B	BK	37.81847	-122.34688	tbd	134.0	1996/02 - current *	BB, Pier E7
YBIB	BK	37.81420	-122.35923	-27.0	61.0	1997/12 - current *	BB, Pier E2
YBAB	BK	37.80940	-122.36450		3.0	1998/06 - current *	BB, YB Anchorage
W05B	BK	37.80100	-122.37370	tbd	36.3	1997/10 - current *	BB, Pier W5
W02B	BK	37.79120	-122.38525	-45	57.6	2003/06 - current	BB, Pier W2
SFAB	BK	37.78610	-122.3893		0.0	1998/06 - current *	BB, SF Anchorage
RSRB	BK	37.93575	-122.44648	-48.0	109.0	1997/06 - current *	RSRB, Pier 34
RB2B	BK	37.93	-122.41	tbd	133.8	in progress	RSRB, Pier 58
SM1B	BK	37.59403	-122.23242		298.0	not recorded	SMB, Pier 343
DB3B	BK	37.51295	-122.10857		1.5	1994/09 - 1994/11	DB, Pier 44
					62.5	1994/09 - 1994/09	
					157.9	1994/07 - current *	
DB2B	BK	37.50687	-122.11566		189.2	1994/07 - current *	DB, Pier 27
					0.0	1992/07 - 1992/11	
DB1B	BK	37.49947	-122.12755		1.5	1994/07 - 1994/09	DB, Pier 1
					71.6	1994/09 - 1994/09	
					228.0	1993/08 - current *	
CCH1	NC	37.7432	-122.0967	226		1995/05 - current	Chabot
CGP1	NC	37.6454	-122.0114	340		1995/03 - current	Garin Park
CSU1	NC	37.6430	-121.9402	499		1995/10 - current	Sunol
CYD1	NC	37.5629	-122.0967	-23		2002/09 - current	Coyote
CMW1	NC	37.5403	-121.8876	343		1995/06 - current	Mill Creek

Table 3.5: Stations of the Hayward Fault Network. Each HFN station is listed with its station code, network id, location, operational dates, and site description. The latitude and longitude (in degrees) are given in the WGS84 reference frame. The elevation of the well head (in meters) is relative to the WGS84 reference ellipsoid. The overburden is given in meters. The start dates indicate either the upgrade or installation time. The abbreviations are: BB - Bay Bridge; BR - Briones Reserve; CMS - Cal Memorial Stadium; CB - Carquinez Bridge; DB - Dumbarton Bridge; MPBO - Mini-Plate Boundary Observatory; RFS - Richmond Field Station; RSRB - Richmond-San Rafael Bridge; SF - San Francisco; SMB - San Mateo Bridge; SMC - St. Mary's College; and YB - Yerba Buena. The \* for stations CMAB and PINB indicates that the station name has not yet been approved and may change. The \* in the Date column indicates the stations that have recorded data from an earlier period (some manually retrieved from tapes), but that are currently off-line. Note that due to Bay Bridge retrofit work, station BBEB now operates only as a telemetry relay station and no longer records seismic activity.

Site	Geophone	Accelerometer	Z	H1	h2	data logger	Notes	Telem.
VALB	Oyo HS-1	Wilcoxon 731A	TBD	TBD	TBD	Q330		FR
PETB	Oyo HS-1	Wilcoxon 731A	TBD	TBD	TBD	TBD		TBD
CMAB	Oyo HS-1	Wilcoxon 731A	TBD	TBD	TBD	TBD		TBD
CRQB	Oyo HS-1	Wilcoxon 731A	-90	251	341	Q4120		FR
HERB	Oyo HS-1	Wilcoxon 731A	-90	TBD	TBD	Q4120		FR
PINB	Oyo HS-1	Wilcoxon 731A	TBD	TBD	TBD	TBD		TBD
BRIB	Oyo HS-1	Wilcoxon 731A	-90	79	349	Q4120	Acc. failed, Dilat.	FR
RFSB	Oyo HS-1	Wilcoxon 731A	-90	256	346	Q4120		FR
CMSB	Oyo HS-1	Wilcoxon 731A	-90	19	109	Q4120		FR
SMCB	Oyo HS-1	Wilcoxon 731A	-90	76	166	None at present	Posthole	FR
SM2B	Oyo HS-1	Wilcoxon 731A	TBD	TBD	TBD	Q4120		FR
SVIN	Mark L-22		-90	298	28	Q4120	Tensor.	FR/Rad.
OHLN	Mark L-22		-90	313	43	Q4120	Tensor.	FR
MHDL	Mark L-22		-90	TBD	TBD	Q4120	Tensor.	FR
SBRN	Mark L-22		-90	347	77	Q4120	Tensor.	FR
OXMT	Mark L-22		-90	163	253	Q4120	Tensor.	FR
BBEB	Oyo HS-1	Wilcoxon 731A	-90	TBD	TBD	None at present	Acc. failed	Radio
E17B	Oyo HS-1	Wilcoxon 731A	-90	TBD	TBD	None at present		
E07B	Oyo HS-1	Wilcoxon 731A	-90	TBD	TBD	None at present		
YBIB	Oyo HS-1	Wilcoxon 731A	-90	257	347	None at present	Z geop. failed	FR/Rad.
YBAB	Oyo HS-1	Wilcoxon 731A	-90	TBD	TBD	None at present		
W05B	Oyo HS-1	Wilcoxon 731A	-90	TBD	TBD	None at present		
W02B	Oyo HS-1	Wilcoxon 731A	-90	TBD	TBD	Q4120		Radio
SFAB	None	LLNL S-6000	TBD	TBD	TBD	None at present	Posthole	
RSRB	Oyo HS-1	Wilcoxon 731A	-90	50	140	None at present	2 acc. failed	FR
RB2B	Oyo HS-1	Wilcoxon 731A	-90	TBD	TBD	None at present	1 acc. failed	
SM1B	Oyo HS-1	Wilcoxon 731A	-90	TBD	TBD	None at present		
DB3B	Oyo HS-1	Wilcoxon 731A	-90	TBD	TBD	None at present	Acc. failed	
DB2B	Oyo HS-1	Wilcoxon 731A	-90	TBD	TBD	None at present		
DB1B	Oyo HS-1	Wilcoxon 731A	-90	TBD	TBD	None at present	Acc. failed	
CCH1	Oyo HS-1	Wilcoxon 731A	-90	TBD	TBD	Nanometrics HRD24	Dilat.	Radio
CGP1	Oyo HS-1	Wilcoxon 731A	-90	TBD	TBD	Nanometrics HRD24	Dilat.	Radio
CSU1	Oyo HS-1	Wilcoxon 731A	-90	TBD	TBD	Nanometrics HRD24	Dilat.	Radio
CYD1	Oyo HS-1	Wilcoxon 731A	-90	TBD	TBD	Nanometrics HRD24	Dilat.	Radio
CMW1	Oyo HS-1	Wilcoxon 731A	-90	TBD	TBD	Nanometrics HRD24	Dilat.	Radio

Table 3.6: Instrumentation of the HFN as of 06/30/2008. Every HFN downhole package consists of collocated 3-component geophones and accelerometers, with the exception of MPBO sites which have only 3-component geophones and are also collecting tensor strainmeter data. Six HFN sites (5 of the SHFN and 1 of the NHFN) also have dilatometers (Dilat.). Currently, 13 NHFN sites have Quanterra data loggers with continuous telemetry to the BSL. The remaining backbone sites are either still being developed with support from Caltrans or are being upgraded to Quanterra data loggers. The 5 SHFN sites have Nanometrics data loggers with radio telemetry to the USGS. The orientation of the sensors (vertical - Z, horizontals - H1 and H2) are indicated where known or identified as "to be determined" (TBD).

The remaining 6 sites (PETB, RB2B, E07B, W05B, CMAB, and PINB) are in the process of being added to the NHFN backbone. Four of the sites have been drilled and instrumented and are awaiting installation of their infrastructures, electronics, and telemetry (PETB, RB2B, E07B, and W05B). As of the writing of this report, drilling (provided by Caltrans) has begun on an

additional site (CMAB) located at the Cal Maritime Academy. This site is intended to replace a particularly noisy backbone station at the south end of the Carquinez bridge (CRQB). With support for drilling and the purchase of a sensor package from Caltrans, the plan is to transfer the surface infrastructure and recording equipment at CRQB to the Cal Maritime site once drilling has

Sensor	Channel	Rate (sps)	Mode	FIR
Accelerometer	CL?	500.0	T	Ca
Accelerometer	HL?	200.0	C	Ca
Accelerometer	BL?	20.0	C	Ac
Accelerometer	LL?	1.0	C	Ac
Geophone	DP?	500.0	T,C	Ca
Geophone	EP?	200.0	C	Ca
Geophone	EP?	100.0	C	Ca
Geophone	BP?	20.0	C	Ac
Geophone	LP?	1.0	C	Ac

Table 3.7: Typical data streams acquired at NHFN sites, with channel name, sampling rate, sampling mode, and FIR filter type. C indicates continuous, T triggered, Ca causal, and Ac acausal. Typically, the DP1 continuous channel is archived and the remaining high sample rate data (i.e., CL and DP channels) are archived as triggered snippets. Prior to September 2004, however, only triggered data was archived for all high sample rate channels. Currently operational stations CRQB, HERB, BRIB, RFSB, CMSB, SM2B, and W02B record at maximum sample rates of 500 Hz; VALB at maximum 200 Hz and MPBO sites (SVIN, OHLN, MHDL, SBRN, OXMT) at maximum 100 Hz.

been completed.

After complex negotiations involving (among others) the East Bay Regional Parks District and UNAVCO, permission was given to create an additional site (PINB) at Pt. Pinole Regional Park. However, it has now been recognized that installation of a deep borehole at this site is potentially not feasible due to environmental issues (in the past, the park had been a dynamite manufacturing facility, leaving the possibility that liberation of chemical contaminants may occur from extraction of borehole materials during drilling). We are currently in the process of evaluating the situation further to decide whether or not the PINB installation will need to be abandoned in favor of an alternative future site.

*Installation/Instrumentation:* The NHFN Sensor packages are generally installed at depths ranging between 100 and 200 m, the non-backbone, non-operational Dumbarton bridge sites being exceptions with sensors at multiple depths (Table 3.5).

The five former MPBO sites that are now part of the NHFN have 3-component borehole geophone packages. Velocity measurements for the MPBO sites are provided by Mark Products L-22 2 Hz geophones (Table 3.6). All the remaining backbone and non-backbone NHFN sites have six-component borehole sensor packages. The six-component packages were designed and fabricated at LBNL’s Geophysical Measurement Facility and have three channels of acceleration, provided by

Wilcoxon 731A piezoelectric accelerometers, and three channels of velocity, provided by Oyo HS-1 4.5 Hz geophones.

The 0.1-400 Hz Wilcoxon accelerometers have lower self-noise than the geophones above about 25-30 Hz, and remain on scale and linear to 0.5 g. In tests performed in the Byerly vault at UC Berkeley, the Wilcoxon is considerably quieter than the FBA-23 at all periods, and is almost as quiet as the STS-2 between 1 and 50 Hz.

All 13 operational NHFN backbone sites have Quanterra data loggers with continuous telemetry to the BSL. Signals from these stations are digitized at a variety of data rates up to 500 Hz at 24-bit resolution (Table 3.7). The data loggers employ causal FIR filters at high data rates and acausal FIR filters at lower data rates.

*Data Rates and Channels:* Because of limitations in telemetry bandwidth and disk storage, 7 of the 8 (excluding VALB) six-component NHFN stations transmit maximum 500 Hz data, one channel of geophone data continuously (i.e., their vertical geophone channels), and an additional 3 channels of triggered data in 90 sec. snippets. A Murdock, Hutt, and Halbert (MHH) event detection algorithm (*Murdock and Hutt, 1983*) is operated independently at each station on 500 sps data for trigger determinations. Because the accelerometer data is generally quieter, the 3 triggered channels are taken from the Wilcoxon accelerometers when possible. However, there is a tendency for these powered sensors to fail, and, in such cases, geophone channels are substituted for the failed accelerometers. Station VALB also transmits data from only 4 channels; however, all channels are transmitted continuously at a maximum of 200 Hz sampling. Continuous data for all channels at reduced rates (20 and 1 sps) are also transmitted to and archived at the BSL. The five MPBO originated sites transmit their 3-component continuous geophone data streams, which are also archived at BSL, at 100, 20, and 1 sps.

*Integration with the NCSS, SeisNetWatch, and SeismicQuery:* The NHFN is primarily a research network that complements regional surface networks by providing downhole recordings of very low amplitude seismic signals (e.g., from micro-earthquakes or non-volcanic tremor) at high gain and low noise. Nonetheless, we have now also completed the integration of data flow from all operating NHFN stations into the Northern California Seismic System (NCSS) real-time/automated processing stream for response applications and collection of basic data for long-term hazards mitigation. The NCSS is a joint USGS (Menlo Park) and Berkeley Seismological Laboratory (BSL) entity with earthquake reporting responsibility for Northern California, and data from networks operated by both institutions are processed

jointly to fulfill this responsibility.

Through this integration, the NHFN picks, waveforms, and NCSS event locations and magnitudes are automatically entered into a database where they are immediately available to the public through the NCEDC and its DART (Data Available in Real Time) buffer. The capability for monitoring state of health information for all NHFN stations using SeisNetWatch has also now been added, and up-to-date dataless SEED formatted metadata is now made available by the NCEDC with the SeisQuery software tool.

### Station Maintenance

Ongoing network maintenance involves regular inspection of the collected seismic waveform data and spectra of nearby seismic events, and also of noise samples. Other common problems include changes to background noise levels due to ground loops and failing preamps, as well as power and telemetry issues. Troubleshooting and remediation of problems often benefit from a coordinated effort, with a technician at the BSL examining seismic waveforms and spectra while the field technicians are still on site. BSL technicians and researchers regularly review data and assist in troubleshooting.

The NHFN station hardware has proven to be relatively reliable. Nonetheless, numerous maintenance and performance enhancement measures are still carried out. In particular, when a new station is added to the backbone, extensive testing and correction for sources of instrumental noise (e.g., grounding related issues) and telemetry through-put are carried out to optimize the sensitivity of the station. Examples of maintenance and enhancement measures that are typically performed include: 1) testing of radio links to ascertain reasons for unusually large numbers of dropped packets, 2) troubleshooting sporadic problems with numerous frame relay telemetry dropouts, 3) manual power recycle and testing of hung Quanterra data loggers, 4) replacement of blown fuses or other problems relating to dead channels identified through remote monitoring at the BSL, 5) repair of frame relay and power supply problems when they arise, and 6) correcting problems that arise due to various causes, such as weather or cultural activity.

As an example, this year maintenance visits were necessary at several of the MPBO stations. At OHLN, BSL and USGS instruments are collocated. Power is provided by the local school district. Several times during the past year, power to the seismic site failed mysteriously and was restored after BSL personnel contacted the school. In May of 2009, BSL engineers contacted the school district to replace the AC circuit breaker. Since it was replaced, power has not failed again. All of the back up batteries that were originally installed in 2001 were also replaced. At the station SBRN, all of the batteries were replaced, and additional

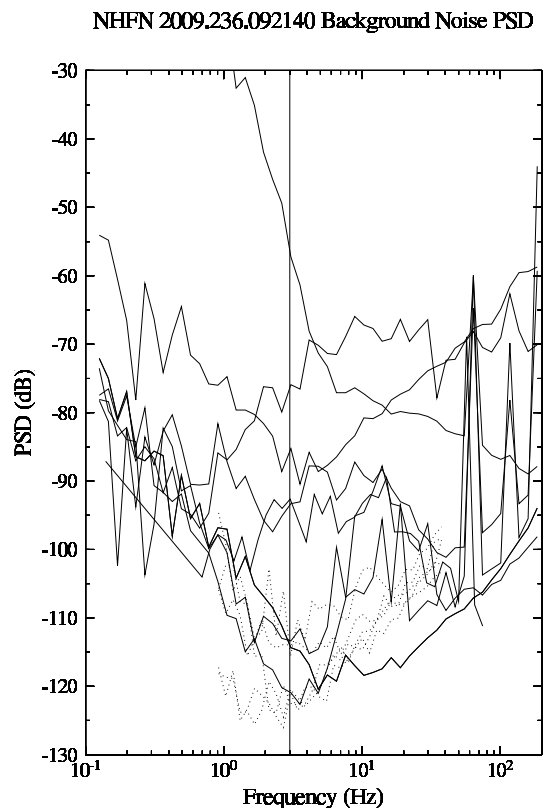


Figure 3.11: Plot showing typically observed background noise PSD for the NHFN borehole stations (including the MPBO in dashed lines) as a function of frequency. The data are for a 50 sec period on August 24, 2009 beginning at 02:21:40 (AM) local time on a Monday morning. Note that there is considerable variation in the general level and structure of the individual station background noise PSD estimates. The signals from three of the stations (RFSB, SM2B, and VALB) have 60 Hz noise (sometimes accompanied by 120 and 180 Hz harmonics), which is indicative of the presence of ground loops that need to be addressed. The PSD ranking (lowest to highest) of the stations at 3 Hz (near minimum PSD for most NHFN stations) is:

- OXMT.BK.EP1 -122.49
- SVIN.BK.EP1 -120.97
- CMSB.BK.DP1 -120.94
- OHLN.BK.EP1 -120.46
- SBRN.BK.EP1 -115.60
- BRIB.BK.DP1 -114.34
- MHDL.BK.EP1 -113.98
- SM2B.BK.DP1 -113.35
- HERB.BK.DP1 -93.31
- VALB.BK.EP1 -92.63
- RFSB.BK.DP1 -85.24
- CRQB.BK.DP1 -75.93
- W02B.BK.DP1 -57.26

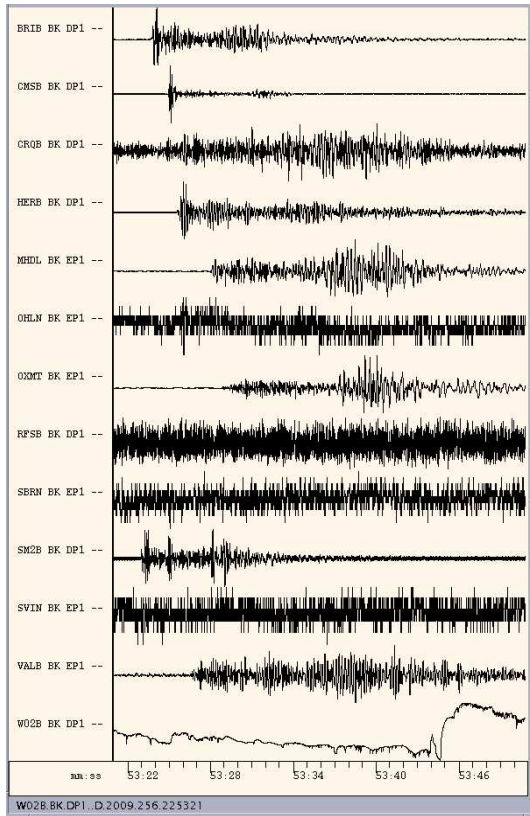


Figure 3.12: Plot of unfiltered P-wave seismograms, recorded on the geophones of the 13 NHFN borehole stations operational at the time of a recent Bay Area earthquake (13 September 2009, M3.2 Brentwood, CA). This event was exceptionally deep (14.1 km depth) and occurred  $\sim 40$  km east of the center of the NHFN. Despite its distance and small magnitude, the event was well recorded by several of the NHFN stations. However, it is also clear from the varied responses of the stations that some stations are either much more sensitive or more noisy than others. In addition, some stations were entirely unresponsive to seismic signals from this event. Both conditions indicate that the NHFN was under-performing during this event, and corrective actions are being taken.

batteries were installed to increase the reserve capacity. At SVIN, the internal disk drive of the data logger failed and was replaced.

#### Quality Control

- **Power Spectral Density Analyses:** One commonly used quality check on the performance of the borehole installed network includes assessment of the power spectral density (PSD) distributions of background noise. Figure 3.11 shows PSD of background noise for vertical geophone components of the 13 operating NHFN stations for a 50 second interval on August 24, 2009, beginning at 02:21:40 PDT (early Monday morning).

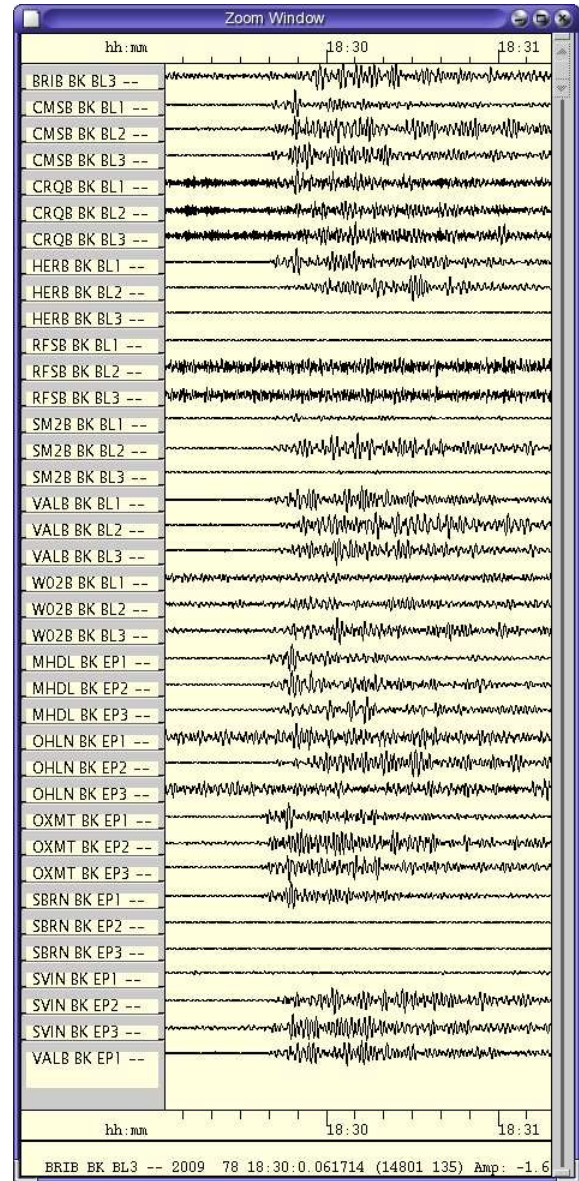


Figure 3.13: Plot of P-wave seismograms of the teleseismic  $M_w$  7.6 earthquake in the Tonga region (Lat.: 23.050S; Lon.: 174.668W; depth 34 km) occurring on March 19, 2009 18:17:40 (UTC) recorded on the DP1 (vertical) channels of the 13 NHFN borehole stations in operation at the time. Here, vertical component geophone (velocity) data have been 0.1-0.5 Hz bandpass filtered, and the highest available sampling rate for a given component is plotted. In this case, corrections for differences in instrument responses (e.g., between geophones and accelerometers) were not made.

By periodically generating such plots, we can rapidly evaluate the network's recording of seismic signals across the wide high-frequency spectrum of the borehole NHFN sensors. Changes in the re-

sponses often indicate problems with the power, telemetry, or acquisition systems or with changing conditions in the vicinity of station installations that are adversely affecting the quality of the recorded seismograms. In general, background noise levels of the borehole NHFN stations are more variable and generally higher than those of the Parkfield HRSN borehole stations (see Parkfield Borehole Network section). This is due in large part to the significantly greater cultural noise in the Bay Area and the siting of several near-field NHFN sites in proximity to bridges.

On average, the MPBO component of the NHFN sites is more consistent and somewhat quieter. This is due in large part to the greater average depth of the MPBO sensors, the locations of MPBO stations in regions with generally less industrial and other cultural noise sources, and possibly to the absence of powered sensors (i.e. accelerometers) in their borehole sensor packages.

One of the most pervasive problems at NHFN stations equipped with the Q4120 data loggers is power line noise (60 Hz and its harmonics at 120 and 180 Hz). This noise reduces the sensitivity of the MHH detectors and can corrupt research based on full waveform analyses. When NHFN stations are visited, the engineer at the site and a seismologist at the BSL frequently work together to identify and correct ground-loop problems, which often generate 60, 120, and 180 Hz contamination from inductively coupled power line signals.

- **Real Event Displays:** Another method for rapid assessment of network performance is to generate and evaluate the seismograms from moderate local and large teleseismic earthquakes recorded by the NHFN stations. This is an essential component of NHFN operations because the seismic data from local, regional, and teleseismic events is telemetered directly to the BSL and made available to the Northern California Seismic System (NCSS) real-time/automated processing stream within a few seconds of being recorded by the NHFN for seismic response applications.

Shown in Figure 3.12 is an example display of NHFN geophone channels for a local M3.2 event (13 September 2009, M3.2 near Brentwood, CA) occurring ~ 40 km east of the center of the NHFN at 14.1 km depth. It is immediately apparent from this simple display that the vertical components at stations OHLN, RFSB, SBRN, SVIN, and W02B were either insensitive to or entirely unresponsive to this event, indicating an immediate need for attention by field personnel. Upon closer inspection, the presence of a 60 Hz buzz exists at stations

SBRN and HERB, indicating that the grounding schemes for these channels is in need of modification. At any given station, 60 Hz related noise sources can change over periods of weeks to months, requiring continued vigilance and adaptability of the grounding scheme in order to maintain the desired high sensitivity to low amplitude seismic signals. recorded on the DP1 (vertical) channels of the 13 NHFN borehole stations in operation at the time. Here, vertical component geophone (velocity) data have been 0.1-0.5 Hz bandpass filtered, and the highest available sampling rate for a given component is plotted.

Figure 3.13 shows a plot of 0.1-0.5 Hz bandpass filtered ground velocity P-wave seismograms from the teleseismic  $M_w$  7.6 earthquake in the Tonga region (Lat.: 23.050S; Lon.: 174.668W; depth 34 km) occurring on March 19, 2009 18:17:40 (UTC) as recorded by all operational channels (geophones and accelerometers) of the NHFN borehole stations. On this date and for this frequency band overall network performance appears significantly better than that observed for the local event shown in Figure 3.12. This serves to illustrate the value of routine evaluation of both local (higher frequency) and teleseismic (lower frequency) events when monitoring the state of health of the NHFN.

Owing to their near similar source-receiver paths, signals from teleseismic events also serve as a good source for examining the relative responses of the BK borehole network station/components to seismic ground motion, after correction for differences in instrument response among the stations. By rapidly generating such plots (particularly with correction for instrument response) following large teleseismic events, quick assessment of the NHFN seismometer responses to real events are easily done and corrective measures implemented with relatively little delay.

- **Geophone Calibration Tests:** Comparisons of the inferred ground accelerations generated by local earthquakes from co-sited NHFN geophone and accelerometer pairs show that the waveforms generally are quite coherent in frequency and phase response, but that their inferred ground accelerations differ significantly. At times, the amplitudes differ by up to a factor of 2 while the times of the peak amplitudes are identical. This implies that the free period and damping of the geophones are well characterized. However, it also indicates that the generator constant is not accurate (assuming that the corresponding ground accelerations inferred from the accelerometers are accurate).

Generally speaking, the accelerometers, being an

active device, are more accurate and also more stable than the geophones, so it is reasonable to assume that the most likely reason for the difference is that the assumed generator constants for the geophones are inaccurate. *Rodgers et al.* (1995) describe a way to absolutely calibrate the geophones in situ and to determine their generator constant, free period and fraction of critical damping. The only external parameter that is required is the value of the geophone's inertial mass.

We have built a calibration test box which allows us to routinely perform the testing described by *Rodgers et al.* during site visits. The box drives the signal coil with a known current step and rapidly switches the signal coil between the current source and the data logger input. From this information, expected and actual sensor response characteristics can be compared and corrections applied. Also, changes in the sensor response over time can be evaluated so that adjustments can be made, and pathologies arising in the sensors due to age can be identified. Once a geophone is absolutely calibrated, we also check the response of the corresponding accelerometer.

### 3.3 2008-2009 Activities

Over the past year, in addition to routine maintenance, operations, quality control, and data collection, NHFN project activities have included: b) efforts to obtain additional funds for future upgrade and expansion of the network, c) leveraging NHFN activities through partnerships with various institutions outside of BSL, d) network adaptations to compensate for changing conditions associated with retrofit work on Bay Area bridges, and e) new station additions and network expansion efforts.

#### Additional Funding

Operation of this Bay Area borehole network is funded by the ANSS and through a partnership with the California Department of Transportation (Caltrans). ANSS provides operations and maintenance (O&M) support for a fixed subset of 9 operational stations that were initiated as part of previous projects in which the USGS was a participant. Caltrans provides developmental and O&M support for an additional 10 stations that have been or are in the process of being added to the network with Caltrans partnership grants. Caltrans also continues to provide additional support for upgrade and expansion when possible.

Currently, we are also in the process of preparing a competitive proposal to Caltrans to continue to expand the NHFN with additional borehole installations and to upgrade several NHFN sites with strong-motion surface sensors to provide up-hole down-hole data for fundamen-

tal research on amplification effects in the upper  $\sim 1$ -200 meters.

#### Partnerships

The NHFN is heavily leveraged through partnerships with various institutions, and we have continued to nurture and expand these relationships. Over the past year we have continued our collaborative partnerships with Caltrans, St. Mary's College, the Cal Maritime Academy, the East Bay Parks District, UNAVCO, Lawrence Berkeley National Laboratory, and non-ANSS components of the USGS (e.g., regarding potential installation at the WildCat site).

#### New Installations

Since reorganization of engineering support for the NHFN project this past year significant progress on the development has been made at 2 sites (PETB and RB2B) that we expect to have operational within a few months. At these sites deep boreholes have been drilled and instrumented, and infrastructure, power, and telemetry are in the final stages of being completed. Testing and noise reduction efforts will follow completion. Two additional sites have been instrumented and are awaiting completion of the retrofit of the Bay Bridge before being completed and brought on-line (E07B and W05B).

As of the writing of this report, permission and citing has been completed and drilling (provided by Caltrans) has begun on an additional site (CMAB) located at the Cal Maritime Academy. This site is intended to replace a particularly noisy backbone station at the south end of the Carquinez bridge (CRQB). With support for drilling and the purchase of a sensor package from Caltrans, the plan is to transfer the surface infrastructure and recording equipment at CRQB to the Cal Maritime site once drilling has been completed.

This year, complex negotiations involving (among others) the East Bay Regional Parks District and UNAVCO were finally completed, giving us permission to create borehole site (PINB) at Pt. Pinole Regional Park. However, it has now been recognized that installation of a deep borehole at this site is potentially problematic due to environmental issues (in the past, the park had been a dynamite manufacturing facility, leaving the possibility that liberation of chemical contaminants may occur from extraction of borehole materials during drilling). We are currently in the process of evaluating the situation further to decide whether or not the PINB installation will need to be abandoned in favor of an alternative future site (possibly at the Wildcat location).

### 3.4 Acknowledgments

Thomas V. McEvelly, who passed away in February 2002, was instrumental in developing the Hayward Fault

Network, and, without his dedication and hard work, the creation and continued operation of the NHFN would not have been possible.

Under Bob Nadeau's and Doug Dreger's general supervision, Rich Clymer, Doug Neuhauser, Bob Uhrhammer, Bill Karavas, John Friday, Taka'aki Taira, and Rick Lellinger all contribute to the operation of the NHFN. Bob Nadeau prepared this section with help from Taka'aki Taira and Bob Uhrhammer.

Support for the NHFN is provided by the USGS through the NEHRP grant program (grant no. 07HQAG0014) and by Caltrans through grant no. 59A0578. Pat Hipley of Caltrans has been instrumental in the effort to continue to upgrade and expand the network. Larry Hutchings and William Foxall of LLNL have also been important collaborators on the project in years past.

### 3.5 References

Rodgers, P.W., A.J. Martin, M.C. Robertson, M.M. Hsu, and D.B. Harris, Signal-Coil Calibration of Electromagnetic Seismometers, *Bull. Seism. Soc. Am.*, 85(3), 845-850, 1995.

Murdock, J. and C. Hutt, A new event detector designed for the Seismic Research Observatories, *USGS Open-File-Report 83-0785*, 39 pp., 1983.

## 4 Parkfield Borehole Network (HRSN)

### 4.1 Introduction

The operation of the High Resolution Seismic Network (HRSN) at Parkfield, California began in 1987, as part of the United States Geological Survey (USGS) initiative known as the Parkfield Prediction Experiment (PPE) (*Bakun and Lindh, 1985*).

Figure 3.14 shows the location of the network, its relationship to the San Andreas fault, sites of significance from previous and ongoing experiments using the HRSN, double-difference relocated earthquake locations from 1987-1998, routine locations of seismicity from August 2002 to July 2003, nonvolcanic tremor locations from 27 July 2001 through 21 February 2009, and the epicenter of the 1966 and 2004 M6 earthquakes that motivated much of the research. The HRSN records exceptionally high-quality data, owing to its 13 closely-spaced three-component borehole sensors (generally emplaced in the extremely low attenuation and background noise environment at 200 to 300 m depth (Table 3.8), its high-frequency wide bandwidth recordings (0-100 Hz; 250 sps), and its sensitivity to very low amplitude seismic signals (e.g., recording signals from micro-earthquakes with magnitudes below magnitude 0.0  $M_L$ ).

Several aspects of the Parkfield region make it ideal for the study of small earthquakes and nonvolcanic tremors and their relationship to tectonic processes and large earthquakes. These include the fact that the network spans the SAFOD (San Andreas Fault Observatory at Depth) experimental zone, the nucleation region of earlier repeating magnitude 6 events and a significant portion of the transition from locked to creeping behavior on the San Andreas fault, the availability of three-dimensional P and S velocity models (*Michelini and McEvilly, 1991*), a long-term HRSN seismicity catalogue (complete to very low magnitudes and that includes at least half of the M6 seismic cycle), a well-defined and simple fault segment, the existence of deep nonvolcanic tremor (NVT) activity, and a relatively homogeneous mode of seismic energy release as indicated by the earthquake source mechanisms (over 90% right-lateral strike-slip).

In a series of journal articles and Ph.D. theses, the cumulative, often unexpected, results of UC Berkeley's HRSN research efforts (see: [http://seismo.berkeley.edu/seismo/faq/parkfield\\_bib.html](http://seismo.berkeley.edu/seismo/faq/parkfield_bib.html)) trace the evolution of a new and exciting picture of the San Andreas fault zone responding to its plate-boundary loading, and they are forcing new thinking on the dynamic processes and conditions within the fault zone at the sites of recurring small earthquakes and deep nonvolcanic tremors.

The Parkfield area has also become an area of focus of the EarthScope Project (<http://www.earthscope.org>)

through the deep borehole into the San Andreas Fault, the SAFOD experiment (<http://www.earthscope.org/observatories/safod>), and the HRSN is playing a vital role in this endeavor. SAFOD is a comprehensive project to drill into the hypocentral zone of repeating M  $\sim$  2 earthquakes on the San Andreas Fault at a depth of about 3 km. The goals of SAFOD are to establish a multi-stage geophysical observatory in close proximity to these repeating earthquakes, to carry out a comprehensive suite of down-hole measurements in order to study the physical and chemical conditions under which earthquakes occur, and to monitor and exhume rock, fluid, and gas samples for extensive laboratory studies (*Hickman et al., 2004*).

### 4.2 HRSN Overview

Installation of the HRSN deep (200-300m) borehole sensors initiated in late 1986, and recording of triggered 500 sps earthquake data began in 1987. The HRSN sensors are 3-component geophones in a mutually orthogonal gimbaled package. This ensures that the sensor corresponding to channel DP1 is aligned vertically and that the others are aligned horizontally. Originally a 10 station network, completed in 1988, the HRSN was expanded to 13 borehole stations in late July 2001, and the original recording systems (see previous Berkeley Seismological Laboratory (BSL) Annual Reports) were upgraded to 24 bit acquisition (Quanterra 730s) and 56K frame relay telemetry to UCB. Properties of the sensors are summarized in Table 3.9.

The 3 newest borehole stations (CCRB, LCCB, and SCYB) were added, with NSF support, at the NW end of the network as part of the SAFOD project to improve resolution of the structure, kinematics, and monitoring capabilities in the SAFOD drill-path and target zones. Figure 3.14 illustrates the location of the drill site, the new borehole sites, and locations of earthquakes recorded by the initial and upgraded/expanded HRSN.

These 3 new stations have a similar configuration to the original upgraded 10 station network and include an additional channel for electrical signals. Station descriptions and instrument properties are summarized in Tables 3.8 and 3.9. All the HRSN data loggers employ FIR filters to extract data at 250 and 20 Hz (Table 3.10).

The remoteness of the drill site and new stations required an installation of an intermediate data collection point at Gastro Peak, with a microwave link to our facility on the California Department of Forestry's (CDF) property in Parkfield. The HRSN stations use SLIP to transmit TCP and UDP data packets over bidirectional spread-spectrum radio links between the on-site data ac-

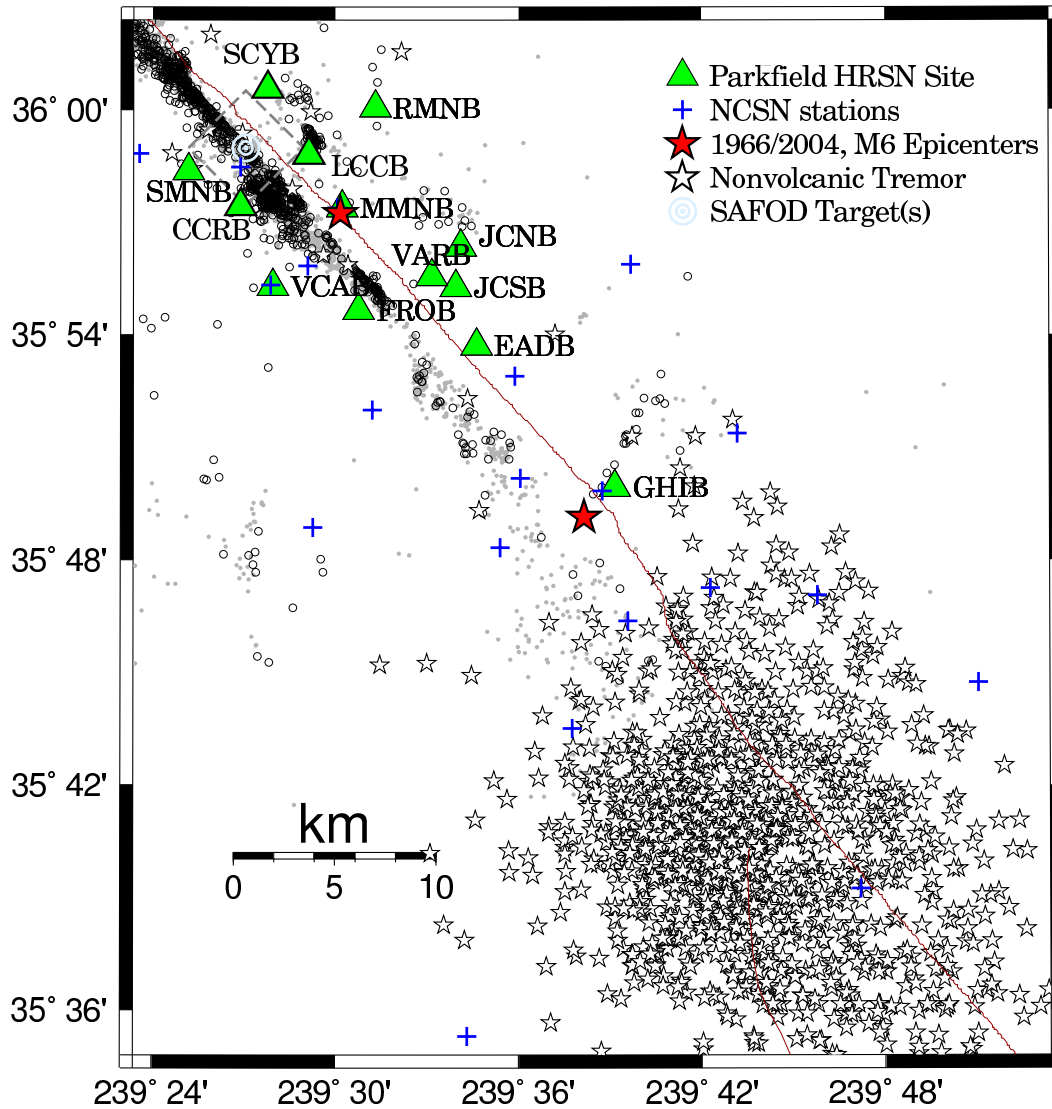


Figure 3.14: Map showing the San Andreas Fault trace and locations of the 13 Parkfield HRSN stations, the repeating M2 SAFOD targets (a 4 km by 4 km dashed box surrounds the SAFOD zone), and the epicenters of the 1966 and 2004 M6 Parkfield main shocks. Also shown are locations of nonvolcanic tremors in the Cholame, CA area (27 July 2001 through 21 February 2009), routine locations of earthquakes recorded by the expanded and upgraded 13 station HRSN (small open circles) and locations of events recorded by the earlier vintage 10 station HRSN relocated using an advanced 3-D double-differencing algorithm applied to a cubic splines interpolated 3-D velocity model (*Michelini and McEvilly, 1991*).

Site	Net	Latitude	Longitude	Surf. (m)	Depth (m)	Date	Location
EADB	BP	35.89525	-120.42286	466	245	01/1988 -	Eade Ranch
FROB	BP	35.91078	-120.48722	509	284	01/1988 -	Froelich Ranch
GHIB	BP	35.83236	-120.34774	400	63	01/1988 -	Gold Hill
JCNB	BP	35.93911	-120.43083	527	224	01/1988 -	Joaquin Canyon North
JCSB	BP	35.92120	-120.43408	455	155	01/1988 -	Joaquin Canyon South
MMNB	BP	35.95654	-120.49586	698	221	01/1988 -	Middle Mountain
RMNB	BP	36.00086	-120.47772	1165	73	01/1988 -	Gastro Peak
SMNB	BP	35.97292	-120.58009	699	282	01/1988 -	Stockdale Mountain
VARB	BP	35.92614	-120.44707	478	572	01/1988 - 08/19/2003	Varian Well
VARB	BP	35.92614	-120.44707	478	298	08/25/2003 -	Varian Well
VCAB	BP	35.92177	-120.53424	758	200	01/1988 -	Vineyard Canyon
CCRB	BP	35.95718	-120.55158	595	251	05/2001 -	Cholame Creek
LCCB	BP	35.98005	-120.51424	640	252	08/2001 -	Little Cholame Creek
SCYB	BP	36.00938	-120.53660	945	252	08/2001 -	Stone Canyon

Table 3.8: Stations of the Parkfield HRSN. Each HRSN station is listed with its station code, network id, location, date of initial operation, and site description. The latitude and longitude (in degrees) are given in the WGS84 reference frame. The surface elevation (in meters) is relative to mean sea level, and the depth to the sensor (in meters) below the surface is also given. Coordinates and station names for the 3 new SAFOD sites are given at the bottom.

Site	Sensor	Z	H1	H2	RefTek 24	Quanterra 730
EADB	Mark Products L22	-90	170	260	01/1988 - 06/1998	03/2001 -
FROB	Mark Products L22	-90	338	248	01/1988 - 06/1998	03/2001 -
GHIB	Mark Products L22	90	failed	unk	01/1988 - 06/1998	03/2001 -
JCNB	Mark Products L22	-90	0	270	01/1988 - 06/1998	03/2001 -
JCSB	Geospace HS1	90	300	210	01/1988 - 06/1998	03/2001 -
MMNB	Mark Products L22	-90	175	265	01/1988 - 06/1998	03/2001 -
RMNB	Mark Products L22	-90	310	40	01/1988 - 06/1998	03/2001 -
SMNB	Mark Products L22	-90	120	210	01/1988 - 06/1998	03/2001 -
VARB	Litton 1023	90	15	285	01/1988 - 06/1998	03/2001 -
VCAB	Mark Products L22	-90	200	290	01/1988 - 06/1998	03/2001 -
CCRB	Mark Products L22	-90	N45W	N45E	-	05/2001 -
LCCB	Mark Products L22	-90	N45W	N45E	-	08/2001 -
SCYB	Mark Products L22	-90	N45W	N45E	-	08/2001 -

Table 3.9: Instrumentation of the Parkfield HRSN. Most HRSN sites have L22 sensors and were originally digitized with a RefTek 24 system. The WESCOMP recording system failed in mid-1998 and after an approximate 3 year hiatus the network was upgraded and recording was replaced with a new 4-channel system. The new system, recording since July 27, 2001, uses a Quanterra 730 4-channel system. Three new stations were also added during the network upgrade period (bottom) with horizontal orientations that are approximately N45W and N45E. More accurate determinations of these orientations will be made as available field time permits.

Sensor	Channel	Rate (sps)	Mode	FIR
Geophone	DP?	250.0	C	Ca
Geophone	BP?	20.0	C	Ac

Table 3.10: Data streams currently being acquired at operational HRSN sites. Sensor type, channel name, sampling rate, sampling mode, and type of FIR filter are given. C indicates continuous; Ac acausal; Ca causal. “?” indicates orthogonal, vertical, and 2 horizontal components.

quisition systems and the central recording system at the CDF. Prior to June, 2008, six of the sites transmitted directly to a router at the central recording site. The other seven sites transmitted to a router at Gastro Peak, where the data are aggregated and transmitted to the central site over a 4 MBit/second digital 5.4 GHz microwave link. All HRSN data are recorded to disk at the CDF site. Due to disproportionately increasing landowner fees for access to the Gastro Peak site, we reduced our dependence on that site in the summer and fall of 2008 in cooperation with the USGS, and, as of this report, data from five of the stations previously telemetering through Gastro Peak have been re-routed through an alternative site at Hogs Canyon (HOGS).

The upgraded and expanded system is compatible with the data flow and archiving common to all the elements of the BDSN/NHFN and the NCEDC (Northern California Earthquake Data Center), and is providing remote access and control of the system. It has also provided event triggers with better timing accuracy and is also now recording continuous 20 and 250 sps data for all channels of the HRSN, which flow seamlessly into both the USGS automated earthquake detection system and into Berkeley’s NCEDC for archiving and online access to the community. The new system also helps minimize the problems of timing resolution, dynamic range, and missed detections, in addition to providing the added advantage of conventional data flow (the old system (1987-2001) recorded SEG Y format).

Another feature of the new system that has been particularly useful both for routine maintenance and for pathology identification has been the Internet connectivity of the central site processing computer and the station data loggers with the computer network at BSL. Through this connection, select data channels and on-site warning messages from the central site processor are sent directly to BSL for evaluation by project personnel. If, upon these evaluations, more detailed information on the HRSN’s performance is required, additional information can also be remotely accessed from the central site processing computer at Parkfield. Analysis of this remotely acquired information has been extremely useful for trouble shooting by allowing field personnel to schedule and

plan the details of maintenance visits to Parkfield. The connectivity also allows certain data acquisition parameters to be modified remotely when needed, and commands can be sent to the central site computer and data loggers to modify or restart processes when necessary.

The network connectivity and seamless data flow to the NCEDC also provides near-real-time monitoring capabilities that are useful for rapid evaluation of significant events as well as the network’s overall performance level. For example, shown in Figure 3.15 are P-wave seismograms of the teleseismic  $M_w$  7.6 earthquake in the Tonga region (Lat.: 23.050S; Lon.: 174.668W; depth 34 km) occurring on March 19, 2009 18:17:40 (UTC) recorded on the DP1 (vertical) channels of the 11 HRSN borehole stations in operation at the time. The seismic data from the quake was telemetered to Berkeley and available for analysis by the Northern California Seismic System (NCSS) real-time/automated processing stream within a few seconds of being recorded by the HRSN.

This is a good signal source for examining the relative responses of the BP borehole network station/components to seismic ground motion, and these and corresponding waveform plots for the horizontal (DP2 and DP3 channels) indicate that the following stations were not responding normally to seismic ground motions at the time of this event:

- JCSB.BP.DP2 - spiking - no seismic response
- JCSB.BP.DP3 - digitizer bit noise - no seismic response
- LCCB.BP.DP1 - no seismic response
- LCCB.BP.DP2 - no seismic response
- LCCB.BP.DP3 - no seismic response
- JCNB.BP.DP1 - no seismic response
- JCNB.BP.DP2 - no seismic response
- JCNB.BP.DP3 - no seismic response
- MMNB.BP.DP1 - low frequency drift - no response
- MMNB.BP.DP2 - low frequency drift - no response

In addition, the ground velocities inferred from the two horizontal components at RMNB and the DP2 horizontal at VCAB are significantly higher than the corresponding ground velocities inferred from the other operating BP network horizontal components. By rapidly generating such plots following large teleseismic events, quick assessment of the HRSN seismometer responses to real events is easily done and corrective measures implemented with relatively little delay.

## Data Flow

*Initial Processing Scheme.* Continuous data streams on all HRSN components are recorded at 20 and 250 sps on disk on the local HRSN computer at the CDF facility. These continuous data are transmitted in near-real-time to the Berkeley Seismological Laboratory (BSL) over a T1 link and then archived at the NCEDC. In addition, the near-real-time data are being transmitted over the T1 circuit to the USGS at Menlo Park, CA, where they are

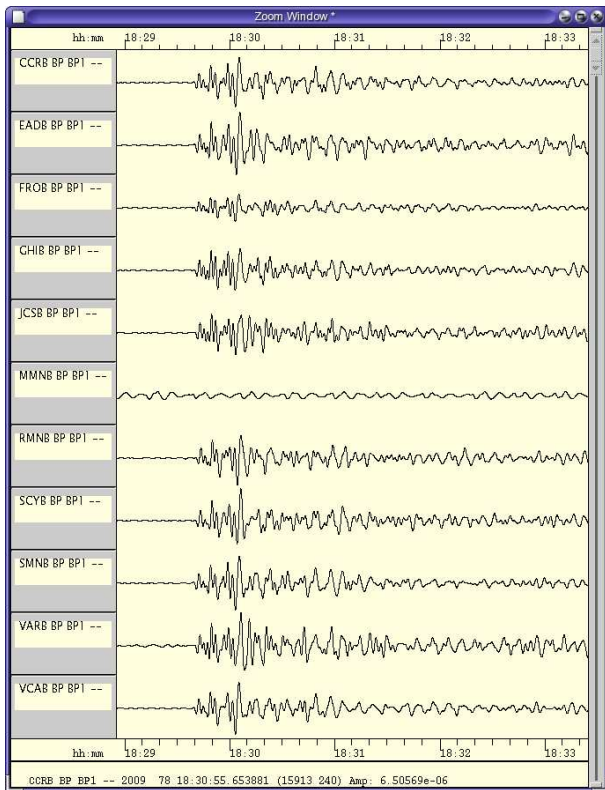


Figure 3.15: Plot of P-wave seismograms of the teleseismic  $M_w$  7.6 earthquake in the Tonga region (Lat.: 23.050S; Lon.: 174.668W; depth 34 km) occurring on March 19, 2009 18:17:40 (UTC) recorded on the DP1 (vertical) channels of the 11 HRSN borehole stations in operation at the time. Here, vertical component geophone (velocity) data have been 0.1-0.5 Hz bandpass filtered.

integrated into the Northern California Seismic System (NCSS) real-time/automated processing stream. This integration has also significantly increased the sensitivity of the NCSN catalog at lower magnitudes, effectively doubling the number of small earthquake detections in the critical SAFOD zone.

Shortly after being recorded to disk on the central site HRSN computer, event triggers for the individual station data are also determined, and a multi-station trigger association routine then processes the station triggers and generates a list of potential earthquakes. For each potential earthquake that is detected, a unique event identification number (compatible with the NCEDC classification scheme) is also assigned. Prior to the San Simeon earthquake of December 22, 2003, 30 second waveform segments were then collected for all stations and components and saved to local disk as an event gather, and event gathers were then periodically telemetered to BSL and included directly into the NCEDC earthquake database (dbms) for analysis and processing.

Because of its mandate to detect and record very low magnitude events in the Parkfield area, the HRSN is extremely sensitive to changes in very low amplitude seismic signals. As a consequence, in addition to detecting very small local earthquakes at Parkfield, the HRSN also detects numerous regional events and relatively distant and small amplitude nonvolcanic tremor events. For example, spot checks of aftershocks following the  $M_{6.5}$  San Simeon earthquake of December 22, 2003 using continuous data and HRSN event detection listings have revealed that the overwhelming majority of HRSN detections following San Simeon resulted from seismic signals generated by San Simeon's aftershocks, despite the HRSN's  $\sim 50$  km distance from the events. Data from the California Integrated Seismic Network (CISN) show that there were  $\sim 1,150$  San Simeon aftershocks with magnitudes  $> 1.8$  in the week following San Simeon, and during this same period, the number of HRSN event detections was  $\sim 10,500$  (compared to an average weekly rate before San Simeon of 115 detections). This suggests that, despite the  $\sim 50$  km distance, the HRSN is detecting San Simeon aftershocks well below magnitude 1.

*Current Processing.* Since the beginning of the network's data collection in 1987, and up until 2002, the local and regional events were discriminated based on analyst assessment of S-P times, and only local events with S-P times less than  $\sim 2.5$  s at the first arriving station were picked and located as part of the HRSN routine catalog. However, because of the network's extreme sensitivity to the large swarm of aftershocks from the San Simeon and  $M_6$  Parkfield earthquakes of September 2004 (e.g., in the first 5 months following the San Simeon mainshock, over 70,000 event detections were made by the HRSN system, compared to an average 5 month detection rate of 2500 prior to San Simeon) and because of

ever declining funding levels, this approach has had to be abandoned.

The dramatic increase in event detections vastly exceeded the HRSN's capacity to process both the continuous and triggered event waveform data. To prevent the loss of seismic waveform coverage, processing of the triggered waveform data has been suspended to allow the telemetry and archiving of the 20 and 250 sps continuous data to continue uninterrupted. Subsequent funding limitations have precluded reactivation of the processing of triggered waveform data. Cataloging of the event detection times from the modified REDI real-time system algorithm is continuing, however, and the continuous waveform data is currently being telemetered directly to the BSL and USGS over the T1 link for near-real-time processing and archiving at the NCEDC, for access to the research community.

Funding to generate catalogs of local events from the 10s of thousands of aftershock detections has not been forthcoming, and, as a consequence, major changes in our approach to cataloging events have been implemented. The HRSN data is now integrated into NCSN automated event detection, picking, and catalog processing (with no analyst review). In addition, a high resolution procedure is now being developed to automatically detect, pick, locate, double-difference relocate, and determine magnitudes for similar and repeating events down to very low magnitudes (i.e., below magnitude  $-1.0M_L$ ). These new schemes are discussed in more detail in the activities section below.

### 4.3 2008-2009 Activities

In addition to the routine operations and maintenance of the HRSN (California's first and longest operating borehole seismic network), HRSN project activities this year have been focused on: a) processing of ongoing similar and repeating very low magnitude seismicity and integrating this information into network SOH (state of health) monitoring, b) lowering operational (primarily landowner fee) and catalog production costs, c) monitoring non-volcanic tremor activity in the Parkfield-Cholame area, and d) SAFOD related activities.

#### Routine Operations and Maintenance

Routine maintenance tasks required this year to keep the HRSN in operation include cleaning and replacement of corroded electrical connections; grounding adjustments; cleaning of solar panels; re-seating, resoldering, and replacing faulty pre-amp circuit cards; testing and replacement of failing batteries; and insulation and painting of battery and data logger housings to address problems with low power during cold weather. Remote monitoring of the network's health using the Berkeley Seismological Laboratory's SeisNetWatch software is also performed to identify both problems that can be resolved

over the Internet (e.g. rebooting of data acquisition systems due to clock lockups) and more serious problems requiring field visits. Over the years, such efforts have paid off handsomely by providing exceptionally low noise recordings of very low amplitude seismic signals produced by microearthquakes (below magnitude  $0.0M_L$ ) and non-volcanic tremors.

In the spring of 2008, signals from HRSN station JCNB began showing signs of deterioration. Shortly thereafter, data flow from this station stopped completely. Field investigation showed that the borehole sensor and cable had been grouted to within  $\sim 34$  feet of the surface and that a rodent had found itself trapped in the upper 100 foot void space and chewed through the cable, thus severing the connection to the deep borehole package. At this time, costs for reestablishing connection to the cable at depth have been prohibitive, and it is also likely that the grouted-in sensor has been compromised by fluids running down the exposed cable. Hence, plans are being made to substitute either a surface seismometer or a borehole sensor package within the open 34 foot section of the borehole to provide continued seismic coverage at the JCNB site. A long-idle sensor package has been identified as a possible replacement and it is now being assessed by BSL's engineering group to confirm functionality.

The network connectivity over the T1 circuit also allows remote monitoring of various measures of the state of health of the network in near-real-time, such as background noise levels. Shown in Figure 3.16 are power spectral density (PSD) plots of background noise for the 12 operational vertical components of the HRSN for a 50 second period beginning at 2:41 AM local time on day 9/07/2009 (Monday morning). By periodically generating such plots, we can rapidly evaluate, through comparison with previously generated plots, changes in the network's station response of seismic signals across the wide band high-frequency spectrum of the borehole HRSN sensors. Changes in the responses often indicate problems with the power, telemetry, or acquisition systems, or with changing conditions in the vicinity of station installations that are adversely affecting the quality of the recorded seismograms.

Once state of health issues are identified with the PSD analyses, further remote tests can be made to more specifically determine possible causes for the problem, and corrective measures can then be planned in advance of field deployment within a relatively short period of time.

#### Similar Event Catalog

The increased microseismicity (1000's of events) resulting from the San Simeon M6.5 (SS) and Parkfield M6 (PF) events, the lack of funds available to process and catalog the increased number of micro-earthquakes, and the increased interest in using the micro-quakes in repeat-

### HRSN 2009.250.094050 Background Noise PSD

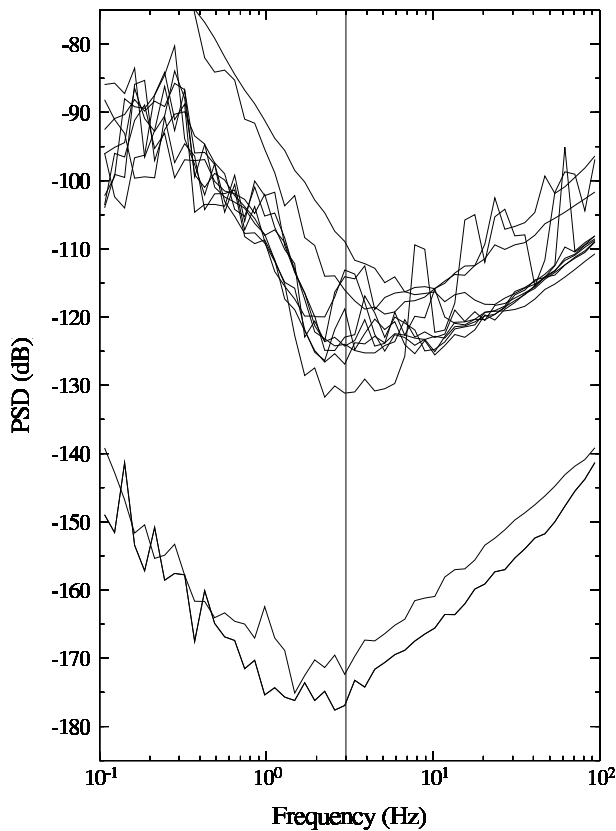


Figure 3.16: Background noise Power Spectral Density (PSD) levels as a function of frequency for the 12, 250 sps vertical component channels (DP1) of the HRSN borehole stations in operation during the 50 second period analyzed, beginning 2:41 AM local time on day 9/07/2009 (Monday morning). The approximate 2 Hz minimum of the PSD levels occurs because of the 2 Hz sensors used at these sites. Below 2 Hz, noise levels rise rapidly, and the peak at 5 to 3 sec (.2 to .3 Hz) is characteristic of teleseismic noise observed throughout California. The PSD (dB) ranking (lowest to highest) at 3 Hz (intersection with vertical line) for the vertical channels is:

CCRB.BP.DP1 -176.92  
 LCCB.BP.DP1 -172.36  
 SCYB.BP.DP1 -131.14  
 FROB.BP.DP1 -126.88  
 SMNB.BP.DP1 -124.26  
 RMNB.BP.DP1 -124.00  
 GHIB.BP.DP1 -122.93  
 EADB.BP.DP1 -118.79  
 MMNB.BP.DP1 -116.03  
 VCAB.BP.DP1 -114.06  
 JCSB.BP.DP1 -113.11  
 VARB.BP.DP1 -108.92

ing earthquake and SAFOD research have required new thinking on how to detect and catalog microearthquakes recorded by the HRSN.

One action taken to help address this problem has been to integrate HRSN data streams into the NCSN event detection and automated cataloging process. This approach has been successful at detecting and locating a significantly greater number of micro-earthquakes over the previous NCSN detection and location rate (essentially doubling the number of events processed by the NCSN). However, the HRSN sensitized NCSN catalog is still only catching about 1/2 the number of local events previously cataloged by the HRSN using the old HRSN-centric processing approach. Furthermore, triggered waveforms for the additional small NCSN processed events are not typically made available; they are not reviewed by an analyst, nor do they generally have NCSN magnitude determinations associated with them.

These limitations severely hamper research efforts relying on similar and characteristically repeating micro-seismicity such as earthquake scaling studies, SAFOD related research, deep fault slip rate estimation, and the compilation of recurrence interval statistics for time-dependent earthquake forecast models. They also reduce, to some degree, the use of recurring micro-seismicity as a tool for monitoring the state-of-health (SOH) of either the HRSN or NCSN.

To help overcome these limitations this year, we have further developed and are in the process of implementing an automated similar event cataloging scheme based on pattern matching (match filter) scans using cross-correlation of the continuous HRSN data. The method uses a set of reference events whose waveforms, picks, locations, and magnitudes have been accurately determined, and it automatically detects, picks, locates, and determines magnitudes for events similar to the reference event to the level of accuracy and precision that only relative event analysis can bring.

The similar event detection is also remarkably insensitive to the magnitude of the reference event used, allowing similar micro-events ranging over about 3 magnitude units to be fully cataloged using a single reference event, and it does a remarkably good job at discriminating and fully processing multiple superposed events.

Once a cluster of similar events has been processed, an additional level of resolution can then be achieved through the identification and classification of characteristically repeating microearthquakes (i.e., near identical earthquakes) occurring within the similar event family (Figure 3.17). The pattern scanning approach also ensures optimal completeness of repeating sequences owing to scans of the matching pattern through all available continuous data (critical for applications relying on recurrence interval information). For example, while the March 3 and April 28, 2006 events shown in Figure 3.17

were not picked up by the NCSN-HRSN integrated network, the pattern scanning approach we employ picked up both of these earthquakes.

It is immediately apparent from Figure 3.17 that on March 3, 2006, the DP1 channel was experiencing significant high amplitude step-decay spiking (due to pre-amp malfunction) and that on August 22, 2008, the signal amplitude was greatly attenuated (due to excess tension and separation of the signal cable wiring). Armed with this type of information, field engineers can quickly identify and address major problems. In addition to a visual assessment, the extreme similarity of the events lends itself to the application of differencing techniques in the time and frequency domains to automatically identify detailed SOH issues on all channels within a network.

Repeating sequences of this magnitude typically repeat every 1 to 2 years, and we are currently monitoring 25 of these sequences. Hence, on average, evaluations of this type can be made approximately every month on an automated basis. However, there are on the order of 200 such sequences known in the Parkfield area, leaving the possibility that automated SOH analyses could take place every 2 to 3 days.

For other networks recording continuously in the Parkfield area (e.g., NCSN, BDSN) it is also a relatively simple process to extend the SOH analysis using characteristic repeating events to their stations. Furthermore, numerous repeating event sequences are also known to exist in the San Francisco Bay and San Juan Bautista areas, where continuous recording takes place. Hence application of the repeating event SOH technique to these zones should also be feasible.

We are continuing to expand the number of pattern events and resulting multi-year scans to increase the frequency of sampling of similar and repeating event sequences for SOH purposes and for expanding the catalog of very small similar and repeating microearthquakes (down to  $M_p$  of -0.5). We are also adapting the codes to take advantage of faster computing now available.

Further development of the similar event processing approach also holds promise in other applications where automated and precise monitoring of bursts of seismic activity to very low magnitudes is desirable (e.g. in aftershock zones or in volcanic regions) or where automated updates of preexisting repeating sequences and their associated deep slip estimates are desired.

### Reducing Operational costs

In recent years increased scientific activity in the rural Parkfield area due to SAFOD has led to an increased demand for site access and development on privately owned property and a corresponding increase in access fees charged by private land owners. As a result, land use fees paid by the HRSN project have increased dramatically from less than \$1000 annually prior to the SAFOD

effort to over \$14,000. This represents over 15% of the entire HRSN budget, with no corresponding increase in support from the project's funding agency. To compensate for the increased landowner costs, maintenance efforts had to be cut back, and, as a result, network performance suffered.

To help alleviate the problem, this year we implemented (through cooperation with the USGS) plans to minimize our dependence on access to private lands. This primarily involved establishing alternative telemetry paths for roughly half of the HRSN sites.

To date, telemetry paths for five HRSN sites (SMNB, CCRB, MMNB, VARB, and SCYB) have been redirected from the Gastro Peak relay site to an alternative relay site at Hogs Canyon (HOGS) through an agreement with the USGS. Telemetry of GHIB data has also been redirected from Gastro Peak through an alternative path. Plans to redirect telemetry of an additional site from Gastro Peak (LCCB) are being examined and field tested for viability. This year, the landowner also chose not to renew our access agreement for Gastro-Peak, saving us approx. \$9800 in annual fees. However, the owner has allowed us to continue operating one station (RMNB) located at the Gastro-Peak site free of charge for an unspecified period of time. Until alternative telemetry is implemented, the RMNB station is also serving as a repeater for station LCCB.

### Tremor Monitoring

The HRSN data played an essential role in the discovery of nonvolcanic tremors along the San Andreas Fault (SAF) below Cholame, CA (*Nadeau and Dolenc, 2005*). The Cholame tremors occupy a critical location between the smaller Parkfield ( $\sim M6$ ) and much larger Ft. Tejon ( $\sim M8$ ) rupture zones of the SAF (Figure 3.14). Because the time-varying nature of tremor activity is believed to reflect time-varying deep deformation and presumably episodes of accelerated stressing of faults, because an anomalous increase in the rate of Cholame tremor activity preceded the 2004 Parkfield  $M6$  by  $\sim 21$  days, and because periodic episodes and continued elevated tremor activity have continued since the 2004 Parkfield event in the Parkfield-Cholame and Monarch Peak areas (*Nadeau and Guilhem, 2009*), we are continuing to monitor the tremor activity observable by the HRSN to look for anomalous rate changes that may signal an increased likelihood for another large SAF event in the region. Some recent results of the monitoring effort are described further in the "Research" section of this report.

### Efforts in Support of SAFOD

An intensive and ongoing effort by the EarthScope component called SAFOD (San Andreas Fault Observatory at Depth) is underway to drill through, sample, and monitor the active San Andreas Fault at seismogenic

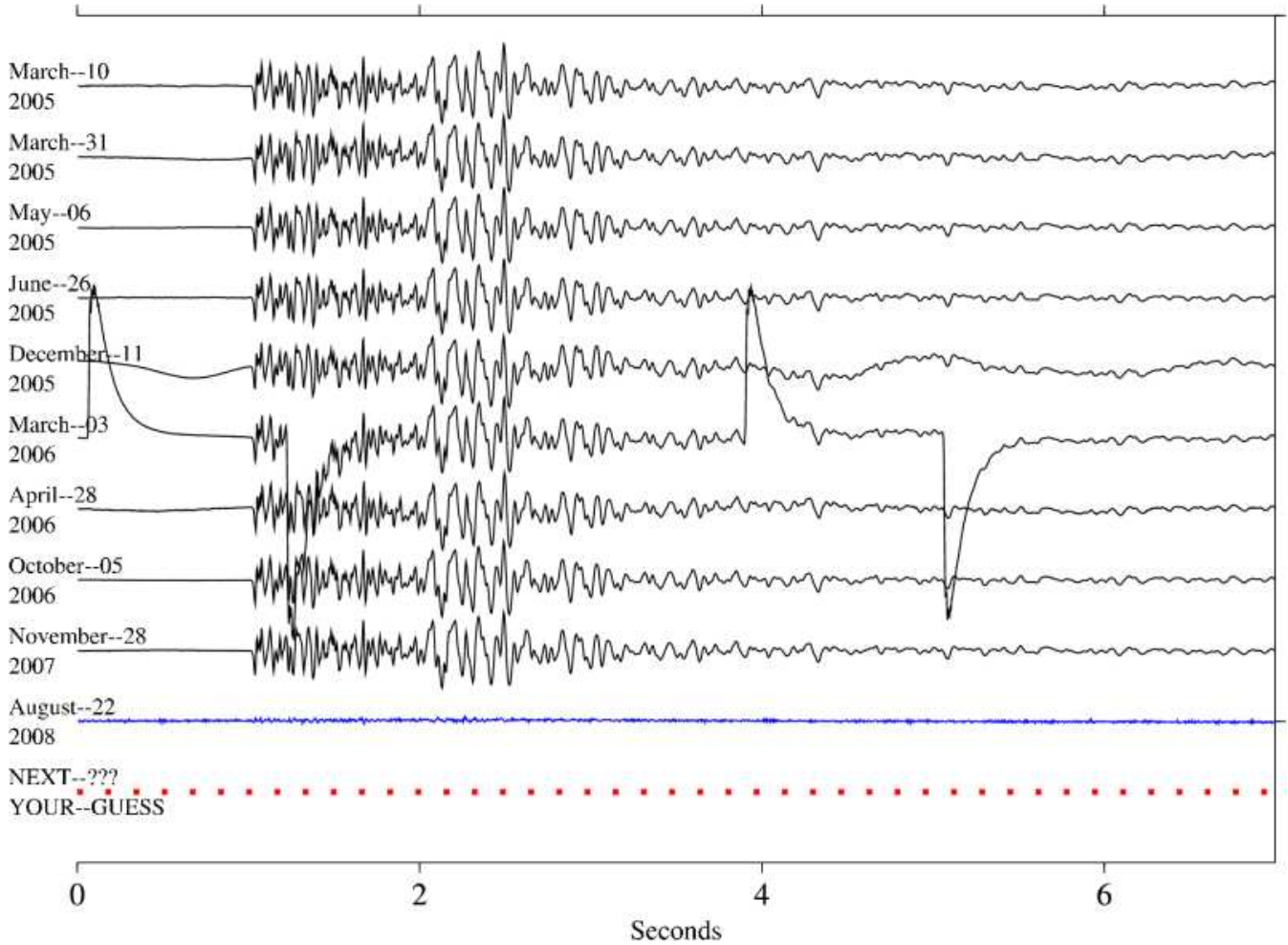


Figure 3.17: Ten most recent repeats of a characteristic sequence of repeating magnitude 0.9 (Mp, USGS preferred magnitude) microearthquakes recorded by vertical (DP1) channel of HRSN station MMNB. High-precision location and magnitude estimates of these events show they are extremely similar in waveform (typically 0.95 cross-correlation or better), nearly collocated (to within 5-10 m) and of essentially the same magnitude (+/- 0.13 Mp units). The dashed line labeled “NEXT” serves to illustrate that events in these types of sequences continue to repeat and that they can, therefore, be used for monitoring ongoing channel response relative to past performance.

depths and in very close proximity (within a few 10s of km or less) to a repeating magnitude 2 earthquake site. The HRSN data plays a key role in these efforts by providing low noise and high sensitivity seismic waveforms from active and passive sources, and by providing a backbone of very small earthquake detections and continuous waveform data.

As of early September, 2007, SAFOD drilling had penetrated the fault near the HI repeating target sequence and collected core samples in the fault region that presumably creeps and surrounds the repeatedly rupturing HI patch. Unfortunately, due to complications during drilling, penetration and sampling of the fault patch involved in repeating rupture was not possible. Future efforts will be focused on long-term monitoring of the ongoing chemical, physical, seismological, and deformational properties in the zone (particularly any signals that might be associated with the next repeat of the SAFOD repeating sequences).

HRSN activities this year have contributed in three principal ways to these and longer-term SAFOD monitoring efforts:

- 1) Integration and processing of the HRSN data streams with those from the NCSN in the Parkfield area continues, effectively doubling the number of small events available for monitoring seismicity in the target zone and for constraining relative locations of the ongoing seismic activity.

- 2) Telemetry of all HRSN channels (both 20 and 250 sps data streams) continues to flow directly from Parkfield, through the USGS Parkfield T1 and the NCEMC T1, to the USGS and the BSL for near-real-time processing, catalog processing, and data archiving on the web-based NCEDC. This also provides near immediate access of the HRSN data to the SAFOD community without the week- or month-long delay associated with the previous procedure of having to transport DLT tapes to Berkeley to upload and quality check the data.

- 3) We have also continued to apply our prototype similar event automated catalog approach to the primary, secondary, and tertiary SAFOD target zones as a continued effort to monitor the SAFOD target zone activity at very high relative location precision.

These efforts and the free access of HRSN waveform data to the SAFOD seismology group confirmed the latest repeat of the HI sequence on Aug 29 of 2008. Our monitoring efforts were also the first to report repeats of the SF and LA sequences occurring on December 19 and 20, 2008, respectively. Of particular interest were the SF and LA repeats which were recorded on the SAFOD main hole seismometer which had been installed in October.

## 4.4 Acknowledgments

Under Robert Nadeau's and Doug Dreger's general supervision, Rick Lellinger, Rich Clymer, Bob Uhrhammer, Taka'aki Taira, Doug Neuhauser, Peter Lombard, Bill Karavas, and John Friday all contribute to the operation of the HRSN. Bob Nadeau prepared this section with help from Bob Uhrhammer and Taka'aki Taira. During this reporting period, operation, maintenance, and data processing for the HRSN project was supported by the USGS, through grant 07HQAG0014.

## 4.5 References

- Bakun, W. H., and A. G. Lindh, The Parkfield, California, prediction experiment, *Earthq. Predict. Res.*, *3*, 285-304, 1985.
- Hickman, S., M.D. Zoback and W. Ellsworth, Introduction to special section: Preparing for the San Andreas Fault Observatory at Depth, *Geophys. Res. Lett.*, *31*, L12S01, doi:10.1029/2004GL020688, 2004.
- Michelini, A. and T.V. McEvilly, Seismological studies at Parkfield: I. Simultaneous inversion for velocity structure and hypocenters using B-splines parameterization, *Bull. Seismol. Soc. Am.*, *81*, 524-552, 1991.
- Nadeau, R.M. and D. Dolenc, Nonvolcanic Tremors Deep Beneath the San Andreas Fault, *SCIENCE*, *307*, 389, 2005.
- Nadeau, R.M. and A. Guilhem, Nonvolcanic Tremor Evolution and the San Simeon and Parkfield, California, Earthquakes, *SCIENCE*, *325*, 191, 2009.

## 5 Bay Area Regional Deformation Network

### 5.1 BARD overview

#### Background

BARD (Bay Area Regional Deformation network) is a network of permanent, continuously operating GPS receivers which monitors crustal deformation in the San Francisco Bay Area and northern California. Started in 1991 with two stations spanning the Hayward Fault, BARD has been a collaborative effort between the Berkeley Seismological Laboratory (BSL), the USGS at Menlo Park (USGS/MP), and several other academic, commercial and governmental institutions. At its peak, BARD collected data continuously from over 60 permanent stations in northern California, of which about half were operated by the BSL. Most of the BSL stations were collocated with broadband seismic stations of the Berkeley Digital Seismic Network (BDSN), allowing the acquisition of GPS data in real time through shared telemetry (Romanowicz *et al.*, 1994). Data are archived at the Northern California Earthquake Data Center (NCEDC), where they are available to the public over the internet. BARD has also made its data available to the community through the UNAVCO seamless archive (formerly GSAC). With the advent of the Plate Boundary Observatory (PBO), many of the BARD stations have been folded into the PBO C-GPS network. Currently, 26 stations remain in BARD, and are operated and maintained by the BSL. These stations are located along hazardous faults in the San Francisco Bay Area, and/or are collocated with seismic broadband stations of the BDSN (3.18). One station is in the process of being installed (BDM1, Black Diamond Mine). Typically acquiring data at standard sampling intervals of 15 or 30 s, many of these stations have been upgraded to high rate sampling (1Hz) over the last few years. These are stations where the combination of receiver type and telemetry bandwidth have allowed this upgrade (Table 3.11).

Of the 26 BARD sites, eleven (Table 3.11) are collocated with broadband seismic stations of the BDSN with which they share continuous frame-relay telemetry to UC Berkeley. Where old GPS receivers are installed at these sites, the Quanterra data loggers store GPS data converted to MiniSEED format so they can be retrieved (Perin *et al.*, 1998). This provides more robust data recovery from onsite backup on the Quanterra disks following a telemetry outage. New receivers have data storage and retrieval capabilities. One station is contributed by UC Davis (UCD1). Data from this station are collected continuously over the Internet.

Five stations (SVIN, MHDL, OHLN, OXMT and SBRN) were installed between 2002 and 2006 in the SFBA and in particular along the Hayward fault. These

stations represent Berkeley's part, with significant participation of the USGS/MP, of a multi-institutional effort funded by the Major Research Infrastructure (MRI) program of the NSF to improve strain monitoring in the SFBA using an integrated approach (Murray *et al.*, 2002a). The instrumentation at these stations includes borehole tensor strainmeters, three-component borehole seismic velocity sensors, downhole pore pressure and tilt sensors, and GPS receivers. This project served as a prototype for the strainmeter installations planned for PBO (Plate Boundary Observatory), which faces many of the same station installation, configuration, and data retrieval issues we have addressed. Consequently, these 5 stations have received the nickname *mini-PBO*. From July 2001 to August 2002, five boreholes were drilled to about 200-m depth and equipped with tensor strainmeters recently developed by CIW and 3-component L22 (velocity) seismometers. We developed a self-centering GPS antenna mount for the top of the borehole casings. These are mechanically isolated from the upper few meters of the ground. The system provides a stable, compact monument that allows access to the top of the borehole casing for downhole maintenance. GPS receivers were progressively installed at these sites and connected to Quanterra 4120 data loggers, which provide backup and telemetry capabilities. In addition, low sampling rate data (600 sec sampling) are retrieved from all the mini-PBO sites by the USGS via a GOES satellite system. All the sites are successfully measuring strains due to tidal effects and to local and teleseismic earthquakes (Murray *et al.*, 2002b). The remaining ten BSL/BARD stations record only C-GPS data.

There is growing interest in collecting data at higher rates for a variety of applications. For example, GPS measurements can accurately track the propagation of earthquake dynamic motions both on the ground (e.g., Larson *et al.*, 2003) and in the atmosphere (e.g., Artru *et al.*, 2001, Ducic *et al.*, 2003), providing complementary information to seismic observations (calibration of integrated acceleration and velocity sensor data) and estimates of earth structure (direct observation of surface wave propagation over the oceans). We started collecting 1 Hz observations at 2 stations (DIAB and MONB) in 2003. We have progressively upgraded the telemetry to continuous 1 Hz telemetry: 21 stations currently provide 1Hz data, with varying degrees of robustness. At stations collocated with broadband seismic sensors, the seismic data has priority for telemetry because it is used in the Northern California real-time earthquake notification system (see <http://www.cisn.org/ncmc/>). At stations equipped with Ashtech A-Z12's, this upgrade is

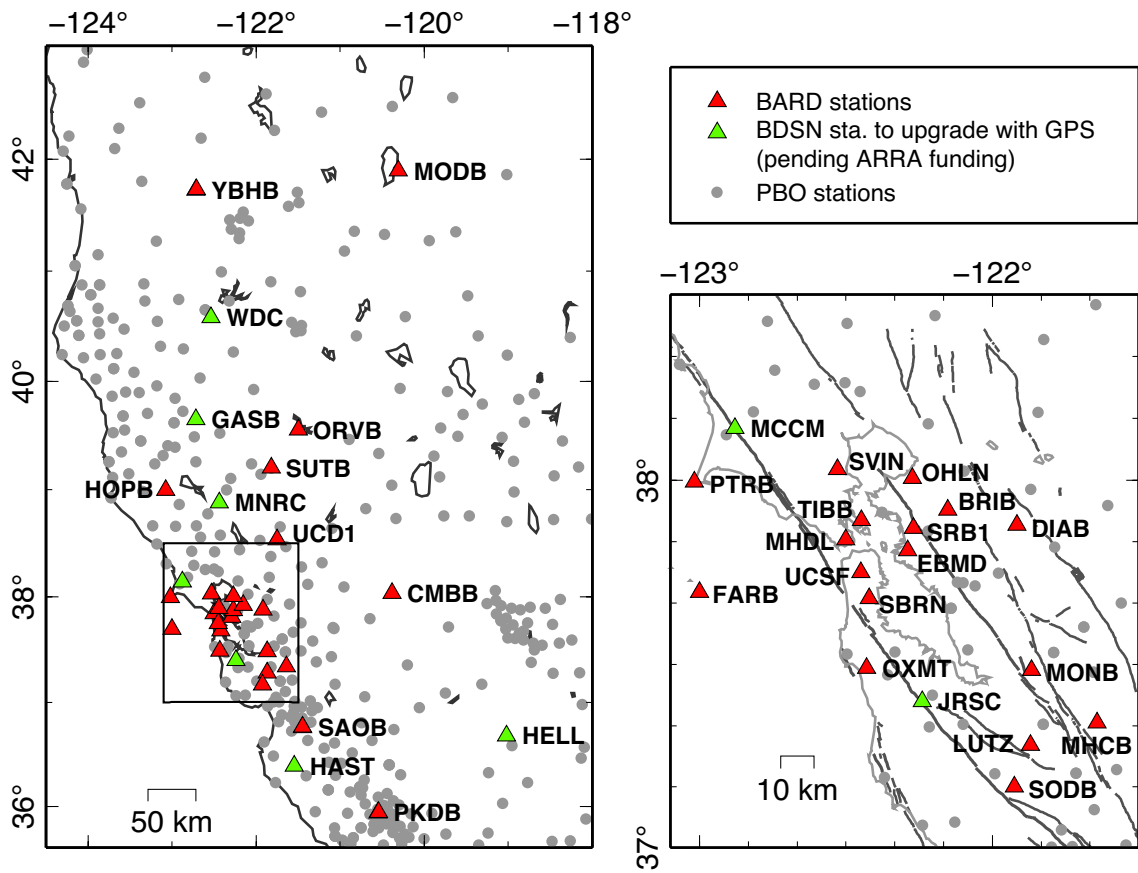


Figure 3.18: Map of the BARD network and surrounding PBO sites in northern California.

in general not feasible because of insufficient data compression.

All data collected from BARD/BSL are publicly available at the NCEDC (<http://www.ncedc.org/bard/>).

### BARD Station equipment

Ten BARD stations are currently equipped with high performance NETRS receivers, which have sufficient internal buffering to allow robust real time telemetry at 1Hz. Most recently recently we upgraded MODB to NETRS (Sept 2009). This allows us to telemeter 1Hz data from this site using the USGS VSAT system that collects seismic broadband data as part of the National Seismic Network (NSN). Other stations are still equipped with aging Z-12 receivers, which were originally programmed to record data once every 30 s. At these sites, the data are collected using direct serial connections and are susceptible to data loss during telemetry outages. Several stations are equipped with Ashtech MicroZ-CGRS (uZ). We also changed our data strategy by allowing some data to be transferred by web-based telemetry (ADSL lines). This will reduce our communication operational costs and we hope will not affect our ability to react in a large event.

We hope to upgrade the remaining old receivers over the next 2 years with ARRA funding, for which we applied to the USGS in October 2009. We also propose to install new C-GPS stations at 7 sites collocated with BDSN stations that have sufficient skyview.

The BARD stations with old GPS receivers that are collocated with broadband seismometers use the BDSN Quanterra data loggers (Table 3.11) for data acquisition. With the support of IRIS (Incorporated Research Institutions in Seismology), we developed software that converts continuous GPS data to MiniSEED opaque blockettes that are stored and retrieved from the Quanterra data loggers (*Perin et al., 1998*), providing more robust data recovery from onsite disks following telemetry outages.

Each BSL/BARD station uses a low-multipath choking antenna. With the exception of the “mini-PBO” sites, these are mounted to a reinforced concrete pillar approximately 0.5-1.0 meter above the ground level. The reinforcing steel bars of the pillar are drilled and cemented into rock outcrop to improve long-term monument stability. Low-loss antenna cable is used to minimize signal degradation at sites where long cable runs would normally require signal amplification. Low-voltage cutoff devices are installed to improve receiver performance following power outages. The antennas are equipped with SCIGN antenna adapters and hemispherical domes, designed to provide security and protection from weather and other natural phenomena, and to minimize differential radio propagation delays.

### Parkfield Stations

BSL is acquiring high rate GPS data from 13 stations in the Parkfield (CA) region that are operated and maintained by UC San Diego. These stations were installed as part of the collaborative NSF/MRI program between the BSL, UC San Diego and Carnegie Institution of Washington nicknamed “mini-PBO”. Since September 2009, 1Hz GPS data from these 13 stations flow through the T1 line from Parkfield to Menlo Park and then on to Berkeley. From here it is sent back to UCSD via a NTRIP server. We plan to participate in a State wide real time geodetic network that will eventually be integrated with the CIGN for earthquake notification purposes. The acquisition of real time data from the Parkfield subnetwork is the first step towards linking southern and northern California real time GPS networks.

### Data archival

The NCEDC, operated jointly by the BSL and USGS, archives all permanent-site GPS data currently being collected in Northern California. We also archive data from the Federal Aviation Administration (FAA) sites all along the Pacific coast (the closest one is ZOA1). Data importation and quality assurance are automated, although some manual correction of unusual data problems is still required.

As part of the activities funded by the USGS through the BARD network, the NCEDC has established an archive of the 7000+ survey-mode occupations collected by the USGS since 1992. The NCEDC continues to archive non-continuous survey GPS data. The initial dataset archived is the survey GPS data collected by the USGS Menlo Park for Northern California and other locations. The NCEDC is the principal archive for this dataset. Significant quality control efforts were implemented by the NCEDC (*Romanowicz et al., 1994*) to ensure that raw data, scanned site log sheets, and RINEX data are archived for each survey. All of the USGS MP GPS data has been transferred to the NCEDC and virtually all of the data from 1992 to the present has been archived and is available for distribution. Together with graduate students in the department who now use the GAMIT software to process survey-mode data in the San Francisco Bay area, we are working to combine the survey-mode and C-GPS solutions into a self-consistent velocity field for Northern California. The campaign velocity field computed from campaign measurements by UCB and USGS groups has been published by *d’Alessio et al., (2005)*.

Data from five of our sites (HOPB, MHCB, CMBB, OHLN, and YBHB) are sent to the National Geodetic Survey (NGS) in the framework of the CORS (Continuous Operating Reference Stations) project (<http://www.ngs.noaa.gov/CORS/>). The data from these five sites are also distributed to the public through the CORS

	Sites	Lat. (deg.)	Lon. (deg)	Receiver	Telem.	Sampling rate	Collocated Network	Location
1	BRIB	37.91	237.84	NETRS	T1	1Hz	BDSN	Briones Reservation, Orinda
2	CMBB	38.03	239.61	NETRS	FR	1Hz	BDSN	Columbia College, Columbia
3	DIAB	37.87	238.08	A-Z12	FR	1Hz		Mt. Diablo
4	EBMD	37.81	237.71	T-5700	R	1Hz		East Bay Mud Headquarters
5	FARB	37.69	236.99	NETRS	R-FR/R	1Hz	BDSN	Farallon Island
6	HOPB	38.99	236.92	NETRS	FR	1Hz	BDSN	Hopland Field Stat., Hopland
7	LUTZ	37.28	238.13	A-Z12	FR	30 s		SCC Comm., Santa Clara
8	MHCB	37.34	238.35	A-Z12	FR	1Hz	BDSN	Lick Obs., Mt. Hamilton
9	MHDL	37.84	237.50	T-NETRS	FR	1Hz	mini-PBO	Marin Headlands
10	MODB	41.90	239.69	A-UZ12	NSN	15 s		Modoc Plateau
11	MONB	37.48	238.13	A-Z12	FR	1Hz		Monument Peak, Milpitas
12	OHLN	38.00	237.72	A-UZ12	FR	1Hz	mini-PBO	Ohlone Park, Hercules
13	ORVB	39.55	238.49	NETRS	FR	1 Hz	BDSN	Oroville
14	OXMT	37.49	237.57	A-UZ12	FR	1Hz	mini-PBO	Ox Mountain
15	PKDB	35.94	239.45	NETRS	FR	30 s	BDSN	Bear Valley Ranch, Parkfield
16	PTRB	37.99	236.98	A-Z12	R-FR	1Hz		Point Reyes Lighthouse
17	SAOB	36.76	238.55	NETRS	FR	1 Hz	BDSN	San Andreas Obs., Hollister
18	SBRN	37.68	237.58	A-Z12	FR	1Hz	mini-PBO	San Bruno
19	SODB	37.16	238.07	A-Z12	R-FR	30 s		Soda Springs, Los Gatos
20	SRB1	37.87	237.73	T-SSE	FR	1Hz		SRB building, Berkeley
21	SUTB	39.20	238.17	A-Z12	R-FR	30 s	BDSN	Sutter Buttes
22	SVIN	38.03	237.47	A-UZ12	R-FR	1Hz	mini-PBO	St. Vincents
23	TIBB	37.89	237.55	A-UZ12	R	1Hz		Tiburon
24	UCD1	38.53	238.24	NETRS	WEB	1Hz		UC - Davis
25	UCSF	37.75	237.55	NETRS	FR	1Hz		UC-San Francisco, San Francisco
26	YBHB	41.73	237.28	NETRS	FR	1Hz s	BDSN	Yreka Blue Horn Mine, Yreka
27	BDM	37.95	238.13	NETRS			BDSN	Black Diamond Mines Park, Antioch
28	MCCM	38.14	237.12	NETRS			BDSN	Marconi Conference Center, Marshall
29	PTP1	38.00	237.64	NETRS			NHFN	Point Pinole Regional Park

Table 3.11: List of BARD stations maintained by the BSL. Five models of receiver are operating now: Trimble 4000 SSE (T-SSE), Trimble 4000 SSI (T-SSI), Trimble NETRS, (T-NETRS), Ashtech Z12, and Ashtech Micro Z (A-UZ12). The replacement of the Ashtech Z12 by Trimble NETRS will make the receiver park more homogeneous. The telemetry types are listed in column 6. FR = Frame Relay, R = Radio, Mi= Microwave, WEB = DSL line. Some sites are transmitting data over several legs with different telemetry. Changes from the last year's network table are highlighted in bold typography. Sites 27 to 29 are in progress. For these 3 sites, permit request procedures are well advanced.

FTP site.

## 5.2 Recent developments

### Collaboration with East Bay Regional Parks

In 2008, we started a collaboration with Mr. Jim Swanson, of East Bay Regional Parks (EBRP) to establish robust high rate telemetry from 11 PBO stations located on EBRP land to UC Berkeley, as part of BARD (Figure 3.19). The EBRP interest is in establishing on the fly differential GPS measurements using a hand-held device (RTK corrections), to support surveyors in the Parks. This work has been stalled, but we have proposed to establish the necessary radio telemetry using ARRA support. Five sites have line-of-sight to one of our BARD stations (DIAB or MONB). The data can be transmitted via simplex radio connections to and from these sites, and use existing frame-relay lines. For the remaining 6 sites, we propose a solution involving radio telemetry through three repeater sites. These will be equipped with switches to combine data from 2-3 stations and relay them to Berkeley. PBO is currently streaming data from these sites using an NTRIP server, but over cell modems, in a fashion that is not reliable enough for use in earthquake notification (cell modems will likely not perform well in the case of a large damaging earthquake, in particular due to saturation of the network). We hope to finalize this project within the next year, with the help of ARRA funds.

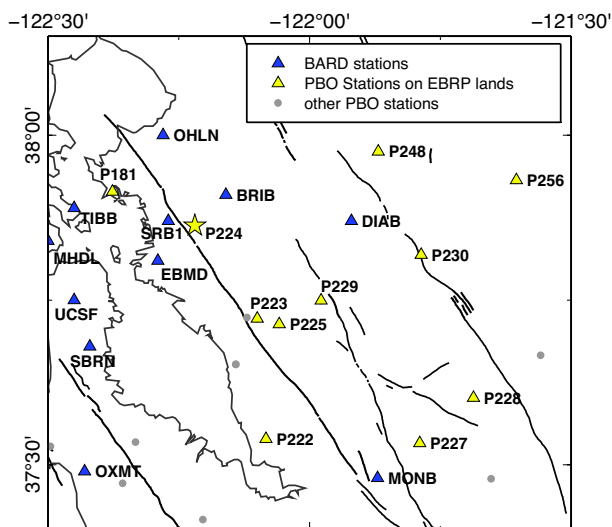


Figure 3.19: Locations of PBO stations on EBRP lands (yellow triangles), and nearby BARD stations (blue triangles). We hope to upgrade the telemetry of the EBRP stations to allow robust streaming of high rate real time data using ARRA funds.

**Permit requests:** The permit for PTP1 has been approved by EBRP and delayed by the Real Estate Office

at Berkeley. The administrative problems have been resolved, and drilling as well as the installation of the GPS equipment is imminent.

**Meteorological Sensors and troposphere:** In the past year, we performed some calibration tests using different meteorological sensors and collecting data at stations SBRN and BRIB (see chapter (7)). We hope to install such sensors at all BARD stations to provide tropospheric corrections and achieve higher accuracy.

## 5.3 Data Processing

We use the GAMIT/GLOBK software developed at MIT and SIO to process data from BARD and other nearby continuous GPS networks (*King and Bock, 1999, Herring, 2005*). Data from more than 80 stations, including global IGS stations, are included in daily solutions by GAMIT. The loosely constrained solutions are then combined using a Kalman filter approach and stabilized to a defined reference frame within GLOBK. The estimated relative baseline determinations typically have 2-4 mm long-term scatter in the horizontal components and 10-20 mm scatter in the vertical. The BARD dataset has been processed in the ITRF2000 (*Altamimi et al., 2002*). All the BARD sites have been processed jointly with IGS sites in California. No *a priori* constraints are assumed. The solutions (*Houlié and Romanowicz, 2009*) are in good agreement with previous campaign solutions (e.g. *d'Alessio et al., 2005*). BARD stations are also an important component of the Bay Area velocity unification (BAVU), undertaken by Prof. Roland Bürgmann. BAVU uses the BARD routine daily solutions and combines them with continuous and campaign GPS data from multiple agencies throughout the greater SFBA (Figure 3.20).

## 5.4 Acknowledgements

Since the departure of Mark Murray at the end of 2005 and Nicolas Houlié in July 2009, Barbara Romanowicz oversees the BARD program, with help from Ingrid Johanson who will take over in February 2010. Rich Clymer, Bill Karavas, Rick Lellinger, John Friday, Nicolas Houlié, and Doug Neuhauser contributed to the operation of the BARD network in 2008-09. The operation of the BARD network is partially supported by funding from the USGS/NEHRP program.

## 5.5 References

Altamimi, Z., P. Sillard, and C. Boucher, ITRF2000: A new release of the International Terrestrial Reference Frame for earth science applications, *J. Geophys. Res.*, 107(B10), 2214, doi:10.1029/2001JB000561, 2002  
Artru, J., P., Lognonné and E., Blanc, Normal modes modeling of post-seismic ionospheric oscillations, *Geophys. Res. Lett.*, 28, 697-700, 2001  
d'Alessio, M. A., I. A. Johanson, R. Bürgmann, D. A. Schmidt, and M. H. Murray, Slicing up the San Francisco Bay

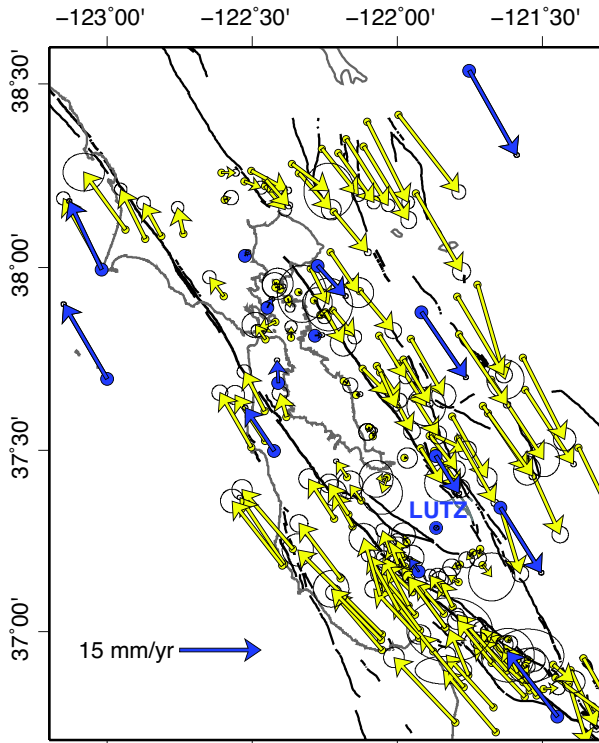


Figure 3.20: Site velocities from BAVU2 within the SFBA, including BARD (in blue), PBO and campaign stations. Shown relative to station LUTZ. BAVU website: <http://seismo.berkeley.edu/~burgmann/RESEARCH/BAVU/>

Area: Block kinematics from GPS-derived surface velocities, *J. Geophys. Res.*, 110, B06403, doi:10.1029/2004JB003496, 2005.

Ducic, V., J. Artru and P. Lognonné, Ionospheric remote sensing of the Denali Earthquake Rayleigh surface waves, *Geophys. Res. Lett.*, 30, 18, 2003

Houlié, N. and Romanowicz, B., CALREF, a stable reference frame for the Northern California, in revision, PEPI.

Larson, Using 1-Hz GPS Data to Measure Deformations Caused by the Denali Fault Earthquake, *Science*, 300, 1421–1424, 2003

Murray, M., Neuhauser D., Gee, L., Dreger, D., Basset, A., and Romanowicz, B., Combining real-time seismic and geodetic data to improve rapid earthquake information, *EOS. Trans. AGU*, 83(47), G52A-0957, 2002.

Perin, B. J., C. M. Meertens, D. S. Neuhauser, D. R. Baxter, M. H. Murray, and R. Butler, Institutional collaborations for joint seismic and GPS measurements, *Seismol. Res. Lett.*, 69, 159, 1998.

Romanowicz, B., B. Bogaert, D. Neuhauser, and D. Oppenheimer, Accessing northern California earthquake data via Internet, *EOS Trans. AGU*, 75, 257–260, 1994.

## 6 Northern California Earthquake Data Center

### 6.1 Introduction

The Northern California Earthquake Data Center, a joint project of the Berkeley Seismological Laboratory (BSL) and the U.S. Geological Survey at Menlo Park, serves as an online archive and distribution center for various types of digital data relating to earthquakes in Central and Northern California. The NCEDC is located at the Berkeley Seismological Laboratory, and has been accessible to users via the Internet since mid-1992.

The primary goal of the NCEDC is to provide a stable and permanent archival and distribution center of digital geophysical data for networks in Northern and Central California. These data include seismic waveforms, electromagnetic data, GPS data, strain, creep, and earthquake parameters. The seismic data comes principally from the Berkeley Digital Seismic Network (BDSN) operated by the Seismological Laboratory, the Northern California Seismic Network (NCSN) operated by the USGS, the Berkeley High Resolution Seismic Network (HRSN) at Parkfield, the EarthScope USArray Transportable Array stations in Northern California, the various Geysers networks, and selected stations from adjacent networks such as the University of Reno, Nevada network and the Southern California Seismic Network (SCSN). GPS data are primarily from the Bay Area Regional Deformation (BARD) GPS network and the USGS/Menlo Park GPS surveys. The collection of NCSN digital waveforms dates from 1984 to the present, the BDSN digital waveforms date from 1987 to the present, and the BARD GPS data date from 1993 to the present. The BDSN includes stations that form the specialized Northern Hayward Fault Network (NHFN) and the MiniPBO (MPBO) borehole seismic and strain stations in the SF Bay Region. Additional seismic and strain data from the EarthScope Plate Boundary Observatory (PBO) and the San Andreas Fault Observatory at Depth (SAFOD) are also archived at the NCEDC. Figure 3.23 shows the total data volume by year, as itemized in table 3.12.

The NCEDC also provides support for earthquake processing and archiving activities of the Northern California Earthquake Management Center (NCEMC), a component of the California Integrated Seismic Network (CISN). The CISN is the California regional organization of the Advanced National Seismic System (ANSS).

Figure 3.22 shows the location of stations archived at the NCEDC (excluding EarthScope stations located outside of CA).

### 6.2 2008-2009 Activities

By its nature, data archiving is an ongoing activity. In 2008-2009, the NCEDC continued to expand its data

holdings and enhance access to the data. Projects and activities of particular note include:

- Distributed over 1644 GB of waveform data to external users.
- Read and archived continuous high-rate (250 samples/second) HRSN data from 2003-2004, thus completing the archive of continuous HRSN data from 2001-present.
- Began the process of replacing waveforms rapidly collected in real-time for earthquake event analysis with QC-ed waveforms from the BK and BP networks.
- Supported the NCEMC earthquake analysis by providing real-time access to earthquake parameters and waveforms from the NCEDC for the CISN *Jiggle* earthquake review software.
- Completed the process on reading and archiving continuous NCSN seismograms from tapes for 2001-2005.
- In collaboration with USGS Menlo Park, provided QC procedures to evaluate the intermediate conversion of older 1990's NCSN waveform tapes into a format that could be processed and archived at the NCEDC, and archived selected data from that time.

### 6.3 BDSN/NHFN/MPBO Seismic Data

Archiving current BDSN (Section 1), NHFN (Section 3), and Mini-PBO (Section 3) (all stations using the network code BK) seismic data is an ongoing task. These data are telemetered from 48 seismic data loggers in real-time to the BSL, where they are written to disk files, used for CISN real-time earthquake processing and earthquake early warning (EEW) development, and delivered in real-time to the DART (Data Available in Real Time) system on the NCEDC, where they are immediately available to anyone on the Internet. In September 2004, the NCEDC began to archive continuous high frequency data (80 Hz and 100 Hz) from all of the BDSN broadband, strong motion, and strainmeter sensors. Previously, 20 Hz and lower rate data channels were archived continuously, and high frequency data was archived only for events. In early 2006, the NCEDC started to receive all of the BK stations in real-time and make them available to users through the DART. All timeseries data from the Berkeley networks continue to be processed and archived by

Data Type	GBytes
BDSN/NHFN/MPBO (broadband, electric and magnetic field, strain) waveforms	6,103
NCSN seismograms	21,719
Parkfield HRSN seismograms	3,233
BARD GPS (RINEX and raw data)	2,041
UNR Nevada seismograms	1,080
SCSN seismograms	1,827
Calpine/Unocal Geysers region seismograms	38
EarthScope SAFOD seismograms	1,935
EarthScope USArray seismograms	271
EarthScope PBO strain waveforms	875
PG&E seismograms	372
USGS low frequency geophysical waveforms	3
Misc data	1,901
Total size of archived data	41,398

Table 3.12: Volume of Data Archived at the NCEDC by network

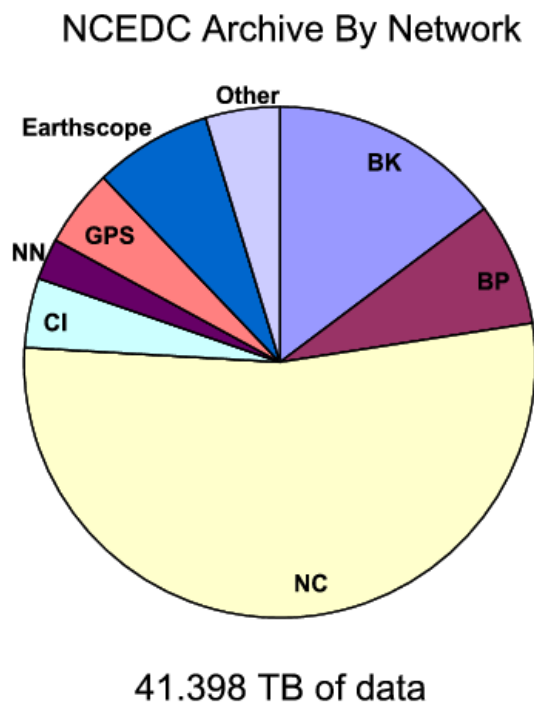


Figure 3.21: Chart showing the relative proportion of each data set at the NCEDC. (BK - Berkeley Digital Seismic Network; BP - Berkeley High-resolution Seismic Network in Parkfield; NC - Northern California Seismic Network and collaborators; CI - Southern California Seismic Network; NN - University of Nevada, Reno Seismic Network; GPS - various GPS datasets, including BARD; EarthScope - data from various EarthScope activities; Other - various small data sets)

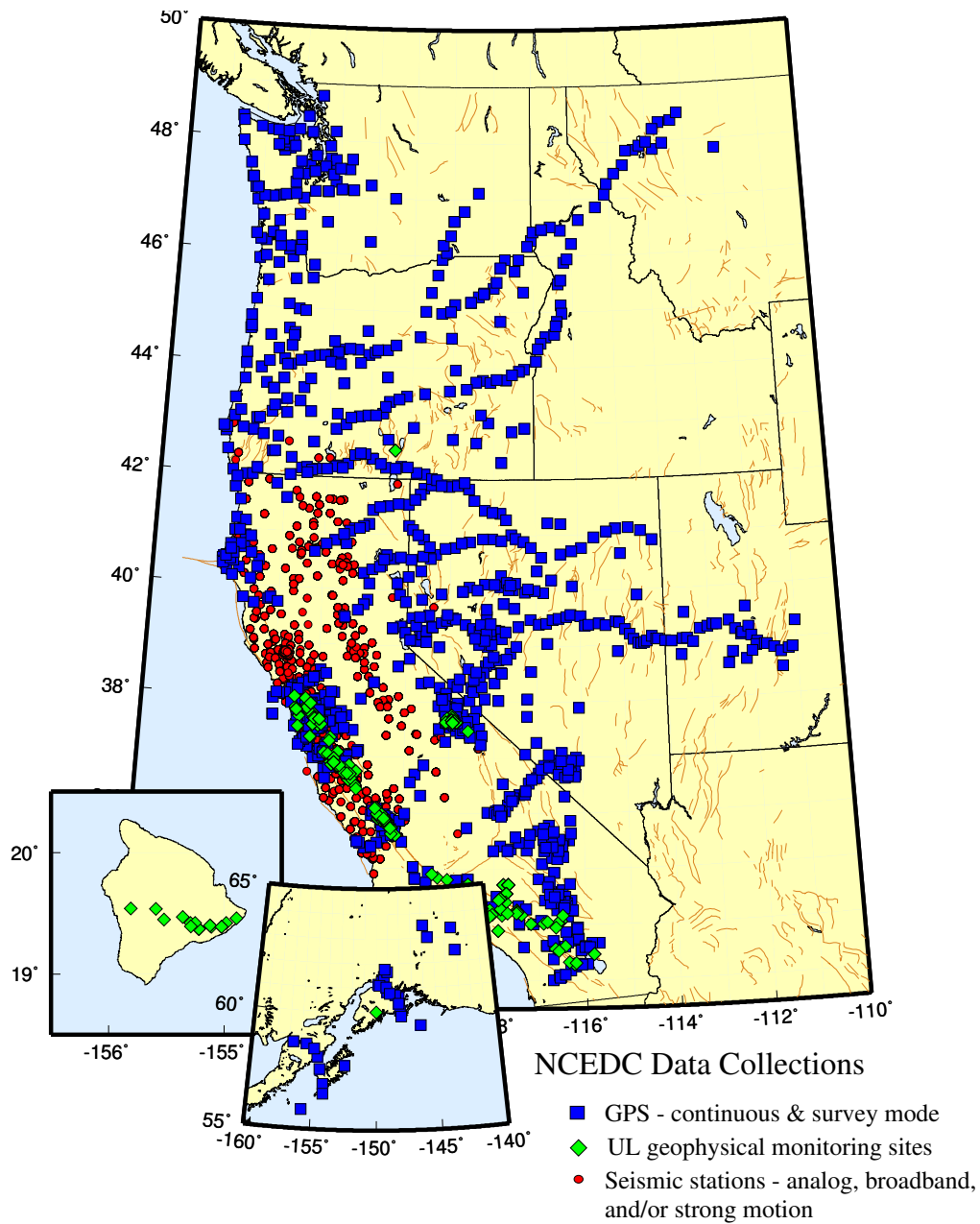


Figure 3.22: Map showing the location of stations whose data are archived at the NCEDC. Circles are seismic sites, squares are GPS sites, and diamonds are the locations of USGS low-frequency experiments.

an NCEDC analyst using *calqc* in order to provide the highest quality and most complete data stream to the NCEDC.

#### NCSN Seismic Data

NCSN continuous waveform data are sent in real-time to the NCEDC via the internet, and are made available

to users in real-time through the NCEDC DART. NCSN event waveform data, as well as data from all other real-time BSL and collaborating networks, are automatically collected by the NCEMC waveform archiver and stored at the NCEDC for event review and analysis and for distribution to users. All NCSN and NCEMC data are archived in MiniSEED format.

The NCEDC also maintains a list of historic teleseismic events recorded by the NCSN, since these events do not appear in the NCSN catalog.

A description of the successive improvements in the acquisition of NCSN data, leading to the acquisition of complete NCSN waveform data in early 2006, can be found in the 2005-06 BSL Annual Report. We have finished the first phase of the NCSN continuous waveform archiving project by reading, converting and archiving NCSN seismograms from all available NCSN tapes for mid-2001 through early 2006. Figure 3.23 shows the total data volume by year.

### **Parkfield High Resolution Seismic Network Data**

The history of upgrades to the acquisition and archival of HRSN data can be found in the 2005-06 BSL Annual Report.

In early 2006, the NCEDC started to receive the HRSN 20 Hz data and a subset of the 250 Hz data in real-time for distribution through the DART. The NCEDC continued to archive continuous 250 Hz and 20 Hz data streams from the HRSN tapes written in Parkfield and processed at the NCEDC. In early 2007, the BSL established a radio telemetry link from the HRSN recording center at the California Department of Forestry (CDF) in Parkfield to Carr Hill, and started to telemeter all HRSN continuously to UCB. These data are fed into the NCSN backup Earthworm system at Carr Hill, and are also routed through the USGS Parkfield T1 circuit to USGS/MP and through the NCEMC T1 circuit to the BSL for real-time processing by the NCEMC earthquake processing system. The data are also made available to users through the NCEDC DART and are continuously archived at the NCEDC. In 2008-2009, the NCEDC completed its archive of continuous HRSN data by reading from tapes and archiving all continuous 250 Hz HRSN data from early 2003 through late 2004. The NCEDC now has all of the continuous data from the HRSN from its upgrade in 2001 to the present.

### **EarthScope Plate Boundary Observatory (PBO) strain data**

The NCEDC is one of two funded archives for PBO EarthScope borehole and laser strain data. Strain data are collected from all of the PBO strain sites and are processed by UNAVCO. MiniSEED data are delivered to the NCEDC using SeedLink, and raw and XML processed data are delivered to the NCEDC using Unidata's Local

Data Manager (LDM). The MiniSEED data are inserted into the NCEDC DART and are subsequently archived from the DART. UNAVCO provides EarthScope funding to the NCEDC to help cover the processing, archiving, and distribution costs for these data.

### **EarthScope SAFOD**

The NCEDC is an archive center for the SAFOD event data and will also process the continuous SAFOD data. Starting in July 2002, scientists from Duke University successfully installed a three component 32 level downhole-seismic array in the pilot hole at the EarthScope SAFOD site in collaboration with Steve Hickman (USGS), Mark Zoback (Stanford University), and the Oyo Geospace Engineering Resources International (GERI) Corporation. High frequency event recordings from this array have been provided by Duke University for archiving at the NCEDC. We converted data from the original SEG-2 format data files to MiniSEED, and have developed the SEED instrument responses for this data set. Continuous 4 KHz data from SAFOD are written to tape at SAFOD and are periodically sent to the BSL to be converted, archived, and forwarded to the IRIS DMC. SAFOD EarthScope funding to the NCEDC is to cover the processing, archiving, and distribution costs for these data. A small subset of the continuous SAFOD data channels are also incorporated into the NCSN, are available in real-time from the NCEDC DART, are archived at the NCEDC, and are forwarded to the IRIS DMC. From March 2008 through April 2009, SAFOD installed a Guralp broadband and accelerometer package in the Pilot Hole, which sent continuous data for 6 channels at 200 samples-per-second to the NCEDC.

### **UNR Broadband data**

The University of Reno in Nevada (UNR) operates several broadband stations in western Nevada and eastern California that are important for Northern California earthquake processing and analysis. Starting in August 2000, the NCEDC has been receiving and archiving continuous broadband data from four UNR stations. The data are transmitted in real-time from UNR to UC Berkeley, where they are made available for CISN real-time earthquake processing and for archiving. Initially, some of the stations were sampled at 20 Hz, but all stations are now sampled and archived continuously at 100 Hz.

The NCEDC installed Simple Wave Server (SWS) software at UNR, which provides an interface to UNR's recent collection of waveforms. The SWS is used by the NCEDC to retrieve waveforms from UNR that were missing at the NCEDC due to real-time telemetry outages between UNR and UC Berkeley.

In early 2006, the NCEDC started to archive continuous data from the UNR short-period stations that are

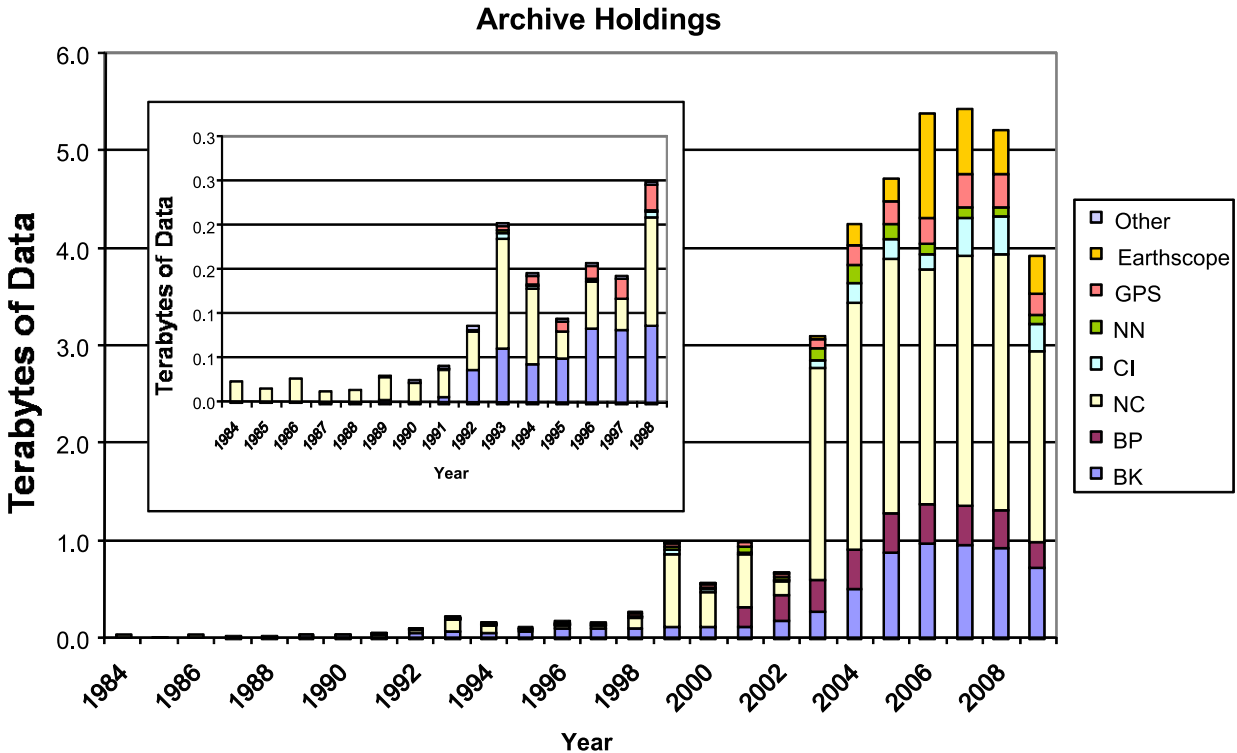


Figure 3.23: Figure showing the total volume of data archived at the NCEDC, broken down by data year.

contributed to the NCSN. Both the broadband and short-period UNR stations contributed to the CISN are available in real-time through the NCEDC DART.

### Electro-Magnetic Data

The NCEDC continues to archive and process electric and magnetic field data acquired at several UC Berkeley sites. The BSL operates both magnetic and electric field sensors at PKD and SAO. However, most of these channels have been down for repair during the 2008-2009 year. Through a collaboration with Dr. Simon Klemperer at Standord University, we acquire magnetic and electric field channels at BSL sites JRSC and BRIB, and magnetic field channels at site MHDL. The three magnetic field channels and either two or four electric field channels are digitized at 40 Hz, 1 Hz, and 0.1 Hz, and are telemetered in real-time along with seismic data to the Berkeley Seismological Laboratory, where they are processed and archived at the NCEDC in a similar fashion to the seismic data.

### GPS Data

The NCEDC continues to archive GPS data through the BARD (Bay Area Regional Deformation) network of continuously monitored GPS receivers in Northern California (Section 5). The NCEDC GPS archive now includes 67 continuous sites in Northern California. There are approximately 50 core BARD sites owned and op-

erated by UC Berkeley, USGS (Menlo Park and Cascade Volcano Observatory), LLNL, UC Davis, UC Santa Cruz, Trimble Navigation, and Stanford. Data are also archived from sites operated by other agencies including East Bay Municipal Utilities District, the City of Modesto, the National Geodetic Survey, and the Jet Propulsion Laboratory.

In addition to the standard 15 second or 30 second continuous GPS datastream, the NCEDC is now privately archiving high-rate 1 Hz continuous GPS data from most of the BSL-operated BARD stations. In collaboration with UCSD/SIO and USGS/MP, the BSL is now streaming real-time 1 Hz continuous data from the 13 PBO stations in Parkfield through the USGS Parkfield T1 and NCSS T1 circuits to the BSL, where it makes the data available to researchers in real-time through an Ntrip-caster.

The NCEDC also archives non-continuous survey GPS data. The initial dataset archived is the survey GPS data collected by the USGS Menlo Park for Northern California and other locations. The NCEDC is the principal archive for this dataset. Significant quality control efforts were implemented by the NCEDC to ensure that the raw data, scanned site log sheets, and RINEX data are archived for each survey.

## Geysers Seismic Data

The Calpine Corporation operated a micro-seismic monitoring network in the Geysers region of Northern California. Prior to 1999 this network was operated by Unocal. Through various agreements, both Unocal and Calpine have released triggered event waveform data from 1989 through 2000 along with preliminary event catalogs for the same time period for archiving and distribution through the NCEDC. This dataset represents over 296,000 events that were recorded by Calpine/Unocal Geysers network and are available via research accounts at the NCEDC.

The Lawrence Berkeley Laboratory (LBL), with funding from the California Energy Commission, currently operates a 22 station network in the Geysers region with an emphasis on monitoring seismicity related to well water injection. The earthquake locations and waveforms from this network are sent to the NCEDC, and the locations are forwarded to the NCSN so that they can be merged into the NCSN earthquake catalog. In August 2007, the NCSN installed an Earthworm system at the Geysers to receive continuous LBL Geysers data, and this system provides event waveforms in real-time for the NCEMC earthquake processing and the NCEDC event archives. The event data from LBL Geysers event waveforms collected from April 2004 to August 2007 will be associated with events from the NCSN catalog and will be included with the existing waveforms for these events.

## USGS Low Frequency Data

Over the last 30 years, the USGS at Menlo Park, in collaboration with other principal investigators, has collected an extensive low-frequency geophysical data set that contains over 1300 channels of tilt, tensor strain, dilatational strain, creep, magnetic field, and water level as well as auxiliary channels such as temperature, pore pressure, rain and snow accumulation, and wind speed. In collaboration with the USGS, we assembled the requisite information for the hardware representation of the stations and the instrument responses for many channels of this diverse dataset, and developed the required programs to populate and update the hardware database and generate the instrument responses. We developed the programs and procedures to automate the process of importing the raw waveform data and converting it to MiniSEED format. Since these data are delivered to the NCEDC on a daily basis and immediately archived, these data are not inserted into the NCEDC DART.

We have currently archived timeseries data from 887 data channels from 167 sites, and have instrument response information for 542 channels at 139 sites. The waveform archive is updated on a daily basis with data from 350 currently operating data channels. We will augment the raw data archive as additional instrument response information is assembled by the USGS for the

channels and will work with the USGS to clearly define the attributes of the “processed” data channels.

## SCSN/Statewide seismic data

In 2004, the NCEDC started to archive broadband and strong motion data from 15 SCSN (network CI) stations that are telemetered to the Northern California Management Center (NCEMC) of the California Integrated Seismic Network (CISN). These data are used in the prototype real-time state-wide earthquake processing system and also provide increased coverage for Northern California events. Since the data are telemetered directly from the stations in real-time to both the SCSN and to the NCEMC, the NCEDC archives the NCEMC’s copy of the data to ensure that at least one copy of the data will be preserved.

In early 2006, the NCEDC started to continuously archive all of the selected SCSN short-period stations that are contributed to the NCSN. All of these data are also available in real-time from the NCEDC DART.

## Earthquake Catalogs

*Northern California:* The NCEDC provides searchable access to both the USGS and BSL earthquake catalogs for Northern and Central California. The “official” UC Berkeley earthquake catalog begins in 1910 and runs through 2003, and the “official” USGS catalog begins in 1966. Both of these catalogs are archived and available through the NCEDC, but the existence of 2 catalogs has caused confusion among both researchers and the public.

In late 2006, the NCEMC began to archive and distribute a single unified Northern California earthquake catalog in real-time to the NCEDC through database replication from the NCEMC’s real-time systems. The NCEDC developed and tested the required programs used to enter all previous NCSN catalog data into the NCEDC database. In 2008, we migrated all of the historic NCSN catalog, phase, and amplitude data from 1967 - 2006 into the NCEMC catalog. In addition, we spent considerable effort addressing the mapping of phase data in the BSL catalog to SEED channel names. We plan to merge the BSL catalog with the NCEMC catalog to form a single unified Northern California catalog from 1910 to the present. The BSL and the USGS have spent considerable effort over the past years to define procedures for merging the data from the two catalogs into a single Northern and Central California earthquake catalog in order to present a unified view of Northern California seismicity. The differences in time period, variations in data availability, and mismatches in regions of coverage all complicate the task.

*Worldwide:* The NCEDC, in conjunction with the Council of the National Seismic System (CNSS), produced and distributed a world-wide composite catalog of earthquakes based on the catalogs of the national and

various U.S. regional networks for several years. Each network updates their earthquake catalog on a daily basis at the NCEDC, and the NCEDC constructs a composite world-wide earthquake catalog by combining the data, removing duplicate entries that may occur from multiple networks recording an event, and giving priority to the data from each network's *authoritative region*. The catalog, which includes data from 14 regional and national networks, is searchable using a Web interface at the NCEDC. The catalog is also freely available to anyone via ftp over the Internet.

With the demise of the CNSS and the development of the Advanced National Seismic System (ANSS), the NCEDC was asked to update its Web pages to present the composite catalog as a product of the ANSS. This conversion was completed in the fall of 2002. We continue to create, house, distribute, and provide a searchable web interface to the ANSS composite catalog, and to aid the regional networks in submitting data to the catalog.

## 6.4 NCEDC Operations

In 2005, the NCEDC relocated its archive and distribution system from McCone Hall to a new state-of-the-art computer facility in a new seismically braced building on the Berkeley campus. The facility provides seismically braced equipment racks, gigabit ethernet network, air conditioning, and power conditioning. The entire facility is powered by a UPS with generator backup.

The currently installed NCEDC facilities consist of a mass storage environment hosted by a Sun X4150 host computer, a 100 slot LTO3 tape library with two tape drives and a 20 TByte capacity, and 60 TBytes of RAID storage, all managed with the SAM-FS hierarchical storage management (HSM) software. In 2008-2009, the tape library was upgraded from LTO2 to LTO3 drives, and all online tape data was re-archived on LTO3 tapes. DART data are collected and distributed on a Sun 280R computer and RAID storage. A Sun x4150 system provides Web services for the NCEDC, a dual Sun 280R processor provides data import and export services, and a Sun V20Z computer is used for quality control procedures. Two AIT tape libraries are used to read NCSN continuous data tapes. Two 64-bit Linux system hosts redundant Oracle databases. Two Sun X64 processors provide additional data processing support for the NCEDC.

The SAMFS hierarchical storage management (HSM) software used by the NCEDC is configured to automatically create multiple copies of each data file in the archive. The NCEDC creates one copy of each file on an online RAID, a second copy on LTO2 tape which is stored online in the tape library, and a third copy on LTO2 tape which is stored offline and offsite. All NCEDC data are stored online and rapidly accessible by users.

The NCEDC operates two instances of its Oracle database, one for internal operations and one for external

use for user data queries and data distribution programs. The databases are synchronized using multi-master replication.

## Data Quality Control

The NCEDC developed a GUI-based state-driven system *calqc* to facilitate the quality control processing that is applied to the continuously archived data sets at the NCEDC.

The quality control procedures for these datasets include the following tasks:

- data extraction of a full day of data,
- quickcheck program to summarize the quality and stability of the stations' clocks,
- determination if there is missing data for any data channel,
- provided procedures to retrieve missing data from the stations and incorporate it into the day's data,
- optional creation of multi-day timeseries plots for state-of-health data channels,
- optional timing corrections for data,
- optional extraction of event-based waveforms from continuous data channels,
- optional repacking of MiniSEED data,
- creating waveform inventory entries in the NCEDC database,
- publishing the data for remote access on the NCEDC.

*Calqc* uses previously developed programs to perform each function, but it provides a graphical point-and-click interface to automate these procedures, and to provide the analyst with a record of when each process was started, whether it executed correctly, and whether the analyst has indicated that a step has been completed. *Calqc* is used to process all data from the BDSN network, and all continuous broadband data from the NCSN, UNR, SCSN, and HRSN networks that are archived by the NCEDC. The remainder of the continuously archived data are automatically archived without any analyst interaction.

The NCEDC is developing programs and procedures to replace waveforms collected for event analysis in near real-time with QC-ed waveforms from the UCB QC-ed waveform archive. This procedure will also be used to augment the NCSN event-based waveform collection from 1991 - 2006 with the appropriate waveforms from the UCB seismic networks.

## 6.5 Database Development

The NCEDC continues to support the Northern California Earthquake Management Center (NCEMC) by providing information and resources vital to the NCEMC's role of rapid earthquake analysis and data dissemination. The NCEDC receives earthquake parametric data in real-time from the NCEMC real-time systems and provides real-time access to the NCEDC database for *jiggle*, the CISN event analysis tool. The NCEMC continues to support the maintenance and distribution of the hardware configurations and instrument responses of the UCB, USGS/MP NCSN, and other seismic stations used by the NCEMC. During 2002-2004, the NCEDC and NCSN jointly developed a system consisting of an extensive spreadsheet containing per-channel information that describes the hardware of each NCSN data channel and provides each channel with a SEED-compliant channel name. This spreadsheet, combined with a limited number of files that describe the central-site analog digitizer, FIR decimation filters, and general characteristics of digital acquisition systems, allows the NCSN to assemble its station history in a format that the NCEDC can use to populate the hardware tracking and instrument response database tables for the NCSN. BSL staff currently chairs the CISN Schema Change working group, which coordinates all databaser schema changes and enhancements within the CISN.

The NCEDC instrument response schema represents full multi-stage instrument responses (including filter coefficients) for the broadband data loggers. The hardware tracking schema represents the interconnection of instruments, amplifiers, filters, and data loggers over time, and is used to describe all of the UC Berkeley and USGS stations and channels archived at the NCEDC.

The NCEDC has developed XML import and export procedures to provide better maintenance of the hardware tracking information and resulting instrument responses for stations in our database. When changes are made to either existing hardware or to station configurations, we export the current view in XML format, use a GUI-based XML editor to easily update the information, and import the changes back into the database. When adding new stations or hardware, we can easily use information from existing hardware or stations as templates for the new information. This allows us to treat the database as the authoritative source of information, and to use off-the-shelf tools such as the XML editor and XML differencing programs as part of our database maintenance procedures.

All NCSN event waveforms originally collected with the USGS CUSP processing system have been converted to MiniSEED, and are available along with the UC Berkeley data and data from the other networks archived at the NCEDC in full SEED format.

Additional details on the joint catalog effort and

database schema development may be found at <http://www.ncedc.org/db>

## 6.6 Data Distribution

The NCEDC continues to use the World Wide Web as a principal interface for users to request, search for, and receive data from the NCEDC. In fall 2005, the NCEDC acquired the domain name *ncedc.org*. The NCEDC's Web address is now <http://www.ncedc.org/> In the 12 months from July 2008 through June 2009, the NCEDC distributed over 1644 GB of waveform data to external users.

### Earthquake Catalogs

The NCEDC provides users with searchable access to Northern California earthquake catalogs and to the ANSS world-wide catalog via the web. Users can search the catalogs by time, magnitude, and geographic region, and can retrieve either hypocenter and magnitude information or a full set of earthquake parameters including phase readings, amplitudes, and codas. Moment tensor results are now being added to the NCEMC California earthquake catalog.

### Station Metadata

In addition to the metadata returned through the various data request methods, the NCEDC provides dataless SEED volumes and SEED RESP files for all data channels archived at the NCEDC. The NCEDC currently has full SEED instrument responses for 12,989 data channels from 1,909 stations in 20 networks. This includes stations from the California Geological Survey (CGS) strong motion network that will contribute seismic waveform data for significant earthquakes to the NCEDC and SCEDC.

### SeismiQuery

We ported and installed the IRIS *SeismiQuery* program at the NCEDC, which provides a common interface to query network, station, and channel attributes and query the availability of archived timeseries data.

### DART (Data Available in Real Time)

The DART (Data Available in Real Time) represents the first step in NCEDC's effort to make current and recent timeseries data from all networks, stations, and channels available to users in real-time. The NCEDC developed DART in December 2005 to provide a mechanism for users to obtain access to real-time data from the NCEDC. All real-time timeseries data streams delivered to the NCEDC are placed in MiniSEED files in a Web-accessible directory structure. The DART waveforms can be accessed by Web browsers or http command-line programs such as *wget*, a *FISSURES* waveform server, and

a Berkeley-developed Simple Wave Server (SWS) which provides programmatic access to the DART data by specified SEED channel and time interval. We will be providing users with a client program to retrieve data from the SWS in the near future. The DART currently provide access to the most recent 35 days of data.

We are using the Freeorb software, an enhanced version of the open-source orb software developed by the IRIS-funded Joint Seismic Project (JSP), as the primary method for delivering real-time data to the NCEDC and into the DART. The freeorb package implements an object ring buffer (ORB) and orbserver, which provides a reliable storage ring buffer and an interface for orb client programs to read, write, and query the orbserver. Orbserver clients running at the NCEDC computer connect to remote orbserver at the BSL and USGS/Menlo Park, retrieve the MiniSEED timeseries data records, and write them to daily channel files in the NCEDC DART. Strain data from the EarthScope PBO network are delivered to the NCEDC using SeedLink and are inserted into the DART using a similar SeedLink client program.

The NCEDC developed an automated data archiving system to archive data from the DART on a daily basis. It allows us to specify which stations should be automatically archived, and which stations should be handled by the NCEDC's Quality Control program *calqc*, which allows an analyst to review the waveforms, retrieve missing data from stations or waveservers that may have late-arriving, out-of-order data, and perform timing corrections on the waveform data. The majority of data channels are currently archived automatically from the DART.

## NetDC

In a collaborative project with the IRIS DMC and other worldwide datacenters, the NCEDC helped develop and implement *NetDC*, a protocol which will provide a seamless user interface to multiple datacenters for geophysical network and station inventory, instrument responses, and data retrieval requests. The *NetDC* builds upon the foundation and concepts of the IRIS *BREQ\_FAST* data request system. The *NetDC* system was put into production in January 2000 and is currently operational at several datacenters worldwide, including NCEDC, IRIS DMC, ORFEUS, Geoscope, and SCEDC. The *NetDC* system receives user requests via email, automatically routes the appropriate portion of the requests to the appropriate datacenter, optionally aggregates the responses from the various datacenters, and delivers the data (or ftp pointers to the data) to the users via email.

## STP

In 2002, the NCEDC wrote a collaborative proposal with the SCEDC to the Southern California Earthquake Center, with the goal of unifying data access between the

two data centers. As part of this project, the NCEDC and SCEDC are working to support a common set of 3 tools for accessing waveform and parametric data: *SeisQuery*, *NetDC*, and *STP*.

The *Seismogram Transfer Program* or *STP* is a simple client-server program, developed at the SCEDC. Access to *STP* is either through a simple direct interface that is available for Sun or Linux platforms, or through a GUI Web interface. With the direct interface, the data are placed directly on a user's computer in several possible formats, with the byte-swap conversion performed automatically. With the Web interface, the selected and converted data are retrieved with a single ftp command. The *STP* interface also allows rapid access to parametric data such as hypocenters and phases.

The NCEDC has continued work on *STP*, working with the SCEDC on extensions and needed additions. We added support for the full SEED channel name (Station, Network, Channel, and Location), and are now able to return event-associated waveforms from the NCSN waveform archive.

## EVT\_FAST

In order to provide Web access to the NCSN waveform before the SEED conversion and instrument response for the NCSN has been completed, the NCEDC implemented *EVT\_FAST*, an interim email-based waveform request system similar to the *BREQ\_FAST* email request system. Users email *EVT\_FAST* requests to the NCEDC and request NCSN waveform data based on the NCSN event ID. Initially, the NCSN waveform data was converted to either SAC ASCII, SAC binary, or AH format, and placed in the anonymous ftp directory for retrieval by the users. *EVT\_FAST* event waveforms can now also be provided in MiniSEED format and are now named with their SEED channel names.

## FISSURES

The *FISSURES* project developed from an initiative by IRIS to improve earth scientists' efficiency by developing a unified environment that can provide interactive or programmatic access to waveform data and the corresponding metadata for instrument response, as well as station and channel inventory information. *FISSURES* was developed using CORBA (Common Object Request Broker Architecture) as the architecture to implement a system-independent method for the exchange of this binary data. The IRIS DMC developed a series of services, referred to as the *Data Handling Interface (DHI)*, using the *FISSURES* architecture to provide waveform and metadata from the IRIS DMC.

The NCEDC has implemented the *FISSURES Data Handling Interface (DHI)* services at the NCEDC, which involves interfacing the DHI servers with the NCEDC database schema. These services interact with the

NCEDC database and data storage system and can deliver NCEDC channel metadata as well as waveforms using the *FISSURES* interfaces. We have separate *FISSURES DHI* waveform servers to serve archived and DART data streams. Our *FISSURES* servers are registered with the IRIS *FISSURES naming services*, which ensures that all *FISSURES* users have transparent access to data from the NCEDC.

## GSAC

Since 1997, the NCEDC has collaborated with UNAVCO and other members of the GPS community on the development of the *GPS Seamless Archive Centers (GSAC)* project. This project allows a user to access the most current version of GPS data and metadata from distributed archive locations. The NCEDC is participating at several levels in the *GSAC* project: as a primary provider of data collected from core BARD stations and USGS MP surveys, and as a wholesale collection point for other data collected in Northern California. We helped to define database schema and file formats for the *GSAC* project and have produced complete and incremental monumentation and data holdings files describing the data sets that are produced by the BARD project or archived at the NCEDC so that other members of the *GSAC* community can provide up-to-date information about our holdings. Currently, the NCEDC is the primary provider for over 138,000 data files from over 1400 continuous and survey-mode monuments. The data holdings records for these data have been incorporated into the *GSAC* retailer system, which became publicly available in late 2002.

In addition, the NCEDC is archiving and distributing high-rate 1 Hz GPS data from most BSL-operated BARD stations in addition to the normally sampled 15 second or 30 second data. These high-rate data are now publicly available to the entire community.

## 6.7 Acknowledgements

The NCEDC is a joint project of the BSL and the USGS Menlo Park and is funded primarily by the BSL and the USGS Cooperative Agreement 07HQAG0013. Additional funding for the processing and archiving of the EarthScope PBO and SAFOD data were provided by EarthScope subawards EAR0732947-07-06 through UNAVCO.

Doug Neuhauser is the manager of the NCEDC. Stephane Zuzlewski, Rick McKenzie, Mario Aranha, Nicolas Houlie, Bob Uhrhammer, Jennifer Taggart, and Peggy Hellweg of the BSL and David Oppenheimer, Hal Macbeth, Lynn Dietz, and Fred Klein of the USGS Menlo Park contribute to the operation of the NCEDC. Doug Neuhauser and Peggy Hellweg contributed to the preparation of this section.

## 7 Data Acquisition and Quality Control

### 7.1 Introduction

Stations from the networks operated by the BSL transmit data continuously to the BSL facilities on the UC Berkeley campus for analysis and archival. In this section, we describe activities and facilities which pertain to the individual networks described in Sections 1, 3, and 4, including procedures for data acquisition and quality control, and sensor testing capabilities and procedures. Some of these activities are continuous from year to year and have been described in prior BSL annual reports. In this section, we describe changes or activities which are specific to 2008-2009.

### 7.2 Data Acquisition Facilities

The computers and the associated telemetry equipment are now located in the campus computer facility in Warren Hall at 2195 Hearst Avenue. This building was constructed to current “emergency grade” seismic codes and is expected to be operational even after a  $M$  7 earthquake on the nearby Hayward Fault. The hardened campus computer facility within was designed with special attention for post-earthquake operations. The computer center contains state-of-the art seismic bracing, UPS power and air conditioning with generator backup, and extensive security and equipment monitoring.

### 7.3 Data Acquisition

Central-site data acquisition for data from the BDSN/HRSN/NHFN/MPBO networks is performed by two computer systems in the Warren Hall data center (Figure 3.24). These acquisition systems also collect data from the Parkfield-Hollister electromagnetic array and the BARD network. A third system is used primarily for data exchange with the USNSN and transmits data to the USNSN from HOPS, CMB, SAO, WDC, HUMO, MOD, MCCM, and YBH. Data for all channels of the HRSN are now telemetered continuously from Parkfield to the BSL over the USGS T1 from Parkfield to Menlo Park, and over the NCEMC T1 from Menlo Park to Warren Hall.

The BSL uses the programs `comserv` and `qmaserv` developed by Quanterra for central data acquisition. These programs receive data from remote Quanterra data loggers and redistribute it to one or more client programs. These clients include `data_log`, which writes the data to disk files for archival purposes, `wdafill`, which writes the data to the shared memory region for processing with the network services routines, and other programs such as the seismic alarm process, the DAC480 system, and the feed for the Memento Mori Web page.

The two computers performing data acquisition are also “network services” computers that reduce waveforms for processing with the CISN software (Figure 3.25). To facilitate processing, each system maintains a shared memory region containing the most recent 30 minutes of data for each channel.

Each BDSN data logger using frame relay telemetry is configured to enable data transmission simultaneously to two different computers over two different frame relay T1 circuits to UCB. Normally, only one of these circuits is actively enabled at any given time. The `comserv/qmaserv` client program `cs2m` receives data and multicasts it over a private ethernet. The program `mcast`, a modified version of Quanterra’s `comserv` program, receives the multicast data from `cs2m`, and provides a `comserv`-like interface to local `comserv` clients. Thus, each network services computer has a `comserv/qmaserv` server for every station, and each of the two systems has a complete copy of all waveform data.

We have extended the multicasting approach to handle data received from other networks such as the NCSN and UNR. These data are received by Earthworm data exchange programs and are then converted to MiniSEED and multicast in the same manner as the BSL data. We use `mserv` on both network services computers to receive the multicast data and handle it in the same way as the BSL MiniSEED data.

In 2006, the BSL established a real-time data feed of all BSL waveforms between the BSL acquisition systems and the NCEDC computers using the open source Freeorb software. This allows the NCEDC to provide near-real-time access to all BSL waveform data through the NCEDC DART (Data Available in Real Time) system.

We monitor seismic stations and telemetry using the program `seisnetwatch`. This program extracts current information such as time quality, mass positions, and battery voltage and allows it to be displayed. If the parameter departs from the nominal range, the station is marked with yellow or red to indicate a possible problem.

### 7.4 Seismic Noise Analysis

BSL seismic data are routinely monitored for state-of-health. An automated analysis is computed regularly to characterize the seismic noise level recorded by each broadband seismometer.

#### PSD Noise Analysis

The estimation of the Power Spectral Density (PSD) of the ground motion recorded at a seismic station, as documented in the 2000-2001 BSL annual report

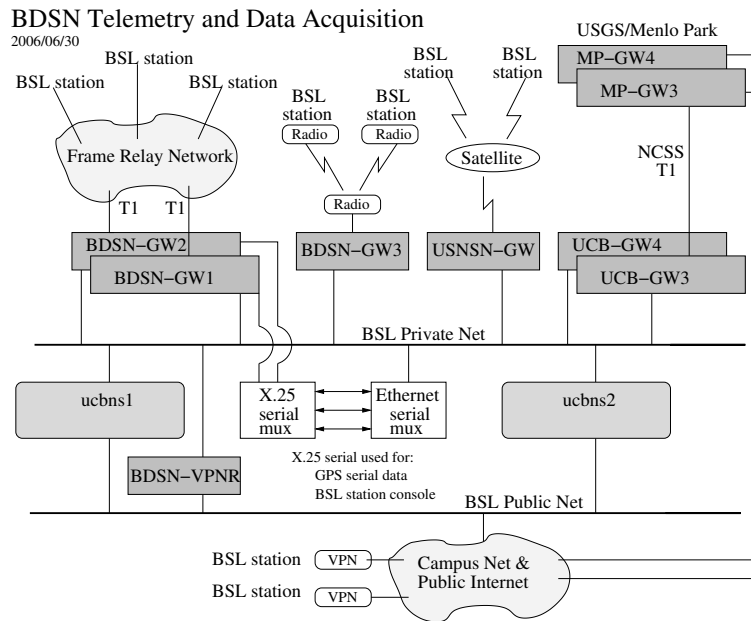


Figure 3.24: Data flow from the BDSN, NHFN, MPBO, HRSN and BARD network into the BSL central processing facility.

([http://seismo.berkeley.edu/annual\\_report/](http://seismo.berkeley.edu/annual_report/)), provides an objective measure of background seismic noise characteristics over a wide range of frequencies. It also provides an objective measure of seasonal and secular variation in noise characteristics and supports early diagnoses of instrumental problems. In the early 1990s, a PSD estimation algorithm was developed at the BSL for characterizing the background seismic noise and as a tool for quality control. The algorithm generates a bar graph output in which all the BDSN broadband stations can be compared by component. We also use the weekly PSD results to monitor trends in the noise level at each station. Cumulative PSD plots are generated for each station and show the noise level in 5 frequency bands for the broadband channels. The plots make it easier to spot certain problems, such as failure of a sensor. In addition to the station-based plots, a summary plot is produced for each channel is produced. The figures are presented as part of a noise analysis of the BDSN on the web at <http://www.seismo.berkeley.edu/seismo/bdsn/psd/>.

### PDF PSD Noise Analysis

In addition to the PSD analysis developed by Bob Uhrhammer, the BSL has implemented the Ambient Noise Probability Density Function (PDF) analysis system developed by *McNamara and Buland* (2004). This system performs its noise analysis over all the data of a given time period (week or year), including earthquakes, calibration pulses, and cultural noise. This is in contrast to Bob Uhrhammer's PSD analysis, which looks at only the quietest portion of data within a day or

week. Pete Lombard of the BSL extended the McNamara code to cover a larger frequency range and support the many different types of sensors employed by the BSL. Besides the originally supported broadband sensors, our PDF analysis now includes surface and borehole accelerometers, strain meters, and electric and magnetic field sensors. These enhancements to the PDF code, plus a number of bug fixes, were provided back to the McNamara team for incorporation in their work. The results of the PDF analysis are presented on the web at <http://www.ncedc.org/ncedc/PDF/>. One difficulty with using these plots for review of station quality is that it is necessary to look at data from each component separately. To provide an overview, we have developed summary figures for all components in two spectral bands, 30 - 60 s and 0.125 - 0.25 s, which These will soon be available on the web.

### 7.5 Sensor Testing Facility

The BSL has an Instrumentation Test Facility in the Byerly Seismographic Vault where the characteristics of up to eight sensors can be systematically determined and compared. The test equipment consists of an eight-channel Quanterra Q4120 high-resolution data logger and a custom interconnect panel. The panel provides isolated power and preamplification, when required, to facilitate the connection and routing of signals from the sensors to the data logger with shielded signal lines. The vault also has a GPS rebroadcaster, so that all data loggers in the Byerly vault operate on the same time base. Upon acquisition of data at up to 200 sps from the instruments under

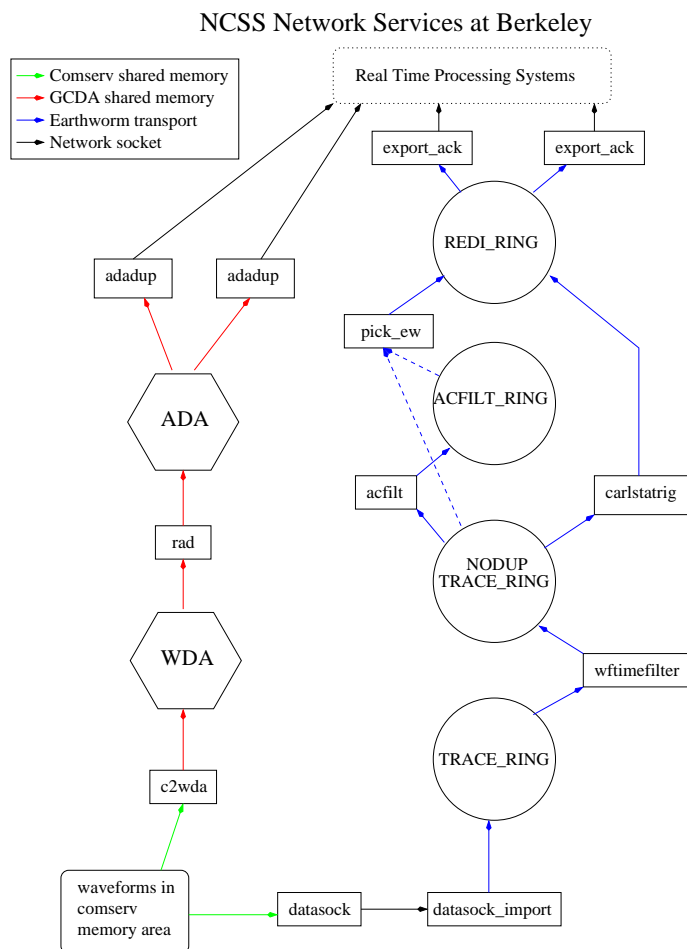


Figure 3.25: Flow of data from `comserv` areas through network services processing. One stream of the network services provides picks (and currently still provides codas) determined using the programs shown in the right flow path. Every 5 seconds, ground motion parameters are also determined, including PGA, PGV, PGD, and ML100 (left flow column). Parameters from the network services are available to the CISN software for event detection and characterization. Data are also logged to disk (via `datalog`), distributed to other computers (`mserv`), and spooled into a trace ring for export.

test, PSD analysis, coherence analysis, and other analysis algorithms are used to characterize and compare the sensor performance. Tilt tests and seismic signals with a sufficient signal level above the background seismic noise are also used to verify the absolute calibration of the sensors. A simple vertical shake table is used to assess the linearity of a seismic sensor. The sensor testing facility of the BSL is described in detail in the 2001-2002 Annual Report (<http://www.seismo.berkeley.edu/>).

Several projects made use of the sensor testing facility in 2008-2009. These included final testing of the new STS-1 electronics (E300) and initial testing of the STS-1 type sensors being developed jointly by Metrozet and the BSL. Data were also collected from the new pressure/temperature sensors (see below).

### Meteorological Sensors

A new meteorological (MET) sensor package which measures temperature, relative humidity, and pressure (THP) is being developed and tested at BSL as a replacement for the aging temperature and pressure sensors now at the BDSN stations. Temperature and pressure measurements at the stations are useful for reducing the components of the seismic background noise that are correlated with these parameters. A hygrometer has been added to the sensor package to allow measurement of the local relative humidity, a parameter which is potentially useful for estimating and correcting for GPS tropospheric propagation delays.

During the past year we have tested the BSL THP sensor package on the McCone Hall roof and at SBRN. In

a cluster test at BRIB, a pair of the BSL MET sensor packages were operated with a pair of commercial MET sensors (a Paroscientific 1477-005 and a Vaisala WXT-510). Specifications for the commercial MET sensors, and specifications and calibration of the BSL MET sensors are given below.

*Commercial MET Sensors* A Paroscientific sensor (Model 1477-005; s/n 101728), the most accurate of the MET sensors being tested, is used as the reference standard. The pressure accuracy is  $\pm 8\text{Pa}$ , the temperature accuracy is  $\pm 0.5\text{ }^\circ\text{C}$ , and the relative humidity accuracy is  $\pm 2\%$  (<http://paroscientific.com/pdf/MET.pdf/>). The Vaisala MET sensor (Model WXT-510; s/n C4760003), on loan from UNAVCO, is being tested for possible use at BARD stations. The pressure accuracy is  $\pm 50\text{Pa}$ , the temperature accuracy is  $\pm 0.3\text{C}$ , and the relative humidity accuracy is  $\pm 3\%$  (<http://www.vaisala.com/instruments/products/weathermultisensor.html/>). In addition, this sensor measures wind speed and direction with accuracies of  $\pm 3\%$  and  $\pm 3^\circ$ , respectively.

*BSL MET Sensors* The sensor elements in the BSL MET package are manufactured by Honeywell (<http://sensing.honeywell.com>). The pressure sensing element, Honeywell SDX15A2-A, is temperature compensated and has a typical accuracy of  $\pm 0.25\%$ . The specification sheet indicates that the sensor range of 0-15 psi in absolute pressure results in a 90mv ( $\pm 1\%$ ) differential change on the outputs when the bridge is excited with 12V. The sensor is operated in a bridge circuit configuration and its sensitivity is:

$$P(\text{Pa}) = 689.825 * V + 92643$$

where: V is the bridge output in Volts.

The thin film platinum resistance temperature detector (RTD) is a Honeywell HEL-700 with a resistance of  $1\text{k}\Omega$  at  $0^\circ\text{C}$  and with an accuracy of  $\pm 0.3^\circ\text{C}$ . The RTD is operated in a circuit with offset and gain and its sensitivity is:

$$T(^{\circ}\text{C}) = 2.8877 * V + 26.248$$

where: V is the output in Volts.

The humidity sensing element is a Honeywell HIH-4602C which is sensitive to the relative humidity with an accuracy of  $\pm 3.5\%$ . The sensor is operated in a circuit which results in a overall calibrated sensitivity of:

$$\%RH = ((V + 9.29)/3.168 - Z)/S$$

where: %RH is the percent relative humidity and V is the voltage output. S and Z are given in the factory calibration sheet as  $Z \sim 0.826\text{ mV}$  and  $S \sim 31.5\text{ mv}/\%RH$ . Thus:

$$\%RH = 10.021 * V + 66.87.$$

where: V is the output in Volts.

The factory specification sheet indicates that the response time is  $\sim 50$  seconds and the accuracy is  $\pm 3.5\%RH$ .

The absolute humidity (AH) is a function of temper-



Figure 3.26: Cluster of MET sensors under test at BRIB. The sensors from left to right are; Paroscientific; BSL MET 2, BSL MET 1, and Vaisala. The electronics for the BSL MET sensors are remotely located approximately 40 feet away in the vault which contains the BRIB supporting hardware.

ature, and, given the temperature, AH can be derived from relative humidity (RH) via:

$$AH(g/m^3) = (0.000002T^4 + 0.0002T^3 + 0.0095T^2 + 0.337T + 4.9034) * RH$$

where: T is the temperature in  $^\circ\text{C}$ .

*BRIB MET sensor Cluster Test* Four MET sensors (the Paroscientific, the Vaisala, and two BSL instruments) have been operating in a closely spaced cluster at BRIB since 2009.211 as seen Figure 3.26.

*Data Acquisition* The Paroscientific and Vaisala MET sensors output digital data and they are connected to port 2 of two different NetRS (Trimble GPS reference stations) and embedded in the GPS data streams at a rate of 1 sample per minute. The two BSL MET sensor output voltages proportional to temperature, relative humidity and pressure which are digitized/recorded by a single 6-channel Quanterra Q4120 data logger at a rate of 1 sample per second. The Paroscientific and Vaisala MET data are extracted from the GPS data streams using the teqc program and the BSL MET 1 and 2 data were extracted using the qmerge program.

One problem which was encountered is that there are gaps in MET data from the Paroscientific and Vaisala sensors, the zero minute of each hour and occasionally at other times are missing and we are currently investigating the cause.

*Test Results* Ten days of MET data (2009.211-220) was

retrieved for the four sensor packages and the data were interpolated/decimated to 1 sample per minute for analysis.

The two BSL MET sensors were calibrated via least squares using the Paroscientific as the reference. The calibration of the two BSL MET sensors channels are given in terms of the offset (a) and the sensitivity (b) with the McLauren series form:  $f(c) = a + b * \text{counts}$ . The results are presented in Table 3.13. Note that the a and b values for the second relative humidity sensor are anomalously large owing to a malfunction in the electronics. Even so the calibration is reasonable given the 5.1 percent standard error.

Comparing the Vaisala MET sensor with the reference Paroscientific MET sensor data, we find that the pressure, temperature and relative humidity standard errors are: 0.159mbar (15.9Pa), 0.292°C, and 4.38%. All values are within the factory specifications for accuracy of the Vaisala WXT-510 and thus the differences are not significant.

In summary, the BSL in-house MET sensors perform very well. Their accuracy and resolution are sufficient for use to reduce the components of the seismic background noise that are correlated with temperature and pressure and for estimating and correcting for geodetic GPS tropospheric propagation delays.

MET	Sensor	a	b	se
1	D	93093	0.0016902	31.7
2	D	93144	0.0016531	63.0
1	K	14.83	0.0000047665	1.13
2	K	21.88	0.0000054509	1.07
1	I	5391.	0.0023869	5.12
2	I	58.70	0.000019885	3.92

Table 3.13: Calibration parameters for BSL MET sensors where D is pressure in Pa, K is temperature in °C, and I is relative humidity in % .

### STS 1 Development and testing

The BSL is participating in the NSF-funded re-development of the STS1 instruments. BSL's role has principally been to objectively test, evaluate, and compare the old STS1s with new instruments developed by Metrozet. Additionally, with input from Metrozet, BSL has developed and fabricated a new baseplate for installing these seismometers.

In December 2008, Metrozet brought newly developed STS1-H instruments to Berkeley for initial evaluation. These instruments were installed at the test facility on the new baseplate.

Several problems typical of any new installation were encountered. These include difficulties with cabling, insulation, connector orientation, and vacuum leaks.

The problems were quickly resolved and the evaluation proceeded. Initial assessments indicate that both the Metrozet seismometer and the Berkeley designed baseplate are promising.

As many of the problems experienced with STS1 seismometers over time are related to their installation, the BSL has focused on developing both a new baseplate and an acceptable retrofit to the original warpless baseplate. We have developed and are testing replacement parts that would ensure the vacuum on the instruments.

### 7.6 Acknowledgements

Doug Neuhauser, Bob Uhrhammer, Peggy Hellweg, Pete Lombard, Rick McKenzie, and Jennifer Taggart are involved in the data acquisition and quality control of BDSN/HRSN/NHFN/MBPO data. Development of the sensor test facility and analysis system was a collaborative effort of Bob Uhrhammer, Tom McEvelly, John Friday, and Bill Karavas. IRIS and DTRA provided, in part, funding for and/or incentive to set up and operate the facility, and we thank them for their support. Vaisala WXT-510 MET sensor package was on loan from UN-AVCO. Bob Uhrhammer, Peggy Hellweg, Pete Lombard, Doug Neuhauser, and Barbara Romanowicz contributed to the preparation of this section. The STS-1 project is funded by the NSF through the IRIS/GSN program (IRIS Subaward Agreement number 388). This is a collaborative project with Tom VanZandt of Metrozet, LLC (Redondo Beach, CA).

### 7.7 References

- Ekström, G. and M. Nettles, <http://www.seismology.harvard.edu/~ekstrom/Projects/WQC.html>, 2005.
- Gardner, W. A., A unifying view of coherence in signal processing, *Signal Processing*, 29, p. 113-140, 1992.
- Ingate, S. et al, Workshop Report from Broadband Seismometer Workshop, Lake Tahoe, CA, <http://www.iris.edu/stations/seisWorkshop04/report.htm>, 2004.
- McNamara, D. and R. Buland, Ambient Noise Levels in the Continental United States *Bull. Seism. Soc. Am.*, 94, 4, 2004.
- Scherbaum, Frank. Of Poles and Zeros: Fundamentals in Digital Seismology, Volume 15 of Modern Approaches in Geophysics, G. Nolet, Managing Editor, Kluwer Academic Press, Dordrecht, xi + 257 pp., 1996.
- Tapley, W. C. and J. E. Tull, SAC - Seismic Analysis Code: Users Manual, *Lawrence Livermore National Laboratory*, Revision 4, 388 pp., March 20, 1992.
- Wielandt, E. and G. Streckeisen, The leaf spring seismometer: design and performance, *Bull. Seis. Soc. Am.*, 72, 2349-2367, 1982.
- Wielandt, E. and Steim, J. M., A digital very broad band seismograph, *Annales Geophysicae*, 4 B(3), 227-232, 1986.

## 8 Northern California Earthquake Monitoring

### 8.1 Introduction

Routine analysis of the data produced by BSL networks begins as the waveforms are acquired by computers at UC Berkeley, and ranges from automatic processing for earthquake response to analyst review for earthquake catalogs and quality control.

In the mid 1990s, the BSL developed an automated earthquake notification system (*Gee et al.*, 1996; 2003a) called Rapid Earthquake Data Integration (REDI). This system determined earthquake parameters rapidly, producing near real-time locations and magnitudes of Northern and Central California earthquakes, estimates of the rupture characteristics and the distribution of ground shaking following significant earthquakes, and tools for the rapid assessment of damage and estimation of loss. Then, in 1996, a collaboration began between the BSL and the USGS for reporting on Northern and Central California earthquakes. Programs in Menlo Park and Berkeley were merged into a single earthquake notification system using data from the NCSN and the BDSN. The USGS and the BSL now form the Northern California Earthquake Management Center (NCEMC) of the California Integrated Seismic Network (Section 2). In the most recent step of a long cooperative integration process, the CISN software became the production software for earthquake reporting in the NCEMC in June 2009.

With partial support from the USGS, the BSL is also participating in the development and assessment of a statewide prototype system for warning of imminent ground shaking in the seconds after an earthquake has initiated but before strong motion begins at sites that may be damaged. (See Research Study 17.)

### 8.2 Northern California Earthquake Management Center

In this section, we describe how the Northern California Earthquake Management Center fits within the CISN system. Figure 3.9 in Section 2 illustrates the NCEMC as part of the the CISN communications ring. The NCEMC is a distributed center, with elements in Berkeley and in Menlo Park. The 35 mile separation between these two centers is in sharp contrast to the Southern California Earthquake Management Center, where the USGS Pasadena is located across the street from the Caltech Seismological Laboratory. As described in Section 2, the CISN partners are connected by a dedicated T1 communications link, with the capability of falling back to the Internet. In addition to the CISN ring, the BSL and the USGS Menlo Park have a second dedicated communications link to provide bandwidth for shipping waveform

data and other information between their processing systems.

Figure 3.27 provides more detail on the system operating at the NCEMC since mid-June, 2009. Now, complete earthquake information processing systems operate in parallel in Menlo Park and Berkeley. Incoming data from each network is processed locally at the two data centers in the network services computers. The continuous reduced data, which include picks, codas, ground motion amplitudes and ML100, are exchanged between the data centers and fed into both processing streams. Real time analysis is coordinated using up-to-date information from the local real time database, which is replicated to the local data center database. Event review and automatic downstream processes such as computation of fault plane solutions access the internal data center databases. To maintain redundancy, robustness, and completeness, these two databases replicate each other across the Bay. They also replicate with the public database, from which information is made available to the outside. The system includes the production of location and origin time as well as estimates of  $M_d$ ,  $M_L$ , and  $M_w$ . For events with  $M > 3.5$  ShakeMaps are also calculated on two systems, one in Menlo Park and one in Berkeley. Finite fault calculation is not yet integrated into the new processing system. It is only calculated at the BSL at this time.

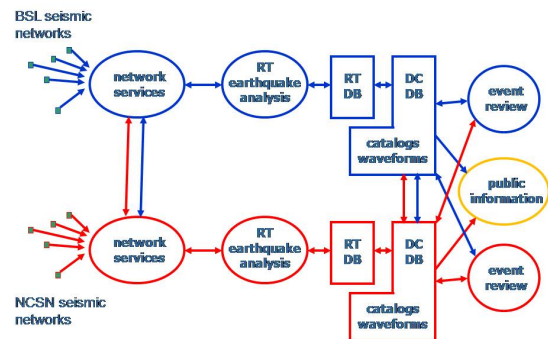


Figure 3.27: Details of the new Northern California processing system which has been operational since mid-June, 2009. Network service processing, that is, production of picks, ground motion amplitudes, and other reduced information, occurs at both datacenters, and the information is exchanged. Complete earthquake information processing systems exist on both sides of the Bay, and up-to-date information is exchanged by database replication.

This new system combines the advantages of the NCSN with those of the BDSN. The dense network of the NCSN provides rapid and accurate earthquake locations, low magnitude detection thresholds, and first-motion mechanisms. The high dynamic range data loggers, digital telemetry, and broadband and strong-motion sensors of the BDSN provide reliable magnitude determination, moment tensor estimation, calculation of peak ground motions, and estimation of source rupture characteristics. With the advent of the new system, we have lost the capability of publishing robust preliminary hypocenters, or “Quick Looks” within about 25 seconds after the origin time, but we are working to reestablish it. Thus, locations are now published when preliminary coda magnitudes are available, within 2-4 minutes of the origin time. Estimates of local magnitude are generally available 30-120 seconds later, and other parameters, such as the peak ground acceleration and moment magnitude, follow within 1-4 minutes (Figure 3.28).

Earthquake information is now distributed to the web through EIDS and is available through the USGS Earthquake Notification Service <http://sslearnquake.usgs.gov/ens>. Organizations with the need for more rapid earthquake information should use CISN Display <http://www.cisn.org/software/cisndisplay.htm>. The *recenteqs* site has enjoyed enormous popularity since its introduction and provides a valuable resource for information which is useful not only in the seconds immediately after an earthquake, but in the following hours and days as well.

### 8.3 2008-2009 Activities

#### Transition to New Production System: CISN Software

In June, 2009, we began operating the CISN software as the production system in the Northern California Seismic System (NCSS) for monitoring and reporting on Northern California earthquakes. This came as the result of a long effort to adapt and test software developed for the Trinet system and operating in Southern California. Now, nearly identical systems operate at the USGS and UC Berkeley. Very similar systems function in Southern California. Data flow in the new Northern California system (Figure 3.29) has been modified to allow for local differences (such as very different forms of data acquisition and variability in network distribution). In addition, the BSL and the USGS want to minimize use of proprietary software in the system. One exception is the database program, Oracle. The NCEDC Oracle database has now been expanded to host all earthquake information and parameters associated with the real time monitoring system. It is the centerpoint of the new system, providing up-to-date information to all processing modules. Reliability and robustness are achieved by contin-

uously replicating the databases. The public, read-only, database provides event and parametric information to catalog users and the public.

During the last few years, BSL staff members, particularly Pete Lombard, have become extremely familiar with elements of the TriNet software. The software is now adapted for Northern California, with many adjustments and modifications completed along the way. For example, Pete Lombard adapted the TriNet magnitude module to Northern California. Pete made a number of suggestions on how to improve the performance of the magnitude module and has worked closely with Caltech and the USGS/Pasadena on modifications.

The BSL and the USGS Menlo Park have implemented a system to exchange “reduced amplitude timeseries.” One of the important innovations of the TriNet software development is the concept of continuous processing (*Kanamori et al.*, 1999). Waveform data are constantly processed to produce Wood Anderson synthetic amplitudes and peak ground motions. A program called *rad* produces a reduced timeseries, sampled every 5 seconds, and stores it in a memory area called an “Amplitude Data Area” or ADA. Other modules can access the ADA to retrieve amplitudes to calculate magnitude and ShakeMaps as needed. The BSL and the USGS Menlo Park have collaborated to establish tools for ADA-based exchange. As part of the software development in Northern California, a number of modules have been developed.

#### Moment Tensor Solutions with *tmts* and Finite Fault Analysis

The BSL continues to focus on the unique contributions that can be made from the broadband network, including moment tensor solutions and finite fault analysis. Caltech developed a Java and web-based moment tensor processing system and review interface for the complete waveform modeling technique of *Dreger and Romanowicz* (1994). The web-based review interface was upgraded during 2007 to include new mechanism-related tables, and has been used in Northern California since July 2007. During the first six months of 2009, the automatically running version for real time analysis was extensively tested and updated by Pete Lombard, with updates made to the review interface as well. With the transition to the new software, automatic moment tensor analysis now proceeds through the *tmts* system. At the same time, we changed our reporting rules so that automatically produced solutions of high quality are now published to the web.

From July 2008 through June 2009, BSL analysts reviewed many earthquakes in Northern California and adjoining areas of magnitude 3.2 and higher. Reviewed moment tensor solutions were obtained for 56 of these events (through 6/30/2009). Figure 3.30 and Table 3.14 display the locations of earthquakes in the BSL moment

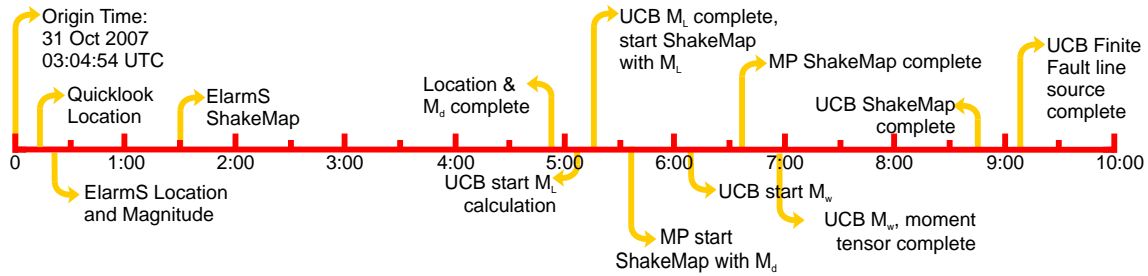


Figure 3.28: Illustration of the earthquake products timeline for the  $M_w$  5.4 Alum Rock earthquake of October 30, 2007. Note that all processing was complete within 10 minutes of the origin time.

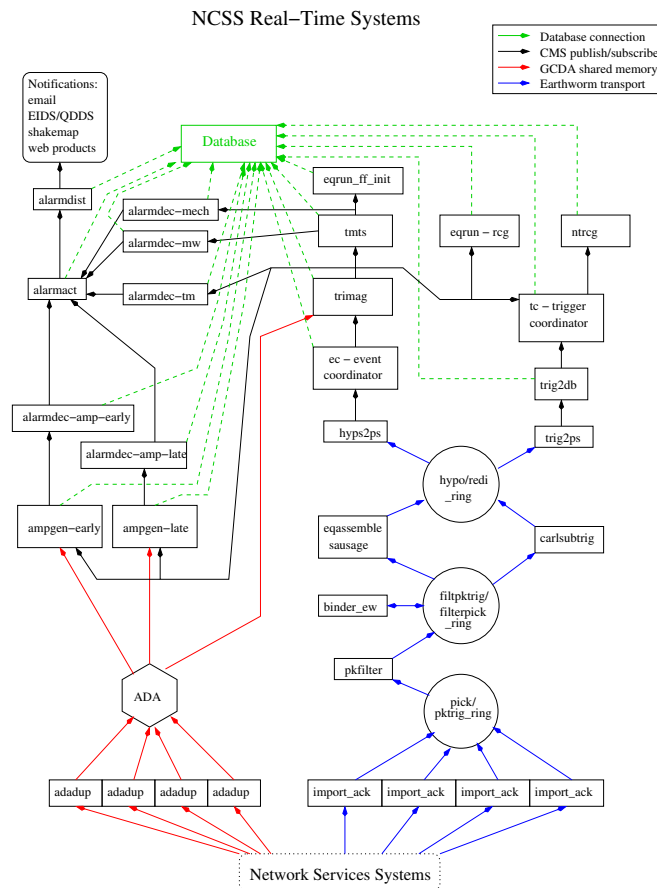


Figure 3.29: Schematic diagram of processing in the NCSS system. The design combines elements of the Earthworm, TriNet, and REDI systems

tensor catalog and their mechanisms. During this year, no earthquakes were large enough to allow finite fault inversions to be performed.

#### trimag and $M_L$

With the transition to the new software, local magnitudes are no longer calculated with the REDI code. As part of the transition to the new software, we worked with Southern California to develop a statewide proce-

cedure for calculating  $M_L$ . A new  $\log A_o$  function was been developed that is valid throughout the state, and a corresponding set of corrections calculated for the collocated broadband and strong motion stations. Southern California began using these parameters in early 2008, and they are now being used in Northern California as well.  $M_L$  determinations by Southern and Northern California with their respective stations for a sequence of events south of Bishop compare very well.

## 8.4 Routine Earthquake Analysis

In fiscal year 2008-2009, more than 21,500 earthquakes were detected and located by the automatic systems in Northern California. This compares with over 26,000 in 2007-2008, 23,000 in 2006-2007, 30,000 in 2005-2006 and 38,800 in 2004-2005. Many of the large number of events in 2004-2005 are aftershocks of the 2003 San Simeon and 2004 Parkfield earthquakes. Of the more than 21,500 events, about 140 had preliminary magnitudes of three or greater. Thirteen events had  $M_L$  greater than 4. The largest event recorded by the system occurred off the coast of Cape Mendocino on 28 October 2008. It had  $M_w$  4.9.

Although BSL staff are no longer reading BDSN records for local and regional earthquakes (see Annual Report of 2003-2004), they are now participating in timing and reviewing earthquakes with `Jiggle`, mainly working on events from past sequences that have not yet been timed. This work contributes to improving the earthquake catalog for Northern California, but also ensures robust response capabilities, should the Menlo Park campus be disabled for some reason.

## 8.5 Acknowledgements

Peggy Hellweg oversees our earthquake monitoring system and directs the routine analysis. Peter Lombard and Doug Neuhauser contribute to the development of software. Rick McKenzie, Taka'aki Taira, Doug Dreger, Holly Brown, Shan Dou, Sean Ford, Kelly Grijalva, Aurelie Guilhem, Ahyi Kim, Ved Lekic, Rob Porritt, Jennifer Taggart, Amanda Thomas, and Gilead Wurman contribute to the routine analysis of moment tensors. Peggy Hellweg, Doug Neuhauser, and Bob Uhrhammer contributed to the writing of this section. Partial support for the development and maintenance of the REDI system is provided by the USGS.

## 8.6 References

Dreger, D., and B. Romanowicz, Source characteristics of events in the San Francisco Bay region, *USGS Open File Report 94-176*, 301-309, 1994.

Gee, L., J. Polet, R. Uhrhammer, and K. Hutton, Earthquake Magnitudes in California, *Seism. Res. Lett.*, 75(2), 272, 2004.

Gee, L., D. Neuhauser, D. Dreger, M. Pasyanos, R. Uhrhammer, and B. Romanowicz, The Rapid Earthquake Data Integration Project, *Handbook of Earthquake and Engineering Seismology*, IASPEI, 1261-1273, 2003a.

Gee, L., D. Dreger, G. Wurman, Y. Gung, B. Uhrhammer, and B. Romanowicz, A Decade of Regional Moment Tensor Analysis at UC Berkeley, *Eos Trans. AGU*, 84(46), Fall Meet. Suppl., Abstract S52C-0148, 2003b.

Gee, L., D. Neuhauser, D. Dreger, M. Pasyanos, B. Romanowicz, and R. Uhrhammer, The Rapid Earthquake Data Integration System, *Bull. Seis. Soc. Am.*, 86, 936-945, 1996.

Pasyanos, M., D. Dreger, and B. Romanowicz, Toward real-time estimation of regional moment tensors, *Bull. Seis. Soc. Am.*, 86, 1255-1269, 1996.

Romanowicz, B., D. Dreger, M. Pasyanos, and R. Uhrhammer, Monitoring of strain release in central and northern California using broadband data, *Geophys. Res. Lett.*, 20, 1643-1646, 1993.

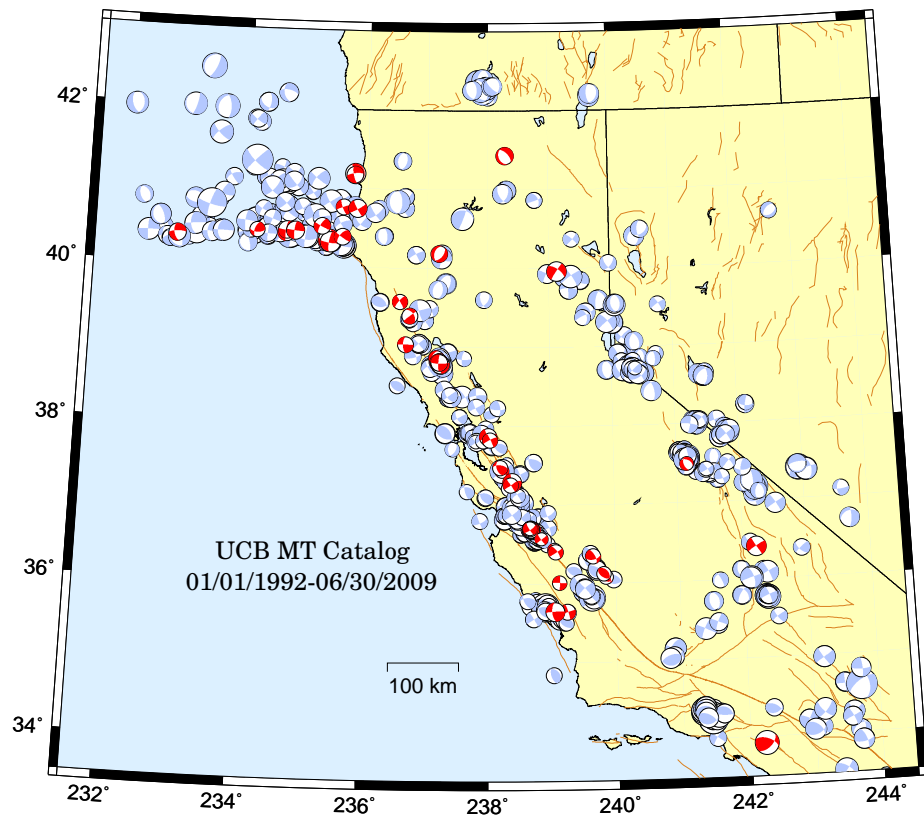


Figure 3.30: Map comparing reviewed moment tensor solutions determined by the BSL from past years (blue/gray) with those from the fiscal year 2008-2009 (red/dark).

Location	Date	UTC Time	Lat.	Lon.	MT Depth	$M_l$	$M_w$	Mo	Str.	Dip	Rake
Paso Robles, CA	7/6/2008	20:25:54	35.64	-120.76	8	3.64	3.7	4.00E+21	252	90	-6
Toms Place, CA	7/10/2008	23:35:35	37.49	-118.84	5	3.29	3.2	6.89E+20	158	56	-63
Petrolia, CA	7/30/2008	13:39:34	40.43	-125.33	18	3.5	4.2	2.88E+22	96	82	169
Tennant, CA	8/7/2008	18:11:39	41.43	-121.72	5	3.39	3.4	1.60E+21	316	61	-100
Trinidad, CA	8/17/2008	5:56:59	41.19	-124.22	18	4.37	4.6	9.99E+22	159	79	84
Alamo, CA	9/6/2008	4:00:15	37.86	-122.01	14	4.12	4.1	1.51E+22	247	90	4
Willits, CA	9/12/2008	13:04:04	39.39	-123.28	5	3.35	3.6	3.65E+21	232	88	-44
The Geysers, CA	9/13/2008	20:27:52	38.79	-122.76	5	3.39	3.6	2.91E+21	120	81	-144
The Geysers, CA	9/15/2008	1:34:46	38.79	-122.77	5	3.21	3.5	2.43E+21	340	74	-150
Petrolia, CA	10/26/2008	9:27:22	40.34	-124.63	18	4.86	4.9	3.34E+23	101	82	171
Trinidad, CA	10/26/2008	16:07:48	41.17	-124.22	18	3.5	3.9	8.72E+21	168	76	-16
Avenal, CA	11/5/2008	16:05:49	36.08	-120.16	18	3.43	3.4	1.52E+21	325	48	110
Alum Rock, CA	11/10/2008	19:56:25	37.43	-121.78	14	3.34	3.2	8.86E+20	229	89	-7
The Geysers, CA	11/12/2008	11:10:59	38.86	-122.84	5	3.21	3.5	2.07E+21	48	54	-70
Petrolia, CA	11/13/2008	5:03:54	40.44	-125.28	24	3.49	4	1.26E+22	97	87	169
San Juan Bautista, CA	11/13/2008	18:24:10	36.8	-121.53	21	3.42	3.4	1.69E+21	167	87	-173
Petrolia, CA	11/16/2008	5:43:16	40.31	-124.6	18	4.57	4.6	9.97E+22	97	80	167
San Ardo, CA	11/17/2008	14:27:29	36.01	-120.88	11	3.79	3.3	1.27E+21	273	89	-4
Tres Pinos, CA	12/21/2008	17:35:37	36.67	-121.3	5	4.36	4	1.33E+22	224	81	10
Tres Pinos, CA	12/21/2008	20:09:33	36.68	-121.3	8	3.91	3.6	2.86E+21	225	82	17
East Quincy, CA	12/26/2008	12:19:40	39.96	-120.87	5	4.98	4.5	6.11E+22	215	77	-23
The Geysers, CA	1/4/2009	17:27:10	38.78	-122.77	5	4.14	4.3	3.17E+22	262	87	14
Ukiah, CA	1/10/2009	9:18:11	39.03	-123.34	11	3.79	3.8	5.17E+21	271	88	25
Tres Pinos, CA	1/15/2009	14:44:08	36.68	-121.33	8	3.94	3.7	4.36E+21	226	83	11
Tres Pinos, CA	1/20/2009	6:06:00	36.7	-121.33	8	4	3.9	7.87E+21	41	82	-19
Tres Pinos, CA	1/20/2009	8:14:43	36.7	-121.33	8	3.83	3.8	5.90E+21	43	88	-21
Tres Pinos, CA	1/20/2009	8:57:23	36.7	-121.33	8	3.55	3.49	2.11E+21	252	69	29
Tres Pinos, CA	1/20/2009	9:12:27	36.69	-121.32	8	4	3.8	5.40E+21	38	88	-10
Tres Pinos, CA	1/21/2009	20:49:43	36.7	-121.33	8	3.69	3.5	2.20E+21	42	81	-12
Tres Pinos, CA	2/6/2009	0:20:29	36.69	-121.32	8	3.91	3.7	4.98E+21	242	85	19
The Geysers, CA	2/20/2009	10:29:28	38.81	-122.81	5	3.37	3.7	4.03E+21	334	82	-138
Pinnacles, CA	2/21/2009	15:27:07	36.43	-120.95	11	3.13	3.2	7.99E+20	63	83	16
The Geysers, CA	3/5/2009	23:06:26	38.83	-122.78	5	3.22	3.3	1.29E+21	47	49	-78
Milpitas, CA	3/8/2009	14:47:20	37.47	-121.8	8	3.53	3.5	2.02E+21	277	60	45
New Idria, CA	3/9/2009	3:07:53	36.4	-120.93	8	3.43	3.5	1.85E+21	57	85	19
Avenal, CA	3/12/2009	13:59:43	36.12	-120.18	8	3.28	3.4	1.55E+21	127	54	83
Cantua Creek, CA	3/15/2009	5:23:31	36.34	-120.35	5	3.6	3.5	2.26E+21	332	69	143
Ferndale, CA	3/18/2009	11:04:39	40.54	-124.43	11	3.6	3.8	6.70E+21	325	77	-146
Petrolia, CA	3/23/2009	1:34:24	40.44	-125.32	11	3.77	4.1	1.89E+22	96	89	169
Laytonville, CA	3/23/2009	12:29:21	39.57	-123.45	8	3.2	3.6	2.82E+21	311	87	-167
Humboldt Hill, CA	3/27/2009	8:32:35	40.76	-124.39	18	3.28	3.7	4.76E+21	250	86	14
Morgan Hill, CA	3/30/2009	17:40:29	37.28	-121.62	8	4.67	4.3	3.81E+22	169	89	166
Ferndale, CA	4/3/2009	18:02:23	40.51	-124.75	14	3.66	3.8	7.27E+21	117	85	160
The Geysers, CA	4/17/2009	15:09:40	38.82	-122.8	5	3.51	3.7	3.86E+21	50	64	-48
Morgan Hill, CA	4/30/2009	22:50:55	37.25	-121.64	8	3.77	3.51	2.31E+21	56	89	3
Pine Hills, CA	5/3/2009	17:54:05	40.75	-124.16	30	4.28	4.17	2.21E+22	151	83	-172
The Geysers, CA	5/18/2009	11:40:34	38.82	-122.82	5	3.11	3.37	1.41E+21	177	83	169
Petrolia, CA	5/29/2009	3:35:16	40.36	-127.14	30	3.82	4	1.26E+22	267	75	-147
Petrolia, CA	6/2/2009	17:04:40	40.45	-125.82	5	3.6	3.48	2.03E+21	200	62	34
Petrolia, CA	6/8/2009	7:54:04	40.38	-124.41	18	4.11	3.91	9.05E+21	119	78	139
Danville, CA	6/8/2009	22:15:05	37.82	-121.96	8	3.44	3.51	2.28E+21	334	83	-172
Tres Pinos, CA	6/9/2009	2:19:18	36.7	-121.34	8	3.14	3.23	8.68E+20	148	81	-167
Pinnacles, CA	6/10/2009	10:02:12	36.57	-121.16	5	3.06	3.08	5.14E+20	54	86	-6
Lake Nacimiento, CA	6/20/2009	12:32:48	35.64	-120.95	5	4.72	4.39	4.72E+22	267	86	28
Red Bluff, CA	6/27/2009	17:29:35	40.19	-122.8	5	3.64	3.82	6.64E+21	39	53	-77
The Geysers, CA	6/30/2009	17:27:28	38.81	-122.79	8	3.57	3.84	7.18E+21	183	82	-170

Table 3.14: Moment tensor solutions for significant events from July 1, 2008 through June 30, 2009 using a complete waveform fitting inversion. Epicentral information is from the UC Berkeley/USGS Northern California Earthquake Management Center. Moment is in dyne-cm and depth is in km.

## 9 Outreach and Educational Activities

### 9.1 Introduction

The BSL is involved in a variety of outreach activities ranging from lectures to lab tours and educational displays. Recorded information on current earthquake activity is updated regularly on our information tape (510-642-2160). Additional basic information on earthquakes and seismic hazards for northern and central California, as well as other information about seismology and our research, can be found on our extensive set of web pages at <http://seismo.berkeley.edu/>.

### 9.2 Highlights of 2008-2009

#### 1868 Hayward Earthquake 140th Anniversary

The Hayward Fault runs through the UCB campus. It last ruptured on October 21, 1868. Since then, new scientific insights put the average interval between large earthquakes on the Hayward Fault at 140 years; 2008 represented an important anniversary.

The 1868 Earthquake Alliance used the 140th anniversary as a unique opportunity to increase public awareness of seismic hazard posed by the Hayward Fault and other East Bay Faults, promote earthquake preparedness and mitigation, and explore the ways in which the 1868 Hayward earthquake affected the personal lives, culture, economy, and development of the greater San Francisco Bay Area (<http://1868alliance.org>). The BSL contributed to the commemoration activities and participated in their organization. Around the time of the anniversary, Peggy Hellweg led several tours of the Hayward Fault on the UC Berkeley Campus. The tour for the readers of Bay Nature (and others) was so popular that she took two groups to Memorial Stadium and beyond. On a Saturday in November, the members of the Northern California Geological Society visited the Campus to see the fault as well as the retrofit projects. Several teacher training workshops also featured talks and presentations by Peggy Hellweg on the Hayward Fault and earthquake hazards in the Bay Area and around the world.

The 140th anniversary of the Hayward Earthquake was also the impetus for holding the “Third Conference on Earthquake Hazards in the Eastern San Francisco Bay Region,” which took place October 22-26, 2008, at Cal State University East Bay (Hayward). The previous two conferences were held in 1982 and 1992. The BSL co-organized this conference, with Roland Bürgmann and Peggy Hellweg serving on the organizing committee. The meeting included three days of technical sessions, a public forum, and field trips. Many members of the BSL presented their recent work at the meeting.

#### Outreach Web Page Upgrade

Dr. Kevin Mayeda is currently heading a major outreach project designed to raise awareness of seismic hazard posed by the Hayward Fault. One goal is to develop a series of age-appropriate presentations and pamphlets for BSL scientists to use when giving talks at area schools and other community organizations. A second goal of this project is to revamp the existing BSL outreach web site, with new activities and teacher resources, videos about the Hayward Fault and research by BSL scientists, and a new look and feel. The Richard and Rhoda Goldman Foundation provided startup funding for this project. This summer, the BSL hired three UC Berkeley undergraduate students, Sam Peach, Matt DeMartini, and Chris Rawles, to produce presentations and videos about the Hayward Fault, earthquakes, and current earthquake research. With Jennifer Taggart, they also redesigned the outreach portion of the BSL web page. This project is expected to continue, with more presentations and videos being created over time as funding allows. This new suite of web pages is available at <http://seismo.berkeley.edu/outreach>

#### Lawson Lecture

In this year’s Lawson Lecture, Chris Poland of Degenkolb Engineers spoke on “Building Resilient Communities: Fresh Challenges for Earthquake Professionals.” In many cases, the need to develop and implement earthquake resistance founders in misunderstanding, complacency, and poor funding. The best way to ensure that a municipality can recover from a natural disaster is prepare for it in advance. A city such as San Francisco needs to name the hazard, define performance, and establish goals that represent the resiliency needed to support the community’s natural ability to rebound from such a major seismic event, and then work toward those goals. The Lawson Lectures are webcast at [http://seismo.berkeley.edu/news/lawson\\_lecture](http://seismo.berkeley.edu/news/lawson_lecture).

### 9.3 On-Going Activities

#### Tours and Presentations

As in every year, tours and presentations formed an important part of BSL’s public relations activities. Each month, several groups, ranging from middle-school students to scientists and engineers, tour our laboratory under the guidance of a graduate student or a member of the staff.

During 2008-2009 the BSL conducted several tours, both for local schools and groups from around the world. Several school classes at different grade levels received

tours. BSL graduate students also visited local elementary, middle, and high schools to talk about earthquakes and how we measure them. This year, particular attention was given to updating and rejuvenating our hallway displays. Jennifer Taggart provided the basic themes and backdrops for displaying BSL's past and current role in seismology, complete with the instrumentation and networks used along the way.

In addition to the tours, Drs. Allen, Dreger, Hellweg, Mayeda, and Uhrhammer presented talks on earthquakes and related phenomena to public groups and the media.

### Open House

The BSL again participated in *CalDay*. This annual event happened to occur on the anniversary of the 1906 San Francisco Earthquake this year. Attendance was exceptionally good. The visitors learned about UC Berkeley's role in earthquake monitoring, watched a streaming feed of earthquake data, jumped up and down to "make a quake," played with the earthquake machine, made P and S-waves with springs, learned about earthquake preparedness, and were given sample seismograms. The BSL co-sponsored a lecture with the Earth and Planetary Science department on "A Tectonic Time Bomb in Our Backyard: Earthquake Potential of the Hayward Fault" by Associate Research Seismologist Kevin Mayeda.

### Displays

The BSL provides local waveform feeds for helicorders at visitor centers associated with BDSN stations (CMB and MHC). Organizations such as LHS, KRON, and KPIX receive feeds from BKS via dedicated phone lines for display, while the USGS Menlo Park uses data from CMB for display in the lobby of the seismology building.



Figure 3.31: The group from "Sees the Day" has visited us now each summer for several years.

### BSL on the Web

We continue to maintain and update our presence on the Internet. The Web pages are intended to provide a source of earthquake information for the public. They also present information about the networks we operate, including station profiles. This benefits the research community as well. The BSL Web pages publicize seminar schedules, advertise courses, and describe our research, as well as our operations. They offer updates on recent earthquake activity, details on Bay Area seismicity and hazards, and links to other earthquake and earth science servers. We also use the web server to distribute information internally among BSL personnel, with such details as the computing and operational resources, rosters, and schedules for various purposes.

Since September, 2008 the BSL has hosted its own blog (<http://seismo.berkeley.edu/seismo.blog>). These pages are full of fascinating examples of geophysical science written with a clarity that can be appreciated by all. The entries are usually related to the latest happenings in the seismic world and are thus very current, increasing their interest even more.

### Earthquake Research Affiliates Program

The UC Berkeley Earthquake Research Affiliates (ERA) Program is an outreach project of the BSL. The purpose is to promote the support of earthquake research while involving corporations and governmental agencies in academic investigation and education activities such as conferences and field trips. The ERA program provides an interface between the academic investigation and practical application of earthquake studies.

## 9.4 Acknowledgements

Peggy Hellweg oversees the outreach activities at the BSL. Barbara Romanowicz, Bob Uhrhammer, Rick McKenzie, Jennifer Taggart, and many other faculty, staff, and students at the BSL contribute to the outreach activities. Rick McKenzie, Jennifer Taggart, and Peggy Hellweg contributed to the preparation of this section.

# Glossary of Common Acronyms

Table 3.15: Standard abbreviations used in this report.

Acronym	Definition
AMR	Accelerating Moment Release
ANSS	Advanced National Seismic System
BARD	Bay Area Regional Deformation
BAVU	Bay Area Velocity Unification
BDSN	Berkeley Digital Seismic Network
BSL	Berkeley Seismological Laboratory
CALREF	California Reference Frame
CDF	California Department of Forestry
CFS	Coulomb Failure Stress
CGS	California Geological Survey
CISN	California Integrated Seismic Network
CLVD	Compensated Linear Vector Dipole
CSMIP	California Strong Motion Instrumentation Program
CW	Complete Waveform
DART	Data Available in Real Time
DC	Double Couple
DNA07	Dynamic North America model of 2007
EM	Electromagnetic
ElarmS	Earthquake Alarm Systems
FA	Flexible Array
FACES	FlexArray along Cascadia Experiment for Segmentation
FAME	Flexible Array Mendocino Experiment
FFT	Fast Fourier Transform
FRAD	Frame Relay Access Device
GVF	Green Valley Fault
HF	Hayward Fault
HRSN	High Resolution Seismic Network
ICB	Inner Core Boundary
IG	Infragravity
IMS	International Monitoring System
InSAR	Interferometric Synthetic Aperture Radar
IRIS	Incorporated Research Institutions in Seismology
K-NET	Kyoshin Net, Japan
LBL	Lawrence Berkeley National Laboratory
LFES	Low-frequency Earthquakes
LLNL	Lawrence Livermore National Laboratory
LP	Long Period
MBARI	Monterey Bay Aquarium Research Institute
MMI	Modified Mercalli Intensity
MORB	Mid Ocean Ridge Basalts

*continued on next page*

Table 3.15: *continued*

Acronym	Definition
MPBO	Mini-Plate Boundary Observatory
MT	Magnetotelluric
NCEDC	Northern California Earthquake Data Center
NCEMC	Northern California Earthquake Management Center
NCF	Noise Correlation Functions
NCSN	Northern California Seismic Network
NCSS	Northern California Seismic System
NHFN	Northern Hayward Fault Network
NSMP	National Strong Motion Program
NTS	Nevada Test Site
NVT	Non-volcanic Tremor
OES	California Governor's Office of Emergency Services
PBO	Plate Boundary Observatory
PDF	Probability Density Function
PGV	Peak Ground Velocity
PSD	Power Spectral Density
PVC	Permanent Virtual Circuit
QDDS/EIDS	Quake Data Distribution System/Earthquake Information Distribution System
RCF	Rodgers Creek Fault
REDI	Rapid Earthquake Data Integration
RES	Repeating Earthquake Sequence
RGF	Reference Green Function
RMS	Root Mean Squared
RMT	Regional Moment Tensor
S/N	Signal to Noise
SAF	San Andreas Fault
SAFOD	San Andreas Fault Observatory at Depth
SCEC	Southern California Earthquake Center
SCEMC	Southern California Earthquake Management Center
SCSN	Southern California Seismic Network
SFBA	San Francisco Bay Area
SMIP	Strong Motion Instrumentation Program
STA/LTA	Short Time Average/ Long Time Average
SW	Surface Wave Inversion
SWD	Spectral Wave Density
THP	Temperature, Humidity, Pressure
UNAVCO	University NAVSTAR Consortium
USGS/MP	United States Geological Survey/ Menlo Park
USNSN	United States National Seismic Network
UUSS	University of Utah Seismic Stations
VLP	Very Long Period

# Appendix I Publications, Presentations, and Panels 2008-2009

## Publications

- Allen, R.M., At First Jolt: Will we have warnings for the next big earthquake? *Geotimes/EARTH*, 53(10), p52-59, 2008.
- Allen, R.M., P. Gasparini and O. Kamigaichi (eds), New Methods and Applications of Earthquake Early Warning. Special Section, *Geophys. Res. Lett.*, 36, L00B01-L00B08, 2009.
- Allen, R.M., H. Brown, M. Hellweg, O. Khainovski, P. Lombard, D. Neuhauser, Real-time earthquake detection and hazard assessment by ElarmS across California, *Geophys. Res. Lett.*, 36 L00B08, doi:10.1029/2008GL036766, 2009.
- Aagaard, B. T., T. M. Brocher, D. Dolenc, D. Dreger, R. Graves, S. Harmsen, S. Hartzell, S. Larsen, and M. L. Zoback, Ground motion modeling of the 1906 San Francisco Earthquake, Part I: Validation using the 1989 Loma Prieta earthquake, *Bull. Seism. Soc. Am.*, 98, 989-1011, 2008.
- Aagaard, B. T., T. M. Brocher, D. Dolenc, D. Dreger, R. Graves, S. Harmsen, S. Hartzell, S. Larsen, K. McCandless, S. Nilsson, N. A. Petersson, A. Rodgers, B. Sjogreen, and M. L. Zoback, Ground motion modeling of the 1906 San Francisco Earthquake, Part II: Ground motion estimates for the 1906 earthquake and scenario events, *Bull. Seism. Soc. Am.*, 98, 1012-1046, 2008.
- Abt, D., K. M. Fischer, S. W. French, H. A. Ford, H. Yuan, and B. Romanowicz, North American Lithospheric Discontinuity Structure Imaged By Ps and Sp Receiver Functions, *J. Geophys. Res.* (submitted)
- Audet, P., M. G. Bostock, N. I. Christensen, and S. M. Peacock, Seismic evidence for overpressured subducted oceanic crust and megathrust fault sealing, *Nature*, 457, 76-78, 2009.
- Banerjee, P., Bürgmann, R., Nagarajan, B., and Apel, E., Intraplate deformation of the Indian subcontinent: *Geophys. Res. Lett.*, 35, doi:10.1029/2008GL035468, 2008.
- Biggs, J., R. Bürgmann, J. Freymueller, Z. Lu, B. E. Parsons, I. Ryder, G. Schmalzle, and T. Wright, The postseismic response to the 2002 M7.9 Denali Fault Earthquake: Constraints from InSAR 2003-2005, *Geophysical Journal International*, 176, doi: 10.1111/j.1365-1246X.2008.03932.x, 2009.
- Brenguier, F., M. Campillo, C. Hadziioannou, N.M. Shapiro, R.M. Nadeau, E. Larose, Postseismic relaxation along the San Andreas fault at Parkfield from continuous seismological observations, *Science*, 321, 1478-1481, 2008.
- Bürgmann, R., Imperfect dominoes (news & views), *Nature Geoscience*, 2, doi:10.1038/ngeo1422, 2009.
- Cammarano, F. and B. Romanowicz, Radial profiles of seismic attenuation in the upper mantle based on physical models, *Geophys. J. Int.*, 175, 116-134, 2008.
- Cannata, A., M. Hellweg, G. Di Grazia, S. Ford, S. Alparone, S. Gresta, P. Montalto, D. Patan: Long Period and Very Long Period events at Mt. Etna volcano: characteristics, variability and causality, and their implications for their sources. *J. Volc. Geotherm. Res.*, in press.
- Cao, A. and B. Romanowicz, Constraints on shear wave attenuation in the Earth's inner core from an observation of PKJKP, *Geophys. Res. Lett.*, 36, L09301, doi:10.1029/2009GL038342, 2009.

- Chandrasekhar, D.V., Bürgmann, R., Reddy, C.D., Sunil, P.S., and Schmidt, D.A., Weak Mantle in NW India Probed by Geodetic Measurements Following the 2001 Bhuj Earthquake, *Earth Planet. Sci. Lett.*, *280*, doi:10.1016/j.epsl.2009.01.039, 2009.
- Chen, K. H., R.M. Nadeau and R.-J. Rau, Characteristic repeating earthquakes in an arc-continent collision boundary zone: The Chihshang fault of eastern Taiwan, *Earth Planet. Sci. Lett.*, *276*, 262-272, doi:10.1016/j.epsl.2008.09.021, 2008.
- Chen, K-H., R. Bürgmann, and R.M. Nadeau, Triggering effect of M 4-5 earthquakes on the earthquake cycle of repeating events at Parkfield, *BSSA* (submitted)
- Cupillard, P. and Y. Capdeville, On the amplitude of surface waves obtained by noise correlation and the capability to recover the attenuation : a numerical approach, *Geophys. J. Int.* (submitted)
- Dreger, D.S., S. R. Ford, and W. R. Walter. Source Analysis of the Crandall Canyon, Utah, Mine Collapse, *Science*, *321*, 217, 2008.
- Fielding, E.J., Lundgren, P.R., Bürgmann, R., and Funning, G.J., Shallow fault-zone dilatancy recovery after the 2003 Bam, Iran earthquake: *Nature*, *458*, doi:10.1038/nature07817, 2009.
- Ford, S.R., D.S. Dreger, W.R. Walter, Source Characterization of the August 6, 2007 Crandall Canyon Mine Seismic Event in Central Utah, *Seismol. Res. Lett.*, *79(5)*, doi:10.1785/gssrl.79.5.637, 2008.
- Ford, S.R., D.S. Dreger, K. Mayeda, W.R. Walter, L. Malagnini, and W.S. Phillips, Regional Attenuation in Northern California: A Comparison of Five 1-D Q Methods, *B. Seismol. Soc. Am.*, *98(4)*, doi:10.1785/0120070218, 2008.
- Ford, S.R., D.S. Dreger, and W.R. Walter, Identifying isotropic events using a regional moment tensor inversion, *J. Geophys. Res.*, B01306, doi:10.1029/2008JB005743, 2009.
- Ford, S.R., W.S. Phillips, W.R. Walter, M.E. Pasyanos, K. Mayeda, D.S. Dreger, Attenuation tomography of the Yellow Sea/Korean Peninsula from coda-source normalized and direct Lg amplitude, *Pageoph* (accepted), 2009.
- Gök, R. L. Hutchings, K. Mayeda, and D. Kalafat, Source parameters for 1999 north Anatolian fault zone aftershocks, *Pageoph*, *166(4)*, doi: 10.1007/s00024-009-0461-x, 2009.
- Goltz, C., D.L. Turcotte, S.G. Abaimov, R.M. Nadeau, N. Uchida, T. Matsuzawa, Rescaled earthquake recurrence time statistics: application to microrepeaters, *Geophys. J. Int.*, *176*, 256-264, 2009.
- Hilley, G. E., K. M. Johnson, M. Wang, Z.-K. Shen, and R. Bürgmann, Earthquake-cycle deformation and fault slip rates in Northern Tibet, *Geology*, *31*, doi:10.1130/G25157A.25151, 2009.
- Houlié, N., Reply to Cayol and Battaglia, *EPSL*, 2009 (in press).
- Johnson, K.M., Bürgmann, R., and Freymueller, J.T., Coupled afterslip and viscoelastic flow following the 2002 Denali Fault, Alaska Earthquake, *Geophys. J. Int.*, *176(3)*, doi: 10.1111/j.1365-1246X.2008.04029.x, 2009.
- Lay, T., R.C. Aster, D.W. Forsyth, B. Romanowicz, R.M. Allen, V.F. Cormier, J. Gombert, J.A. Hole, G. Masters, D. Schutt, A. Sheehan, J. Tromp, M.E. Wyssession, Seismological Grand Challenges in Understanding Earth's Dynamic Systems. Published by the Incorporated Research Institutions for Seismology, Washington DC. 84 pages, 2009.
- Lekic, V., J. Matas, M. Panning and B. Romanowicz, Measurement and implications of frequency dependence of attenuation, *Earth Planet. Sci. Lett.*, *282(1-4)*, p. 285-293, 2009.
- Malagnini, L., L. Scognamiglio, A. Mercuri, A. Akinci, K. Mayeda, Strong evidence for non-similar earthquake scaling in central Italy, *Geophys. Res. Lett.*, *35*, doi:10.1029/2008GL034310, 2008.
- Mayeda, K., and L. Malagnini, Apparent stress and corner frequency variations in the 1999 Taiwan (Chi-Chi) sequence: Evidence for a step-wise increase at  $M_w \sim 5.5$ , *Geophys. Res. Lett.*, *36*, L10308, doi:10.1029/2009GL037421, 2009.
- Motagh, M., R. Wang, T. R. Walter, R. Bürgmann, E. Fielding, J. Anderssohn, and J. Zschau, Coseismic slip model of the 2007 August Pisco earthquake (Peru) as constrained by Wide Swath radar observations, *Geophys. J. Int.*, *174*, doi: 10.1111/j.1365-1246X.2008.03852.x, 2008.

- Murphy, K.R., K. Mayeda, W.R. Walter, Coda spectral peaking for Nevada nuclear test site explosions, *Bull. Seismol. Soc. Am.*, *99*, doi: 10.1785/0120080046, 2009.
- Nadeau, R.M. and A. Guilhem, Nonvolcanic Tremor Evolution and the San Simeon and Parkfield, California Earthquakes, *Science*, *325*, 191-193, doi:10.1126/science.1174155, 2009.
- Panning, M. Y. Capdeville and B. Romanowicz, Do first order 3D Born finite-frequency kernels improve modeling of surface waveforms?, *Geophys. J. Int.*, *177*, 161-178. doi: 10.1111/j.1365-246X.2008.04050.x, 2009.
- Peng, Z., J. E. Vidale, A. G. Wech, R. M. Nadeau, and K. C. Creager, Remote triggering of tremor along the San Andreas Fault in central California, *J. Geophys. Res.*, *114*, B00A06, doi:10.1029/2008JB006049, 2009.
- Ritsema, J., P. Cupillard, B. Tauzin, W. Xu, L. Stixrude, and C. Lithgow-Bertelloni, Joint mineral physics and seismic wave traveltime analysis of upper mantle temperature, *Geology*, *37*, 363-366, 2009.
- Rolandone, F., Bürgmann, R., Agnew, D.C., Johanson, I.A., Templeton, D.C., d'Alessio, M.A., Titus, S.J., DeMets, C., and Tikoff, B., Aseismic slip and fault-normal strain along the central creeping section of the San Andreas fault: *Geophys. Res. Lett.*, *35*, doi:10.1029/2008GL034437, 2008.
- Romanowicz, B., M. Panning, Y. Gung and Y. Capdeville, On the computation of long period seismograms in a 3D earth using normal mode based approximations, *Geophys. J. Int.*, *175*, 520-536, DOI: 10.1111/j.1365-246X.2008.03914.x, 2008.
- Romanowicz, B., P. McGill, D. Neuhauser and D. Dolenc, Acquiring real time data from the broadband ocean bottom seismic observatory in Monterey Bay (MOBB), *Seism. Res. Lett.*, *80*, 196- 204, 2009.
- Romanowicz, B., The thickness of tectonic plates, *Science*, *324*, 474-476, 2009.
- Ryder, I., R. Bürgmann and J. Sun, Tandem afterslip on connected fault planes following the 2008 Nima-Gaize (Tibet) earthquake, *J. Geophys. Res.* (accepted).
- Ryder, I., and R. Bürgmann, Spatial variations in slip deficit on the central San Andreas fault from InSAR, *Geophys. J. Int.*, *175*, doi: 10.1111/j.1365-1246X.2008.03938.x, 2008.
- Shieh, J.T., Y.M. Wu, R.M. Allen, A comparison of tau-c and tau-p-max for magnitude estimation in earthquake early warning *Geophys. Res. Lett.*, *35*, L20301, doi:10.1029/2008GL035611, 2008.
- Shelly, D. R., W. L. Ellsworth, T. Ryberg, C. Haberland, G. S. Fuis, J. Murphy, R. M. Nadeau, and R. Bürgmann, Precise location of San Andreas Fault tremors near Cholame, CA using seismometer clusters: slip on the deep extension of the fault?, *Geophys. Res. Lett.*, *36*, doi:10.1029/2008GL036367, 2009.
- Schmidt, D. A., and R. Bürgmann, Predicted reversal and recovery of surface creep on the Hayward fault following the 1906 San Francisco earthquake, *Geophys. Res. Lett.*, *35*, L19205, doi:10.1029/2008GL035270, 2008.
- Stehly, L., B. Fry, M. Campillo, N.M. Shapiro, J. Guilbert, L. Boschi, D. Giardini, Tomography of the Alpine region from observation of seismic ambient noise, *Geophys. J. Int.*, *178*, 338-350, 2009.
- Sun, J., Z. Shen, X. Xu, and R. Bürgmann, Synthetic normal faulting of the 9 January 2008 Nima (Tibet) earthquake from conventional and along-track SAR interferometry, *Geophys. Res. Lett.*, *35*, doi:10.1029/2008GL035691, 2008.
- Taira, T., P.G. Silver, F. Niu, and R.M. Nadeau, Seismic Evidence for Remote triggering of fault-strength changes on the San Andreas Fault at Parkfield, *Nature*, doi:10.1038/nature08395, (in press).
- Taira, T., P.G. Silver, F. Niu and R.M. Nadeau, Detecting seismogenic stress evolution and constraining fault-zone rheology in the San Andreas Fault following the 2004 Parkfield Earthquake, *J. Geophys. Res.*, *113*, B03303, doi:10.1029/2007JB005151, 2008.
- Taira, T., R.B. Smith, and W.-L. Chang, Seismic evidence for dilatational source deformations accompanying the 2004-2008 Yellowstone accelerated uplift episode, *J. Geophys. Res.*, doi:10.1029/2008JB006281 (accepted), 2009.

- Templeton, D., R.M. Nadeau R. Bürgmann, Behavior of Repeating Earthquake Sequences in Central California and the Implications for Subsurface Fault Creep, *Bull. Seism. Soc. Am.*, 98, 52-65, 2008.
- Templeton, D. C., R. M. Nadeau, and R. Bürgmann, Distribution of postseismic slip on the Calaveras fault, California, following the 1984 M6.2 Morgan Hill earthquake, *Earth and Planetary Science Letters*, 277, doi:10.1016/j.epsl.2008.1009.1024, 2009.
- Thomas, A.M., R.M. Nadeau, and R. Bürgmann, Tremor-tide correlations and near-lithostatic pore pressure on the deep San Andreas fault, *Nature* (in revision).
- Walter, F., J. F. Clinton, N. Deichmann, D. S. Dreger, S. E. Minson, M. Funk, Moment tensor inversions of icequakes on Gornergletscher, Switzerland. *Bull. Seism. Soc. Am.*, 99-2A, doi:10.1785/0120080110, 2009.
- Yuan, H., K. Dueker and J. Stachnik, Crustal Structure and Thickness along the Yellowstone Hotspot Track: Evidence for lower crustal outflow from beneath the eastern Snake River Plain, *Geochem. Geophys. Geosy.* (submitted)
- Zhao, L., R. Allen, T. Zheng, and S. Hung, Reactivation of an Archean craton: constraints from P- and S-wave tomography in North China, *Geophys. Res. Lett.*, doi:10.1029/2009GL039781 (in press), 2009.

## Presentations

### **IRIS Annual Workshop, Stevenson, WA, June 4-6, 2008**

Allen, R.M., M. Xue and S.-H. Hung. The fate of the Juan de Fuca plate (invited).

### **European Union SAFER meeting, Istanbul, Turkey, June 25-27, 2008**

Allen, R.M. ElarmS AlertMaps: An earthquake in California and another near Istanbul (invited).

### **Gordon Research Conference: Rock Deformation - Real-Time Rheology, Tilton School, Tilton, NH, August 3-8, 2008**

Bürgmann, R., Space Geodetic Probing of Lower Crustal Rheology.

### **Annual Workshop of the Working Group “Seismic phenomena associated with volcanic activity” of the European Seismological Commission, Leon, Nicaragua, September 21-27, 2008**

Hellweg, M., A. Cannata, S. Gresta, S. Ford, G. Di Grazia, Moment tensors for Very Long Period Signals at Etna Volcano, Italy.

### **Monitoring Research Review, 2008, Portsmouth, VI, September 23-25, 2008**

Romanowicz, B., A. Cao, P. Cupillard, L. Stehly, A. Kim, M. Pasyanos, and D. Dreger, Calibration of 3D Upper Mantle Structure in Eurasia Using Regional and Teleseismic Full Waveform Seismic Data.

### **3rd Conference on Earthquake Hazards in the Eastern San Francisco Bay Area: Science, Hazard, Engineering, and Risk, CSU East Bay, Hayward, CA, October 22-24, 2008**

Bürgmann, R., Space Geodetic Observations of Active Deformation in the Eastern San Francisco Bay Area.

Hellweg, M., Allen, R.M., Brown, H. and Neuhauser, D., Earthquake Early Warning for California.

Hellweg, M., R. Uhrhammer, D. Dreger, J. Taggart, A. Chung, M.R. McKenzie, F. Waldhauser and D. Schaff, Characterizing Seismicity in the San Francisco East Bay.

Nadeau, R.M., M. Hellweg and D. Dreger, The Borehole Northern Hayward Fault Network (NHFN): Research Applications.

**2008 Fall Meeting of the California Science Teachers Association, San Jose, CA, October 30 - November 2, 2008**

Hellweg, M., A tectonic timebomb: the Hayward Fault.

**American Geophysical Union Fall Meeting, San Francisco, CA, December 15-19, 2008**

- Allen, R.M., M. Xue, S.-H. Hung, Complex geological interactions in the mantle beneath western USA, *Eos Trans., AGU, 89(53)*, Fall Meet. Suppl., Abstract S31D-02, 2008 (invited).
- Allen, R.M., M. Xue, S.-H. Hung, Using finite-frequency methods to improve regional models, *Eos Trans., AGU, 89(53)*, Fall Meet. Suppl., Abstract S21D-02, 2008 (invited).
- Arevalo, R., A. Ghosh, V. Lekic, V.C. Tsai, A.M. Dziewonski, L.H. Kellogg, J. Matas, W.R. Panero and B. Romanowicz, Degree-2 in the Transition Zone and Near the CMB: Bottom up Tectonics? *Eos Trans., AGU, 89(53)*, Fall Meet. Suppl., Abstract DI21A-1744, 2008.
- Audet, P., M. G. Bostock, S. M. Peacock, N. I. Christensen, D. C. Boyarko, M. R. Brudzinski, and R. M. Allen, Seismic evidence for overpressured subducted oceanic crust and sealing of the megathrust: Relations with ETS in Cascadia, *Eos Trans., AGU, 89(53)*, Fall Meet. Suppl., Abstract T23A-2002, 2008.
- Brenguier, F., M. Campillo, C. Hadziioannou, N. Shapiro, R. Nadeau and E. Larose, Postseismic Relaxation Along the San Andreas Fault at Parkfield from Continuous Seismological Observations, *EOS Trans. AGU, 89(53)*, Fall Meet. Suppl., Abstract S51E-03, 2008.
- Brocher, T.M., S. Garcia, B.T. Aagaard, J.J. Boatwright, T. Dawson, M. Hellweg, K.L. Knudsen, J. Perkins, D.P. Schwartz, P.W. Stoffer and M. Zoback, The 1868 Hayward Earthquake Alliance: A Case Study - Using an Earthquake Anniversary to Promote Earthquake Preparedness, *Eos Trans. AGU, 89(53)*, Fall Meet. Suppl., Abstract S14B-07, 2008.
- Brown, H., and Allen, R.M., Analyzing the Capabilities of the ElarmS Methodology Using a Japanese Dataset, *Eos Trans. AGU, 89 (53)*, Fall Meet. Suppl., Abstract S11A-1726, 2008.
- Campillo, M., L. Stehly, B. Froment, C3 (Correlation of Coda of Correlations): Improving the reconstruction of Green functions between stations of a network from noise records, *Eos Trans. AGU, 89 (53)*, Fall Meet. Suppl., Abstract S31A-1891, 2008.
- Chen, K.H., R. Bürgmann and R. Nadeau, Triggering effect of  $M > 4$  earthquakes on the earthquake cycle of repeating events at Parkfield, *EOS Trans. AGU, 89(53)*, Fall Meet. Suppl., Abstract S41A-1825, 2008.
- Cherubini, P., N. Houlié, N. Magdalena, T. Appert, S. Cullotta, Magmatic activity inferred from tree activity at Mt. Etna., *EOS Trans. AGU, 89(53)*, Fall Meeting Suppl., Abstract V11C-2058, 2008.
- Cupillard, P., Capdeville, Y., and Stehly, L., Recovering the attenuation of surface waves from noise correlation : synthetic tests in a spherically symmetric Earth, *Eos Trans., AGU, 89(53)* Fall Meet. Suppl., Abstract S31A-1895, 2008.
- Dolenc, D. and D. Dreger, Modeling of the Byerly's False S phase for the earthquakes off the coast of Northern California, *Eos Trans., AGU, 89(53)*, Fall Meet. Suppl., Abstract S33B-1947, 2008.
- Dou, S., Lekic, V., Romanowicz, B., Smooth Crustal Models Derived from Surface Wave Dispersion Data for Waveform Tomography based on the Spectral Element Method, *Eos Trans. AGU, 89(53)*, Fall Meet. Suppl., Abstract DI21A-1743, 2008.
- Dreger, D. S., Sean R. Ford and I. Ryder, Finite-source study of the February 21, 2008 Mw 6.0 Wells, Nevada, earthquake, *Eos Trans. AGU, 89(53)*, Fall Meet. Suppl., Abstract S51B-1743, 2008 (invited).
- Dreger, D. S., S. R. Ford, and W. R. Walter, Regional moment tensor inversion for source-type identification, *Eos Trans. AGU, 89(53)*, Fall Meet. Suppl., Abstract S13E-01, 2008 (invited).
- Evans, E.L., R. Bürgmann, B. Meade, N. Houlie, R. Nadeau, G.J. Funning, Subsurface Creep and Geometry of the Hayward-Calaveras Stepover, *EOS Trans. AGU, 89(53)*, Fall Meet. Suppl., Abstract S11A-1717, 2008.

- Gardner, J., N. Houlié, G. Funning, J. Friday, R. Bürgmann, and B. Romanowicz, Mitigation of tropospheric effects on site velocities of the Bay Area Regional Deformation network, *EOS Trans. AGU*, 89(53), Fall Meet. Suppl., Abstract G51A-0595, 2008.
- Gresta, S., M. Hellweg, A. Cannata, S. Ford and G. Di Grazia, Moment Tensors for Very Long Period Signals at Etna Volcano, Italy, *Eos Trans. AGU*, 89(53), Fall Meet. Suppl., Abstract V51C-2049, 2008.
- Grijalva, K., Bürgmann, R., and Banerjee, P., Stress Changes on the Sunda Megathrust Preceding the  $M_w$  8.4 2007 Earthquake, *Eos Trans., AGU*, 89(53), Fall Meet. Suppl., Abstract T52B-04, 2008.
- Guilhem, A. and R.M. Nadeau, Nonvolcanic Tremor Activity in the Parkfield-Cholame region of California and the 2003 M6.5 San Simeon and 2004 M6.5 Parkfield Earthquakes, *EOS Trans. AGU*, 89(53), Fall Meet. Suppl., Abstract U33A-0046, 2008.
- Hampton, J., J. Swanson, D. Marshall, F. Frazer, and N. Houlié, Lake Chabot GPS deformation network. From tectonic deformation monitoring to calibration network, *EOS Trans. AGU*, 89(53), Fall Meet. Suppl., Abstract G53B-0643, 2008.
- Hellweg, M, R.M. Allen, M. Bose, H. Brown, G. Cua, D. Given, E. Hauksson, T. Heaton, T. Jordan, O. Khainovski, P. Maechling, D. Neuhauser, D. Oppenheimer, K. Solanki, and M. Zeleznik, Earthquake early warning in California: Evaluating Hardware and Software, *Eos Trans. AGU*, 89(53), Fall Meet. Suppl., Abstract, S14B-05, 2008.
- Hidayat, D., T. Taira, S. Sacks, and A.T. Linde, Pressure Oscillation in Magma Chamber due to Replenishment During Volcanic Eruptions, *Eos Trans., AGU*, 89(53), Fall Meet. Suppl., Abstract V51C-2042, 2008.
- Houlié, N., R. Allen, M. Hellweg, D. Dreger, D. Neuhauser and B. Romanowicz, Collecting and Using Low Latency Data at Berkeley Seismological Laboratory, *Eos Trans. AGU*, 89(53), Fall Meet. Suppl., Abstract G43A-0667, 2008.
- Kim, A., D. S. Dreger, and S. Larsen, Finite-source inversion for the Parkfield earthquake using 3D Green's functions, *Eos Trans. AGU*, 89(53), Fall Meet. Suppl., Abstract S31C-05, 2008.
- Korneev, V. and R.M. Nadeau, Active Seismic Monitoring of the San Andreas Fault at Parkfield, *EOS Trans. AGU*, 89(53), Fall Meet. Suppl., Abstract NG44B-05, 2008.
- Komorowski, J.C., N. Houlié, and J. Dufek, Magmatic Burst into shallow volcanic reservoir. Implication for the quantification of intruded magma volumes, *EOS Trans. AGU*, 89(53), Fall Meet. Suppl., Abstract V11C-2061, 2008.
- Lekic, V. and B. Romanowicz, Global Upper Mantle Radially Anisotropic Model Developed Using the Spectral Element Method, *EOS Trans. AGU*, 89(53), Fall Meet. Suppl., Abstract DI11A-04
- Matas, J., V. Lekic, M. Panning and B. Romanowicz, Frequency dependence of attenuation: new measurements from normal modes and their geophysical implications, *EOS Trans. AGU*, 89(53), Fall Meet. Suppl., Abstract DI31B-1794
- Nadeau R., A. Thomas and R. Bürgmann, Tremor-tide correlations at Parkfield, CA, *EOS Trans. AGU*, 89(53), Fall Meet. Suppl., Abstract U33A-0053, 2008.
- Neuhauser, D.S., R.M. Allen, H. Brown, M. Hellweg, O. Khainovski and P. Lombard, Realtime Earthquake Detection and Hazard Assessment by ElarmS Across California, *Eos Trans. AGU*, 89(53), Fall Meet. Suppl., Abstract S11A-1725, 2008
- Niu, F., P.G. Silver, T. Daley, R.M. Nadeau, T. Taira, X. Cheng, and E. Majer, Seismic Imaging of Stress Transient, *Eos Trans., AGU*, 89(53), Fall Meet. Suppl., Abstract S51E-02, 2008 (invited).
- Peng, Z., J.E. Vidale, A. Wech, R.M. Nadeau, K.C. Creager, Tremor triggered near Parkfield by teleseismic waves, *EOS Trans. AGU*, 89(53), Fall Meet. Suppl., Abstract U32A-04, 2008.
- Porritt, R W, Allen, R, Moschetti, M, Lin, F, Ritzwoller, M, Boyarko, D, Brudzinski, M, Hinojosa, H, Ambient Seismic Noise Tomography in the Pacific Northwest Employing Earthscope Flexible Arrays, *EOS Trans. AGU*, 89(53), Fall Meet. Suppl., Abstract S31A-1881, 2008.

- Rhie, J., D. Dolenc, and B. Romanowicz, Long-period seismic noise at the Farallon Islands: Island's tilting due to infragravity waves as a possible source of Earth's horizontal hum, *Eos Trans., AGU, 89(53)*, Fall Meet. Suppl., Abstract S34A-05, 2008.
- Ryder, I.M., Bürgmann, R. and Fielding, E.J., Exploring the Rheology of Tibet from Postseismic Deformation Following Recent Large Earthquakes, *Eos Trans., AGU, 89(53)*, Fall Meet. Suppl., Abstract T11E-08, 2008.
- Shelly, D.R., W.L. Ellsworth, T. Ryberg, C. Haberland, G. Fuis, J. Murphy, R. Nadeau, R. Bürgmann, Precise Relative Location of San Andreas Fault Tremors Near Cholame, CA, Using Seismometer Clusters: Slip on the Deep Extension of the Fault?, *EOS Trans. AGU, 89(53)*, Fall Meet. Suppl., Abstract U31B-07, 2008.
- Stehly, L., Cupillard, P., Cao, A., and Romanowicz. B., Regional 3D tomography of the upper mantle using a summed source approach, *Eos Trans., AGU, 89(53)*, Fall Meet. Suppl., Abstract DI21A-1733, 2008.
- Taira, T., P.G. Silver, F. Niu, and R.M. Nadeau, Seismic Evidence for Remote Triggering of Fault-Strength Changes on the San Andreas Fault at Parkfield, *Eos Trans., AGU, 89(53)*, Fall Meet. Suppl., Abstract G21B-0694, 2008 (invited).
- Taira, T., R.B. Smith, and W.-L. Chang, Seismic Evidence for Dilatational Source Deformation of the Yellowstone Accelerated Uplift Episode, *Eos Trans., AGU, 89(53)*, Fall Meet. Suppl., Abstract V51D-2067, 2008.
- Thomas, A., and Bürgmann, R., A case study of stress proxies on the Hayward fault, *Eos Trans., AGU, 89(53)*, Fall Meet. Suppl., Abstract S21B-1827, 2008.
- Wurman, G., Allen, R.M., Statistical Investigation of Slip Evolution in Kinematic Source Inversions, *Eos Trans., AGU, 89(53)*, Fall Meet. Suppl., Abstract S51D-1803, 2008.
- Yuan, H., B. Romanowicz, D. Abt and K. Fischer, 3-D Isotropic and Anisotropic S-velocity Structure in the North America Upper Mantle, *Eos Trans. AGU, 89(53)*, Fall Meet. Suppl., Abstract S32B-02

### **PICS IPGP/BSL Collaborative Meeting 2009, Paris, France, January 6-8, 2009**

- Guilhem, A. and R.M. Nadeau, Nonvolcanic tremors and regional earthquakes
- Houlié, N., Can we do seismology with GPS?
- Porritt, R W, Allen, R, Moschetti, M, Lin, F, Ritzwoller, M, Boyarko, D, Brudzinski, M, Hinojosa, H, Ambient Seismic Noise Tomography in the Pacific Northwest Employing Earthscope Flexible Arrays

### **Sixth Annual Northern California Earthquake Hazards Workshop, January 20-21, 2009**

- Hellweg, M., J. Taggart, A. Chung, M. R. McKenzie, and D. Dreger, TMTS, the Interactive Moment Tensor Review Interface and the Berkeley Moment Tensor Catalog.
- Allen, R.M., H. Brown, M. Hellweg, O. Khainovski, P. Lombard, and D.S. Neuhauser, Realtime Earthquake Detection and Hazard Assessment by ElarmS Across California
- Romanowicz, B., M. Hellweg, and D. Neuhauser, Operation of the Northern California Earthquake Management Center (NCEMC): Collaboration between UC Berkeley and the USGS Menlo Park, CA.
- Taira, T., P.G. Silver, F. Niu, and R.M. Nadeau, Seismic Evidence for Remote Triggering of Fault-Strength Changes on the San Andreas Fault at Parkfield.

### **103rd Annual Meeting of the Seismological Society of America, Monterey, CA, April 8-10, 2009**

- Allen, R.M., M. Obrebski, F. Pollitz, M. Xue, S.-H. Hung, Plume vs. plate: Imaging geological interactions beneath North America, *Seism. Res. Lett., 80(2)*, 360, 2009 (invited).
- Chen, K.H., R. Bürgmann and R.M. Nadeau, Quantifying the Interaction Between Small Repeating Earthquake Sequences, *Seism. Res. Lett., 80(2)*, 377, 2009.

- D'Amico, S., Malagnini, L., Akinci, A., Herrmann, R.B., Mayeda, K., Empirical-stochastic Ground-motion Prediction for Taiwan, *Seism. Res. Lett.*, 80(2), 383, 2009.
- Dreger, D.S., R.M. Nadeau, and A. Chung, Finite-Source Models and Scaling of Parkfield Seismicity, *Seism. Res. Lett.*, 80(2), 336, 2009.
- Guilhem, A. and D.S. Dreger, Continuous seismic scanning in the region of the Mendocino Triple Junction, California, *Seism. Res. Lett.*, 80(2), 344, 2009.
- Hellweg, M., D. Dreger and B. Romanowicz, Comprehensive Test Ban Monitoring: Contributions from Regional Moment Tensors to Determine Source Type and Depth. *Seismol. Res. Lett.*, 80(2), 297, 2009.
- Hellweg, M., A. Cannata, S. Gresta, S. Ford, G. Di Grazia, Moment tensors for Very Long Period Signals at Etna Volcano, Italy. *Seismol. Res. Lett.*, 80(2), 349, 2009.
- Johanson I.A. and R. Bürgmann, Complex Rupture During and After the 2003 San Simeon Earthquake Determined from Multiple SAR Interferograms, *Seism. Res. Lett.*, 80(2), 324, 2009.
- Malagnini, L., S. Nilsen, K. Mayeda, Computing Dynamic Friction on Faults: Self-similarity as an Indication of Fault Maturity?, *Seism. Res. Lett.*, 80(2), 336, 2009
- Mayeda, K. and L. Malagnini, Apparent Stress from Coda-derived source ratios: Regional Variations, Similarities, and Differences, *Seism. Res. Lett.*, 80(2), 336, 2009.
- Mayeda, K. and L. Malagnini, Apparent Stress Variations in Japan and Correlation to Average Rupture Velocity, *Seism. Res. Lett.*, 80(2), 342, 2009.
- Nadeau, R.M. and A. Guilhem, Evolution of Non-Volcanic Tremor Beneath the San Andreas Fault at Monarch Peak, CA, *Seism. Res. Lett.*, 80(2), 362, 2009.
- Phillips, W.S., K. Mayeda, L. Malagnini, C.A. Rowe, Developments in Regional Phase Amplitude Tomography, *Seism. Res. Lett.*, 80(2), 360, 2009.
- Porritt, R.W., Allen, R.M., Brudzinski, M.R., Boyarko, D.C., Hinojosa, H.R., Moschetti, M.P., Lin, F., Ritzwoller, M.H., Shapiro, N.M., Imaging Lithospheric Structure in the Pacific Northwest with Ambient Noise Tomography, *Seism. Res. Lett.* 80(2), 371, 2009.
- Viegas, G., R.E. Abercrombie, K. Mayeda, W.-Y. Kim, Earthquake Source Parameters in the Northeastern United States, *Seism. Res. Lett.*, 80(2), 342, 2009.
- Zechar, J.D. and R.M. Nadeau, Predictability Experiments with Repeating Microearthquakes, *Seism. Res. Lett.*, 80, 377, 2009.

## **Second International Workshop on Earthquake Early Warning, Kyoto Univeristy, Uji, Japan, April 21-22, 2009**

- Allen, R.M. Early warning testing and development in California with a focus on ElarmS (invited).
- Allen, R.M, H. Brown, M. Hellweg, O. Khainovski and D. Neuhauser, ElarmS across California: Current realtime performance and future outlook.
- Brown, H., and Allen, R.M., Testing ElarmS with Japanese Earthquakes
- Maechling, P., M. Bse, G. Cua, T.H. Jordan, T. Heaton, E. Hauksson, R. Allen, M. Hellweg, Proposed Time Measurement Model for Earthquake Early Warning Systems.

## **31st Course of the International School of Geophysics International Workshop on Real Time Seismology: Rapid Characterization of the Earthquake Source and of its Effects, Erice, Italy, May 2-5, 2009**

- Dreger, D. S., Moment tensors: an introduction
- Dreger, D. S., Fast source estimation from moment tensors to finite faults

## **EarthScope Annual Meeting, Boise, Idaho, May 12-15, 2009**

- Dueker, K., H. Yuan, J. Stachnick and D. Schutt, New Yellowstone crustal thickness and velocity maps: Constraining magma additions and induced crustal outflow along the eastern Snake River Plain and Yellowstone Park hotspot track
- Johanson I.A., R. Bürgmann, A. Ferretti and F. Novali, Time-Dependent Deformation in the Eastern San Francisco Bay Area from InSAR Permanent Scatterers, SBAS and GPS
- Obrebski, M., Allen, R., Xue, M. and Hung, S.-H., Crossing the Rocky Mountain Front: Imaging tectonic processes across western North America
- Porritt, R., Allen, R., Shapiro, N., Brudzinski, M., Boyarko, D., and O'Driscoll, L., Lithospheric structure of the Pacific Northwest with Ambient Noise Tomography and Flexible Arrays
- Yuan, H., B. Romanowicz, D. Abt and K. Fischer, 3-D Isotropic and Anisotropic S-velocity Structure in the North American Upper Mantle

## **2009 Gordon Research Conference: Interior of the Earth, Mount Holyoke College, South Hadley, MA, May 14-19, 2009**

- Cottaar, S., Cupillard, P., McNamara, A., Romanowicz, B. and Wenk, R., Testing hypotheses for the origin of seismic anisotropy at the base of the mantle
- Yuan, H., B. Romanowicz, D. Abt and K. Fischer, 3-D Isotropic and Anisotropic S-velocity Structure in North America.

## **CIDER'09 Community Workshop, Marshall, CA, May 17-20, 2009**

- Cupillard, P., Capdeville, Y., Stehly, L., and Romanowicz, B., Recovering the attenuation of surface waves from noise correlation : synthetic tests in a spherically symmetric Earth
- Obrebski, M., Allen, R., Xue, M. and Hung, S.-H., Crossing the Rocky Mountain Front: Imaging tectonic processes across western North America

## **American Geophysical Union, 2009 Joint Assembly, Toronto, ON, May 24-27, 2009**

- Audet, P., M. G. Bostock, N. I. Christensen, and S. M. Peacock, The seismic signature of high pore-fluid pressure within subducting oceanic crust using receiver functions, *Eos Trans. AGU, 90(22)*, Jt. Assem Suppl., Abstract T33A-02.
- Audet, P., M. G. Bostock, J. Mercier, and J. F. Cassidy, Mapping the northern limit of subduction in Cascadia using POLARIS broadband seismic stations, *Eos Trans. AGU, 90(22)*, Jt. Assem Suppl., Abstract S34A-01 (Invited).

## **International Scientific Studies Project, 2009 Conference, Vienna Austria, June 10-12, 2009**

- Hellweg, M., D. Dreger and B. Romanowicz. Comprehensive Test Ban Monitoring: Contributions from Regional Moment Tensors to Determine Source Type and Depth.
- Guilhem, A. and D.S. Dreger, Continuous seismic scanning in the region of the Mendocino Triple Junction, California.

## **Speaking Engagements**

- Allen, R.M. Warning for the next earthquake: Rapid data analysis before the ground shakes. Innovators Summit, San Francisco, October 2008.
- Allen, R.M., M. Xue, S.-H. Hung, Plume vs Plate: Convective interactions beneath western North America. Earth Science Colloquium, Lamont-Doherty Earth Observatory, Columbia University, New York, NY, October 2008.

- Allen, R.M., M. Xue, S.-H. Hung, Plume vs Plate: Convective interactions beneath western North America. Division of Geological and Planetary Sciences Seminar, California Institute of Technology, Pasadena, CA, October 2008.
- Allen, R.M. Warning for the next earthquake: Progress and prospects for California and around the world. National Research Council Committee on Committee on Seismology and Geodynamics, Irvine, CA, November 2008.
- Allen, R.M., M. Xue, S.-H. Hung, Plume vs. plate: Convective interactions in the mantle beneath western North America. Institut de Physique du Globe de Paris, Paris, France January 2009.
- Allen, R.M., CISN testing of earthquake early warning algorithms: Status and opportunities. Advisory committee for the California Integrated Seismic Network, Menlo Park, CA. January 2009.
- Allen, R.M. Plume vs. Plate: Convective interactions in the mantle beneath the western US. Earth and Planetary Sciences, UC Santa Cruz, Santa Cruz, CA, February 2009.
- Allen, R.M. Plume vs. Plate: Convective interactions in the mantle beneath the western US. Earth and Space Sciences, UC Los Angeles, Los Angeles, CA, February 2009.
- Allen, R.M. Plume vs. Plate: Convective interactions in the mantle beneath the western US. Geophysics seminar series, Stanford University, Palo Alto, CA, February 2009.
- Allen, R.M., Earthquake imminent warning: An approach and outlook for California. Seismology seminar, California Institute of Technology, Pasadena, CA, February 2009.
- Allen, R.M. Earthquake Alert System: Warning before shaking across California. Earth and Environmental Sciences, New Mexico Tech, Socorro, NM, March 2009.
- Allen, R.M. Warning for the next earthquake Progress and prospects in California and around the world. California Department of Water Resources, Sacramento, CA, March 2009.
- Allen, R.M. California Integrated Seismic Network Early warning status and opportunities. Bay Area Regional Transit, Engineering Division, Oakland, CA, April 2009.
- Audet, P., Subduction zone forearc structure in Cascadia and its relation with episodic tremor and slip”, Berkeley Seismological Laboratory Seminar, UC Berkeley, Berkeley, CA, November 25, 2008.
- Audet, P., Mouvements episodiques aux zones de subduction (Episodic movements at subduction zones), GEOTOP Research Center, Annual Student Meeting, Montreal, Quebec, Canada, January 18, 2009.
- Audet, P., Episodic Tremor and Slip: New insights into fault behavior, McGill University, Dept. of Earth and Planetary Sciences, Montreal, Quebec, Canada, February 9, 2009.
- Audet, P., Subduction forearc structure and its relation with episodic tremor and slip, US Geological Survey, Menlo Park, CA, March 4, 2009.
- Audet, P., Seismic evidence for overpressured subducted oceanic crust and sealing of the megathrust: Relations with episodic tremor and slip, California Institute of Technology, Seismological Laboratory, Pasadena, CA, April 3, 2009.
- Audet, P., Seismic evidence for overpressured subducted oceanic crust and sealing of the megathrust: Relations with episodic tremor and slip, UC Santa Cruz, Institute of Geophysics and Planetary Physics, Santa Cruz, CA, May 1, 2009.
- Audet, P., The fate of water in the forearc of Cascadia subduction zone, Carnegie Institution of Washington, Dept. of Terrestrial Magnetism, Washington, DC, November 4, 2009.
- Bürgmann, R., Lithosphere Rheology from Postseismic Deformation: What’s for Dessert?, University of Southern California, Los Angeles, CA, March 23, 2009.
- Bürgmann, R., Earthquake potential of the Hayward fault, INPA Seminar, LBNL, Berkeley, CA, May 1, 2009.
- Bürgmann, R., Lithosphere Rheology from Postseismic Deformation, Ludwig Maximilian University, Munich, Germany, June 30, 2009.

- Bürgmann, R., Active Tectonics and Non-Tectonics of the San Francisco Bay Area from InSAR, DLR, Oberpfaffenhofen, Germany, July 3, 2009.
- Cupillard, P., Spectral Element simulation of waveforms obtained by seismic noise correlation, Berkeley Seismological Laboratory Seminar, UC Berkeley, Berkeley, CA, October 21, 2008.
- Dreger, D. S., Realtime source analysis at Berkeley, Korean Meteorological Agency, Seoul, Republic of Korea, November 13, 2008.
- Dreger, D. S., Multiscale observations of earthquake rupture kinematics at Parkfield, California, Seoul National University, Seoul, Republic of Korea, November 14, 2008.
- Dreger, D. S., Finite source parameters of microearthquakes at Parkfield California, IPGP, January 6, 2009.
- Grijalva, K., Deformation and Stress Changes on the Sunda Megathrust Preceding the Mw 8.4 2007 Earthquake, USGS Earthquake Seminar Series, Menlo Park, CA, October 29, 2008.
- Hellweg, M., A tectonic timebomb: The Hayward Fault. Teacher training workshop of the Lawrence Hall of Science, UC Berkeley, Berkeley, CA, October 18, 2008.
- Hellweg, M., The Hayward Fault on the UC Berkeley Campus, Field trip for Bay Nature Magazine, November 8, 2008.
- Hellweg, M., Earthquakes at Berkeley? The Hayward Fault, Campus Retrofit and the Seismological Laboratory, Field trip for the Northern California Geological Society, November 15, 2008.
- Hellweg, M., Just a Moment: From Regional Seismograms to Earthquake (and Other) Sources, Stanford University Geophysics Seminar, Stanford, CA, April 9, 2008.
- Hellweg, M., Below Zero: Scaling and Complexity in Small Earthquakes, Istituto Nazionale de Geofisico e Vulcanologia, Catania, June 25, 2009.
- Houlié, N., Can we do seismology with GPS?, Lamont Doherty Observatory, Columbia University, New York, NY, December, 2, 2008.
- Houlié, N., Can we do seismology with GPS?, Institut de Physique du Globe de Strasbourg, EOST, Strasbourg, France, February, 20, 2009.
- Houlié, N., Constraints on volcano processes using Global Positioning System, Earth Observatory of Singapore, Nanyang Technological University, Singapore, Singapore, March, 5, 2009.
- Houlié, N., Can we do seismology with GPS?, Earth Observatory of Singapore, Nanyang Technological University, Singapore, Singapore, March 5, 2009.
- Houlié, N., Constraints on intruded magma volumes into volcanoes, invited presentation, University of Leeds, Leeds, UK, May 11, 2009.
- Houlié, N., Asymmetric deformation across the San Francisco Bay Area faults from GPS observations in northern California, invited presentation, GFZ, Potsdam, Germany, June 15, 2009.
- Johanson, I. A., Stable and transient motion on Kilauea's south flank from InSAR Persistent Scatterers, Lawrence Livermore National Laboratory, Geophysical Monitoring Program Seminar, Livermore, CA, January 6, 2009.
- Johanson, I. A., Stable and transient motion on Kilauea's south flank from InSAR Persistent Scatterers, UC Berkeley, Berkeley Seismological Laboratory Seminar, Berkeley, CA, September 1, 2009.
- Mayeda, K., Small event yield and source characterization using local P and S-wave coda spectra, Air Force Research Laboratory TIM, Hanscom AFB, MA, September 22, 2008.
- Mayeda, K., Earthquake scaling for the Chi-Chi Taiwan sequence and similarity to other recent sequences, IPG, Paris, France, January 8, 2009.
- Mayeda, K., A New Approach to Constrain Earthquake Source Scaling: On the Path to Improving MDAC, Attenuation, and Yield Estimation, Air Force Technical Applications Center, Patrick Air Force Base, FL, March 3, 2009.

- Mayeda, K., Earthquakes and Seismic Hazard in our Backyard, Cal Day, UC Berkeley, Berkeley, CA, April 18, 2009.
- Mayeda, K., Earthquakes and the Hayward Fault, St. Theresa School, Oakland, CA, May 28, 2009.
- Romanowicz, B., Elastic and anelastic tomography of the Earth's mantle: Inferences on global dynamics, Department of Earth Sciences, Arizona State University, October 2008
- Romanowicz, B., Les defies en sismologie globale, Invited Lecture, Ecole d'ete de Physique, Les Houches, France, October 2008.
- Romanowicz, B., The Monterey Bay Ocean Bottom Broadband Observatory, Monterey Bay Aquarium Research Institute: April 10, 2009:
- Romanowicz, B., Waveform tomography of the Earth's mantle: Inferences on global dynamics, seminar Department of Earth Sciences, UC Santa Cruz, May 2009
- Romanowicz, B., Seismic Waveform tomography in the age of high-speed computing, Invited talk, Gordon Research Conference on the Interior of the Earth, June 15, 2009, Mt Holyoke College, Mass.
- Romanowicz, B., What is the Berkeley Seismological Laboratory, California Office of Emergency Services, March 19, 2009
- Romanowicz, B., The Earth's hum: bridging the gap between seismology and oceanography, Distinguished Faculty Speaker, Department of Earth and Planetary Science, U.C. Berkeley. April 10, 2009
- Ryder, I. and Bürgmann, R., Probing the rheology of Tibet using postseismic motion from large earthquakes, USGS Earthquake Seminar, Menlo Park, CA, October 1, 2008.
- Taira, T., Seismic Evidence for Remote Triggering of Fault-Strength Changes on the San Andreas Fault at Parkfield, Lawrence Berkeley National Laboratory Geophysics Friday Seminar, Berkeley, CA, March 20, 2009.
- Taira, T., Seismic Evidence for Remote Triggering of Fault-Strength Changes on the San Andreas Fault at Parkfield, U.S. Geological Survey Earthquake Hazards Seminar, Menlo Park, CA, April 29, 2009.
- Thomas, A., R. Nadeau, R. Bürgmann, and A. Guilhem, Tremor-tide correlations and near-lithostatic pore pressure on the deep San Andreas fault, Tohoku University Seminar, Sendai, Japan, June 26, 2009.

## Panels and Professional Service

### Richard M. Allen

- Chair, IRIS PASSCAL Standing Committee. December 2008-present. Member, December 2007-present.
- Guest Editor, Seismological Research Letters, Special Issue: Application of earthquake early warning around the world. Published September 2009.
- Member, Writing Committee developing the science plan for NSF's Cascadia Amphibious initiative. Lamont, New York. June 2009.
- Member, Organization Committee for 2nd International Earthquake Early Warning Workshop. Kyoto, Japan. April 2009.
- U.S. participant, European Commission project "Seismic Early Warning Across Europe," June 2006 to June 2009.
- Chair, Organization committee, Flexi-RAMP concept development workshop. Monterey, California, April 2009.
- Guest Editor, Geophysical Research Letters, Special Section: New methods and applications of earthquake early warning. Published March 2009.
- Convener, Special session: Investigation and Public Awareness of Earthquake Hazard in Northern California, AGU December 2008.
- Member, Writing Committee for the Long-Range Science Plan for Seismology, October 2008.
- Member, IRIS Nominating Committee. 2008.

### Pascal Audet

- Convener and session chair, AGU Joint Assembly, Toronto, ON, May 24-27, 2009 Seismic Structure and Dynamics of Convergent Boundary Zones (T33A)

## **Roland Bürgmann**

Associate Editor, Bulletin of the Seismological Society of America  
Editorial Advisory Board, Eos  
Editorial Board, Earth and Planetary Science Letters  
Member, UC Berkeley Graduate Fellowship Committee  
Member, NASA proposal review panel, Earth Surface and Interior  
Member, SSA Board Of Directors  
Member, EarthScope PBO Standing Committee  
Vice-chair, WInSAR Standing Committee  
Co-chair, EarthScope Thematic Working Group on Crustal Strain and Deformation

## **Douglas S. Dreger**

Member, COSMOS Board of Directors  
Member, Golden Gate Bridge Instrumentation Committee  
Reviewer of manuscripts for BSSA, GRL, JGR, and PRL.  
Reviewer of proposals submitted to NSF and NNSA.  
Associate Director, BSL, 2002-  
Acting Director, BSL, Jan-July, 2008

## **Margaret Hellweg**

Member, CISN Program Management Committee  
Member, CISN Standards Committee  
Member, CISN Steering Committee  
Member, CISN Outreach Committee  
Member, ANSS Performance Standards Committee  
Member: 1868 Commemoration Committee  
Member: 1868 Commemoration Executive Committee  
Chair: 1868 Committee for Developing Education and Outreach Materials and Programs  
Member: Bay Area Earthquake Alliance Committee  
Member: Bay Area Earthquake Alliance Executive Committee  
Member: Organizing Committee Third Conference on East Bay Earthquake Hazards (Oct 21-25, 2008)  
Member, Editorial Board of Journal of Volcanology and Geothermal Research

## **Douglas S. Neuhauser**

Chair, Standards Group, California Integrated Seismic Network (CISN)  
Acting Member, CISN Program Management Committee

## **Barbara Romanowicz**

Reviewing Editor for Science  
Seismology Coordinator, International Scientific Review of the IMS  
Member, AGU Fellows Committee  
Member, Advisory Committee for College de France, Paris, France  
Member, Conseil d'Administration, Institut de Physique du Globe, Paris, France  
Member, Advisory Committee, Geophysical Institute, University of Alaska, Fairbanks  
Member, National Earthquake Prediction Evaluation Council  
Member, CISN Steering Committee (Chair 2009-2010)  
Member, NRC's Board on Earth Sciences and Resources (BESR)  
Member, Geophysics Panel, NSF  
Lead organizer, CIDER 2008 summer program in Santa Barbara  
Co-Chair, Long Range Science Plan for Seismology, Workshop  
Lead organizer, CIDER Community Workshop, Marconi Center, CA, May 17-20, 2009

## **Robert A. Uhrhammer**

Member, International Association of Seismology and Physics of the Earths Interior, Working Group on Magnitudes  
Member, California Integrated Seismic Network, Magnitude Working Group  
Member, American National Seismic System, Technical Integration Committee, Working Group D, Seismic Instrumentation

## **Taka'aki Taira**

Member, California Integrated Seismic Network, Standards Committee  
Member, California Integrated Seismic Network, ShakeMaps Working Group  
Member, Plate Boundary Observatory, Data Working Group

APPENDIX II  
Seminar Speakers 2008-2009

WATSON, HEATHER  
Lawrence Livermore National Laboratory  
*"Permeability of Core Forming Partial-Melts--Experimental Constraints"*  
Tuesday, August 22, 2008

CAMPILLO, MICHEL  
Université Joseph Fourier de Grenoble  
*"Imaging and monitoring with seismic ambient noise: correlation and disorder"*  
Tuesday, September 2, 2008

NIU, FENGLIN  
Rice University  
*"Seismic imaging of Earth's deep interior: Implications for mantle and core dynamics"*  
Tuesday, September 9, 2008

FREUND, MINORU  
NASA Ames Research Center  
*"The Science for an Earthquake Early Warning System"*  
Tuesday, September 16, 2008

FINNEGAN, NOAH  
Berkeley Seismological Laboratory  
*"Constraints on active volcanic and tectonic processes from integrating InSAR time series analysis and geomorphology"*  
Tuesday, September 23, 2008

RUBINSTEIN, JUSTIN  
US Geological Survey  
*"Stress Triggering of Non-Volcanic Tremor"*  
Tuesday, September 30, 2008

BEGHEIN, CAROLINE  
University of California, Los Angeles  
*"Seismic Anisotropy in the Nevada Great Basin: Evidence for Lithospheric Delamination?"*  
Tuesday, October 7, 2008

PRIETO, GERMÁN  
Stanford University  
*"Anelastic Earth Structure from the Coherency of the Ambient Seismic Field"*  
Tuesday, October 14, 2008

CUPILLARD, PAUL  
Berkeley Seismological Laboratory  
*"Spectral Element Simulation of Waveform Obtained by Ambient Seismic Noise Correlation"*  
Tuesday, October 21, 2008

COCHRAN, ELIZABETH  
University of California, Riverside  
*"Seismic and Geodetic Evidence For Wide, Long-Lived Fault Damage Zones"*  
Tuesday, October 28, 2008

AMPUERO, JEAN PAUL  
California Institute of Technology  
*"Rate-and-state models of slow slip and tremor phenomena"*  
Tuesday, November 4, 2008

McNAMARA, ALLEN  
Arizona State University  
*"In the pursuit of understanding large scale mantle dynamics"*  
Tuesday, November 18, 2008

AUDET, PASCAL  
Berkeley Seismological Laboratory  
*"Subduction zone forearc structure in Cascadia and its relation with episodic tremor and slip"*  
Tuesday, November 25, 2008

SLAWINSKI, MICHAEL  
Memorial University  
*"On seismology as a branch of continuum mechanics"*  
Tuesday, December 2, 2008

MURRAY, JESSICA  
US Geological Survey  
*"Geodetic Estimates of Creep on the Bartlett Springs Fault"*  
Tuesday, December 9, 2008

PASYANOS, MICHAEL  
Lawrence Livermore National Laboratory  
*"Broadband Lg Attenuation Modeling in the Middle East"*  
Tuesday, January 27, 2009

KAPPLER, KARL  
Berkeley Seismological Laboratory  
*"Long-Term Monitoring of ULF Electromagnetic Fields at Parkfield, CA"*  
Tuesday, February 3, 2009

OGLESBY, DAVID  
University of California, Riverside  
*"Fault Dynamics and Ground Motion on  
the North Anatolian Fault in the Sea of  
Marmara"*  
Tuesday, February 10, 2009

MORRIS, STEVE  
University of California, Berkeley  
*"On a similarity principle relating  
attenuation of seismic waves to creep at  
Geological Timescales"*  
Tuesday, February 17, 2009

RYCHERT, CATHERINE  
University of California, San Diego  
*"A Global Lithosphere-Asthenosphere  
Boundary"*  
Tuesday, February 24, 2009

FOUCH, MATT  
Arizona State University  
*"Plate Tectonics and the Mantle Flow Field  
Beneath Western North America"*  
Tuesday, March 3, 2009

STACKHOUSE, STEPHEN  
University of California, Berkeley  
*"Insights into the lower mantle from ab  
initio simulations"*  
Tuesday, March 10, 2009

MYERS, STEVE  
Lawrence Livermore National Laboratory  
*"Numerical experiments investigating the  
source of explosion S-waves"*  
Tuesday, March 17, 2009

OBREBSKI, MATHIAS  
Berkeley Seismological Laboratory  
*"Seismic Anisotropy Around the Northern  
Gulf of California Region from SKS  
Splitting and Receiver Functions"*  
Tuesday, March 31, 2009

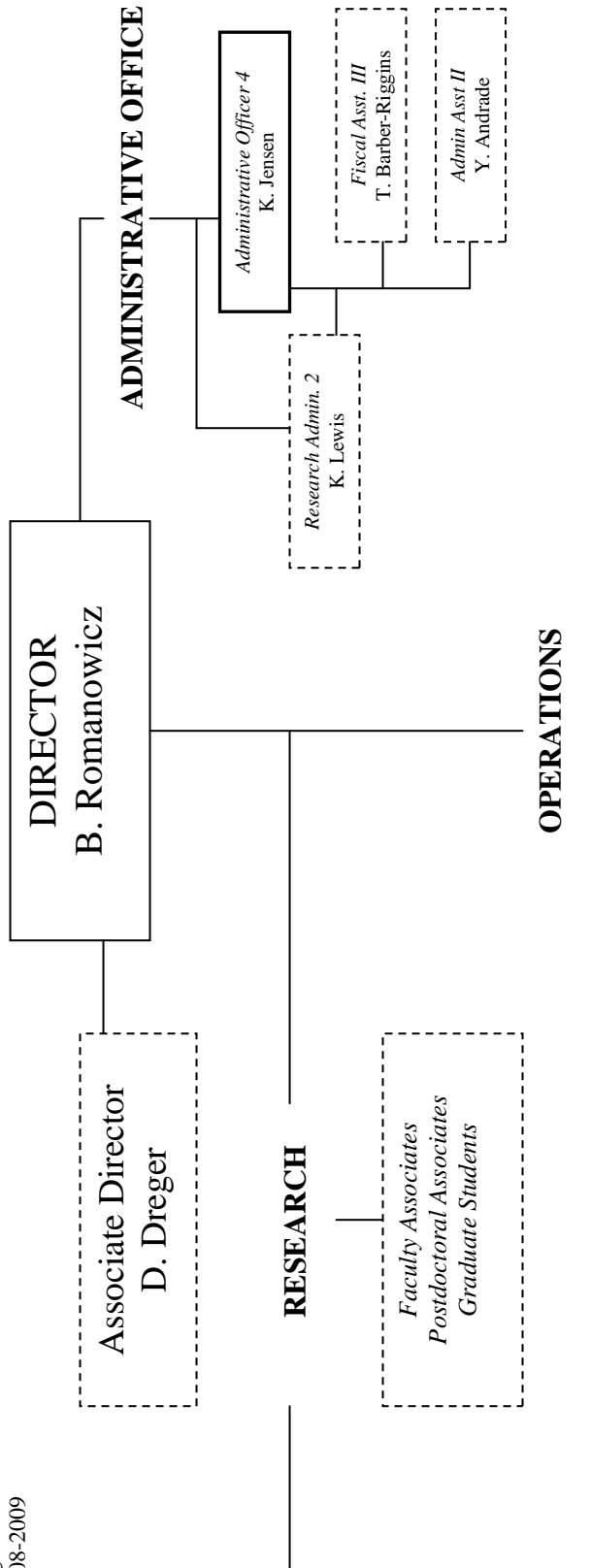
MATSUI, HIROAKI  
University of California, Berkeley  
*"Sub-grid scale model for geodynamo  
simulations"*  
Tuesday, April 7, 2009

POLAND, CHRIS  
Lawson Lecture  
Degenkolb Engineers  
*"Building Resilient Communities: Fresh  
Challenges for Earthquake Professionals"*  
Tuesday, April 14, 2009

KIM, AHYI  
Berkeley Seismological Laboratory  
*"1D and 3D effects on finite source  
inversion: Examples from Parkfield"*  
Tuesday, April 21, 2009

CROWELL, BRENDEN  
University of California, San Diego  
*"California Real Time Network: Test bed  
for early warning systems"*  
Tuesday, April 28, 2009

CUEVAS, NESTOR  
University of California, Berkeley  
*"Electrokinetic coupling in hydraulic  
fracture propagation"*  
Tuesday, May 5, 2009



**BORDER LEGEND**

- Permanently Funded Positions
- - - Temporarily Funded Positions
- . - . Mix of Perm & Temp Funding
- ..... Indirect Supervision